Numerical Simulation and Analysis of a Series of Mesoscale Convective Systems

by
James F. Bresch

Department of Atmospheric Science
Colorado State University
Fort Collins, Colorado

Colorado State University

Department of Atmospheric Science

Paper No. 558

NUMERICAL SIMULATION AND ANALYSIS OF A SERIES OF MESOSCALE CONVECTIVE SYSTEMS

by

James F. Bresch

Department of Atmospheric Science
Colorado State University
Fort Collins, CO 80523

Summer 1994

Atmospheric Science Paper No. 558

ABSTRACT

NUMERICAL SIMULATION AND ANALYSIS OF A SERIES OF MESOSCALE CONVECTIVE SYSTEMS

A case in which a series of mesoscale convective systems (MCSs) traversed across Kansas and Oklahoma (3-4 June 1985), was examined using observations and the MM4 model. The first MCS in the series (MCS1) began north of a stationary front in a region of strong low-level warm advection and moisture convergence near the terminus of a low-level jet (LLJ). Simulations of this system evolved realistically and show that the elevated convection fed on air riding over the frontal inversion. This source air was found to originate in the heated boundary layer over Texas and Oklahoma the previous afternoon. The system-relative circulation of the simulated mature system did not exhibit a front-to-rear upper-level flow, nor an extensive trailing stratiform region as has been observed with other systems.

The second MCS (MCS2) was linked to an upper-level jet streak throughout its lifetime. During its early stages, the simulated MCS2 consisted of high-based convection which intensified as it moved into a region of greater low-level instability. In agreement with previous observational studies, the simulation produced the two precipitation bands within MCS2 that gave it the appearance of a miniature occluded cyclone. The north-south band, located in the southern half of the system, consisted of surface-based convection forced by low-level convergence of convective downdrafts with the environmental flow, while the northeast-southwest band in the northern part of the system was comprised of elevated convection occurring in a frontogenetic zone. Convection in this region was initially triggered by a LLJ induced by transverse ageostrophic circulations about an approaching upper-level jet streak. The strong LLJ was decoupled from the surface by the frontal inversion, and was able to advect high-θ_E air northwestward, destabilizing the airmass. Sensitivity studies show that the LLJ was not the result of outflow from MCS1. A conceptual model of the jet-frontal circulations in the region of an east-west stationary surface front is presented.

The simulation of MCS1 was found to be sensitive to the initial low-level moisture distribution, suggesting that accurate prediction of elevated convection requires initial conditions that include mesoscale details aloft. In agreement with a previous study, the simulation was found to be quite sensitive to the convective trigger function. For weakly-forced cases such as 3-4 June, the trigger function is a critical component of the convective parameterization. The behavior of trigger functions based on low-level vertical motion, on the depth between source air and the level of free convection, and on the convective inhibition are examined.

The results indicate that predicting MCSs (particularly in weakly-forced environments) is quite difficult. Due to the complexity and multiple scales of the systems, further understanding of MCSs will require additional observational studies, especially during their early stages.

ACKNOWLEDGEMENTS

An undertaking of this magnitude would not have been possible without the generous cooperation of many people. My committee members, William Gray, Hariharan Iyer, Ying-Hwa Kuo, and Steven Rutledge provided valuable input. Thanks to Ying-Hwa Kuo of NCAR for providing access to the MM4 model. Georg Grell, Dave Gill, Sue Chen, and Jimy Dudhia of NCAR generously assisted with the MM4 model. Special thanks are extended to Jack Kain of Pennsylvania State University for making his parameterization and trigger function code available. Thanks to Jason Nachamkin, Ray McAnelly, Greg Stumpf, Bill Gallus, Paul Cielsieski, Ken Hart, Michael Dudek, David Stensrud, and Da-Lin Zhang for programming assistance and/or helpful discussions. John Augustine and José Meitín of the National Severe Storms Laboratory supplied the PRE-STORM data. The advice of John Sheaffer and Bruce Macdonald is also appreciated. Thanks to Gail Cordova for help with manuscript preparation and general logistics and to Judy Sorbie-Dunn for drafting some of the figures.

Finally, my greatest appreciation goes to my advisor, Dick Johnson, who shows by example how to be a gentleman and a scientist.

This research was supported by the National Science Foundation Grant ATM-9013112. Computations were performed on the National Center for Atmospheric Research's Cray Y-MP.

LIST OF TABLES

2.1 Characteristics of the 3-4 June 1985 MCSs. 20
3.1 MM4 Version 7 nested grid model characteristics. 89
3.2 Model half-sigma levels. Pressure values are given for a surface pressure of 900 mb and model top of 100 mb. 91
3.3 Adjusted albedo values due to the low-cloud fraction $C_L(\overline{RH})$ 94
3.4 Summary of Simulations. 108

TABLE OF CONTENTS

1 Introduction **1**
1.1 Observational studies of MCSs 1
1.2 Numerical simulations of MCSs 10
1.2.1 Simplified modeling studies 11
1.2.2 Three-dimensional modeling of real-data cases 12

2 Observations of the 3-4 June case **18**
2.1 General overview 18
2.2 Summary of previous 3-4 June studies 21
2.3 Data 28
2.4 Observational analysis of the case 30
2.4.1 Conditions between 3/0000 and 3/1200 30
2.4.2 Conditions between 3/1200 and 4/0000 42
2.4.3 Conditions after 4/0000 82
2.5 Summary 82

3 Description of the MM4 model **88**
3.1 Planetary Boundary Layer Parameterization 93
3.2 Explicit Precipitation 95
3.3 Implicit Precipitation 95
3.3.1 KF scheme 96
3.3.2 AS scheme 97
3.4 Miscellaneous Parameterizations 98
3.5 Initial Conditions 98
3.6 Description of Simulations 106

4 Results from the control experiment **109**
4.1 Overview of the coarse grid simulation 110
4.2 Evolution of MCS1 114
4.3 Evolution of MCS2 135
4.4 Summary 167

5 Some sensitivity experiments **169**
5.1 Sensitivity to changes in the initial data 169
5.1.1 No Upper-Level Jet Streak 169
5.1.2 Dry Run 177
5.1.3 No MCS1 192
5.1.4 NMC First Guess 197
5.1.5 3/0000 Initial Time 204

5.2 Sensitivity to changes in the moist physics parameterizations 223
5.2.1 Convective Trigger Function Tests 223
5.2.2 Arakawa-Schubert Scheme 237
5.2.3 Precipitation Efficiency 244
5.2.4 Increased vertical resolution 247
5.3 Summary 248

6 Summary and Conclusions **252**

REFERENCES **259**

APPENDIX **283**

LIST OF FIGURES

1.1 Composite analysis of features at a) surface, b) 850 mb, and c) 200 mb prior to MCC development. Winds (full barb = 5 m s^{-1} ; flag = 25 m s^{-1}) are plotted at every other grid point. In a), isobars (in mb, solid lines, contoured every 2 mb with the leading "10" omitted), surface divergence (x10^{-5} s^{-1}, dashed), and frontal position are shown. In b) and c), heights (m) are heavy solid, isotherms (° C) are dashed and jet position is indicated by the heavy arrow. In b), mixing ratio (in g kg^{-1}, light solid) and terrain above the 850 mb level (hatched) are shown. (After Maddox 1983 and Uccellini 1990). 2

1.2 Schematic vertical cross sections for late afternoon (top) and night (bottom), over the region of the surface geostrophic wind maximum for cases with large, long-lived MCSs. Isentropes are short-dashed lines with warmer values to the south, solid arrows are the actual wind, dashed arrows are the geostrophic wind, open circles with enclosed x's represent flow into the figure (easterly winds), while the open circle with an enclosed dot indicates flow out of the figure (westerly winds). Long-dashed lines indicate the top of the planetary boundary layer (PBL). (After Augustine and Caracena 1993). 6

2.1 Tracks of the approximate centroids of the four 3-4 June MCSs. Dotted lines indicate Pre-MCC convection, the X symbol shows the termination point of the MCS, and the mean position of the surface stationary front during the episode is shown. Adapted from Trier and Parsons (1993). 19

2.2 Composite conventional radar image from 4/0030 showing the mature MCS2. Alternating shading corresponds to minimum dBZ thresholds as follows: medium gray - 15, light gray - 30, black - 40, medium gray - 46, light gray - 52, and black - 58 dBZ. 22

2.3 Conceptualized three-dimensional overview of the mature MCS2 from a vantage point located southwest of the storm. Broad horizontal arrows represent horizontal relative flow. The bottom panel shows the relevant thermal boundaries. Deeper mesoscale vertical circulations are represented by the broad vertical arrows. Intense updrafts are depicted by the narrow, solid vertical arrows. [From Smull and Augustine 1993]. 23

2.4 Schematic of the surface pressure and flow fields associated with: a) symmetric and b) asymmetric MCS structures. Arrows represent the surface flow. (From Loehrer 1992). 24

2.5 North-south cross-section schematic of the flow and frontal surface associated with MCS4. (From Trier and Parsons 1993). 27

2.6 Locations and identifiers for a) the PAM/SAM mesonetwork; b) surface airways stations; c) Radiosonde stations. 29

2.6 Continued. 30
2.7 Surface analysis for 3/0000. Conventional plot of temperature and dewpoint (° C), winds (one-half barb = 2.5 m s^{-1} and a full barb = 5 m s^{-1}), and isobars (contoured every mb, labels omit the leading "10"). The surface front is indicated by the dark, wide line. 31
2.8 Contours of infrared brightness temperature. Temperature thresholds are -32° C, -54° C, -58° C, -64° C, -70° C, and -76° C with darker shading representing colder temperatures for a) 3/0000, b) 3/0100, c) 3/0200, d) 3/0300, e) 3/0400, f) 3/0500, g) 3/0600, h) 3/0700, i) 3/0800, j) 3/0900, k) 3/1000, and l) 3/1100. 33
2.8 Continued. 34
2.8 Continued. 35
2.8 Continued. 36
2.8 Continued. 37
2.8 Continued. 38
2.9 Geopotential height (m) at 500 mb contoured every 20 m at 3/0000. 39
2.10 Conventional pressure level plot of 850 mb data for 3/0000. Shown are temperature and dewpoint (° C) and heights (dm). A full wind barb represents 5 m s^{-1} , a half-barb 2.5 m s^{-1} , and a flag represents 25 m s^{-1} 40
2.11 As in Fig. 2.10, but for 250 mb. 41
2.12 As in Fig. 2.11, but for 3/0230. 41
2.13 As in Fig. 2.10, but for 3/0530. 42
2.14 As in Fig. 2.11, but for 3/0530. 43
2.15 Surface plot (as in Fig. 2.7) at 3/1200. 44
2.16 As in Fig. 2.8, but for a) 3/1200, b) 3/1300, c) 3/1400, d) 3/1500, e) 3/1600, f) 3/1700, g) 3/1800, h) 3/1900, i) 3/2000, j) 3/2100, k) 3/2200, and l) 3/2300. 45
2.16 Continued. 46
2.16 Continued. 47
2.16 Continued. 48
2.16 Continued. 49
2.16 Continued. 50
2.17 500 mb geopotential heights (as in Fig. 2.9) at 3/1200. 51
2.18 As in Fig. 2.10, but for 3/1200. 51
2.19 Horizontal temperature advection (K (12 h$)^{-1}$) on the 850 mb surface at 3/1200. 52
2.20 Profiles of a) temperature advection (K(12h$)^{-1}$), b), potential vorticity (K m s^{-3} Pa), c) θ_E (K), and d) ω (μb s^{-1}) at 3/1200 for a grid point in the eastern Oklahoma panhandle. 53
2.21 As in Fig. 2.18, but for 500 mb. 54
2.22 As in Fig. 2.18, but for 200 mb. 55
2.23 Lifted index derived from the initial data fields at 3/1200. The minimum lifted index for the levels below 700 mb is shown in a), while the lifted index for the surface parcel is shown in b). The heavy solid line shows the location of the cross section in Fig. 2.24. 57

2.24 North-south cross section along the line shown in Fig. 2.23b of a) θ_E (° K, solid contours) and circulation vectors in the plane of the cross section and b) moist potential vorticity (PVU, contoured every 0.5 PVU, negative values dashed) at 3/1200. The region where the along-cross-section component of the low-level wind exceeds 12 m s^{-1} is lightly stippled in a). Areas with relative humidity of 100% are lightly stippled in b). 58
2.25 850-300 mb thickness (m) for 3/1200. 59
2.26 Skew-T diagrams and hodographs at 3/1200 for a) DDC, b) AMA, c) MAF, d) OKC, and e) SEP. 60
2.26 Continued. 61
2.26 Continued. 62
2.27 Time-height series of the horizontal winds at Liberal, Kansas for a) 3/1100 to 3/1830 and b) 3/1800 to 4/0130. The height scale is in km above sea level. 66
2.27 Continued. 67
2.28 Spectral density for the five-minute surface pressure measurements from PAM 27 between 3/0000 and 4/0300. The smooth solid curve is the null value. Statistically significant peaks are those which exceed the arrow length plotted at the 60 minute period. 69
2.29 Time series of the filtered surface pressure data (see text) for a) PAM 26 and b) PAM 14. 71
2.30 As in Fig. 2.29, but for filtered wind data (see text). 72
2.31 Contours of objectively analyzed surface wind (a), c), e), g), i), k), m), o)) and surface pressure (b), d), f), h), j), l), n), p)) perturbations for a) and b) 3/1030, c) and d) 3/1130, e) and f) 3/1230, g) and h) 3/1330, i) and j) 3/1430, k) and l) 3/1530, m) and n) 3/1630, and o) and p) 3/1715. Negative values are dashed and radar echo outlines are the lightly stippled areas on the pressure perturbation plots. 73
2.31 Continued. 74
2.31 Continued. 75
2.31 Continued. 76
2.31 Continued. 77
2.31 Continued. 78
2.31 Continued. 79
2.31 Continued. 80
2.32 As in Fig. 2.8, but for a) 4/0000, b) 4/0100, c) 4/0300, d) 4/0400, e) 4/0600, f) 4/0700, g) 4/0900, and h) 4/1000. 83
2.32 Continued. 84
2.32 Continued. 85
2.32 Continued. 86

3.1 Model domain with the nested grid area indicated by the solid rectangle. . . . 90
3.2 Model terrain height in meters for a) the coarse grid (contour interval of 100 m) and b) the nested grid (contour interval of 50 m) domains. 92
3.3 Locations of the bogus soundings added to the RAWINS analysis at 3/1200. . . 101
3.4 Bogus soundings added to the 3/1200 RAWINS analysis for the sites shown in Fig. 3.3 from a) GEN, b) WWR, c) IBB, d) END, e) ROW, and f) TDD. . 102
3.4 Continued. 103

3.4 Continued. 104

4.1 Geopotential height (m) at 500 mb contoured every 20 m valid at 4/0000 from a) CTL 12 h simulation and b) RAWINS analysis. 111
4.2 Simulated total rainfall tendency (implicit plus explicit, in mm (3 h)$^{-1}$), on the coarse grid with an uneven contour interval 0.1, 1, 2, 5, and 10 mm valid at a) 3/1500, b) 3/1800, c) 3/2100, and d) 4/000. 112
4.2 Continued. 113
4.3 Simulated convective rainfall, with an uneven contour interval 0.1, 1, 2, 5, and 10 mm a), and observed rainfall with isopleths of 1 and 10 mm b) for the three-hour period ending 3/1500. 115
4.4 Moisture divergence (10^{-7} s^{-1}, with a contour interval of 2 x 10^{-7} s^{-1}, with negative values dashed) on the 800 mb surface at 3/1200. Areas with wind speeds greater than 10 m s^{-1} are lightly stippled. 116
4.5 Vertical profiles of convective heating (H) and drying (D) (° K day^{-1}) from the CTL run for a point in central Kansas, 176 minutes into the simulation (1456 UTC). The solid line drawn along 0° K day^{-1} begins at the surface pressure of this grid point, 964 mb. 117
4.6 Simulated convective rainfall, with an uneven contour interval 0.1, 1, 2, 5, and 10 mm a), and observed rainfall with isopleths of 1 and 10 mm b) for the three-hour period ending 3/1800. 119
4.7 Simulated 850 mb ω (μb s^{-1}) at 3/1800. Contour interval is 2 μb s^{-1} 120
4.8 Simulated column-integrated rain water (g kg^{-1}) at 3/1800. Contour interval is .05 g kg^{-1}. Lines A–B and C–D indicate cross-section locations. 120
4.9 West-east cross section at 3/1800 along the line A–B in Fig. 4.8 of a) cloud water (mg kg^{-1} contoured every 40 mg kg^{-1}, solid) and rain water (mg kg^{-1} contoured every 40 mg kg^{-1}, dashed) and b) θ (° K contoured every 4° K, quasi-horizontal solid lines) and ω (μb s^{-1} , contoured every 5 μb s^{-1} negative values are dashed, positive are solid). The line segments along the bottom of the cross-section represent 100 km. The portion of the cross-section with active implicit convection is indicated by the heavy dashed line in a). 122
4.10 Cross section at 3/1800 a) along the line A–B in Fig. 4.8 of relative circulation in the plane of the cross section (vectors, scale at the bottom right) and θ_E (° K contoured every 4° K) and b) along the line C–D in Fig. 4.8 of actual circulation in the plane of the cross section (vectors scale at the bottom right) and θ_E (° K contoured every 4° K). 124
4.11 As in Fig. 4.6, but for the period ending 3/2100. 128
4.12 Vertical profile of θ_E (curve H) and saturated θ_E (curve Q) (in ° K) for a grid point along the surface front in northern Oklahoma at 3/1840. 129
4.13 Grid point profiles from the same point as in Fig. 4.12 at 3/1840 of a) ω (μb s^{-1}), b) wind speed (m s^{-1}), c) hydrometeors (g kg^{-1}), and d) cloud water (g kg^{-1}). 130
4.14 Sea level pressure (mb, contoured every mb) valid at a) 3/1200 (the initial analysis), b) 3/1500, c) 3/1700, d) 3/1800, e) 3/1900, f) 3/2100, and g) 4/0000. 132
4.14 Continued. 133

4.14 Continued. 134
4.14 Continued. 135
4.15 Integrated rain water as in Fig. 4.8, but for 3/2000 (a) and as in Fig. 4.3a, but for the one-hour convective rainfall tendency for the period ending 3/2000 (b). 138
4.16 As in Fig. 4.5, but at 3/2100 for a point a) within the high-based rain area of MCS2 and b) within the deeper convection over the Texas panhandle. . . . 139
4.17 Convective rainfall, as in Fig. 4.3, but for the period ending 4/0000. 140
4.18 Simulated a) 850 mb water vapor (q_v, g kg^{-1} contoured every 2 g kg^{-1}) and b) 800 mb ω (μb s^{-1} contoured every 2 μb s^{-1} , negative values are dashed) valid at 3/2100. 142
4.19 Equivalent potential temperature (θ_E , K) and winds at the lowest model layer, valid at 3/2300. 143
4.20 Minimum lifted index (as in Fig. 2.23a) valid at 3/2300. 145
4.21 Vertical velocity, as in Fig. 4.18b but for 850 mb valid at 3/2300. 145
4.22 Simulated rain water mixing ratio (g kg^{-1} contoured every .04 g kg^{-1}) at 500 mb for 3/2300. 146
4.23 Grid point profiles from a point in the eastern Oklahoma panhandle at 3/2100 of a) hydrometeors (g kg^{-1}), b) ω (μb s^{-1}), c) wind speed (m s^{-1}), and d) θ_E (K). 147
4.24 As in Fig. 4.23, but for 3/2300. 149
4.25 850 mb ω (contoured every 2 μb s^{-1} , upward motion is dashed) at 4/0000 from a) the CTL simulation and b) the RAWINS analysis. 150
4.26 Simulated surface temperature (° C, contoured every 2° C) and winds at 4/0000.151
4.27 Surface observations at 4/0000 from a) the regular reporting sites and b) the PAM/SAM network. The station model is conventional (as in Fig. 2.7), but the surface pressure in tenths of mb with the leading "9" omitted is plotted to the upper right of each station in b). 152
4.28 900 mb θ_E and system-relative wind barbs at 4/0000 from a) CTL (θ_E contoured every 4° K; one full barb is 5 m s^{-1}) and b) the analysis of Smull and Augustine (1993) (θ_E contoured every 4° K). The relative winds are based on the observed MCS2 motion of 265° at 15 m s^{-1} 154
4.29 900 mb isotachs (m s^{-1} , solid contours) and wind barbs at 3/2300. 155
4.30 Grid point profiles from a point in northwest Kansas at 3/2000 of a) water vapor (g kg^{-1}), b) ω (μb s^{-1}), c) wind speed (m s^{-1}), and d) θ_E (K). . . . 157
4.31 Isotachs (m s^{-1} , solid contours) and wind barbs for 3/1200 at the a) σ = .915 level and b) 200 mb level. 158
4.32 As in Fig. 4.31, but for 3/1500. 159
4.33 As in Fig. 4.31, but for 3/1700. 161
4.34 As in Fig. 4.31, but for 3/1900. 162
4.35 West to east cross-section along the line shown in Fig. 4.34b of wind speed (m s^{-1} , solid contours) and ageostrophic circulation in the plane of the cross-section (vectors) at 3/1900. 163
4.36 850 mb ageostrophic winds at a) 3/1700 and b) 3/1900. 165
4.37 Conventional upper-air station model plot (as in Fig. 2.22) of 200 mb supplemental sounding data at 3/2100. 166

5.1 Isotachs (m s^{-1} , solid contours) and wind barbs for 3/1200 at 200 mb for a) CTL and b) NOJS. 170
5.2 Convective rainfall as in Fig. 4.5a from NOJS for the three-hour period ending a) 3/1500, b) 3/1800, and c) 3/2100. 172
5.2 Continued. 173
5.3 Isotachs (m s^{-1} , solid contours) and wind barbs for 3/1500 at 200 mb for a) CTL and b) NOJS. 174
5.4 Isotachs (m s^{-1} , solid contours) and wind barbs for 3/1800 at 200 mb for a) CTL and b) NOJS. 175
5.5 Isotachs (m s^{-1} , solid contours) and wind barbs for 3/2100 at 200 mb for a) CTL and b) NOJS. 176
5.6 Isotachs (m s^{-1} , solid contours) and wind barbs for 3/1500 at the a) $\sigma = .915$ level and b) 200 mb level for DRY and CTL. 178
5.6 Continued. 179
5.7 Isotachs (m s^{-1} , solid contours) and wind barbs for 3/1800 at the a) $\sigma = .915$ level and b) 200 mb level for DRY and CTL. 180
5.7 Continued. 181
5.8 Isotachs (m s^{-1} , solid contours) and wind barbs for 3/2100 at the a) $\sigma = .915$ level and b) 200 mb level for DRY and CTL. 183
5.8 Continued. 184
5.9 Potential vorticity (PVU, contoured every 1 PVU) at 900 mb from DRY at a) 3/1200, b), 3/1500, c) 3/1800, and d) 3/2100. 185
5.9 Continued. 186
5.10 Temperature (° C, contoured every 2° C) and winds (1 full barb = 10 m s^{-1}) at 900 mb at 3/2100 from DRY. 187
5.11 Surface temperature (° C, contoured every 2° C) and winds (1 full barb = 10 m s^{-1}) at 3/2100 from DRY. 188
5.12 Northwest-southeast cross section along the line shown in Fig. 5.9d of potential vorticity at 3/1800 from DRY. Regions with wind speeds greater than 45 m s^{-1} are shaded. 189
5.13 Vertical velocity, ω (μb s^{-1} , contour interval of 2 μb s^{-1} with negative values dashed) on the 800 mb surface at 3/2100 from a) DRY and b) NOJS. . . . 191
5.14 Three-hour total rainfall tendency (implicit plus explicit, in mm (3 h)$^{-1}$ from NOM1 contoured as in Fig. 4.5a) at a) 3/1500, b) 3/1800, and c) 3/2100. . 193
5.14 Continued. 194
5.15 Isotachs (m s^{-1} , solid contours) and wind barbs for 3/1500 at the a) $\sigma = .915$ level and b) 200 mb level from NOM1. 195
5.16 Isotachs (m s^{-1} , solid contours) and wind barbs for 3/1800 at the a) $\sigma = .915$ level and b) 200 mb level from NOM1. 196
5.17 Isotachs (m s^{-1} , solid contours) and wind barbs for 3/2100 at the a) $\sigma = .915$ level and b) 200 mb level from NOM1. 198
5.18 Divergence (10^{-5} s^{-1}, contoured every 4 x 10^{-5} s^{-1} with negative values dashed) on the $\sigma = .915$ level at 3/2100 from NOM1. 199
5.19 Difference in the 700 mb mixing ratio (g kg^{-1}) between the MM4 first guess initial condition and the NMC first guess initial condition at 3/1200. Contour interval is 1 g kg^{-1} with negative values dashed. 200

5.20 Three-hour convective rainfall tendency for NMCG at a) 3/1500, b) 3/1800, and c) 3/2100. 202
5.20 Continued. 203
5.21 Initial analysis of surface temperature and winds, as in Fig. 5.11 at 3/0000. . . 204
5.22 Initial surface divergence (as in Fig. 5.18) at 3/0000. 205
5.23 Skew-T plot of the model initial data from a point near LTS in southwest Oklahoma at 3/0000. 206
5.24 Surface temperature and winds at 3/0300 (as in Fig. 5.21) from Z0. 207
5.25 Three-hour convective rainfall tendency from Z0 (as in Fig. 4.5a) for the period ending a) 3/0300, b) 3/0600, and c) 3/0900. 208
5.25 Continued. 209
5.26 Backward trajectory from Z0 for a parcel over southwest Kansas at 800 mb at 3/1200. The two-hourly position of the parcel is indicated by the arrows along with its pressure (mb). The pressure of the parcel as a function of time is shown in b). 211
5.27 As in Fig. 5.26a, but for several parcels over central Kansas at 750 mb at 3/1200.212
5.28 As in Fig. 5.26 but for a representative parcel in Fig. 5.27. 213
5.29 Three-hour convective rainfall for the period ending 3/1200 from Z0. 214
5.30 North-south cross-section along the line A-B in Fig. 5.29 of a) θ_E (K, contour interval of 4 K) and winds in the plane of the cross-section and b) cloud water (mg kg^{-1} contoured every 60 mg kg^{-1}, solid) and rain water (mg kg^{-1} contoured every 7 mg kg^{-1}, dashed) at 3/1200 from Z0. 215
5.31 Three-hour rainfall for the period ending 3/1500 from Z0 of a) implicit rain and b) explicit rain. 216
5.32 Three-hour rainfall for the period ending 3/1800 from Z0 of a) implicit rain and b) explicit rain. 217
5.33 Simulated sea level pressure (mb, contour interval of 1 mb) from Z0 at 3/1800). 218
5.34 East-west cross-section along the line shown in Fig. 5.32b at 3/1800 from Z0 of a) θ_E and relative circulation as in Fig. 4.10a and b) cloud and rain water as in Fig. 5.30b, but with a contour interval for the cloud water of 100 mg kg^{-1} and for the rain water of 300 mg kg^{-1}. 219
5.35 Three-hour rainfall for the period ending 4/0000 from Z0 of a) implicit rain and b) explicit rain. 221
5.36 Simulated column-integrated rain water (g kg^{-1}) at 4/0000 from Z0. Contour interval is .05 g kg^{-1}. 222
5.37 Vertical profile of θ_E (curve H) and saturated θ_E (curve Q) (in ° K) for a grid point in southeast Texas at 3/1340. 227
5.38 Implicit rainfall from the three trigger function runs (FCT, LDT, and CIN) at a) 3/1500, b) 3/1800, c) 3/2100, and d) 4/0000 (except for CIN). 230
5.38 Continued. 231
5.38 Continued. 232
5.38 Continued. 233
5.39 Vertical profile of θ_E (curve H) and saturated θ_E (curve Q) (in ° K) for a grid point in northwest Kansas at 3/2020. 236
5.40 Convective rainfall for the 3 h period ending 3/1500, as in Fig. 4.3a, but from the unmodified AS run. 237

5.41 Convective rainfall as in Fig. 4.5a, but from the MAS run at a) 3/1500, b) 3/1800, c) 3/2100, and d) 4/0000. 240
5.41 Continued. 241
5.42 Vertical profile of θ_E (curve H) and saturated θ_E (curve Q) (in ° K) at 3/1200 for a grid point west of PTT near the origin of MCS1. 242
5.43 Precipitation efficiency as a function of wind shear. Adapted from Fritsch and Chappell (1980a), but with the additional results of Fankhauser (1988). . . 245
5.44 Three-hour convective rainfall tendency from PEF (as in Fig. 4.5a) for the period ending 3/1800. 247
5.45 Three-hour rainfall tendency (contoured as in Fig. 4.5a) for the period ending 3/2100 from the 32-level run for a) implicit rainfall and b) explicit rainfall. 249

6.1 Conceptual diagram of the jet-frontal circulations in the vicinity of an east-west surface front. The broad open arrow represents the upper-level jet streak. The thin arrows represent the indirect transverse circulation. The low-level jet (shaded arrow) lies atop the cold wedge of air, destabilizes the airmass and leads to the development of deep convection. 254

Chapter 1

INTRODUCTION

Forecasting of warm-season precipitation over the central United States remains a challenging problem. Large-scale (synoptic) flow patterns over the region often produce areas of instability favorable for the development of mesoscale areas of moist convection. This convection sometimes organizes into coherent systems which produce significant rains over a large area and, in turn, impact upon the larger scale flow. The details of how these mesoscale convective systems (MCSs) initiate, organize, grow to maturity and eventually decay are not completely understood. In addition, operational numerical prediction of these systems and their rainfall is inadequate.

With these points in mind, this study will attempt to answer several questions about a heavy-rain-producing event over the central United States in which a series of MCSs passed over Kansas. In particular, why did several systems form? How were the MCSs triggered? Can these systems be predicted by a state-of-the-art numerical model? If not, what are the critical model components that need improvement? Are conventional synoptic data adequate for generating the initial conditions?

1.1 Observational studies of MCSs

Maddox (1980) identified what he termed Mesoscale Convective Complexes (MCCs) – large, long-lived precipitation systems over the central United States characterized by cold, nearly circular cloud shields detected in infrared satellite imagery. A composite of ten MCC cases (Maddox 1983) revealed the important repetitive conditions that accompanied these storms. MCCs usually begin near a surface front (Fig. 1.1a) in a region of strong low level warm advection (Fig. 1.1b) with a weak upper-level trough located to the west of the genesis region (Fig. 1.1c). This area is beneath the exit region

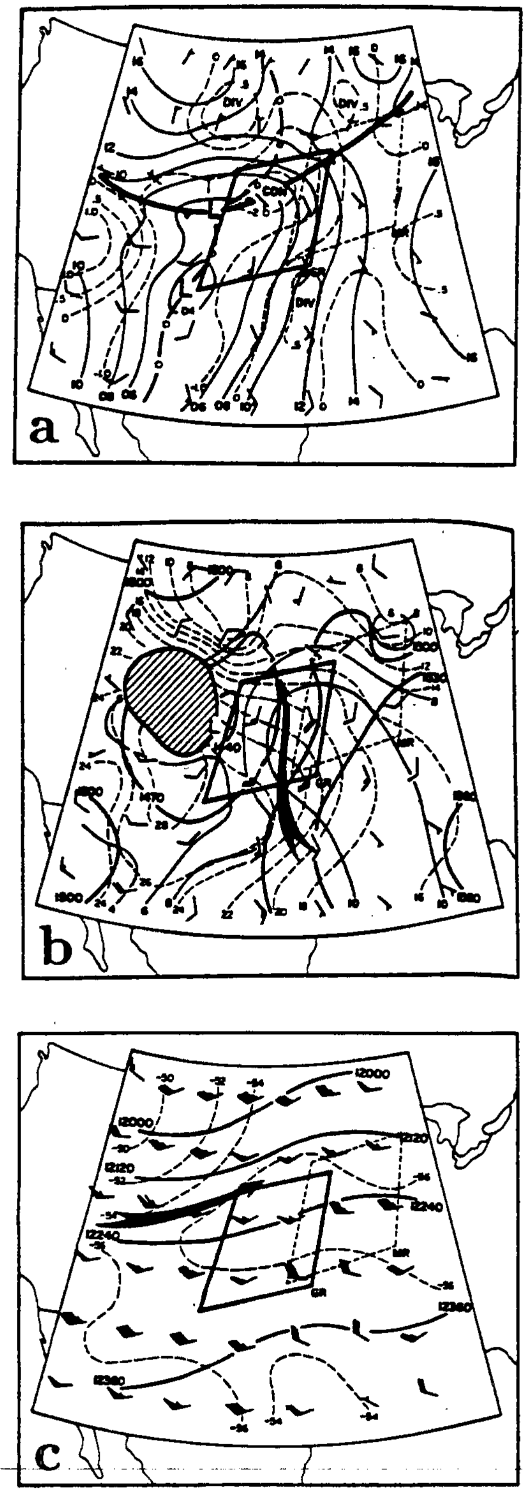

Figure 1.1: Composite analysis of features at a) surface, b) 850 mb, and c) 200 mb prior to MCC development. Winds (full barb = 5 m s^{-1} ; flag = 25 m s^{-1}) are plotted at every other grid point. In a), isobars (in mb, solid lines, contoured every 2 mb with the leading "10" omitted), surface divergence (x10^{-5} s^{-1}, dashed), and frontal position are shown. In b) and c), heights (m) are heavy solid, isotherms (° C) are dashed and jet position is indicated by the heavy arrow. In b), mixing ratio (in g kg^{-1}, light solid) and terrain above the 850 mb level (hatched) are shown. (After Maddox 1983 and Uccellini 1990).

of an upper-level jet and is bisected by a low-level jet. The superposition of the jets within the Maddox composite indicates the importance of jet coupling (Uccellini and Johnson 1979) for the development of MCCs (Uccellini 1990). The mature stage of the MCC is characterized by continued warm advection and veered 850 mb winds. At 700 mb, the temperature changes little, despite the warm advection. At 200 mb, an anticyclonically-curved jet develops north of the MCC and there is a distinct cold core. During the decay stage, the MCC moves into a region of more stable air.

Cotton *et al.* (1989) expanded upon the Maddox (1983) study by dividing the MCC life-cycle into seven subperiods and compositing conventional synoptic data for 134 cases using the objective analysis package of the Colorado State University Regional Atmospheric Modeling System (CSU-RAMS) (Pielke *et al.* 1992). They found that during the Pre-MCC stage, the synoptic scale features combine to produce convergence of moist, potentially unstable air, focused over a mesoscale region. During the MCC initial stage, convective growth occurs near a surface front in a region with low-level convergence and upper level divergence that permits the inflow and outflow of mass necessary for maintaining deep convection. The meso-β scale convection produces a low-level heating maximum and acts to moisten upper levels, providing an environment necessary for the further development of the MCC. The meso-β-scale components of the MCC are often aligned along thermal discontinuities (McAnelly and Cotton 1986). During the MCC growth stage, the vertical gradient of θ_E in low to mid levels continues to provide energy to the system. The low-level convergence, heating, and vertical motion maxima rise to mid-levels during this stage, similar to what was found for GATE (GARP Atlantic Tropical Experiment) systems by Frank and McBride (1989). The mature stage of the MCC is characterized by a mesoscale stratiform anvil cloud. Mesoscale downdrafts are found below 700 mb along with mid-level cyclonic shear and upper-level anticyclonic shear. The MCC begins to decay as it moves into an area with less low-level potential instability.

Merritt and Fritsch (1984) and Kane *et al.* (1987) applied the Maddox *et al.* (1979) synoptic classification scheme to the MCC environment. The cases were separated into four categories: frontal (the most common), synoptic, mesohigh, and extreme-right-moving.

The systems (with the exception of the right-movers) tended to travel parallel to the 850-300 mb thickness contours. Composite precipitation isohyets were elongated along and just to the right of the axis of MCC propagation with maximum rainfall occurring just before maturity.

In a study of ten years of warm season precipitation observations over the central United States, Tollerud and Collander (1993) found that although MCCs are relatively rare, they produce a disproportionately large number of the extreme rainfall events. MCC rainfall was found to have a significant diurnal modulation with peak rainfall occurring during nighttime hours – between 0 UTC and 12 UTC.

Fritsch *et al.* (1986) recognized that under slowly evolving synoptic conditions, a series of convective systems (SCC) can form and travel over the same area producing a rainfall swath similar to an average hurricane. While SCCs occur with any of the synoptic classifications, frontal cases are most common. Frontal MCSs occur to the north of a slowly moving east-west oriented surface front. The front may be a cold, warm, or stationary front, but the cold air mass is relatively shallow. Southerly winds south of the front provide the warm advection pattern typical of MCC cases. Rockwood *et al.* (1984) examined a case in which two frontal MCCs traversed a similar path across southern Kansas and Missouri. The second MCC, following about six to nine hours behind the first system, produced flash flooding when heavy rains fell on already saturated watersheds. Rockwood *et al.* found that interaction of the outflow boundaries from the two storms with each other and with the larger-scale fronts played a significant role in the changes in convective intensity. The lack of detailed observations led them to pose several important questions including how did the two MCCs interact?

Colman (1990a) studied the climatology of “elevated” thunderstorms which he defined as occurring over a surface–based inversion, usually north of a shallow warm or stationary front. While synoptically similar to the frontal MCC case, his study was not restricted to the warm season or MCCs. He found that the elevated storms occurred with pronounced mid-level warm advection and most often in the left exit region of an 850 mb jet. The surface front was crucial in forcing the convection. Because most of the cases occurred when 850 mb air was stable to upright convection he suggested that slantwise convection might be occurring.

Colman (1990b) examined in detail the elevated thunderstorm case of 10 April 1979 over the central United States. Three convective impulses (the first associated with a highly-ageostrophic low-level jet) developed in the warm sector of a slow-moving and intensifying low pressure area. Each impulse formed in a very unstable airmass and propagated to the northeast, traveling across the warm-frontal surface. The storms continued to propagate across the frontal surface despite the absence of upright convective instability. A convective band which developed over the frontal surface formed where parcel trajectories were unstable to slantwise motions that eventually became gravitationally unstable. A gravity wave analysis revealed a close association between pressure waves and the elevated thunderstorms, but the waves apparently did not trigger the storms.

Byrd (1989), in a study of wintertime overrunning cases over the central United States, also found that slantwise convection (or conditional symmetric intability (CSI) (e.g. Emanuel 1983)) may have initiated some of the precipitation bands. CSI has been identified as triggering meso-β-scale convective rainbands (Lemaitre and Scialom 1991) and has been shown to be present in the MCC environment (Fortune 1989).

In an attempt to explain the nocturnal maximum in warm frontal convection, Forbes *et al.* (1984) examined parcel trajectories and found that air from the warm sector planetary boundary layer (PBL) feeds the convection. The most unstable air over the front originates in the warm sector PBL the previous afternoon. In a composite study of MCSs occurring from 1990-1992 over the central United States, Augustine and Caracena (1993) found that large, long-lived MCSs form downwind of the daytime surface geostrophic wind maximum only when the 850 mb boundary downstream of the maximum is frontogenetic. When the frontal boundary is weak or not frontogenetic, significant development is not likely. During the evening, a LLJ forms above the location of the daytime surface geostrophic wind maximum (Figure 1.2). The LLJ encounters the deep frontal zone that has been maintained by frontogenesis, resulting in enhanced mesoscale upward motion (Augustine and Caracena 1993). Sanders (1993) describes another case in which heavy rains are associated with frontogenesis.

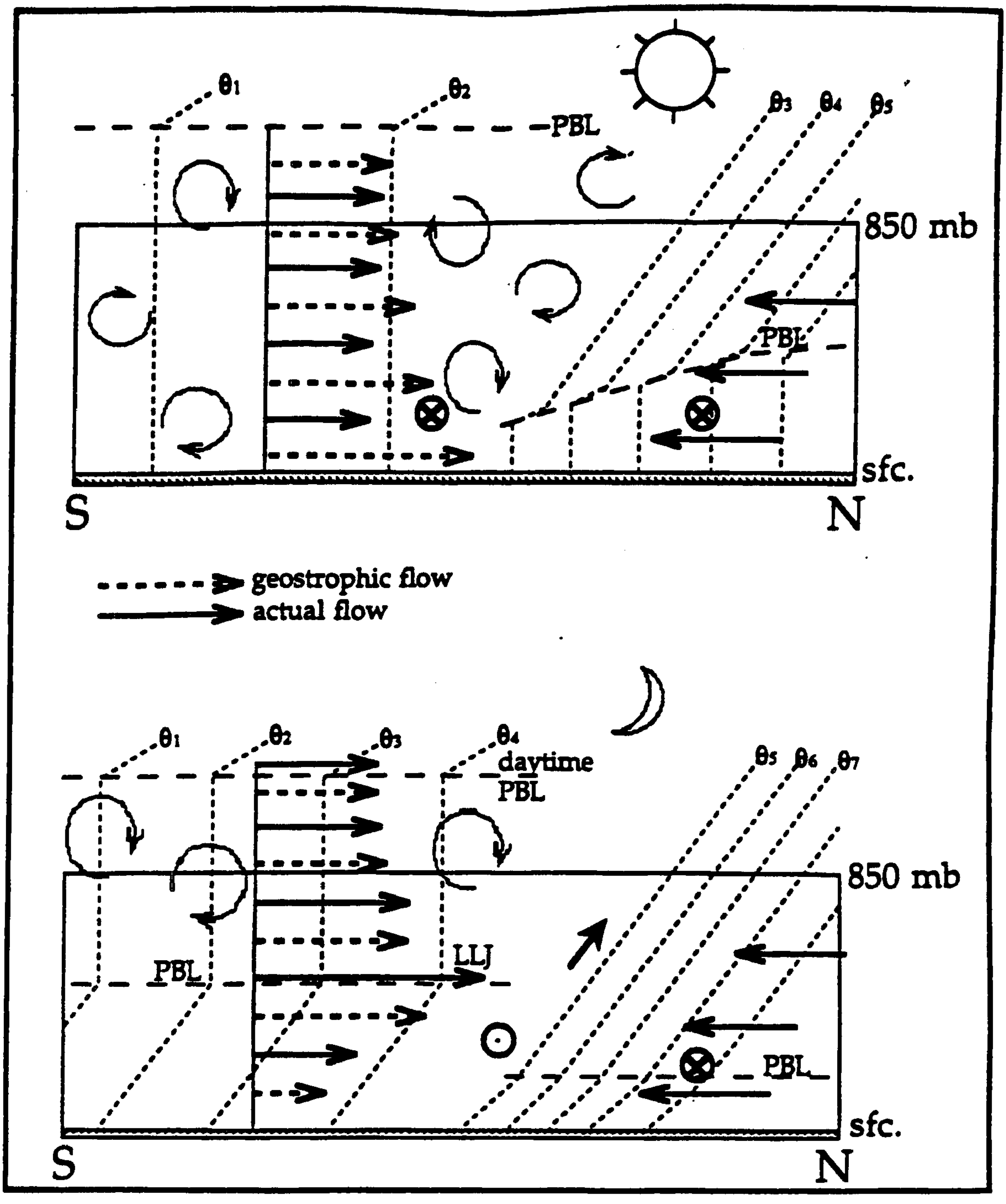

Figure 1.2: Schematic vertical cross sections for late afternoon (top) and night (bottom), over the region of the surface geostrophic wind maximum for cases with large, long-lived MCSs. Isentropes are short-dashed lines with warmer values to the south, solid arrows are the actual wind, dashed arrows are the geostrophic wind, open circles with enclosed x's represent flow into the figure (easterly winds), while the open circle with an enclosed dot indicates flow out of the figure (westerly winds). Long-dashed lines indicate the top of the planetary boundary layer (PBL). (After Augustine and Caracena 1993).

Details about the way in which convection organizes into systems are not clear. Simpson *et al.* (1980) found that downdraft interactions between south Florida cumuli (aided by sea breeze convergence) resulted in cloud mergers. Similar processes were found to exist over tropical Australia (Simpson *et al.* 1993). Based on observations that convection breaks out in the vicinity of pre-existing convection before outflows have reached the area, Mapes (1993) has shown that buoyancy bores forced by the heating within a nascent MCS result in upward displacement of low-level parcels in the vicinity of the heating and thus the surrounding environment becomes more favorable for the development of convection. Even though this gravity wave lifting is not sufficient to trigger additional convection, it does favor additional development (Mapes 1993). Mapes used this theory to explain the clustering of convection in the tropics.

Similar to the Mapes (1993) idea for self-organizing convective systems, McAnelly and Cotton (1992), McAnelly *et al.* (1993) and Nachamkin (1992) hypothesize that a gravity wave excited by initial convection may promote growth of an MCS to maturity. Observations from several cases show that the time evolution of the volumetric rain rate exhibits a rapid increase followed by a period of decreasing values, followed by reintensification. The authors suggest that a deep-tropospheric gravity wave is excited by the latent heating of the initial convection. As the wave propagates away, it initiates a mesoscale circulation which promotes low-level convergence and subsequent development. A study of satellite observations by Tollerud *et al.* (1992) possibly supports this idea. They found that MCSs with explosive initial growth rates generally last longer and grow larger than ones with smaller initial growth rates. Significant differences appear between systems as early as three hours into their life-cycle.

While the gravity wave hypothesis might explain the self-organization and upscale growth of convection into an MCS, the mechanisms that trigger the initial convection are only vaguely understood. Deep moist convection occurs when a parcel is lifted to its level of free convection (LFC). The depth over which a parcel must rise to its LFC (and the amount of negative area which must be overcome) depends on the characteristics of the parcel as well as its environment. The lifting mechanism can be varied as well, for example forced ascent over orography, frontal lifting, convective boundary layer eddies, colliding outflow boundaries, etc. Development of deep convection is a result of complex interactions between these triggers and the environment. Carbone *et al.* (1990) and Crook *et al.* (1990) describe a case during PRE-STORM [the Oklahoma-Kansas Preliminary Regional Experiment for STORM-Central Cunning (1986) (OK PRE-STORM or simply, PRE-STORM)] in which a strong gust front, propagating first as a gravity current, then as an internal undular bore, moved across Kansas, only generating convection when it ran into a favorable environment. The favorable environment was created by separate dynamic processes. Stensrud and Maddox (1988) and Miner (1992) describe other cases in which colliding low-level outflows do not re-generate convection due to other, inhibiting changes in the thermodynamic structure aloft. Koch and Golus (1988), Koch *et al.* (1988) and Koch and Dorian (1988) analyze a case in which pre-existing gravity waves were able to trigger deep convection within an unstable boundary layer. Sanders and Blanchard (1993) describe a case in which mesoscale waves reduced the convective inhibition (CIN) in a small portion of a large, highly unstable area. Ogura *et al.* (1982) explain late afternoon storm formation in the vicinity of the dryline as due to a) diurnal development of the mixed layer, b) differential development of the mixed layer which produces an inland sea breeze effect, or c) symmetric instability caused by heating of the PBL (and reduction of the Richardson number) within a baroclinic zone. A recent preliminary study of convection along the Oklahoma dryline (Ziegler and Hane 1993) shows that initiation of convection is related to a threshold of convective inhibition or negative area. Despite moisture convergence (and upward motion) along the dryline, and varying amounts of CAPE (Convectively Available Potential Energy), convection occurred when the CIN threshold was reached. ~~The mechanisms by which the CIN can be depleted are, of course, varied.~~

Within the warm advection pattern conducive for MCS formation (Maddox 1983) (which is an area of quasi-geostrophic upward motion) development of initial convection may be enhanced by the low-level warm advection which de-stabilizes the airmass or it may be suppressed by warming aloft that caps the most unstable boundary layer air. As pointed out by Raymond (1987), quasi-geostrophic dynamics do not adequately explain the structure and propagation of MCSs. Maddox and Doswell (1982) provide several examples of significant convection which develops in benign synoptic settings due to the de-stabilization caused by low-level warm advection. Doswell (1987) proposes that the initiation of convection is due to mesoscale processes. He defines mesoscale processes as those which are linked to both the large scale and microscale. The mesoscale circulations are therefore constrained by the large-scale quasi-geostrophic processes. Lift provided by the large-scale is too small to initiate convection within a reasonable time period. (Except for some unusual cases, e.g. Bluestein (1985)). The large-scale acts to provide an environment which is favorable for development of deep convection, although sometimes mesoscale processes can overcome a large-scale environment which is initially unfavorable. MCSs such as those studied by Maddox (1980) occur in a favorable large-scale environment that also has mesoscale forcing.

Uccellini (1990) proposes that the warm advection forcing exhibited in the MCC composite (Maddox 1983) and in other cases (Maddox and Doswell 1982) is likely a manifestation of the lower tropospheric response to divergent wind fields that extend throughout the entire troposphere. The large-scale environment, in which jet streaks propagate toward an upper-level ridge, not only provides the differential advection patterns that destabilize the atmosphere, but also provide mechanisms which trigger convection, such as gravity waves (Uccellini and Koch 1987; Uccellini 1990). Sanders and Blanchard (1993) reach a similar conclusion from their study of the 10 May 1985 case, in which the jet provided an environment in which mesoscale disturbances developed. They stated that "No detailed explanation has been offered for the connection between initiation of convection and the larger-scale jet-related ascent".

The link between low-level jets and MCC formation is well-established (e.g. Fig. 1.1b; Maddox 1983; Ralph and Neiman 1993). Shapiro (1982) and Sortais *et al.* (1993) have found that development of convection can depend on the details of the configuration of the jet-frontal circulations. Changes in the jet streak circulations and the development of a low-level jet can lead to rapid de-stabilization and convection (Kocin *et al.* 1986). Augustine and Caracena (1993) found that convection without LLJ support typically dies off after sunset. In a study of many convective systems, Houze *et al.* (1990) found that chaotically-arranged convective areas occurred when there was no LLJ. Climatological studies show that convection is typically found in the left exit region of a low-level jet (Bonner 1966; Colman 1990a) which is a region of relatively strong and deep lifting (Trier and Parsons 1993). The link between upper-level jets and the triggering of convection is more tenuous. Bluestein and Thomas (1984) provide circumstantial evidence that the rising branch of a thermally direct circulation played a role in storm formation and sustenance.

Observational studies have revealed important characteristics of the MCS environment. Unfortunately, not enough observations are available to completely piece together the entire life-cycle of MCSs. With the implementation of new observing systems such as the WSR-88D (Crum and Alberty 1993) and wind profilers (Chadwick and Hassel 1987), more detailed information about MCS environments will soon be available. In the meantime, numerical models have proven to be useful tools for investigation of MCSs. Some results from previous modeling studies are presented in the following section.

1.2 Numerical simulations of MCSs

Because the operational sounding network is too coarse in space and time to adequately sample MCSs and field programs are also of limited extent, numerical models have been used to investigate various aspects of these systems. Advantages of model studies include controlled initial conditions and the ability to test the sensitivity of the simulation to various physical processes. In general, models have improved as computer power has increased. Yet, the size and complexity of MCSs is such that some simplifications in the modeling approach are still necessary. Fully three-dimensional, real-data meso-β-scale simulations have only recently been conducted (e.g. Zhang and Fritsch 1986a). The following is a brief survey of some of the work relevant to the current study. First, some simplified model results (using idealized initial conditions or only two dimensions) will be described, followed by some results from real-data simulations.

1.2.1 Simplified modeling studies

Fritsch and Maddox (1981b) simulated the anticyclonic upper level outflow of an MCC by using analytic initial conditions with the Fritsch and Chappell (1980a, b) numerical model and convective parameterization. The convection forced an area of mean mesoscale ascent and divergent outflow aloft indicative of upscale organization.

Raymond (1987) used a forced gravity wave (or wave-CISK (Lindzen 1974)) model and the moderate shear conditions typical of midlatitude MCSs to examine the self-organizing characteristics of convection. The forced gravity wave mechanism assumes that the convection is always phase-locked with the wave-induced low-level convergence. Raymond (1987) showed that intensification of the gravity waves and convection is due to penetrative downdrafts which displace and lift low-level unstable air. This is in contrast to the Mapes (1993) ideas. Inclusion of conditional convection as well as precipitation advection tend to slow and damp the forced gravity waves. In a real-data modeling study of a midlatitude squall line, Cram (1990) found that the line propagated in a wave-CISK-like manner. However, Cram states that a spectrum of scales of forcing may have been responsible for the squall line propagation. Thus, the propagation mechanism for MCSs are likely more complex than simple wave-CISK ideas would suggest.

Periodic re-development of convective systems ahead of a surface cold front has received some attention. A modeling study by Ogura and Jiang (1985) found a periodicity in convection with a second system developing approximately five hours after the decay of an initial system. Crook (1987) used a more detailed two-dimensional model which included time-dependent convergence to examine re-development. He found that the first convective system forces a geostrophic imbalance at the surface front. As the front and surrounding environment try to return to geostrophic balance, they oscillate while inertial gravity waves propagate away from the imbalanced area. Low-level convergence ahead of the front oscillates with a period of twelve hours. As ascent returns to the vicinity of the front (about 6 hours after the decay of the first system), a second system develops as the atmosphere destabilizes. Crook also examined radar summary charts for several cases and found a periodicity of about twelve hours in convection occurring ahead of a surface cold front. The largest peak occurred near the time of maximum heating. While Crook's modeling study indicates that a convective system might influence subsequent development near a surface front, questions still remain about the process. The lack of a third dimension in the study may be important as Crook found a sensitivity of the second system to an imposed north-south moisture gradient. Differential surface heating should also be important. Finally, are the results for a north-south oriented cold front applicable to other orientations and types of fronts?

An idealized two-dimensional modeling study by Crook and Moncrieff (1988) showed that large-scale convergence acts to aid the generation of convection by lifting air over a wide region to near saturation. Therefore, convection needs little additional lift to initiate or be maintained.

Tripoli (1986) simulated the genesis and growth of an MCS along and to the lee of the Rocky Mountains by using a two-dimensional primitive equation fine-mesh model. Based on the numerical results, he developed a conceptual model containing some important, yet complex, characteristics. While Tripoli's results are closely linked to the mountain-plains solenoidal circulation, some of his results are more generally applicable. Initial convection forms in a region of low-level convergence. Later, a stratiform anvil forms, raising the level of maximum heating. At low levels, cold downdrafts form a mesohigh. The geostrophic response to this forcing results in the development of anti-cyclonic shear aloft and cyclonic shear at low levels. The scale of the circulation thus increases. This effect becomes more pronounced as insolation diminishes and the stratiform anvil top radiatively cools leading to greater instability and a stronger anvil.

1.2.2 Three-dimensional modeling of real-data cases

Maddox *et al.* (1981) and Perkey and Maddox (1985) used the Drexel University model to simulate the real-data case of an MCC over the eastern United States on 25 April 1975 during NASA-AVE IV (National Aeronautics and Space Administration - Atmospheric Variability Experiment). By comparing moist and dry simulations, they found that significant upscale feedbacks occur between the convective system and the large-scale flow. Even though the simulations had a coarse grid spacing (140 km) and so only crudely represented the effects of the convective system, many of the observed features such as the upper level anticyclonic outflow, mean mesoscale ascent, and warm core were reproduced.

As mesoscale models continued to improve, many investigators performed real data simulations of MCSs and squall lines in particular. Some examples of these studies include Chang *et al.* (1981), Ross and Orlanski (1982), Orlanski and Ross (1984), Pointin (1985), Hane *et al.* (1987), Zhang and Fritsch (1986a, b; 1987; 1988a, b), Zhang *et al.* (1989), Zhang and Gao (1989), Schmidt and Cotton (1990), Cram *et al.* (1992a, b). Numerical simulations of MCCs or smaller MCSs have been less common. Molinari and Corsetti (1985), Molinari and Dudek (1986), and Zhang and Fritsch (1986a, b; 1987; 1988a, b) simulated the 1977 Johnstown Flood case analyzed by Bosart and Sanders (1981) which included both a squall line and MCC. Zhang and Fritsch (1988c) examined a case with a warm core vortex, while Dudek (1988) simulated two MCC cases.

The Pennsylvania State University / National Center for Atmospheric Research (PSU/NCAR) model (Anthes and Warner 1978) and its updated version Mesoscale Model Version 4 (MM4) (Anthes *et al.* 1987) has been used in numerous real-data cases.

Anthes *et al.* (1982) simulated two MCS cases from the SESAME-1979 experiment using the PSU/NCAR model (Anthes and Warner 1978) (the 25-26 April case and the 10-11 April case). The model, initialized with synoptic-scale data and having a horizontal grid spacing of 100 km and 10 vertical levels, was able to reproduce many of the observed meso-α scale features found in the two cases such as the MCSs themselves, low-level jets, capping inversions, and upper-level jet streaks. However, large errors in the forecast precipitation were found along with significant low-level temperature errors. They attributed these errors to a poor analysis over the oceans along with an inadequate surface energy budget parameterization.

Benjamin and Carlson (1986) carried out more experiments on the 10-11 April 1979 case using an improved version of the model employed by Anthes *et al.* (1982). Their experiments used 11 vertical levels and a Blackadar-type PBL model (Zhang and Anthes 1982) with horizontally-varying surface characteristics. Their simulations produced an excellent precipitation forecast (although the 111 km resolution prevented reproduction of the details in the rain areas) and an improved surface temperature forecast. They found that effects of the surface heating and topography enhanced the low-level flow into the severe storm region over Texas and Oklahoma. The surface heating also enhanced the transverse circulations associated with jet streaks which aided the low-level flow.

Kalb (1985) also simulated the 10-11 April 1979 case and found that improved results could be obtained with better parameterizations, higher resolution and detailed initial data.

Brill *et al.* (1985) successfully applied the PSU/NCAR model to the case with coupled jet streaks analyzed by Uccellini and Johnson (1979), confirming the results of the observational study. A numerical experiment with a weaker initial upper level jet streak showed that the indirect circulation is quite responsive to the initial structure of the jet streak.

Dudek (1988) used the PSU/NCAR model (Anthes *et al.* 1987) to simulate two MCC cases. His model runs used a nested grid spacing of 40 km with 15 vertical levels and included an explicit rain scheme (Hsie *et al.* 1984), a Kuo-type convective parameterization (Molinari and Dudek 1986), a high-resolution PBL (Zhang and Anthes 1982), and a shallow convective parameterization (Betts 1986). Initial convection associated with both MCCs began in a mesoscale region with low-level upward motion. In one case, this low-level ascent was induced by a combination of cyclonic vorticity advection and low-level warm advection while in the other case only cyclonic vorticity advection was present. Convective heating induced a deep layer of strong ascent. Tropopause-level divergence in a region of low inertial instability moved compensating subsidence away from the convection, and permitted continued development. A nonlinear interaction between the convective heating and the developing mesoscale circulation produced a midlevel warm-core, inertially stable mesovortex within the MCC. Dudek's simulations failed to produce a mesoscale, saturated stratiform region, perhaps due to inadequate moist physics parameterizations. Kuo-type convective schemes have been found to underpredict heating and drying rates (Grell *et al.* 1991) and to underpredict rainfall rates (Grell 1993). Also, ice processes are important within simulated stratiform regions (e.g. Rutledge and Houze 1987; Zhang 1989; Zhang and Gao 1989).

Dudek performed several sensitivity experiments. Shallow convective clouds were found to influence the timing and location of subsequent development of deep convection by creating a partially-mixed layer above the boundary layer, by reducing the strength of the capping inversion, by producing a downward heat flux warming the PBL, by permitting a more realistic interaction with the surface radiation parameterization, and by upward mixing of PBL moisture which allowed a low-level jet to advect the moisture into the region of impending MCC development. Comparison of experiments with and without latent heating clearly showed that the development of the mesovortex and amplification of the mid-level short wave trough was induced by the convective heating. The low-level jet, however, while enhanced by latent heating, is produced by other mechanisms, suggesting that it is a partial cause of MCC development rather than an effect of the MCC. Experiments with only explicit moisture parameterization (omitting the convective parameterization) were unable to simulate the MCC development. Rainfall was unrealistically delayed and, once formed, created numerical point storms (Giorgi 1991; Kalb 1987).

Dudhia (1989) used a two-dimensional version of the PSU/NCAR model to simulate an MCS over the South China Sea. He added an explicit moisture parameterization which included the ice phase and added a radiative transfer scheme. Overall, the MCS was reproduced well. It was found that the ice phase was important in determining the level of maximum heating within the stratiform anvil cloud. Radiative heating was critical for upper level ascent in regions of cirrus outflow. Clear-air cooling was found to aid convection by destabilizing the troposphere and countering the low-level convective warming.

Kuo *et al.* (1988) studied a heavy flooding case in the lee of the Tibetan Plateau using MM4. A run with 80 km grid spacing and simple physical parameterizations was able to simulate the evolution of a mesoscale vortex and the accompanying heavy precipitation (Kuo *et al.* 1988). Sensitivity tests showed that latent heating by condensation and surface sensible and latent heat fluxes were important for the vortex and rainfall simulation.

Lindstrom and Nordeng (1992) added a parameterization of slantwise convection initiated by CSI (Nordeng 1987) to MM4 in order to simulate a mid-western United States wintertime case. They found that the parameterization develops momentum structures in the model similar to observed and produces more realistic precipitation fields as well as other fields such as 500 mb heights (Lindstrom and Nordeng 1992). The parameterization may also have helped initiate upright convection earlier in the model forecast. Kuo and Reed (1988) found that slantwise motions during an explosive oceanic cyclone were able to be simulated by the explicit moist physics parameterization without the need for a separate slantwise convective scheme.

Zhang *et al.* (1986) developed a nested version of the MM4 model and successfully applied it to a study of the Johnstown Flood case (Zhang and Fritsch 1986a; 1986b; 1987; 1988a; 1988b). The model, which included subjectively-analyzed bogus data in the initial conditions, was able to reproduce many of the observed features including a leading squall line and subsequent MCC, outflow boundaries, surface pressure features, and low-level jets.

The nested grid MM4 was also successfully applied to the 10-11 June 1985 PRE-STORM squall line case (Zhang *et al.* 1989; Zhang and Gao 1989; Gao *et al.* 1990; Zhang and Cho 1992; Zhang 1992). Once again the model reproduced many of the observed features, most importantly the rear-inflow jet (Smull and Houze 1987b). Zhang *et al.* (1989) concluded that it was possible to simulate the meso-β-scale features of some convective systems using only synoptic-scale initial data provided the proper physical parameterizations are included in the model.

Zhang and Fritsch (1988c) simulated a squall line which evolved into a long-lived, rotating MCS. The model developed a realistic warm-core mesovortex from the effects of resolvable-scale latent heat release. Zhang's work has stressed the importance of including realistic physical processes in the model such as virtual temperature effects, hydrostatic water loading and ice processes.

Recently, Stensrud (1992) used MM4 to simulate several MCSs which formed within a potentially unstable airmass with weak large scale forcing. Convection formed only where mesoscale circulations were able to overcome a restraining inversion. Model simulations showed that without these mesoscale features in the initial conditions, the MCSs were not predicted well. Also, a poor simulation of MCS propagation and coverage can occur when there is weak large-scale forcing as deficiencies in the convective parameterization become more important than when MCSs are forced by strong large-scale features. Stensrud found that the MCSs were able to propagate upstream due to a combination of effects by density currents and internal gravity waves.

Real-data simulations of non-squall line MCS cases with other models have been rarer. Kaplan *et al.* (1982) describe the development of the National Aeronautics and Space Administration's Mesoscale Atmospheric Simulation System (MASS) and its application to the 10-11 April 1979 severe weather case. MASS is a hydrostatic primitive equation model for use with real-data cases. Successful simulations include the 10-11 April 1979 case (Kaplan *et al.* 1982; Zack and Kaplan 1987), the less-strongly forced 3-4 June 1980 Grand Island tornado case (Kaplan *et al.* 1984; Chang and Wetzel 1991), and the March 1984 Carolina tornado outbreak (Kocin *et al.* 1984). Unfortunately, MASS has fallen into disuse.

An MCC which produced a derecho was simulated by Tremback (1990) using CSU-RAMS. As in the Tripoli (1986) study, the mountain-plains solenoidal circulation was found to be an important forcing mechanism. In addition, a low-level jet supplied moisture to the system, while an upper-level jet aided divergence.

Analysis of model simulations has proved very useful for studying MCSs. Keyser and Uccellini (1987) suggest that mesoscale models have progressed sufficiently so that model output can be used by synopticians as a reliable data source for diagnostic study. In the present work, therefore, the MM4 model is employed as a tool (along with available observations) to investigate a complex SCC case in order to help answer the questions posed at the beginning of this chapter.

Chapter 2

OBSERVATIONS OF THE 3-4 JUNE CASE

One of the most interesting cases of the PRE-STORM experiment was the 3-4 June episode, during which several MCSs formed over the measurement network. As stated by Smull and Augustine (1993), the MCSs on this day were "...found to include a variety of local environments and associated weather, ranging from tornadic thunderstorms to more linear convective bands and widespread chilling rains". Because of the challenge this case presents to both forecasters and numerical modelers, it is worthy of intensive study. Several observational studies of the various MCSs on this day have already been conducted (Augustine and Howard 1988; Stumpf 1988; Stumpf and Johnson 1988; Fortune 1989; Green 1989; Leary and Bals, 1989; Smull and Augustine 1989; Holle *et al.* 1990; Leary and Bals, 1990; McAnelly and Cotton 1990; Smull and Jorgensen 1990; Smull *et al.* 1991; Stumpf *et al.* 1991; Fortune *et al.* 1992; Loehrer 1992; McAnelly and Cotton 1992; Nachamkin 1992; Smull and Augustine 1993; Trier and Parsons 1993) and are summarized in a subsequent section. In this chapter, conventional synoptic analyses will be combined with the results of the previous studies to provide an overview of the current knowledge of the behavior of the 3-4 June MCSs. These analyses can be used as benchmarks for comparison with model output.

2.1 General overview

During the period 3/1200 to 4/1200, four MCSs affected the PRE-STORM measurement area (Cunning 1986). (Henceforth, all dates and times will be presented as UTC day/time. For the PRE-STORM region, the local standard time is UTC minus six hours.) Figure 2.1 (from Trier and Parsons 1993) shows the tracks of the approximate centroid of the cold cloud shield of the four systems. Three of the systems travelled across Kansas,

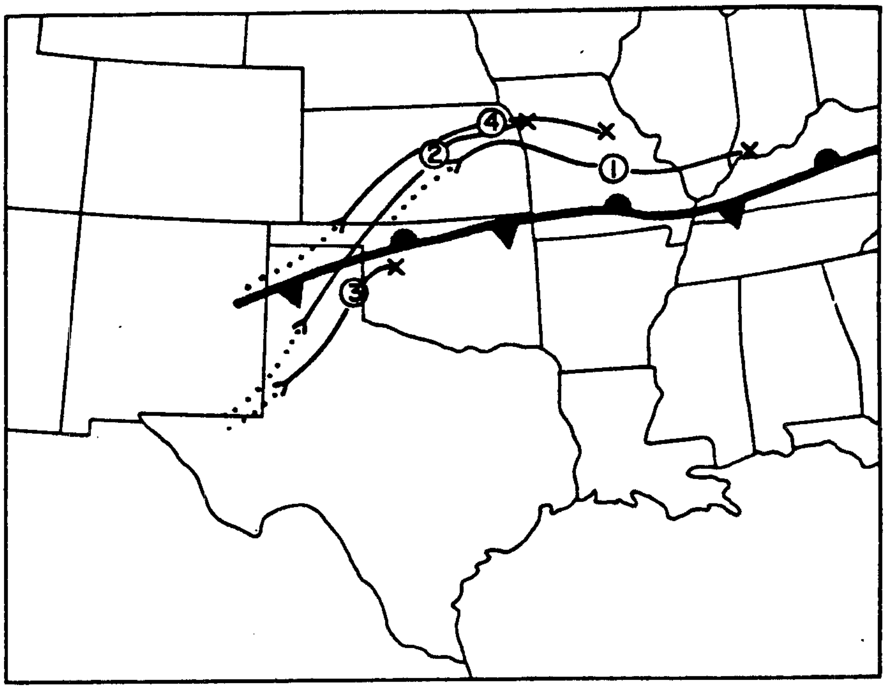

Figure 2.1: Tracks of the approximate centroids of the four 3-4 June MCSs. Dotted lines indicate Pre-MCC convection, the X symbol shows the termination point of the MCS, and the mean position of the surface stationary front during the episode is shown. Adapted from Trier and Parsons (1993).

north of the surface front, in a region climatologically favored for these storms during May and June (Colman 1990a, his Fig. 3). During PRE-STORM, an east-west front was often found across the measurement area (Loehrer 1992) and was associated with MCS development. Other systems similar to those on 3-4 June occurred during the experiment (e.g. Brandes 1990; Loehrer 1992), but the repetitive development of the systems on this date was unique.

Table 2.1 summarizes some characteristics of the four MCSs. Times are from satellite imagery or Augustine and Howard (1988), lightning and radar data are from Holle *et al.* (1990).

All four systems were long-lived and produced significant amounts of precipitation. MCSs 1, 2, and 4 followed quite similar paths thus fitting the qualification for an SCC (Fritsch *et al.* 1986). Flooding was reported in a 80 km wide area from Abilene, Kansas to Emporia, Kansas (NOAA 1985). MCS1 was one of only two MCSs during PRE-STORM

Table 2.1: Characteristics of the 3-4 June 1985 MCSs.

	UTC Date/Time						
	Initial convection	MCC stage	Maximum extent	Decay	lightning flashes	radar rain volume (10^6 m^3)	duration (h)
MCS1	3/1230	3/1600	3/2230	4/0400	5635	1986	15.5
MCS2	3/1400	3/1830	4/0000	4/0430	7011	5449	12.5
MCS3	3/2130	3/0030	4/0500	4/0730	2178	735	10.0
MCS4	4/0000	4/0600	4/1100	4/1530	8666	4504	15.5

which began around sunrise and grew during the daylight hours (Loehrer 1992). The majority of frontal MCSs occur at night (Dexter 1944; Maddox 1980).

2.2 Summary of previous 3-4 June studies

Using various data platforms, Smull and Augustine (1993) performed a detailed multisale analysis of the mature MCS2 between 4/0000 and 4/0130. They determined that the resemblance of the MCS to a developing wave cyclone was just a short-lived superposition of two convective bands: one aligned with the mean tropospheric vertical wind shear and the other perpendicular to the low-level shear. Figure 2.2 shows a composite radar image from 4/0030 showing the mature MCS2. No mesoscale cyclonic circulation was found to exist at any level. As in previous MCS studies, they found a relatively cool core at low levels and warmer temperatures aloft. Figure 2.3 (from Smull and Augustine 1993, Fig. 36) is a three-dimensional conceptual diagram of the mesoscale flow structure through MCS2. The main energy supply for the system was the high θ_E air arriving on low level southeasterlies. The NE-SW oriented convective band was parallel to the 850 mb frontal surface over Kansas. The N-S convective line was oriented perpendicular to the low-level shear, similar to classical squall lines. Midlevel convergence was found in the system's stratiform region, northwest of the intersection of the convective bands. Aloft, characteristic divergent flow was found. They found that the highly three-dimensional airflow through the MCS and the wide variety of instability across the frontal zone led to the storm's complex asymmetric structure. Specifically, ice particles were advected northward sustaining the stratiform region, and intense convection developed preferentially on the MCS's southern flank. There was a two-step structure to the upward motion gliding over the front – shallow ascent over the frontal surface which eventually fed into deep convective towers.

Loehrer (1992) investigated the surface pressure features and precipitation structure of 16 MCSs during PRE-STORM including MCS1, MCS2, and MCS4. Twelve of the sixteen, including those on 3-4 June, developed an asymmetric structure (Fig. 2.4, his Fig. 6.6) with a trailing stratiform region on the north end of the MCS. A surface mesohigh lay beneath

Figure 2.2: Composite conventional radar image from 4/0030 showing the mature MCS2. Alternating shading corresponds to minimum dBZ thresholds as follows: medium gray - 15, light gray - 30, black - 40, medium gray - 46, light gray - 52, and black - 58 dBZ.

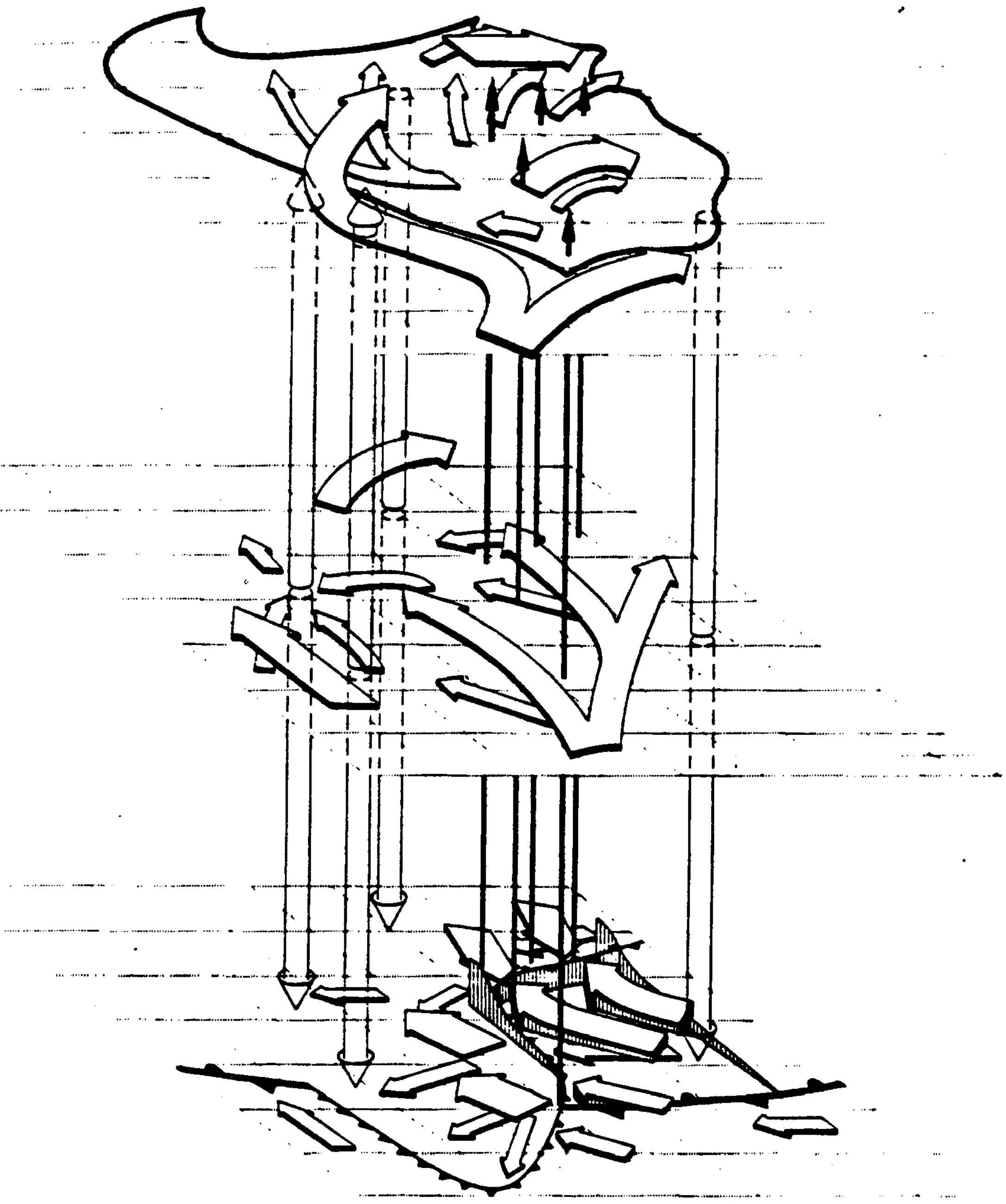

Figure 2.3: Conceptualized three-dimensional overview of the mature MCS2 from a vantage point located southwest of the storm. Broad horizontal arrows represent horizontal relative flow. The bottom panel shows the relevant thermal boundaries. Deeper mesoscale vertical circulations are represented by the broad vertical arrows. Intense updrafts are depicted by the narrow, solid vertical arrows. [From Smull and Augustine 1993].

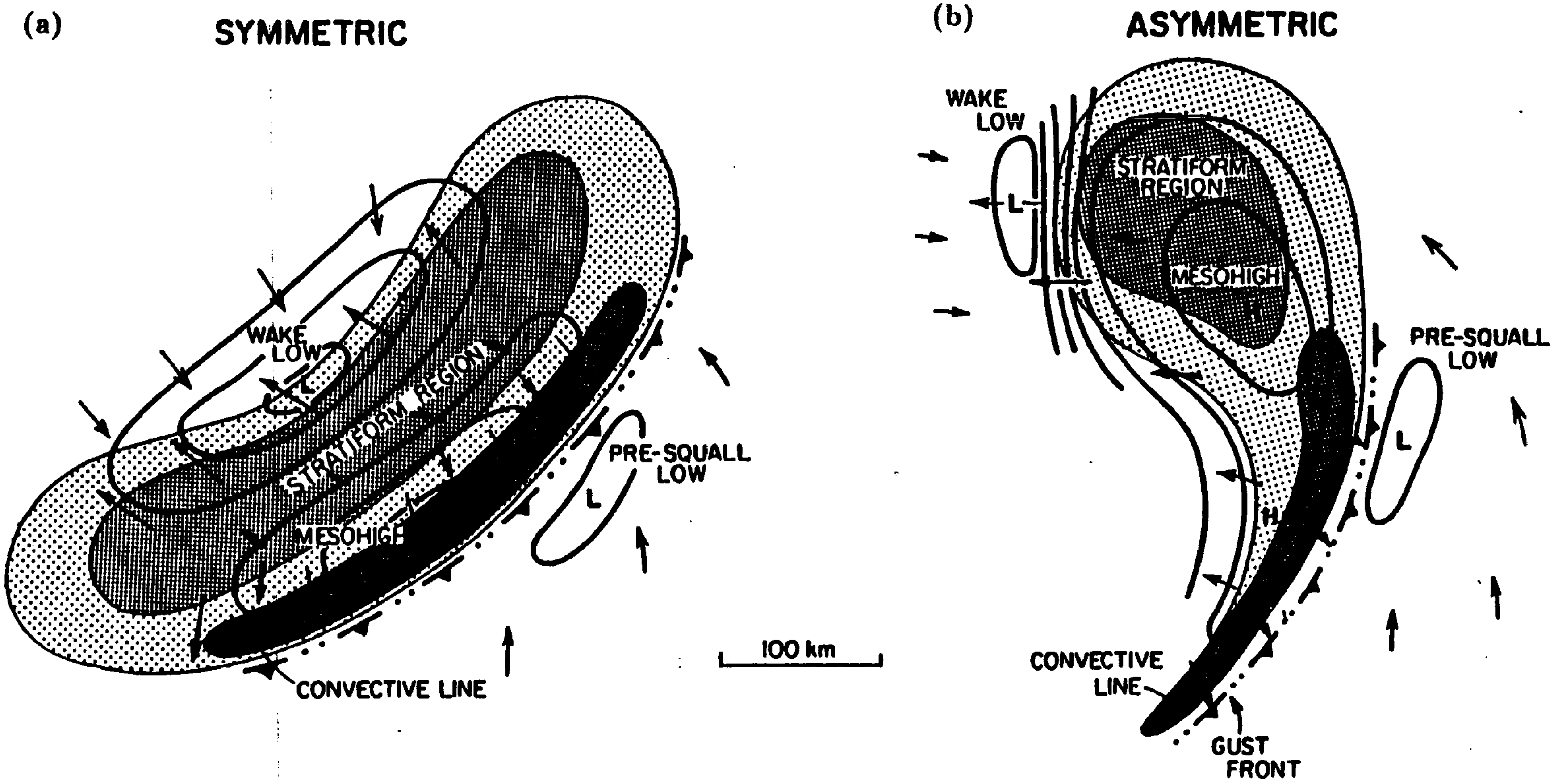

Figure 2.4: Schematic of the surface pressure and flow fields associated with: a) symmetric and b) asymmetric MCS structures. Arrows represent the surface flow. (From Loehrer 1992).

much of the stratiform region and convective line, while a wake low hugged the northern, back edge of the stratiform area. A descending rear inflow jet was responsible for this wake low (Loehrer 1992, his Fig. 6.7). MCS1 and MCS4 developed from an early chaotic structure (Blanchard 1990) into an asymmetric structure as the northern convection in the MCSs became more stratiform and a convective line developed on their southern ends as outflows from the systems converged with the environmental southerly flow. MCS2 developed an asymmetric structure as the stratiform region developed northwest of where the two convective bands intersected.

Fortune *et al.* (1992) performed an observational study of MCS1, MCS2, and MCS4 in order to determine why the convective bands in these systems resembled frontal waves. By examining Doppler radar and rawindsonde data, they identified three airstreams within these systems: a relatively warm, ascending flow from the apex toward the rear of the cloud shield; a dry midlevel inflow which contained both rising and sinking motion into the southern flank of the MCS; and cool inflow below 6 km into the northern flank of the stratiform region. In agreement with Smull and Augustine (1993), they found that the wave-like structure was not due to the development of mesoscale cyclonic vorticity.

A detailed study of the surface pressure features associated with MCS2 including the origins of the wake low was conducted by Stumpf *et al.* (1991). They found that the wake low occurred at the back edge of the trailing stratiform region as found in squall line studies. The wake low was associated with a descending rear inflow jet. The southern part of the the MCS, which had no trailing stratiform region, did not have a descending rear inflow jet or wake low. The maximum sinking of the rear inflow jet coincided with the strongest low-level reflectivity gradient and the strongest surface pressure gradient.

Nachamkin (1992) investigated the upscale evolution of MCS1, in which it grew from a conglomeration of convective elements to an organized system. Analysis of radar reflectivity and Doppler-derived winds showed a sudden, dramatic upscale transition which Nachamkin ascribed to the development of a blocking mesohigh aloft and the subsequent strengthening of the rear inflow jet.

Trier and Parsons (1993) examined the mesoscale environment of MCSs 3 and 4 with particular emphasis on the reasons for the development of MCS4. They found that the development of the diurnal LLJ and its interaction with the sloping frontal surface led to large increases in CAPE. The high CAPEs arose as high θ_E air was advected north over the front, under a region of colder midlevel temperatures. Adiabatic ascent near the terminus of the LLJ led to cooling and reduction of convective inhibition over the front. Deep convection then developed over this region, organizing into MCS4. MCS3, consisting of surface-based convection south of the front, decayed as the LLJ veered and created less favorable low-level shear while the diurnal cooling increased the convective inhibition. Fig. 2.5 (Trier and Parsons 1993, Fig. 22) is a schematic of the environment prior to the development of MCS4.

Green (1989) examined the surface pressure patterns revealed by the PAM (Portable Automated Mesonetwork) data during the 3-4 June episode. Each system developed a pre-MCS mesolow (Hoxit *et al.* 1976), a mesohigh just behind the strongest convective cells, and a wake low at the back edge of the stratiform rain. Green found that the intensity of the wake low was related to the intensity of the stratiform precipitation.

Other studies using data from this case include Holle *et al.* (1990), who used radar and lightning data to relate lightning flashes to the growth stages of the 3-4 June MCSs. McAnelly and Cotton (1992) examined radar data from several MCSs (including MCS1, MCS2, and MCS4) and found that in the growth from initiation to maximum extent, MCSs do not grow monotonically. Their cases exhibited a burst of meso-β scale convection followed by a lull and then continued growth. Similar growth patterns have been shown in modeling studies. McAnelly and Cotton suggest that gravity waves excited by the convection may be responsible for this effect.

While many studies of this case have been completed, the complexities exhibited by the four convective systems leave many questions unresolved, especially about the processes aiding the repetitive formation of the MCSs. Only the mature stage of the systems was well-sampled by the sounding network, with little data gathered during the systems' initial stages. The following sections describe the data and observational analyses which are used as diagnostic tools and for comparison with model results.

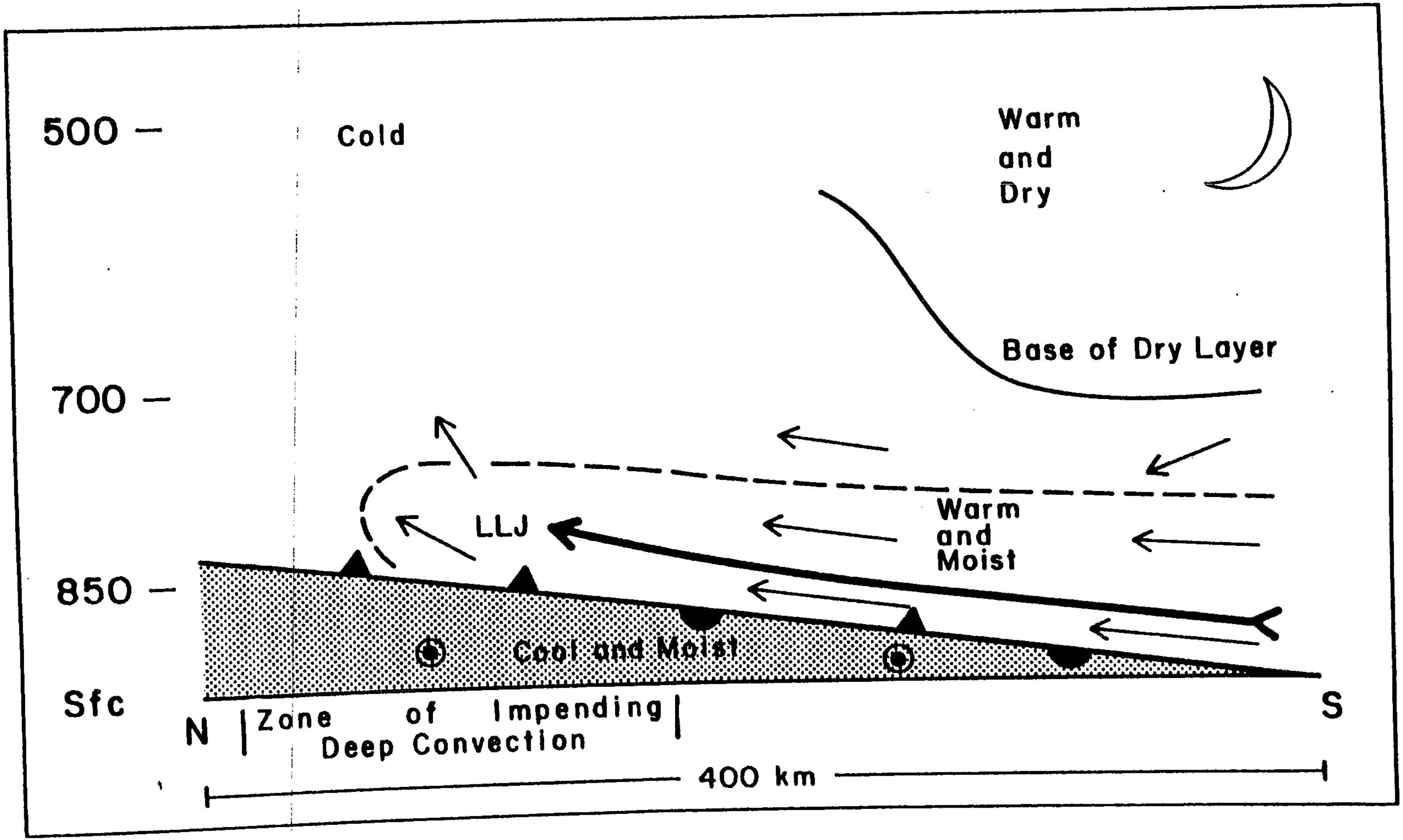

Figure 2.5: North-south cross-section schematic of the flow and frontal surface associated with MCS4. (From Trier and Parsons 1993).

2.3 Data

Figure 2.6 shows the location of many of the PRE-STORM observing systems. Five-minute-averaged surface data from the PAM/SAM (Portable Automated Mesonetwork / Surface Automated Mesonetwork) mesonetwork were available for the duration of the MCS episode (Fig. 2.6a). Surface airway data from the area (Colorado, Kansas, Missouri, Arkansas, Texas, Oklahoma, and New Mexico, Fig. 2.6b) were obtained from the Colorado State University (CSU) archive of FAA-604 data, the National Center for Atmospheric Research National Meteorological Center/Automated Data Processing (NCAR NMC/ADP) data, and from the National Climatic Data Center's (NCDC) hardcopy archive.

A major component of the PRE-STORM project was the supplemental sounding network (Fig 2.6c) consisting of temporary sounding stations along with additional soundings launched from the regular National Weather Service (NWS) sites. Sounding data were obtained from the National Severe Storms Laboratory (NSSL) archive. Additional soundings were obtained from the NCAR NMC/ADP archive and the NCDC hardcopy archive. Unfortunately, no supplementary soundings are available at 3/1200 and no extra NWS soundings were launched during the remainder of the 3-4 June episode. Analysis of soundings from DDC (refer to Fig. 2.6 for the station location) showed that the 3/0900 sounding entered the NMC archive as the 3/1200 sounding. The actual 3/1200 DDC sounding was obtained from NCDC.

Radar data from the six National Weather Service radars equipped with digital recorders were synthesized on a NSSL computer. Printouts of the composite base scans were used to track the location, intensity, and movement of the precipitation systems. The operational NMC radar summary charts were used to supplement the PRE-STORM radar data.

Visible and infrared satellite images from GOES (Geostationary Operational Environmental Satellite) were provided by the National Weather Service. A loop of the 3 June visible images was constructed by digitizing the hard copy images. Cloud-top area and temperature data were obtained from NSSL.

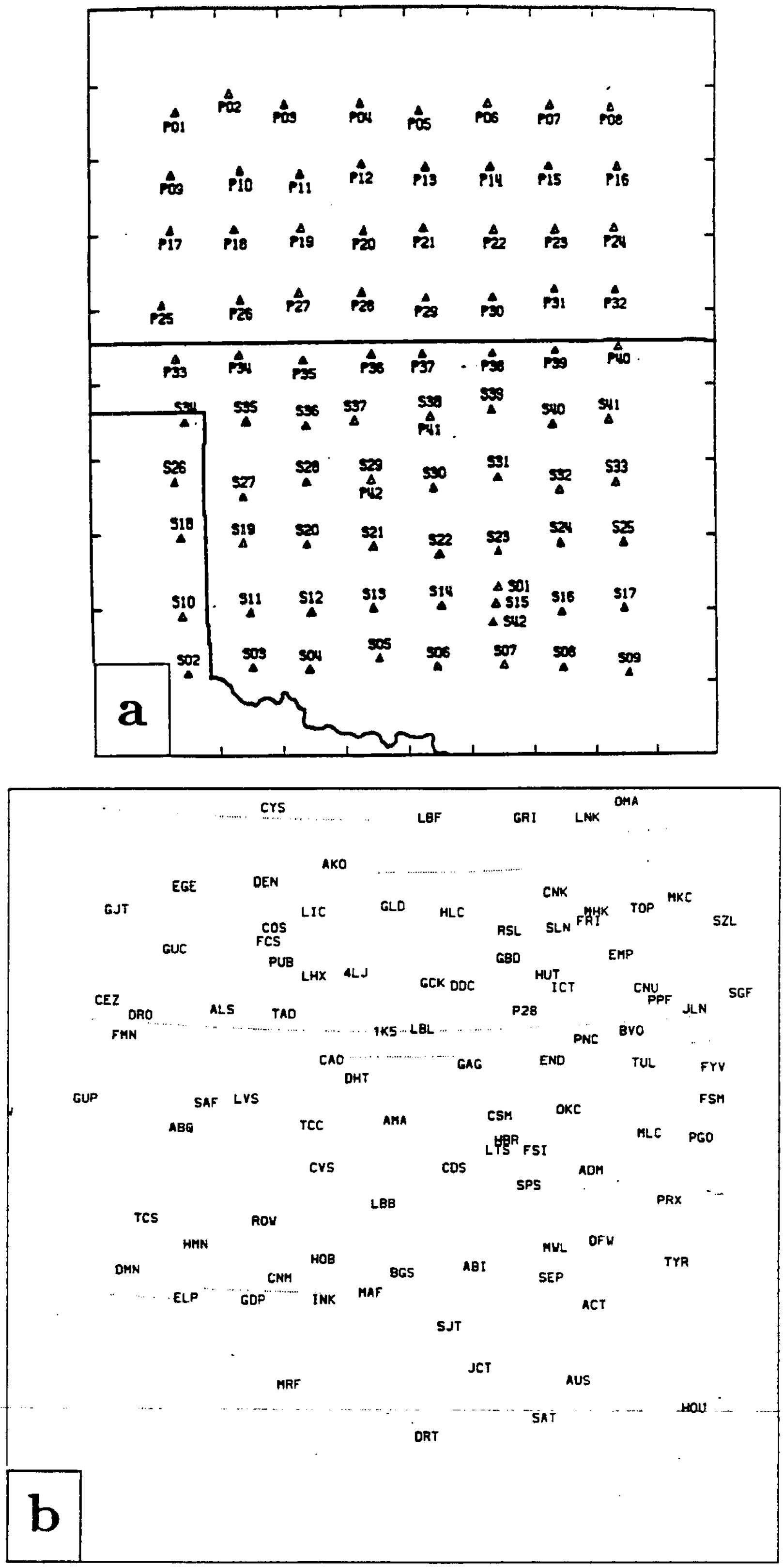

Figure 2.6: Locations and identifiers for a) the PAM/SAM mesonetwork; b) surface airways stations; c) Radiosonde stations.

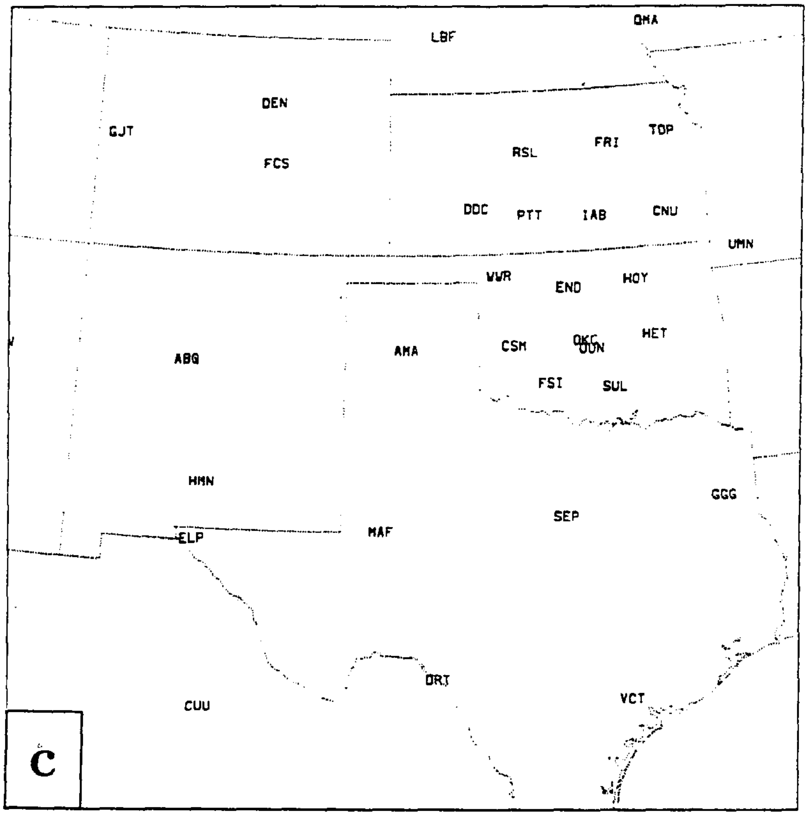

Figure 2.6: Continued.

Wind profiler data were examined for Liberal and McPherson, Kansas, Norman, Oklahoma and Flagler, Colorado. One-hour-averaged horizontal winds were available from 1.8 km to 11 km above ground level (AGL). As pointed out by Augustine and Zipser (1987), these 50-MHz profilers cannot sample the atmosphere below about 1.8 km and so winds from the boundary layer and lower part of the free atmosphere were not available.

Hourly precipitation data were obtained from NCDC and were combined with rain-gauge data from the PAM/SAM network to produce plots of one-, three-, six-, twelve- and twenty-four-hourly rainfall totals.

2.4 Observational analysis of the case

2.4.1 Conditions between 3/0000 and 3/1200

A typical characteristic of SCC cases is a slowly evolving synoptic pattern (Fritsch *et al.* 1986). The 3/0000 surface analysis (Fig. 2.7) shows a stationary front extending from a low in southeast New Mexico, northeastward across Oklahoma into southwest New

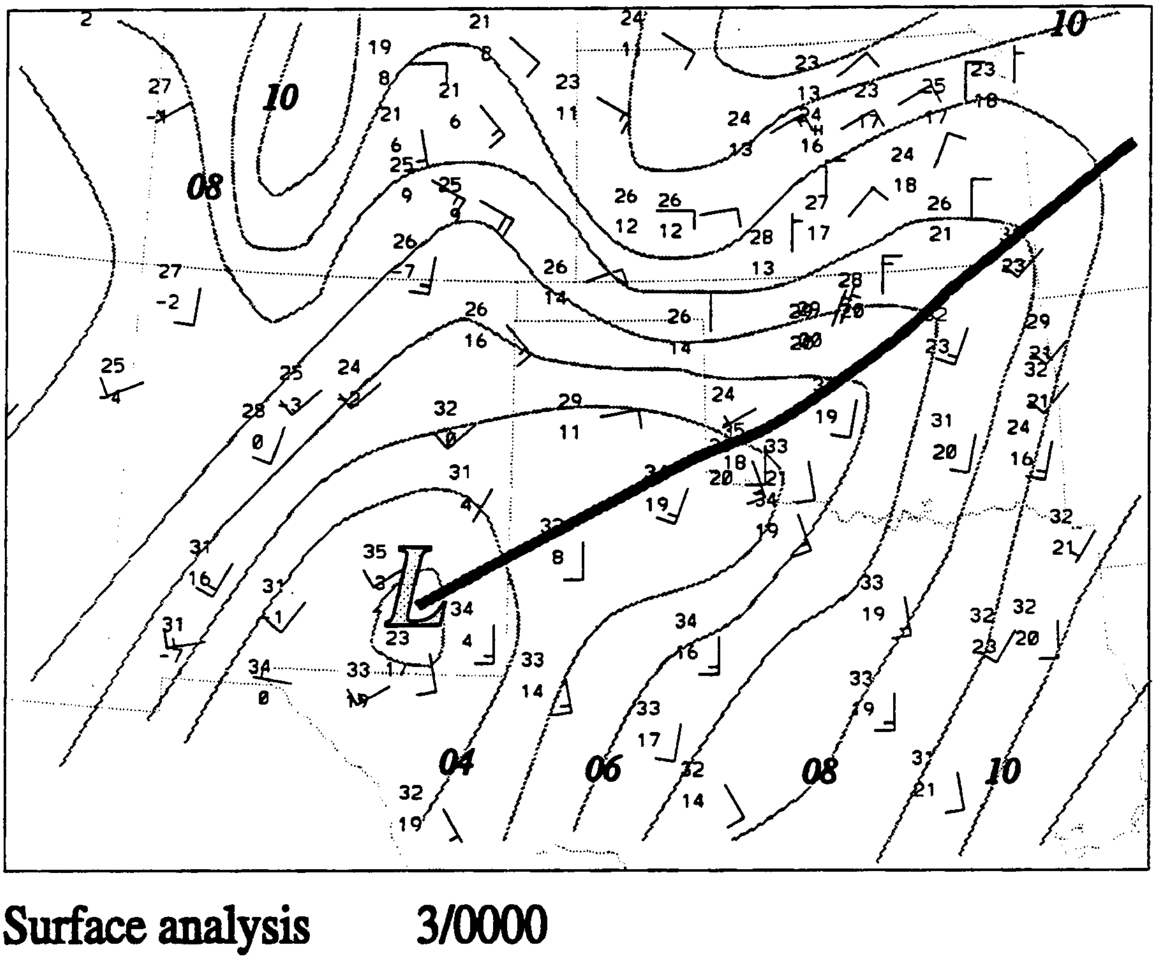

Figure 2.7: Surface analysis for 3/0000. Conventional plot of temperature and dewpoint (° C), winds (one-half barb = 2.5 m s^{-1} and a full barb = 5 m s^{-1}), and isobars (contoured every mb, labels omit the leading "10"). The surface front is indicated by the dark, wide line.

Mexico. South of the front, high θ_E air was being advected northward. Cooler and moist anticyclonic flow was found north of the front with significant convergence occurring along the front. Strong thunderstorms with radar echo tops to 21 km were occurring along the front from the eastern Texas panhandle through central Oklahoma. Satellite data at 3/0000 (Fig. 2.8a) show a narrow band of cold clouds which exhibited a minimum temperature of -70° C by 3/0100 (Fig. 2.8b).

Aloft, at 500 mb, a trough was along the west coast (120° W) with southwesterly flow over the PRE-STORM region (Fig. 2.9). A negatively-tilted ridge axis extended from southern Oklahoma to northwest Wyoming. At 850 mb, (Fig. 2.10) most of Kansas was within the cold air mass, except for IAB and CNU. Southerly winds over western Oklahoma and central Texas were advecting moisture towards the frontal zone, but no prominent low-level jet (LLJ) could be detected, as might be expected in the evening. Above 700 mb little directional shear could be found, but speeds increased with height. At 250 mb (Fig. 2.11) a jet streak centered over WWR with a maximum speed of 45 m s^{-1} curved slightly anticyclonically along the northern edge of the Oklahoma convective system cirrus outflow, as is typical of such systems (e.g. Fritsch and Maddox 1981a; Maddox *et al.* 1981). (It should be noted that the 3/0000 WWR temperature sounding is systematically too warm. The winds, while stronger than surrounding sites, do seem reasonable). Low-level warm advection over this region was relatively weak, but moisture convergence along the front (especially in southwest Oklahoma) was strong and was the apparent trigger for these storms (not shown). An Intensive Observing Period (IOP) began at 2/2100 with special soundings and an aircraft mission to investigate the convection (Meitín and Cunning 1985). The convective storms along the front occupied a relatively small area, but were quite vigorous and were prolific anvil producers (Meitín and Cunning 1985). For example, at 3/0200 (Fig. 2.8c) convection was located over west-central Oklahoma (as indicated by the area of cloud tops colder than -64° C) while the associated anvil clouds extended downstream into Missouri.

By 0300 UTC, the Oklahoma convective system cirrus shield covered much of the state (Fig. 2.8d), but radar indicated that the convection beneath the cloud canopy had

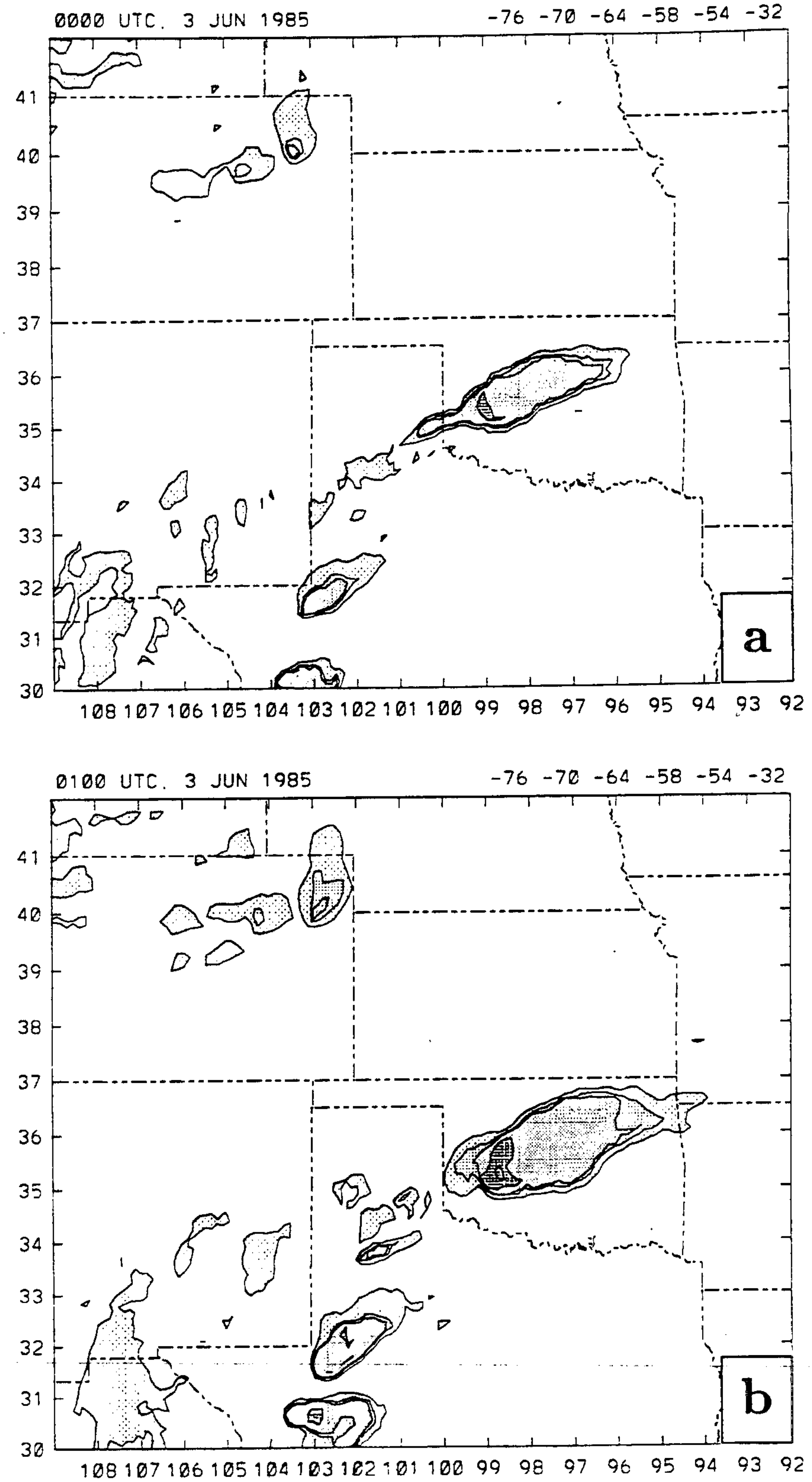

Figure 2.8: Contours of infrared brightness temperature. Temperature thresholds are -32° C, -54° C, -58° C, -64° C, -70° C, and -76° C with darker shading representing colder temperatures for a) 3/0000, b) 3/0100, c) 3/0200, d) 3/0300, e) 3/0400, f) 3/0500, g) 3/0600, h) 3/0700, i) 3/0800, j) 3/0900, k) 3/1000, and l) 3/1100.

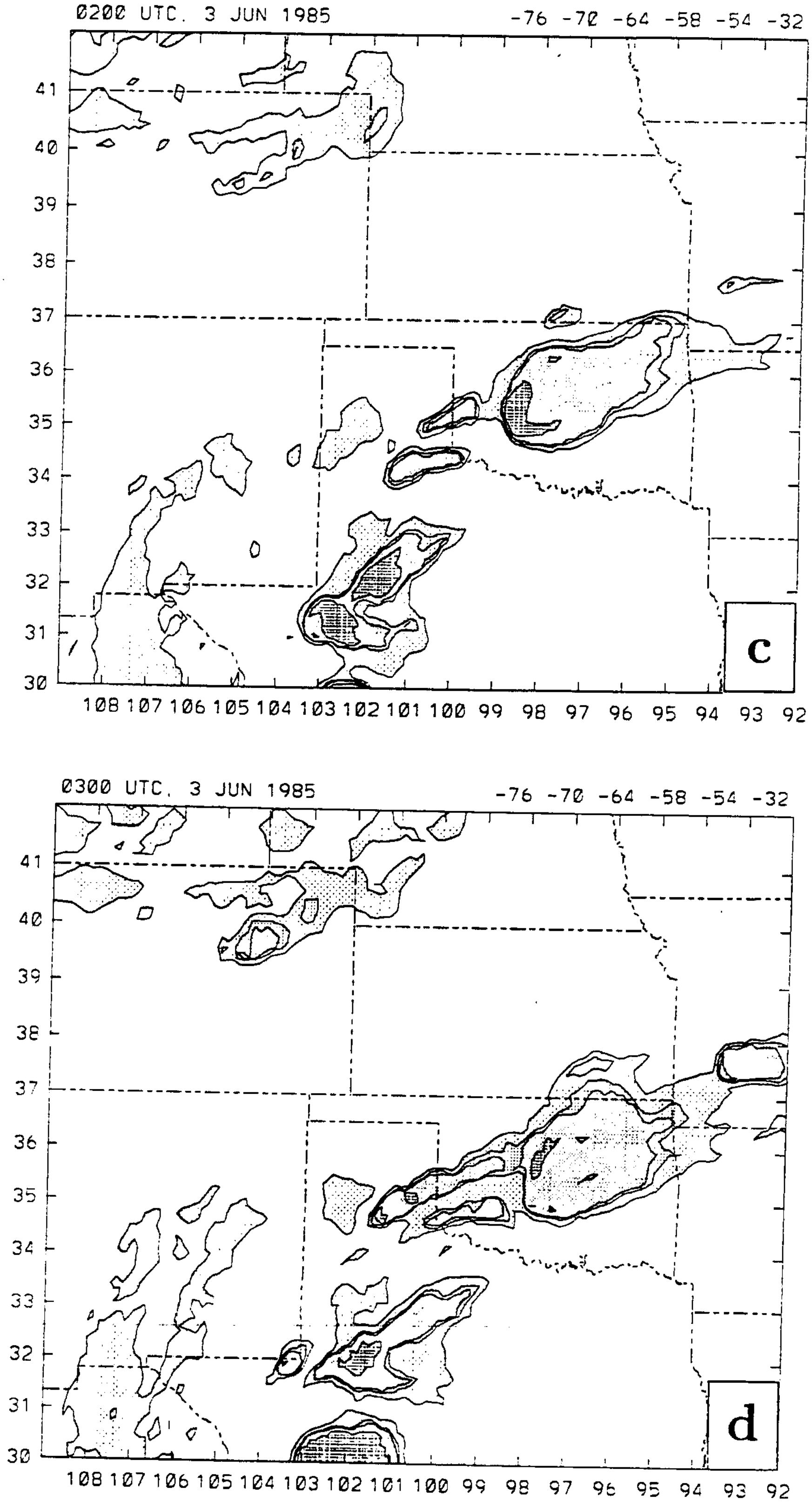

Figure 2.8: Continued.

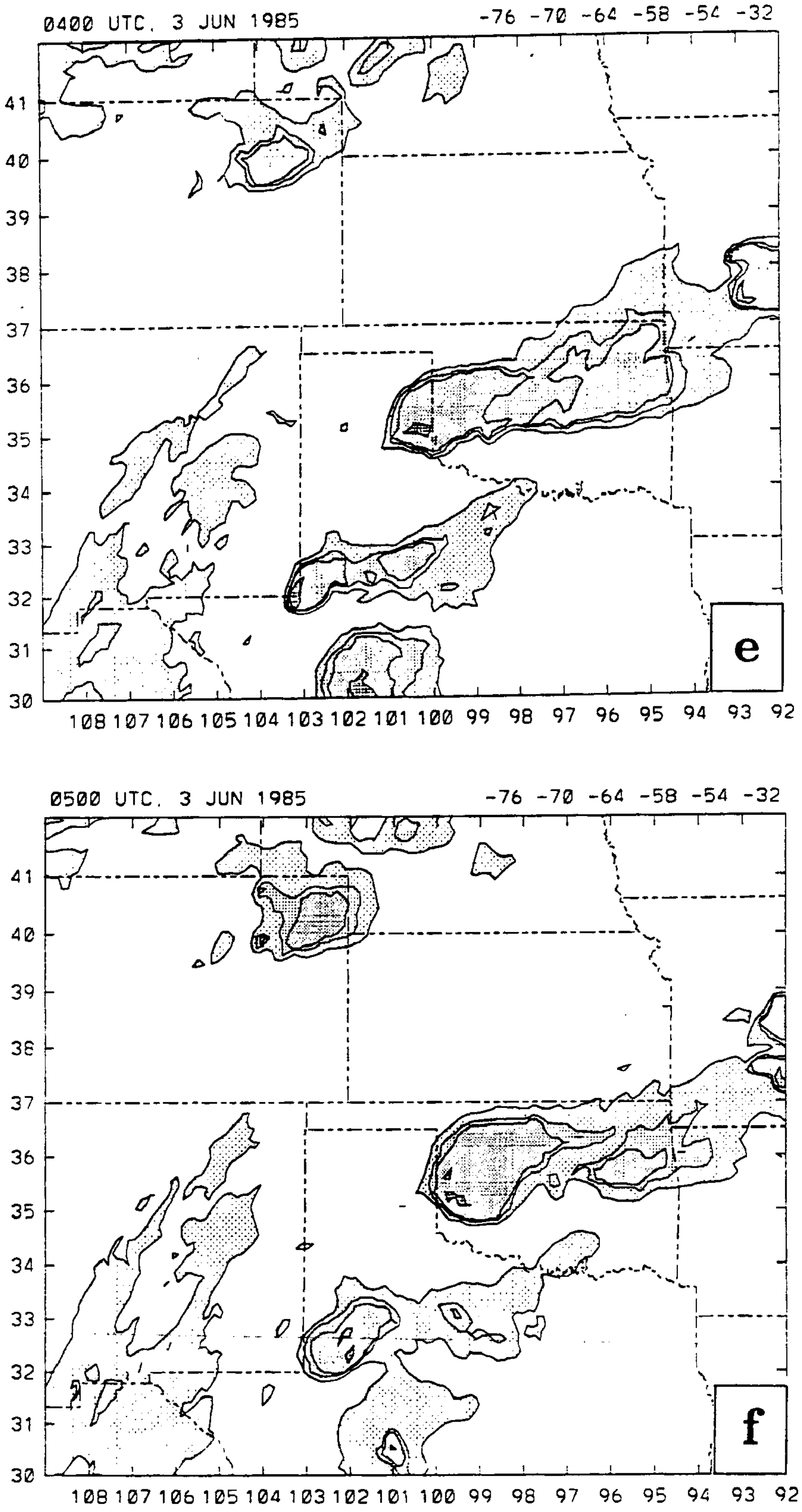

Figure 2.8: Continued.

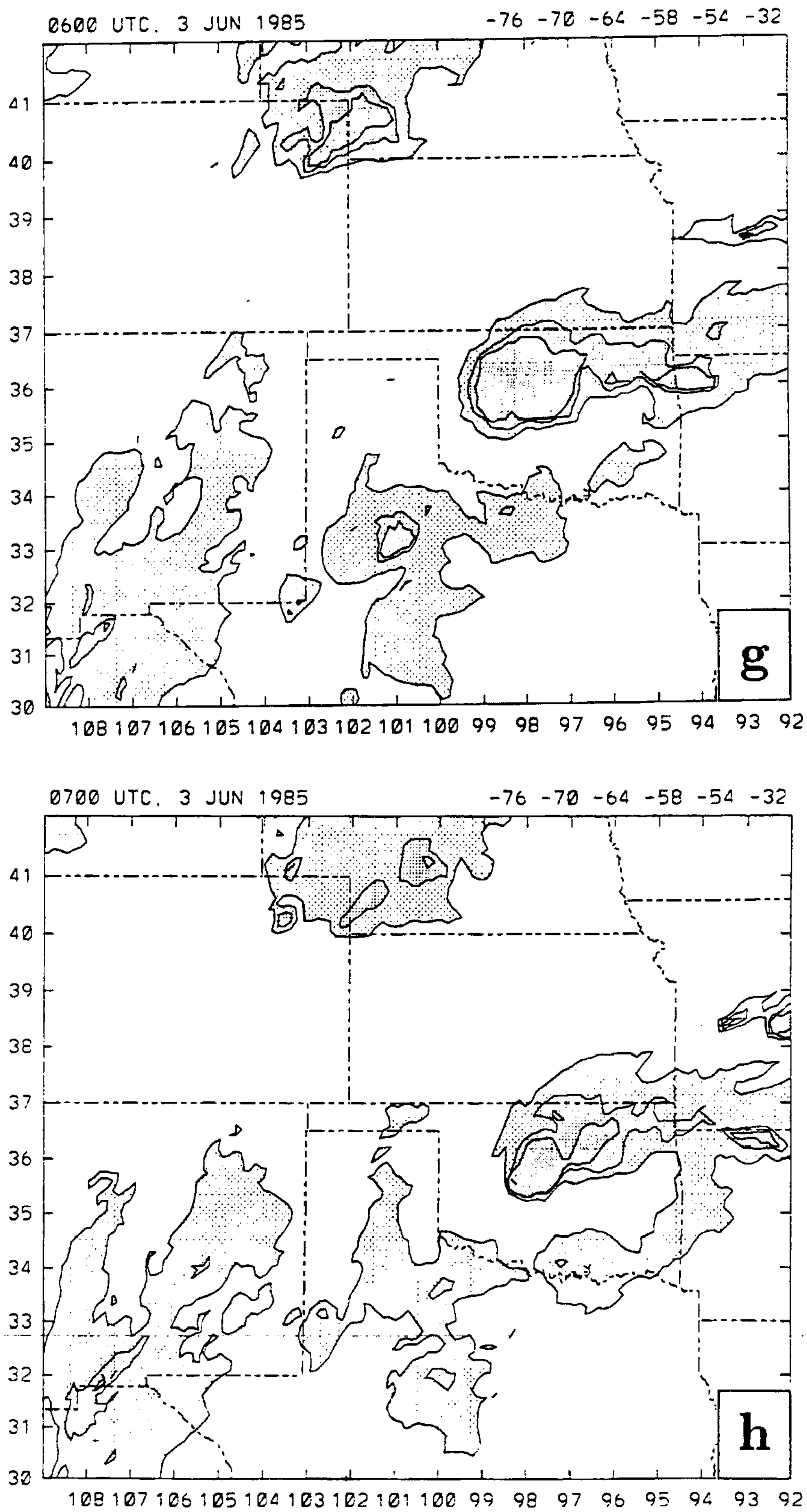

Figure 2.8: Continued.

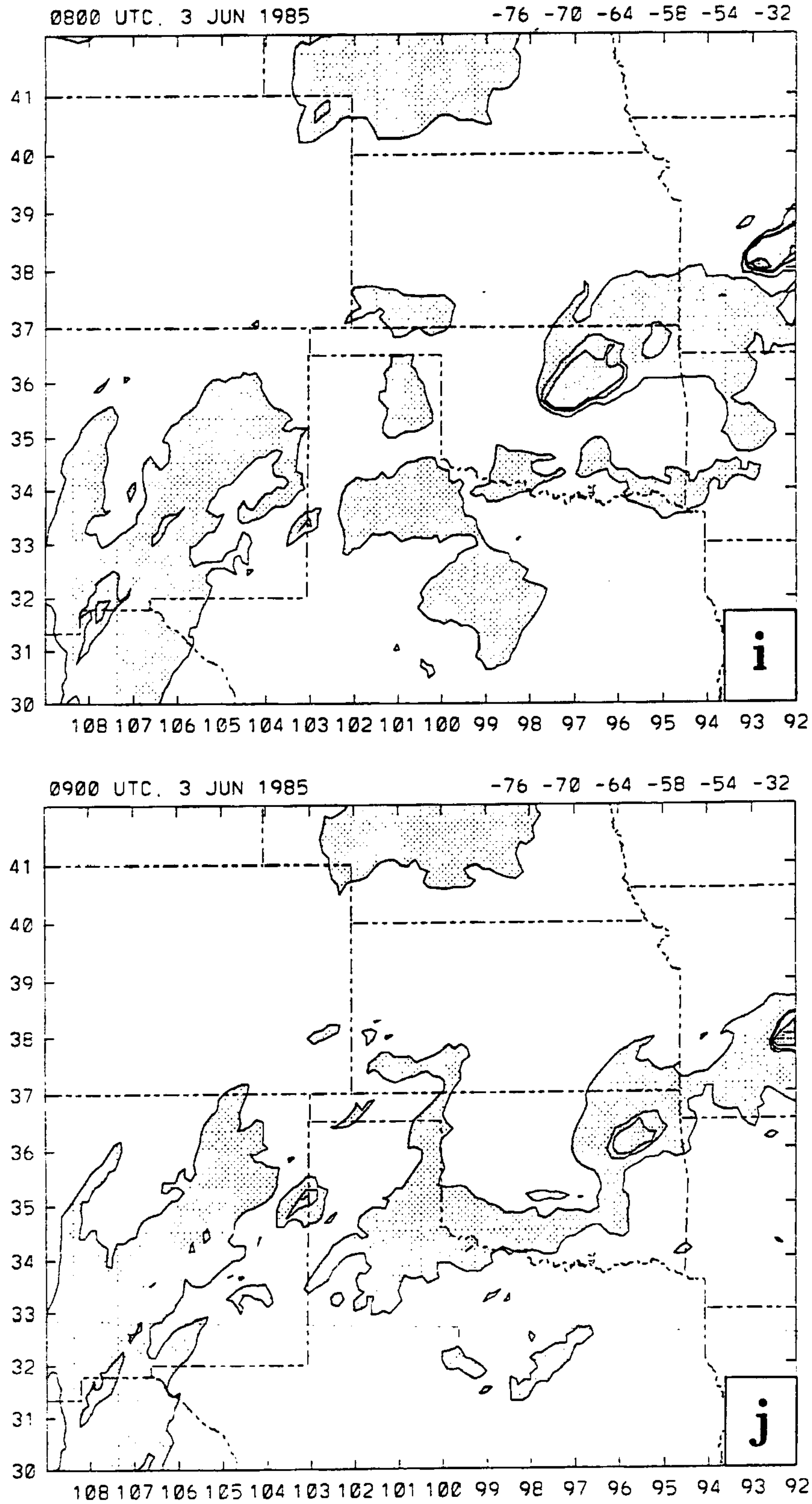

Figure 2.8: Continued.

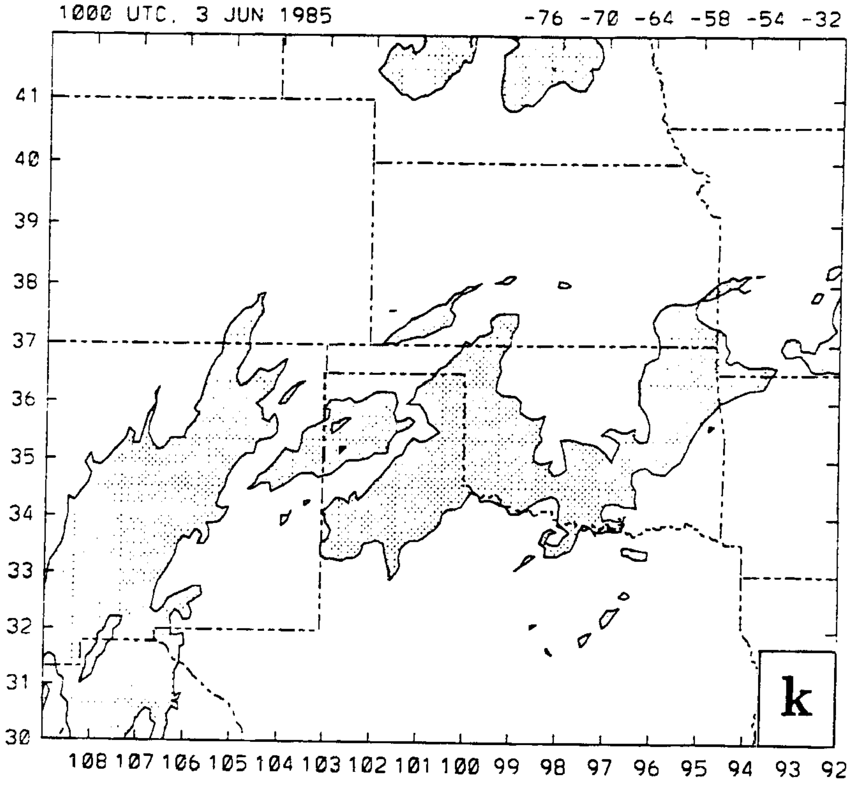

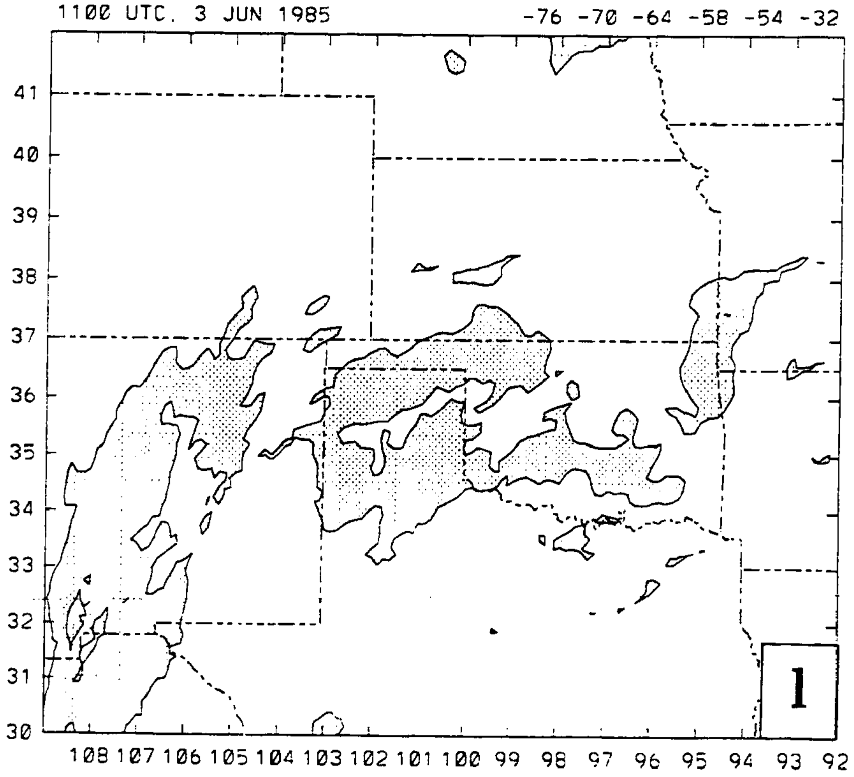

Figure 2.8: Continued.

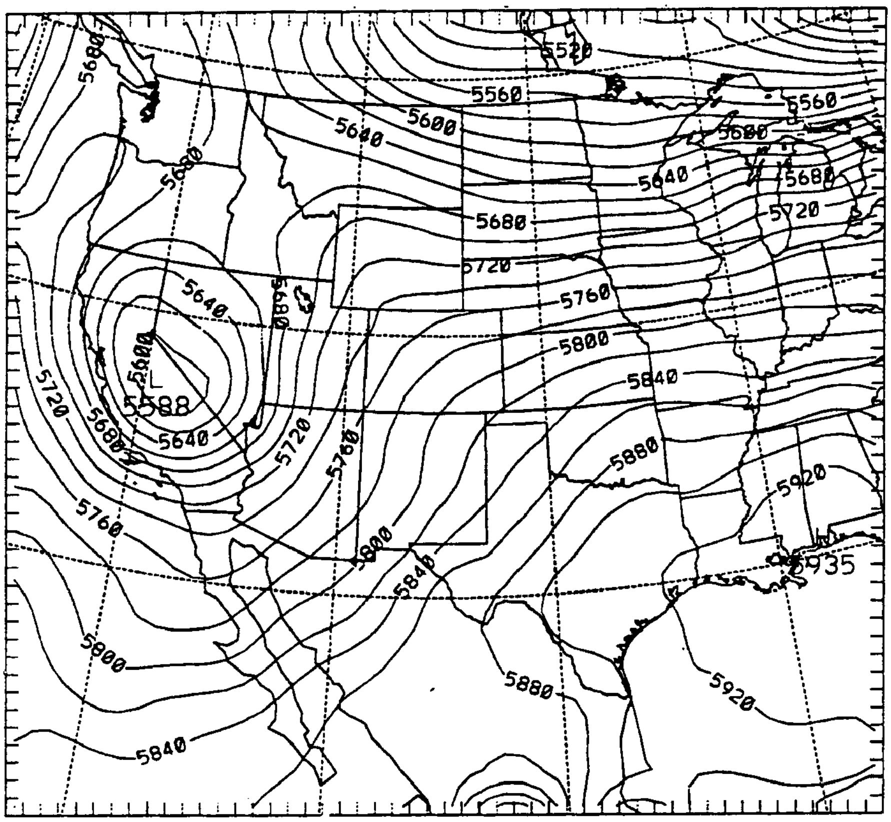

Figure 2.9: Geopotential height (m) at 500 mb contoured every 20 m at 3/0000.

weakened considerably (not shown). Farther to the southwest, new convection developed along the front in a narrow band across the Texas panhandle. Other cells were in a north-south line across west Texas. (These storms drifted northeastward and decayed). The 0230 UTC 850 mb plot (not shown) showed little change in winds, but dewpoints across Oklahoma and southern Kansas had climbed by at least 2° C at every station. At 250 mb a well-defined jet streak curved anticyclonically across southern Kansas with a maximum wind of 52 m s^{-1} at CNU (Fig. 2.12). In fact, the -32° C contour (Fig. 2.8d) exhibits a corresponding curvature in southeastern Kansas.

By 0530 UTC, convection across the area was weakening. However, a LLJ was now apparent at 850 mb across west Texas and west Oklahoma with 15 m s^{-1} winds at MAF, AMA, FSB and WWR (Fig. 2.13). Aloft at 250 mb (Fig. 2.14), the jet streak had moved

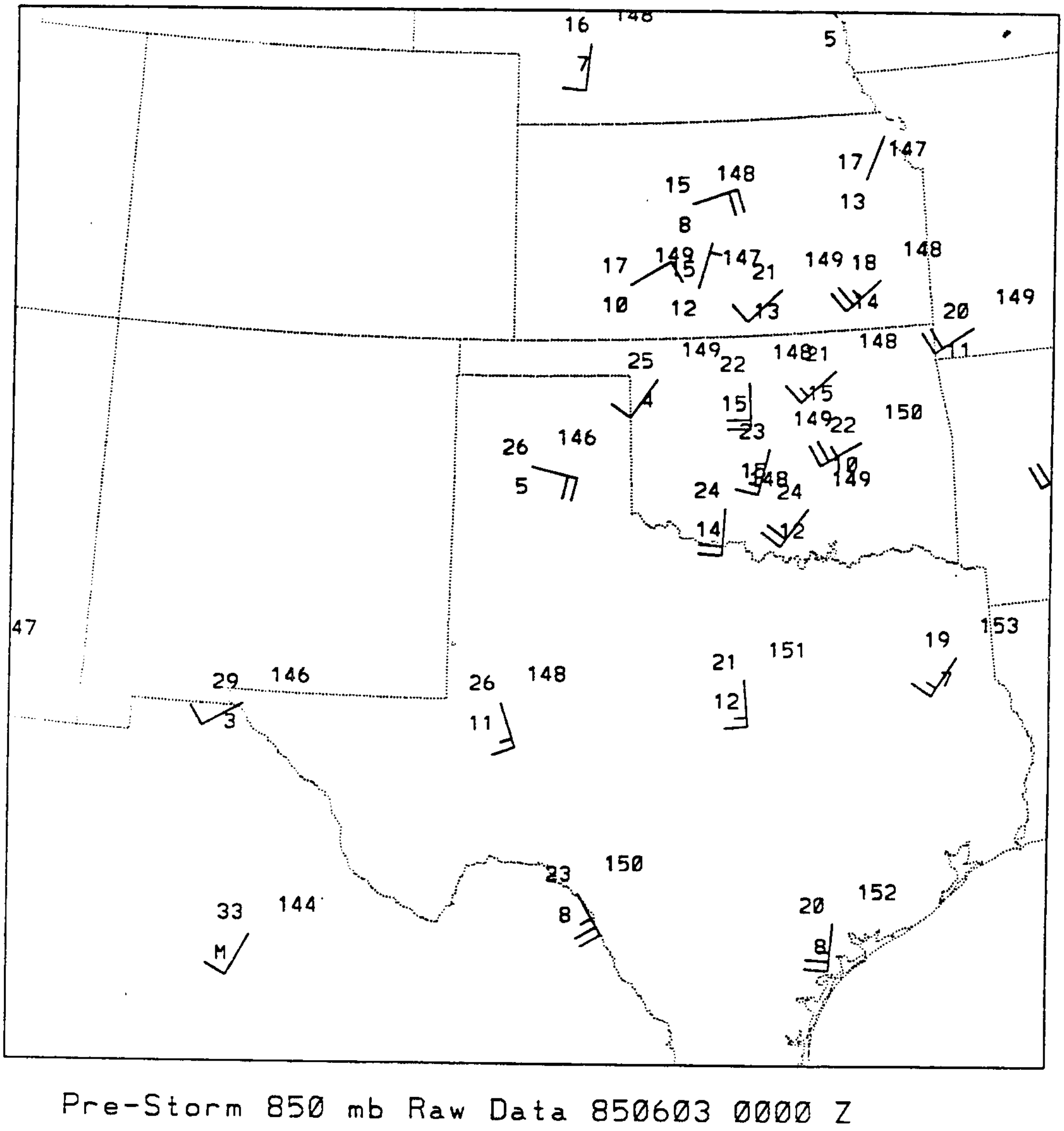

Figure 2.10: Conventional pressure level plot of 850 mb data for 3/0000. Shown are temperature and dewpoint (° C) and heights (dm). A full wind barb represents 5 m s^{-1}, a half-barb 2.5 m s^{-1}, and a flag represents 25 m s^{-1}.

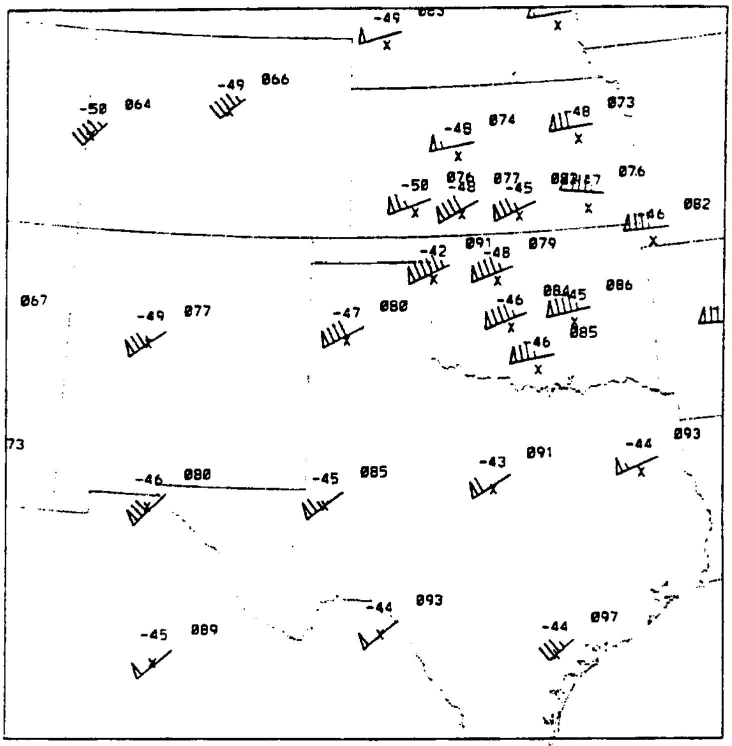

Pre-Storm 250 mb Raw Data 850603 0000 Z

Figure 2.11: As in Fig. 2.10, but for 250 mb.

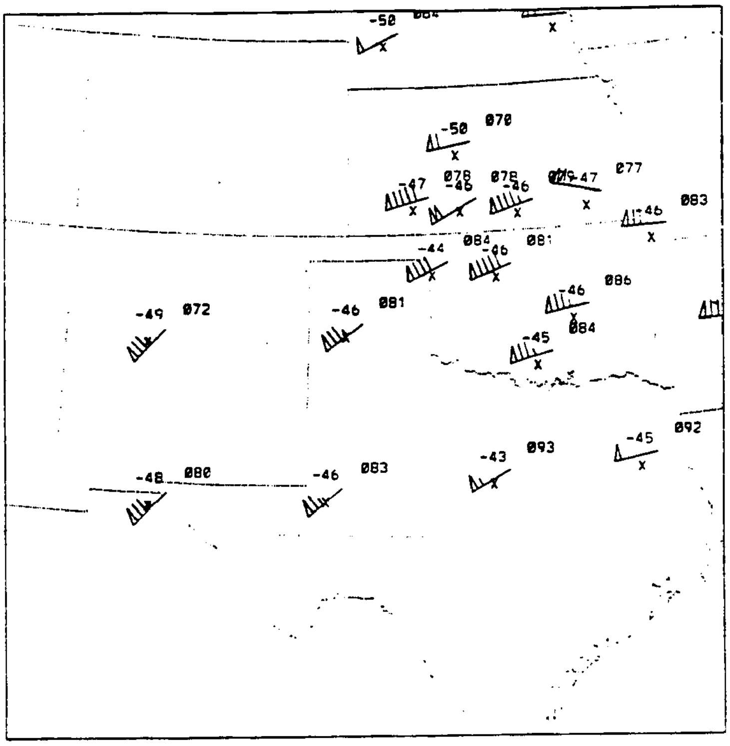

Pre-Storm 250 mb Raw Data 850603 0230 Z

Figure 2.12: As in Fig. 2.11, but for 3/0230.

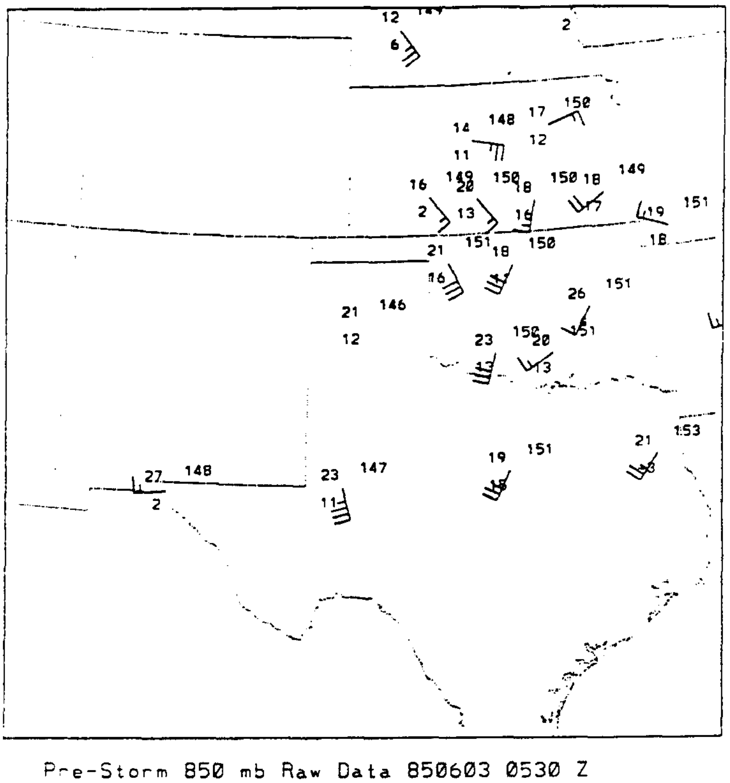

Figure 2.13: As in Fig. 2.10, but for 3/0530.

north away from the cirrus shield, arcing from PTT to western Missouri with a maximum wind of 55 m s^{-1} at FRI. At 0900 only some of the NWS stations launched soundings. The LLJ could be detected at AMA and at DDC where the winds had veered to southerly and increased to 12 m s^{-1} (not shown) as is consistent with an inertial oscillation. Convection across Oklahoma continued to weaken (Figs. 2.8e through 2.8k) so that by 1100 UTC (Fig. 2.8l) only cirrus debris or weak, midlevel convection remained.

2.4.2 Conditions between 3/1200 and 4/0000

Conditions at 3/1200

The 1200 UTC surface chart showed that the front had moved little during the night (Fig. 2.15). However, winds north of the front had veered to a more easterly direction and were less convergent than the previous evening. Moisture had increased north of the front and the upslope flow led to fog and drizzle across western and north central Kansas. A broad surface low was located along the front in southeast New Mexico and moisture was streaming northward across most of Texas.

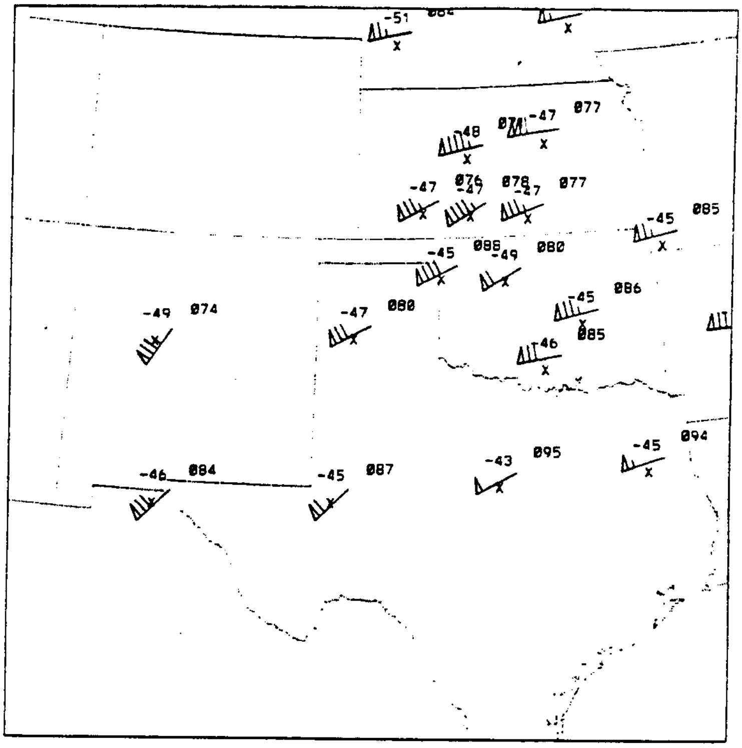

Pre-Storm 250 mb Raw Data 850603 0530 Z

Figure 2.14: As in Fig. 2.11, but for 3/0530.

The 3/1200 IR image (Fig. 2.16a) showed an area of cirrus arcing anticyclonically across New Mexico into southeast Colorado with a sharp poleward edge, indicative of the jet core (Durran and Weber 1988). Much of the Texas panhandle and southern Oklahoma were covered with -32° C clouds, some of which were convective debris, while radar showed that the southern Oklahoma cirrus was associated with some weak, low-topped convection. It will be shown later that this convection was high-based.

The large-scale 500 mb chart showed that the upper trough along the west coast had moved little during the night, with its axis located along 116° W (Fig. 2.17). The entire PRE-STORM region was located between this trough and the downstream ridge axis. At 850 mb (Fig. 2.18), a LLJ was still apparent at AMA and had veered during the night in agreement with the climatological behavior of the LLJ (Hoxit 1975) or with an inertial oscillation (Blackadar 1957). (Winds in the raw AMA sounding were missing between 846 mb and the surface. The 846 mb winds were assigned to the 850 mb level). The 850 mb surface at DDC was back within the cold air, as winds had backed and weakened

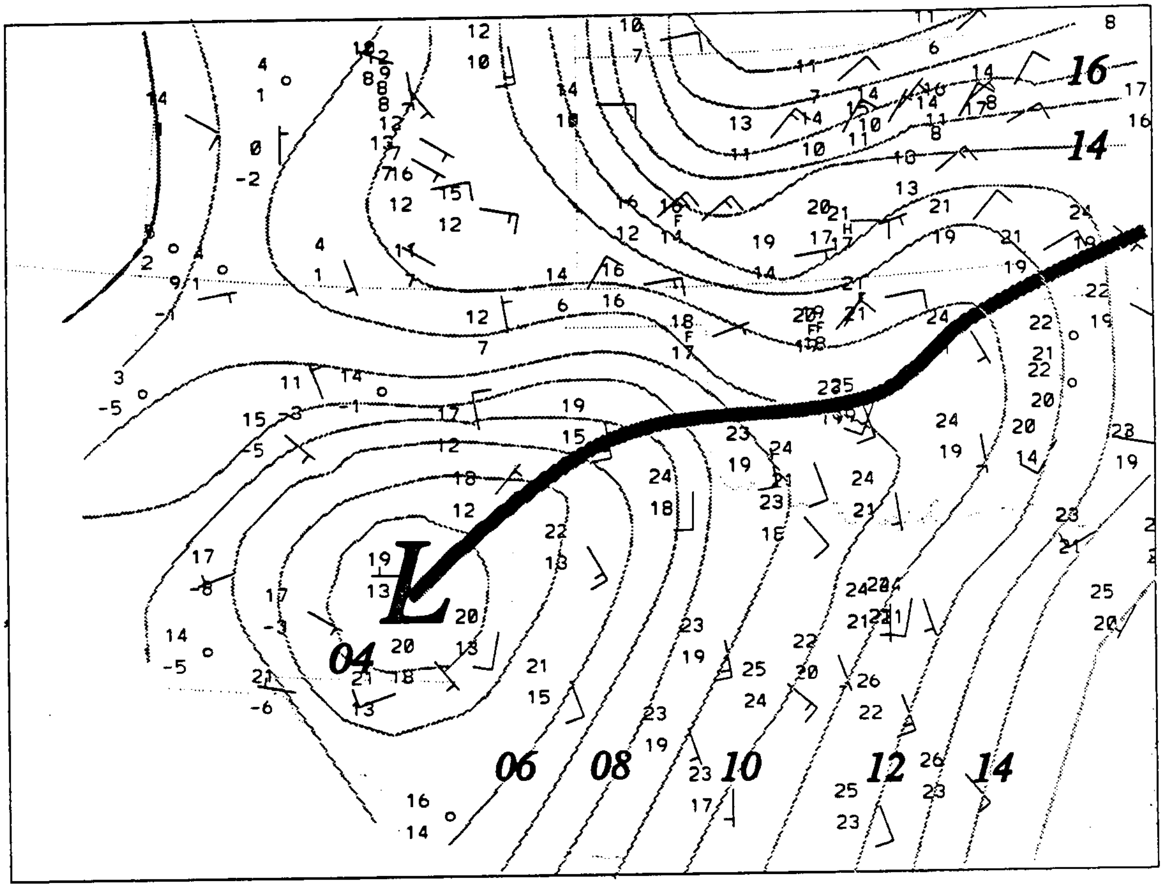

Surface analysis 3/1200

Figure 2.15: Surface plot (as in Fig. 2.7) at 3/1200.

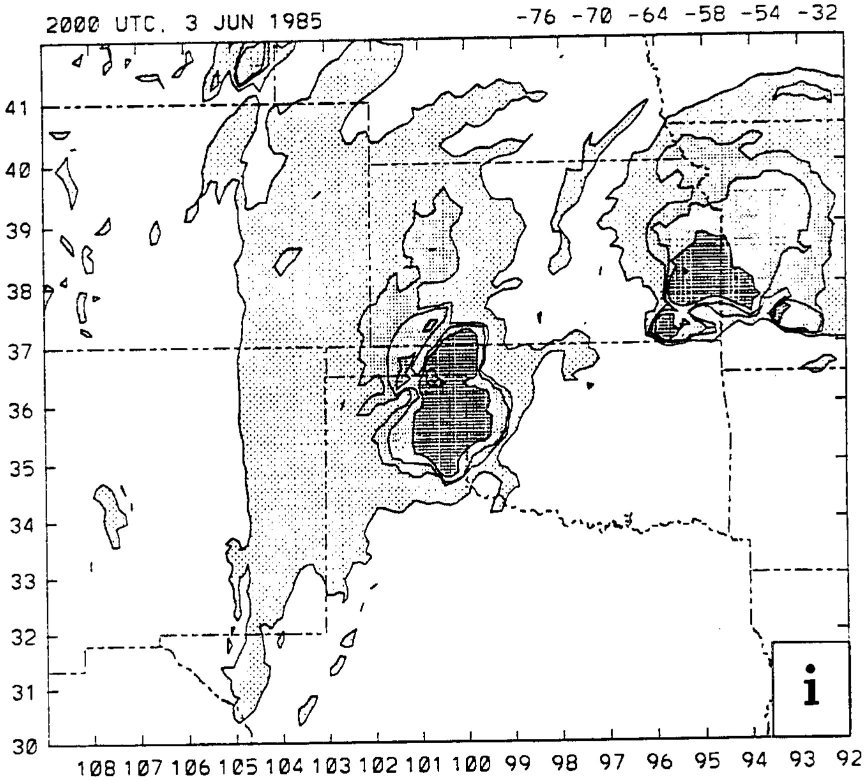

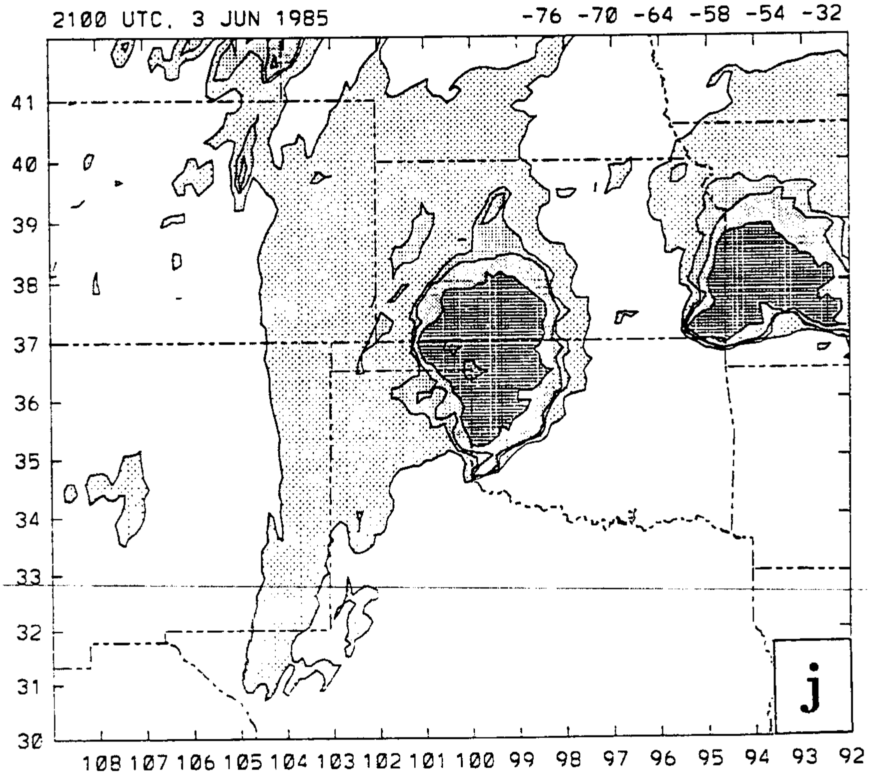

Figure 2.16: Continued.

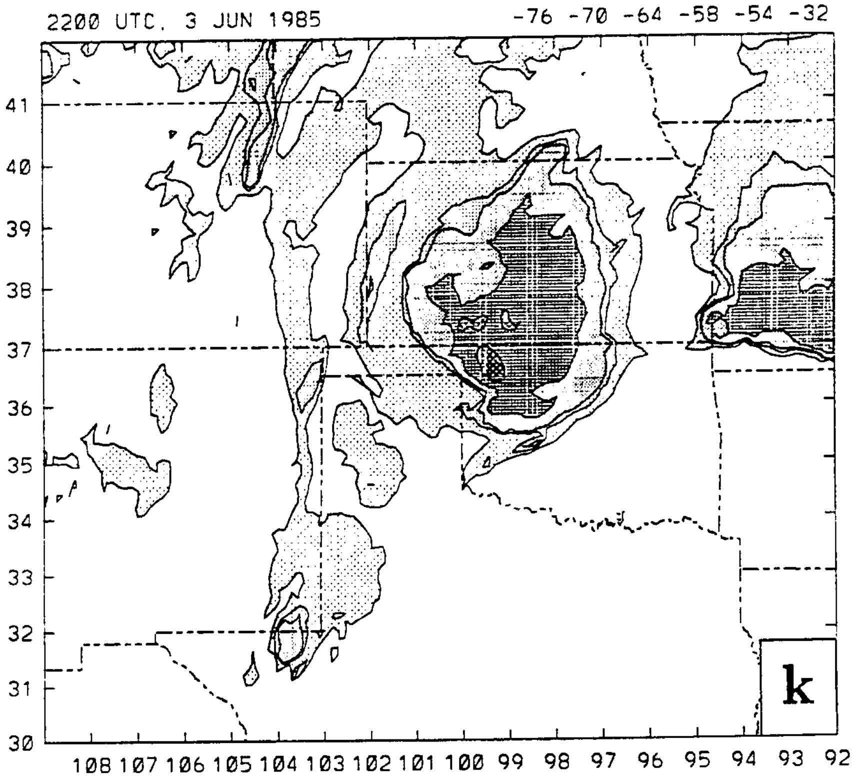

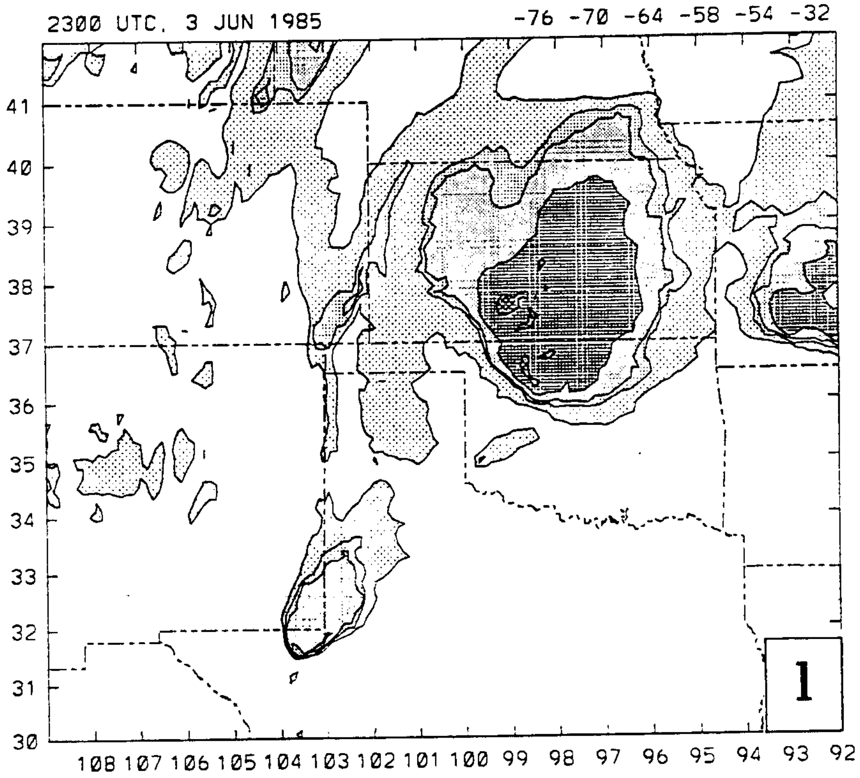

Figure 2.16: Continued.

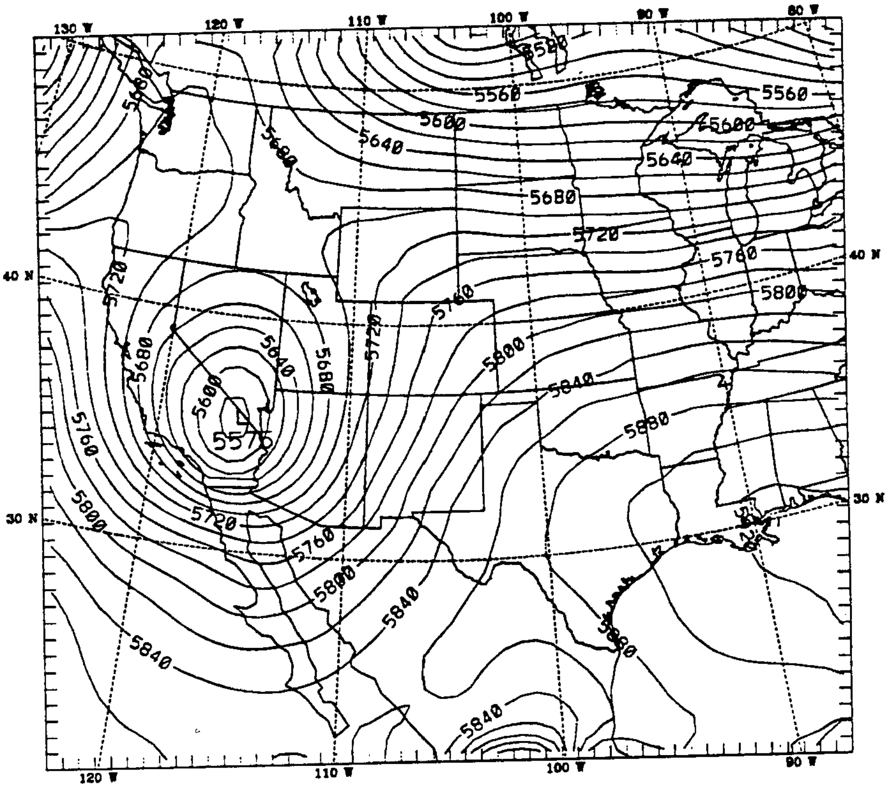

Figure 2.17: 500 mb geopotential heights (as in Fig. 2.9) at 3/1200.

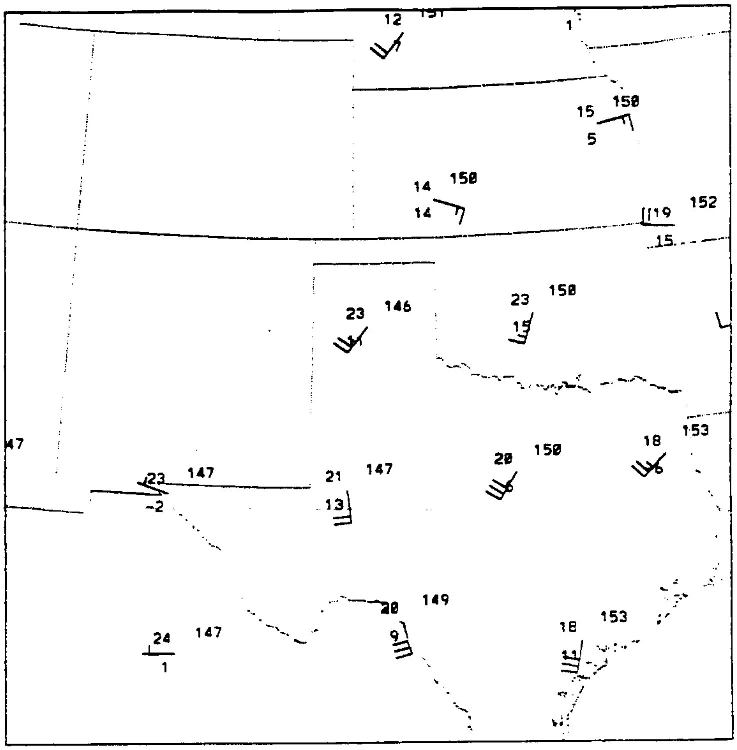

Pre-Storm 850 mb Raw Data 850603 1200 Z

Figure 2.18: As in Fig. 2.10, but for 3/1200.

and the temperature had dropped 2° C since 0800 UTC. It can be inferred that the LLJ was impinging upon the frontal surface between AMA and DDC. Fig. 2.19 shows the 850 mb horizontal temperature advection at 1200 UTC. This plot is based on the objectively-

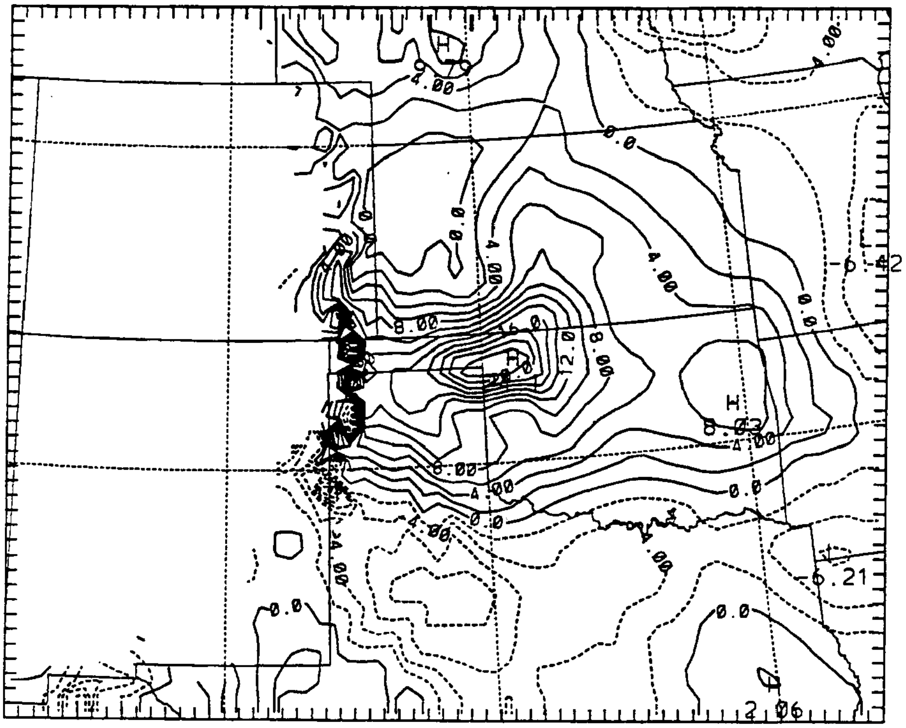

Figure 2.19: Horizontal temperature advection (K (12 h)$^{-1}$) on the 850 mb surface at 3/1200.

analyzed model initial fields which include bogus sounding data as described in Chapter 3. The bogus soundings used in the analysis were derived from a subjective analysis of all the available data. A maximum of warm advection (24.1° K (12h)$^{-1}$) over the eastern end of the Oklahoma panhandle nearly coincided with the location of the first convection associated with MCS1 at 1230 UTC (Fig. 2.16b). A maximum of warm advection at 800 mb (not shown) was co-located with the 850 maximum. Low-level warm advection implies, through quasi-geostrophic theory, upward motion and is often found to be a preferred region for MCS initiation (e.g. Maddox and Doswell 1982). Fig. 2.20 presents grid point profiles of temperature advection, potential vorticity, θ_E and vertical motion at the point in the Oklahoma panhandle with the maximum low-level warm advection. As Doswell (1987) points out, the large-scale quasi-geostrophic ascent is usually much

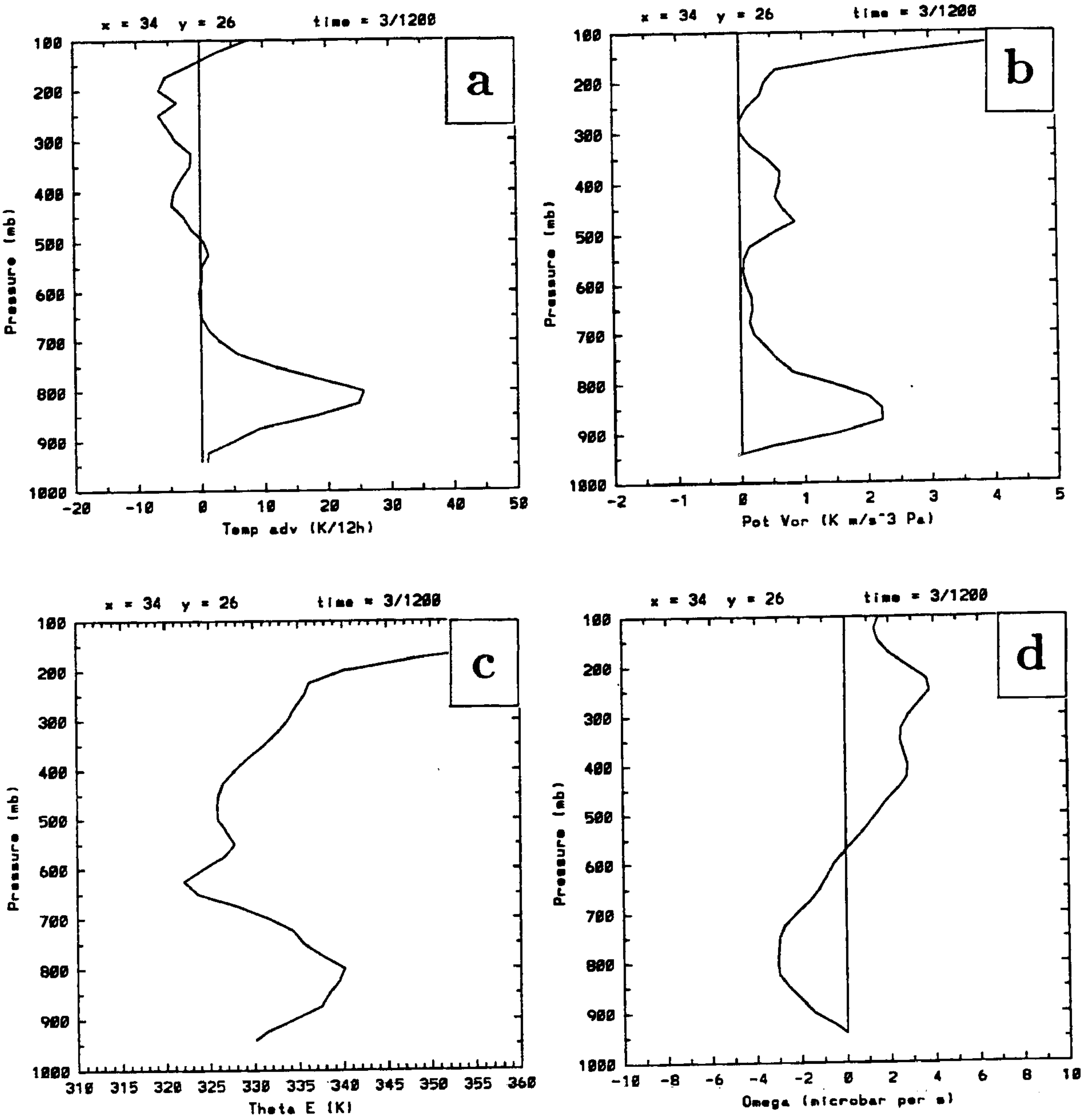

Figure 2.20: Profiles of a) temperature advection (K(12h)$^{-1}$), b), potential vorticity (K m s^{-3} Pa), c) θ_E (K), and d) ω (μb s^{-1}) at 3/1200 for a grid point in the eastern Oklahoma panhandle.

too small to trigger convection. The strong low-level warm advection near the top of the frontal inversion with neutral temperature advection in the mid-troposphere and cold advection in the upper troposphere at this point would act to destabilize the atmospheric column. The frontal surface is marked by a maximum in potential vorticity (Fig. 2.20b). A strong decrease in θ_E with height above the inversion (Fig. 2.20c) suggests considerable convective instability is present, while upward motion peaks at 800 mb (Fig. 2.20d) at this grid point. The adiabatic cooling and cold vertical advection due to the -3 μb s^{-1} ascent should not offset the strong low-level horizontal warm advection.

At 500 mb an obvious shortwave could not be detected over the region (Fig. 2.21) although the winds at ELP and ABQ suggest a shortwave might have been entering

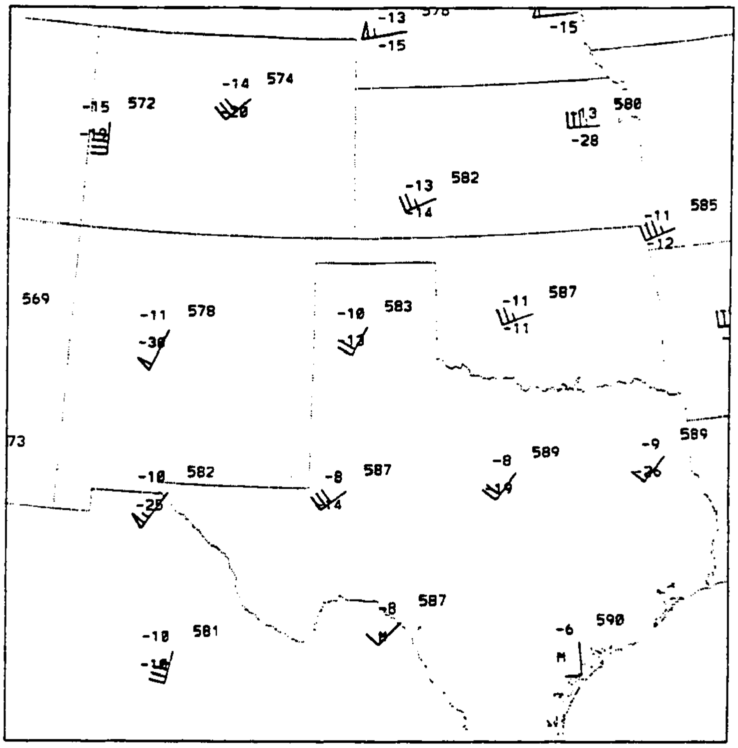

Pre-Storm 500 mb Raw Data 850603 1200 Z

Figure 2.21: As in Fig. 2.18, but for 500 mb.

southwest New Mexico. A Barnes (1973) objective analysis of the 500 mb data shows a slight ripple in the height contours to the southeast of AMA and a weak absolute vorticity maximum to the northeast of MAF (not shown). A stronger vorticity maximum was analyzed over western New Mexico. The 500 mb temperature at DDC was 3° C cooler than at AMA so that a low-level, northward moving air parcel would have experienced an increase in Convective Available Potential Energy (CAPE) as it moved up the frontal surface (assuming that the parcel was travelling faster than any advective changes at 500 mb). This process is called underrunning (Means 1952) and was shown by Trier and Parsons (1993) to be a significant factor in the development of MCS4.

At 250 mb (not shown), the jet streak was less well defined than before, with a maximum wind of 45 m s^{-1} at TOP. Wind speeds increased between 0530 and 1200 at both LBF and OMA suggesting that the jet streak continued moving northward. Fig. 2.22 shows the 200 mb chart. The jet streak at this level is now over Nebraska so that western

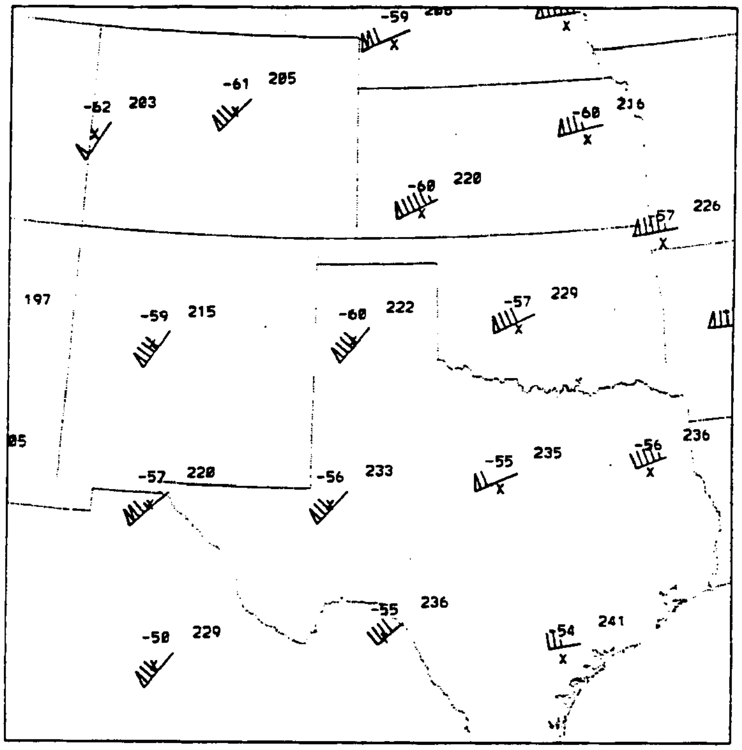

Pre-Storm 200 mb Raw Data 850603 1200 Z

Figure 2.22: As in Fig. 2.18, but for 200 mb.

Kansas was in the right entrance region where the transverse circulation would favor upward motion (e.g. Beebe and Bates 1955). Farther upstream another jet streak is suggested by the 57 m s^{-1} wind at ELP. Upper tropospheric winds at Tucson, AZ were missing, yet were available at higher levels. This frequently occurs when radiosondes encounter a strong jet core and supports the idea that a jet streak was entering New Mexico.

The lifted index (LI), while possibly not as accurate as CAPE since it reflects a parcel temperature excess only at 500 mb, indicates areas of potential instability. Fig. 2.23a shows the minimum LI for 3/1200. The lifted index is computed for each analysis level below 700 mb and the minimum (or most unstable) value is plotted. Fig. 2.23b shows the LI for the surface-level parcel. At 3/1200, the most unstable air with an LI less than -6 (Fig. 2.23a) was located from the extreme northeast Texas panhandle to south-central Kansas – where MCS1 began. Surface LIs in this region were greater than -2 indicating the unstable air was above the surface layer (i.e. above the frontal surface). Over most of Kansas, surface parcels were very stable while the minimum LI was unstable suggesting only elevated thunderstorms could occur (Colman 1990a). South of the surface front in Oklahoma and Texas, the minimum LI and surface LI were similar, indicating that the most unstable parcels are within the surface layer.

A north-south cross section through the MCS1 genesis region at 3/1200 is shown in Fig. 2.24. High θ_E air (greater than 340° K) from low levels over Oklahoma was being advected northward over the frontal surface (Fig. 2.24a). The maximum upward motion was occurring along and north of the surface front in southern Kansas in a region where θ_E decreases rapidly with height. This area was north of the terminus of the LLJ (indicated by the large vectors between 850 and 800 mb near the center of the cross section. Above 450 mb, vertical motions were weak, despite the existence of an upper-level jet. Areas of negative moist potential vorticity (MPV) (Zhang and Cho 1992; Bluestein 1993) indicate the possibility of either conditional symmetric instability or convective instability (Thorpe and Clough 1991). MPV should only be used to approximate areas of instability since its computation involves possibly inaccurate derived quantities and requires high resolution observations (Thorpe and Clough 1991). However, Fig. 2.24b shows that convective instability exists in the warm sector as well as above the frontal surface. Values of θ_E increase with height (Fig. 2.24a) in the vicinity of the -1.5 PVU minimum at 850 mb (Fig. 2.24b). (1 PVU or potential vorticity unit = 10^{-6} m^2 s^{-1} K kg^{-1}) This area is also at the nose of a saturated region indicating moist symmetric instability (e.g. Zhang and Cho 1992). Therefore, slantwise overturning may have been

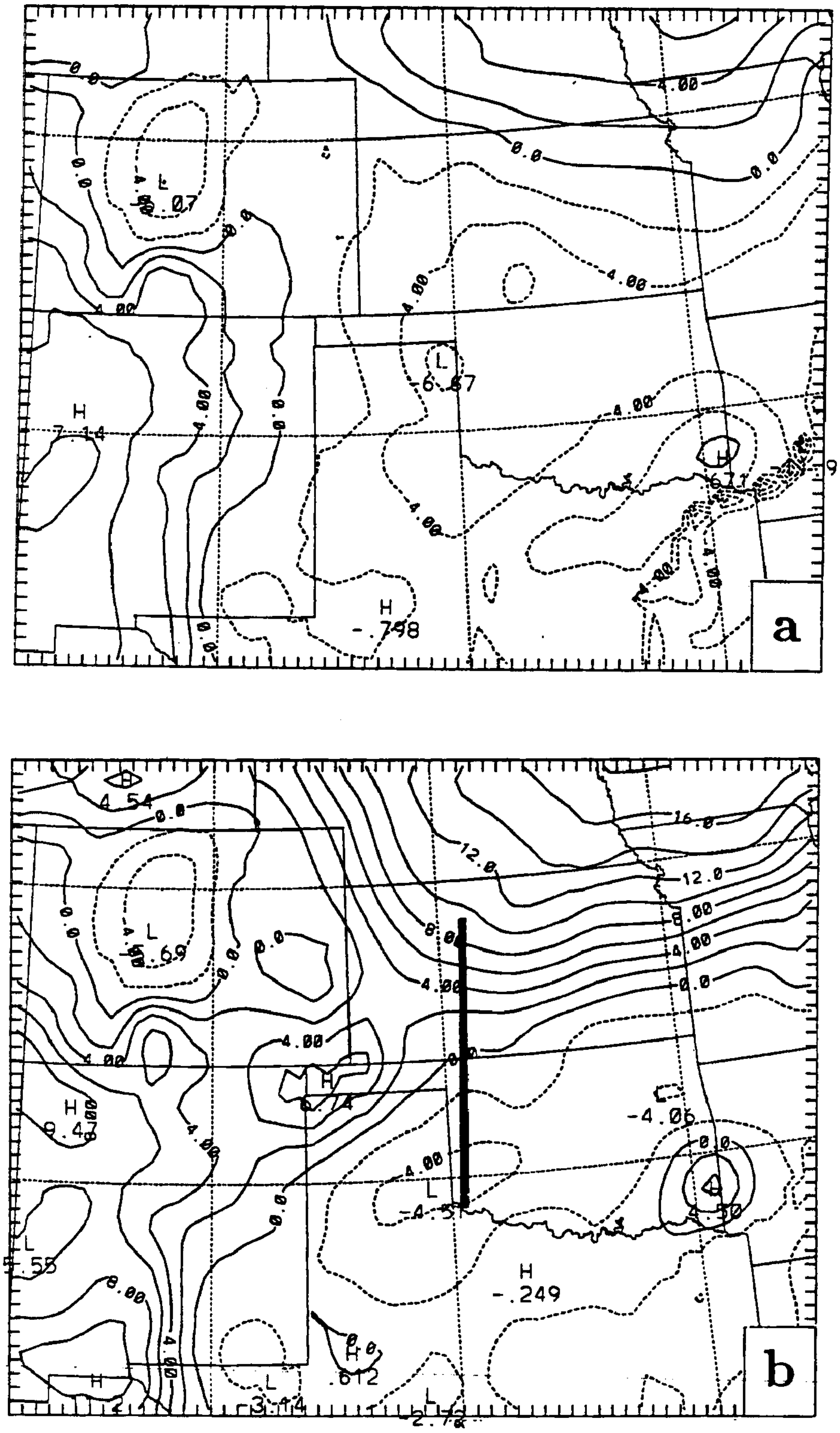

Figure 2.23: Lifted index derived from the initial data fields at 3/1200. The minimum lifted index for the levels below 700 mb is shown in a), while the lifted index for the surface parcel is shown in b). The heavy solid line shows the location of the cross section in Fig. 2.24.

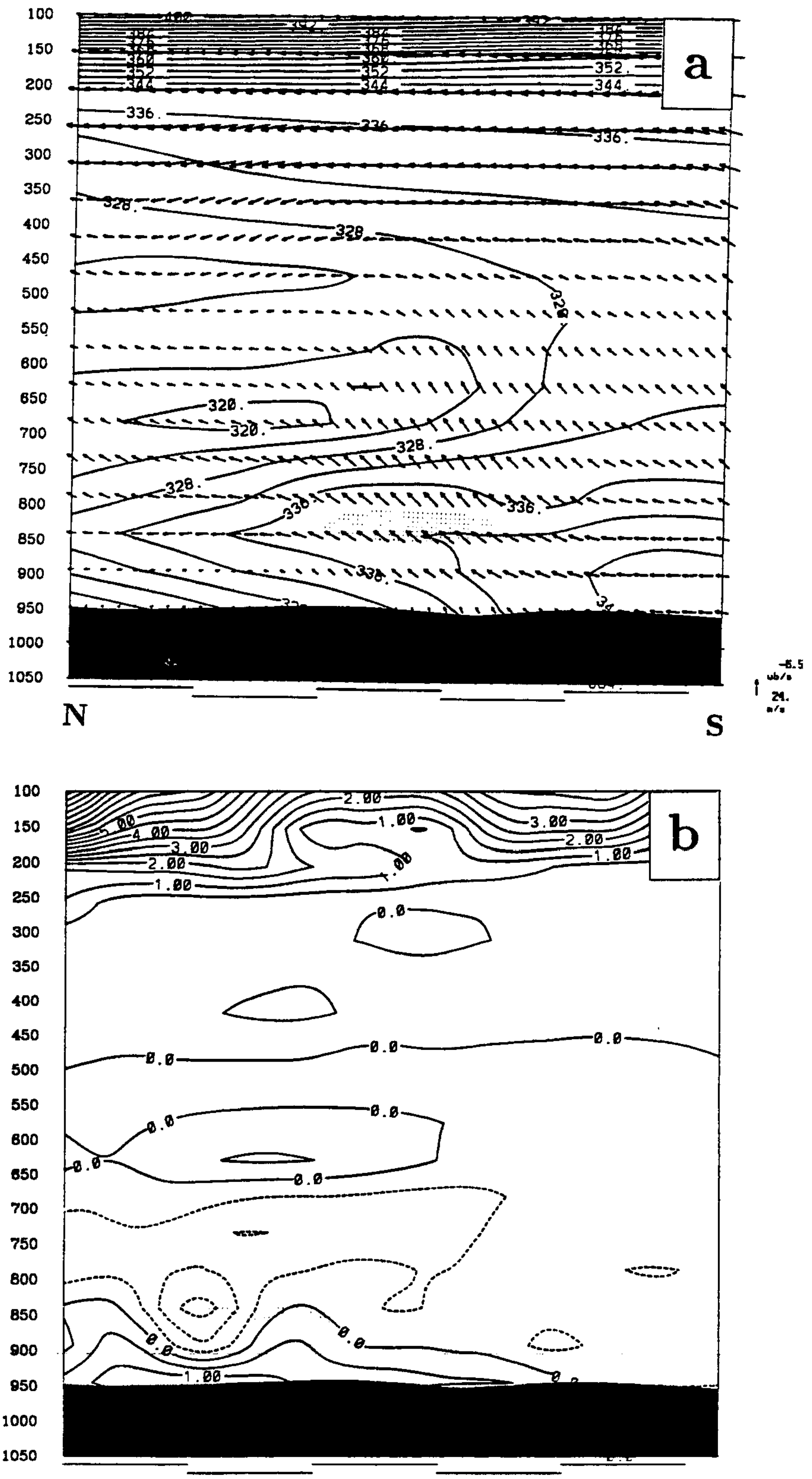

Figure 2.24: North-south cross section along the line shown in Fig. 2.23b of a) θ_E (° K, solid contours) and circulation vectors in the plane of the cross section and b) moist potential vorticity (PVU, contoured every 0.5 PVU, negative values dashed) at 3/1200. The region where the along-cross-section component of the low-level wind exceeds 12 m s^{-1} is lightly stippled in a). Areas with relative humidity of 100% are lightly stippled in b).

present in low levels contributing to the triggering of convection. It appears that low-level forcing (as opposed to an upper-level short wave or jet circulation) was the dominant mechanism for initiation of MCS1 convection.

Fig. 2.25 shows the 850-300 mb thickness. Merritt and Fritsch (1984) have shown that MCSs tend to move parallel to the 850-300 mb thickness contours. For this slowly evolving pattern, systems over southeast New Mexico and western Texas should track northeastward, while systems over Kansas would track eastward. The observed motion of the MCSs (Fig. 2.1) was consistent with this idea.

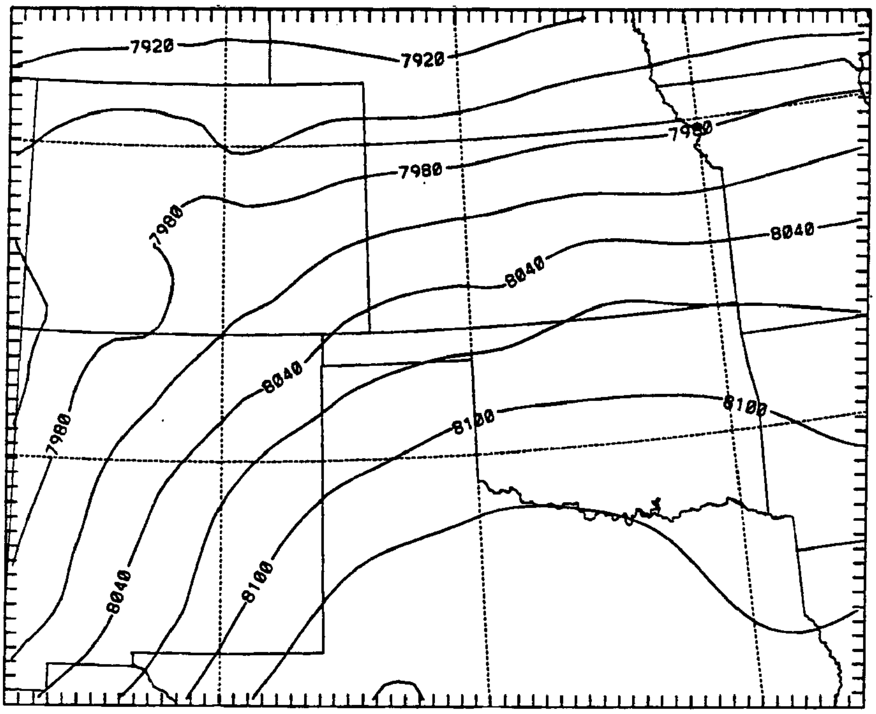

Figure 2.25: 850-300 mb thickness (m) for 3/1200.

As pointed out by Fortune (1989), a wide variety of environmental profiles existed across the region. The closest sounding to the initial convection of MCS1 was DDC (Fig. 2.26a). Within the cold air mass below 780 mb, the atmosphere was saturated with easterly winds below 850 mb. Surface-based convection could not be supported by this sounding. Air parcels riding over the cold airmass (in the 720 to 780 mb layer) would be moderately buoyant if they could be lifted through the capping inversion.

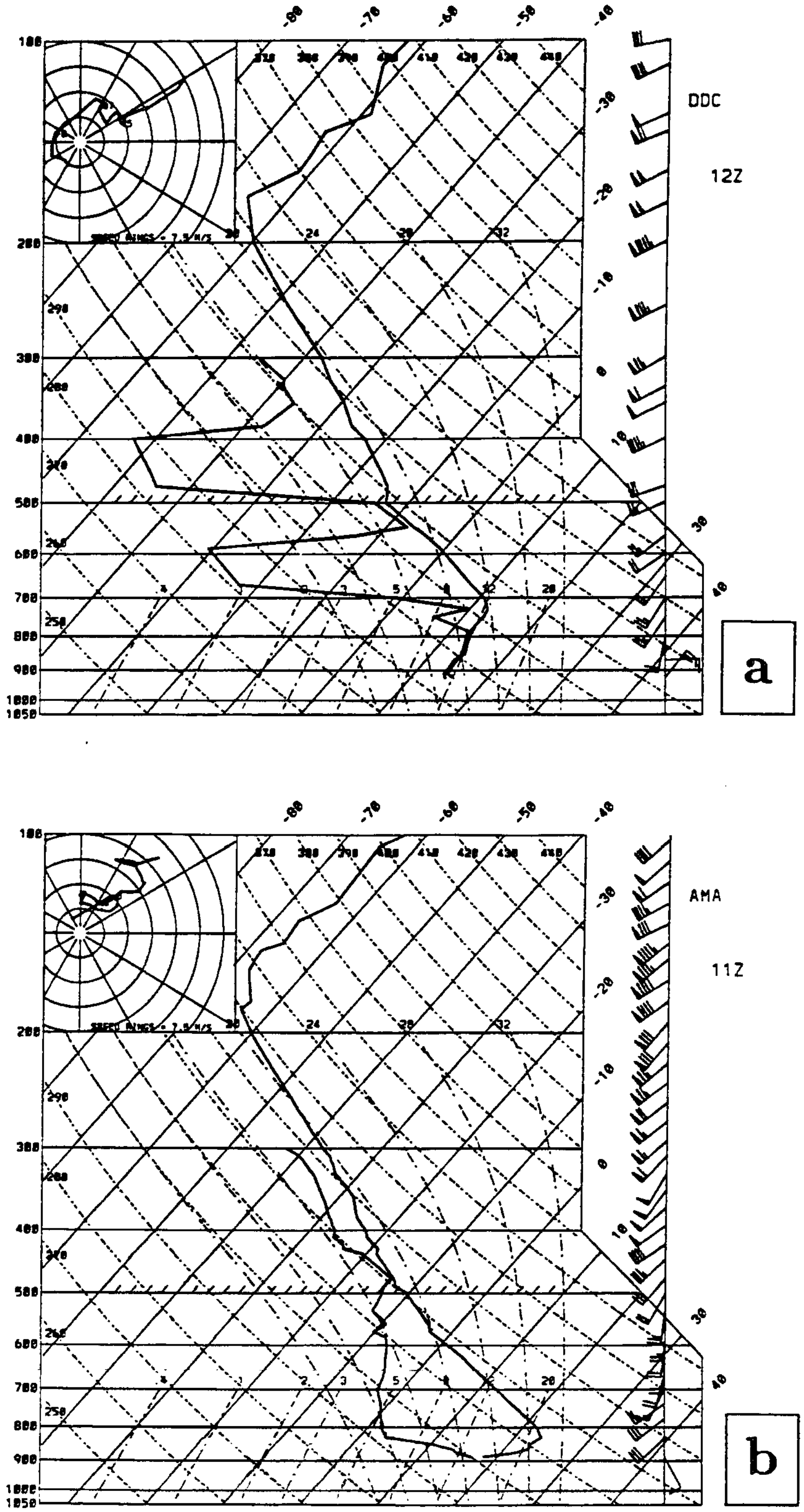

Figure 2.26: Skew-T diagrams and hodographs at 3/1200 for a) DDC, b) AMA, c) MAF, d) OKC, and e) SEP.

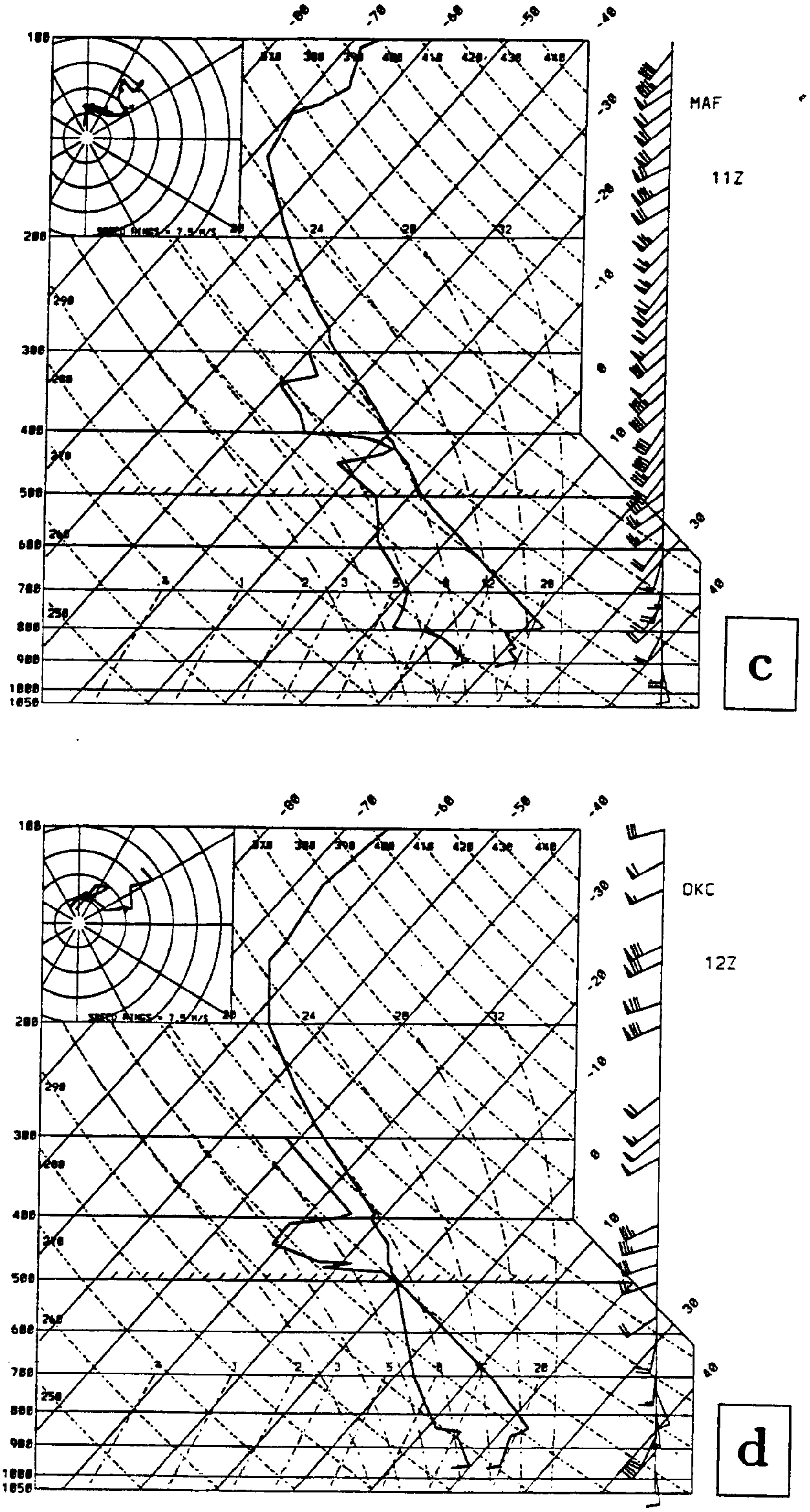

Figure 2.26: Continued.

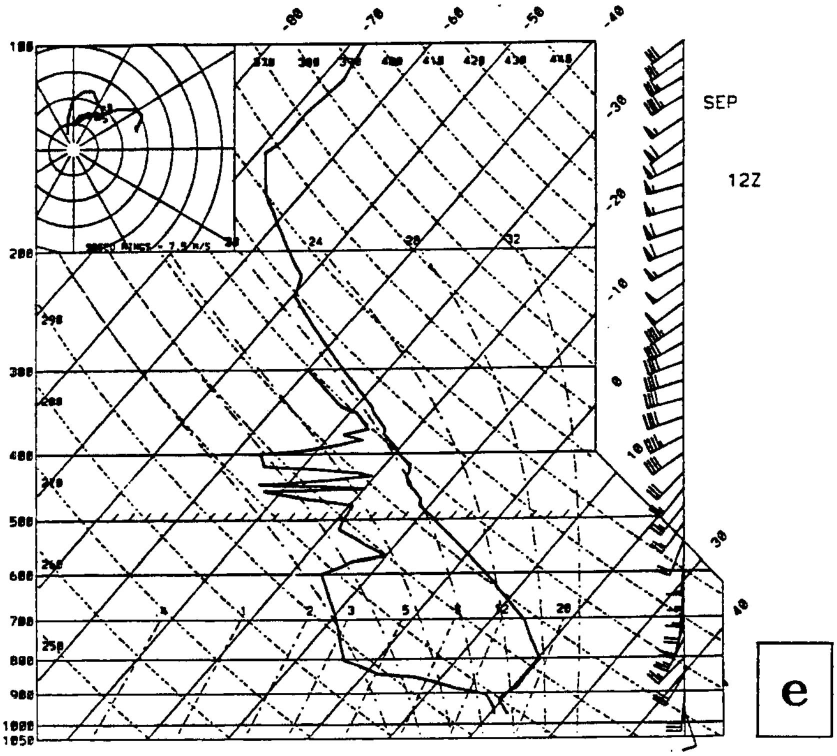

Figure 2.26: Continued.

qualified as an MCC (Augustine and Howard 1988). By 1800 UTC (Fig. 2.16g) MCS1 had changed character with strong convection along the southern edge and an area of stratiform rain with embedded convection to the north. Nachamkin (1992) describes the dramatic upscale transition that occurred between 1630 and 1730. By 1830, an east-west line of convective cells extending from southeast of ICT to southwest Missouri, developed about 20 km north of the Oklahoma border, well south of MCS1. This line moved north and eastward eventually merging into the southern flank of MCS1 by 1930. MCS1 began a turn toward the southeast and by 2100 (Fig. 2.16j) was almost out of Kansas. MCS1 continued eastward decaying over Missouri around 4/0400 (Augustine and Howard 1988).

The first convection associated with MCS2 could be detected in visible satellite images at 3/1400 west of INK. This convection developed within one of at least three lines of midlevel clouds apparent in visible satellite imagery, parallel to the upper tropospheric flow. (Another line might have been hidden beneath cirrus). These lines, east of the jet axis, were approximately 200 km apart and could not be resolved by the available soundings, although the MAF sounding (Fig. 2.26c) does suggest a thin cloud layer near 420 mb. Surface observations at HOB, ROW, and CNM reported midlevel clouds with virga above CNM. At 1500 (Fig. 2.16d) a small cell was located on the Texas-New Mexico border, south of HOB.

Another convective area began near TCC at 1500 UTC, and moved northeast across the extreme western edge of the Oklahoma panhandle and was already weakening along the Colorado-Kansas border at 1800 (Fig. 2.16g). It appears that this area was too far to the northwest to ingest the high θ_E air that was south of the front. This convective area weakened, but appears to have merged into the northern edge of MCS2 (Fig. 2.16h-j).

MCS2 tracked across the Texas panhandle (Fig. 2.16g), becoming an MCC at 1830 (Augustine and Howard 1988). By 2100 UTC (Fig. 2.16j) MCS2 had entered the mesonetork and consisted of a rather disorganized line of convection oriented north-south along the Oklahoma-Texas border and a few convective cells in western Kansas. There was a distinct clear slot between MCS1 and MCS2, indicative of subsidence behind MCS1. In fact, visible images show erosion of the low clouds in Kansas which allowed insolation to warm surface temperatures at ICT to 27° C.

By 2300 UTC (Fig. 2.16l), MCS2 became much better organized with a N-S convective line extending from south-central Kansas through north-central Oklahoma, a northeast-southwest convective line across central Kansas, and a large stratiform area extending north and west of the two convective lines, as shown by Stumpf (1988) (his Fig. 5.4). Initial convection associated with MCS3 began east of GDP at 2130 UTC (Fig. 2.16k) along the dryline, where there was strong surface convergence (not shown).

A time series of horizontal winds from the Liberal profiler is shown in Fig. 2.27. LBL is only about 75 km west of where MCS1 convection began, however the wind profile shows little evidence of a triggering mechanism (Fig. 2.27a). Profiler winds between 3/1100 and 3/1400 exhibit little directional shear with height, and while wind speeds between 9 and 14 km had increased slightly by 3/1230, no well-defined jet streak or shortwave was present. Plots of the low-level wind speed as a function of height for the AMA soundings suggest that the lowest gate at LBL (2.3 km above sea level) might be sampling the top of the nocturnal LLJ. Winds at LBL's lowest gate had backed from 238° at 9 m s^{-1} at 3/0300 to 180° at 12 m s^{-1} by 3/0600 (not shown) and then veered to 226° at 13 m s^{-1} by 3/1000. Since the latter change agrees with the expected behavior of the LLJ (Hoxit 1975), it provides further evidence that a LLJ was present over southern Kansas in the vicinity of where MCS1 began. Low level southerly flow over LBL returned by 3/1700. Active convection associated with MCS2 passed just to the east of LBL between 3/1900 and 3/2200 (Fig. 2.16h through 2.16i). As the convection approached, wind speeds increased above 7 km at 3/1930 (Fig. 2.27b). Convective contamination of the winds caused the quality control software to eliminate much of the data between 8 and 14 km 3/2000 and 3/2130. (The profile at 3/2030 was contaminated and should have been discarded). LBL reported thunder at 3/2050. Following passage of the system, an approaching midlevel shortwave, indicated by the backing and increase in winds between 6 and 10 km, is apparent. Blocking of the midlevel southwesterly environmental flow by the convective system might also be contributing to the enhanced southerlies just behind the MCS.

Many recent studies have linked gravity waves to the initiation and propagation of MCSs (e.g. Koch and Golus 1988; Koch *et al.* 1988; Koch and Dorian 1988 (the ensemble

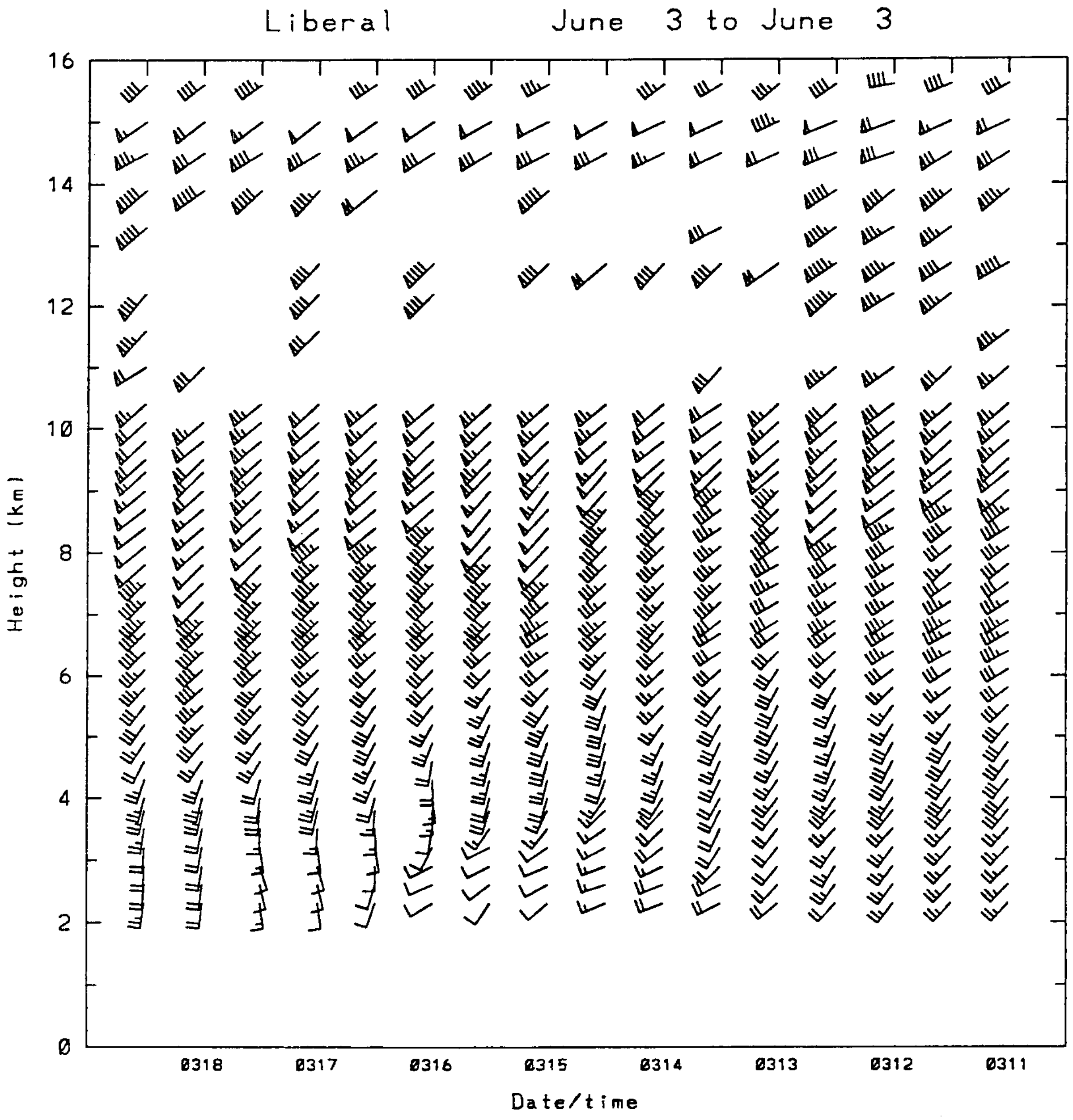

Figure 2.27: Time-height series of the horizontal winds at Liberal, Kansas for a) 3/1100 to 3/1830 and b) 3/1800 to 4/0130. The height scale is in km above sea level.

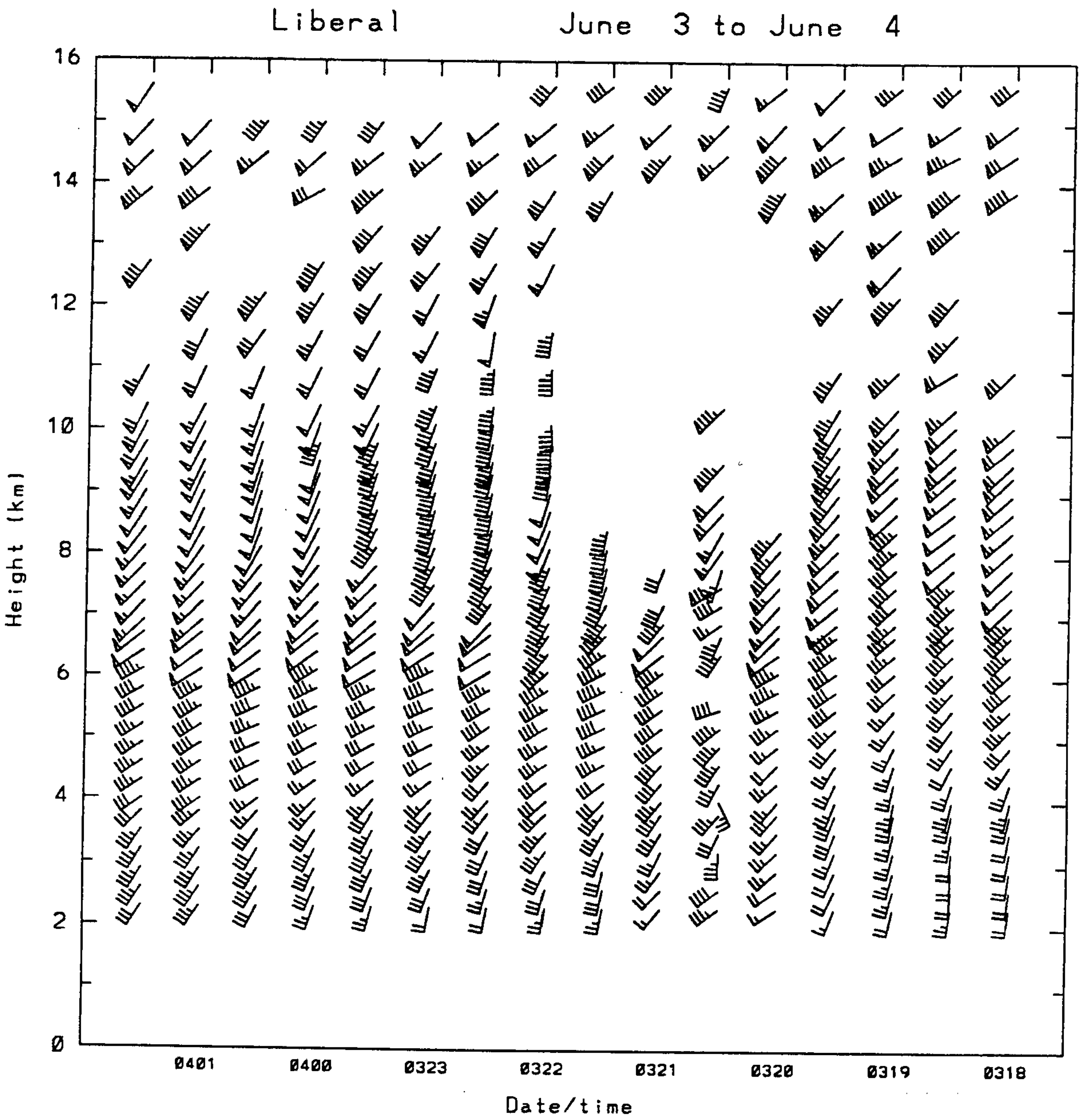

Figure 2.27: Continued.

of papers hereafter referred to as K88); Cram 1990; Stensrud 1992; Hung and Tsao 1991). Because the synoptic situation of the 3-4 June case closely resembles the case studied by K88, a detailed analysis of the surface mesonetork data following the K88 approach was conducted to identify possible gravity waves.

The gravity waves studied by K88 occurred over the Cooperative Convective Precipitation Experiment (CCOPE) mesonetwork in eastern Montana. A surface stationary front was south of the study region while a slowly-evolving upper air pattern consisted of a longwave trough off the west coast with an an anticyclonically curved jet extending downstream and an embedded jet streak over western Montana. The gravity waves were found to originate in the right-exit region of the jet streak and propagated over the region between the 300 mb height inflection axis and the downstream ridge axis, north of the stationary front and south of the jet axis. A series of four wave episodes passed over the network. The first gravity waves only caused high-based rain showers because the lifting could not overcome the low-level inversion. The second and subsequent gravity wave packets arrived over a destabilized boundary layer and initiated strong, long-lived thunderstorms (Koch and Dorian 1988).

Following the method of Koch and Golus (1988) a power spectrum analysis was performed on the PRE-STORM surface pressure data for selected sites (primarily the PAM sites) from 3/0000 to 4/0300. The diurnal tide and station biases were removed from the surface pressure data following Stumpf (1988). Missing data were linearly interpolated in time. No more than one consecutive five minute pressure observation was missing from any of the measurement sites. An example power spectrum for PAM 27 is shown in Fig. 2.28. A statistically significant spectral peak is found with a period of about 150 minutes. A second, less significant peak is found with a period near 80 minutes. Many of the PAM sites across Kansas exhibited a similar double peak structure with the dominant period between 100 and 300 minutes. Northwestern PAM sites (e.g. PAM 2 and PAM 10) and PAM 42 in Oklahoma exhibited no spectral peaks (except weakly at short periods less than 45 minutes) indicating the absence of significant waves. Pressure waves due to transient gravity waves or due to the convective systems were found in the area between the surface stationary front and the northern edge of the MCS tracks.

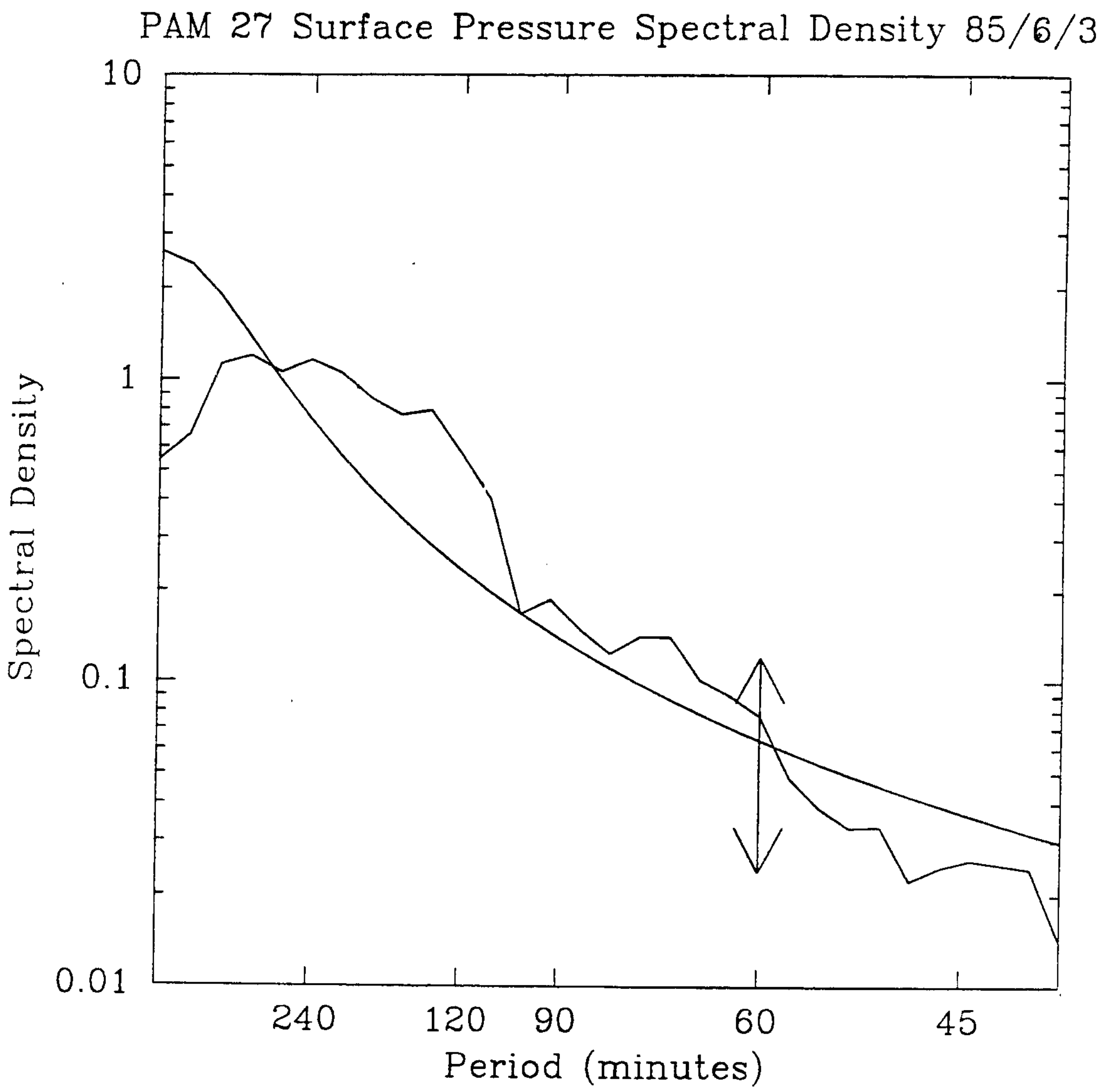

Figure 2.28: Spectral density for the five-minute surface pressure measurements from PAM 27 between 3/0000 and 4/0300. The smooth solid curve is the null value. Statistically significant peaks are those which exceed the arrow length plotted at the 60 minute period.

A bandpass filter was constructed to isolate the waves with periods between 100 and 300 minutes. This filter would yield information about waves with this period whether they were generated by the MCSs themselves or by some other process. As in Koch and Golus (1988), a Lanczos (1956) filter was used with 33 one-sided weights. Time series of the filtered pressure data showed weak, but detectable pressure waves at many of the sites. Fig. 2.29a shows the time series of filtered pressure data from PAM 26. Weak waves (with amplitudes less than 0.3 mb) occurred between 0300 and 1300 UTC, before any significant convection was occurring over the region. In contrast, wave amplitudes found by Koch and Dorian (1988) were on the order of 1 mb. The highest amplitude pressure waves at PAM 26 were associated with the passage of MCS2 – the pre-MCS mesolow just before 2200 UTC, the mesohigh at 2230 and the wake low at 0000 UTC 4 June. Farther to the north, at PAM 14, weak pressure waves were found prior to the arrival of MCS1, but again the strongest wave was associated with the MCS itself (Fig. 2.29b).

An objective analysis (Barnes 1973; Koch *et al.* 1983; Achtemeier 1989) of the perturbation pressure was performed every five minutes between 3/0300 and 4/0100. Contour plots of the perturbation pressure were animated on a workstation to trace the propagation of the waves across the mesonetwork. The predominant direction from which the waves were propagating was 240° . Next, as in Koch and Golus (1988), the surface wind component in the direction of wave propagation, u^*, was computed using,

$$u^* = -u \sin \alpha - v \cos \alpha$$

with $\alpha = 240°$. Thus, u^* values are computed assuming a two-dimensional propagating plane wave. Time series of u^* for PAM 26 and PAM 14 are shown in Fig. 2.30.

For several of the waves there is a high correlation between the perturbation wind and pressure traces. This is indicative of a strong wave signal and suggestive of gravity waves (Koch and Golus 1988). The wind amplitude (as with the perturbation pressure) is not as large as observed by Koch and Golus (1988), except during the passage of the MCSs (3/1600 at PAM 14 and 3/2200 at PAM 26). Objective analyses were also constructed from the wind perturbations. A sequence of the perturbation wind and pressure fields along with radar echo outlines is shown in Fig. 2.31.

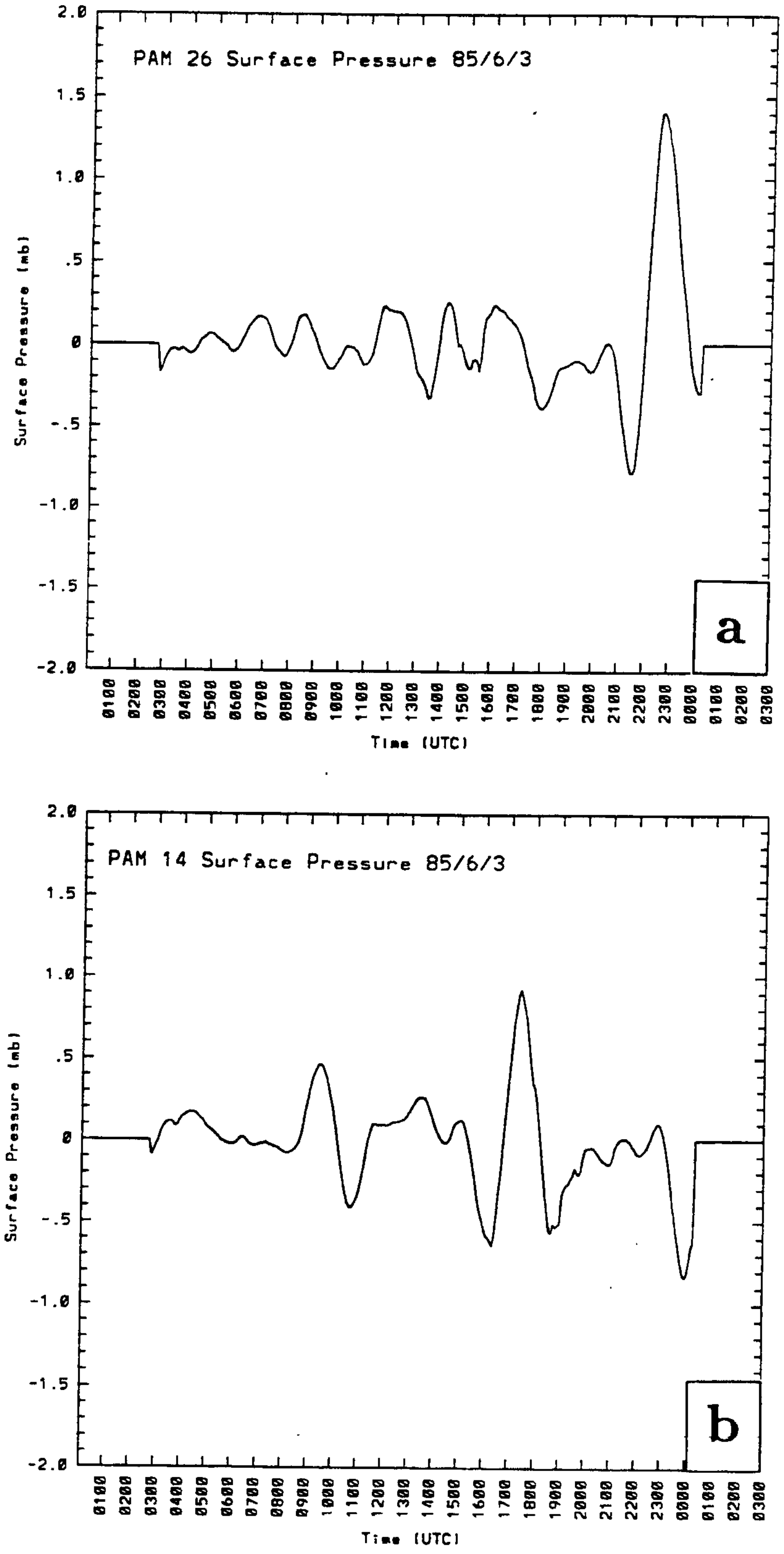

Figure 2.29: Time series of the filtered surface pressure data (see text) for a) PAM 26 and b) PAM 14.

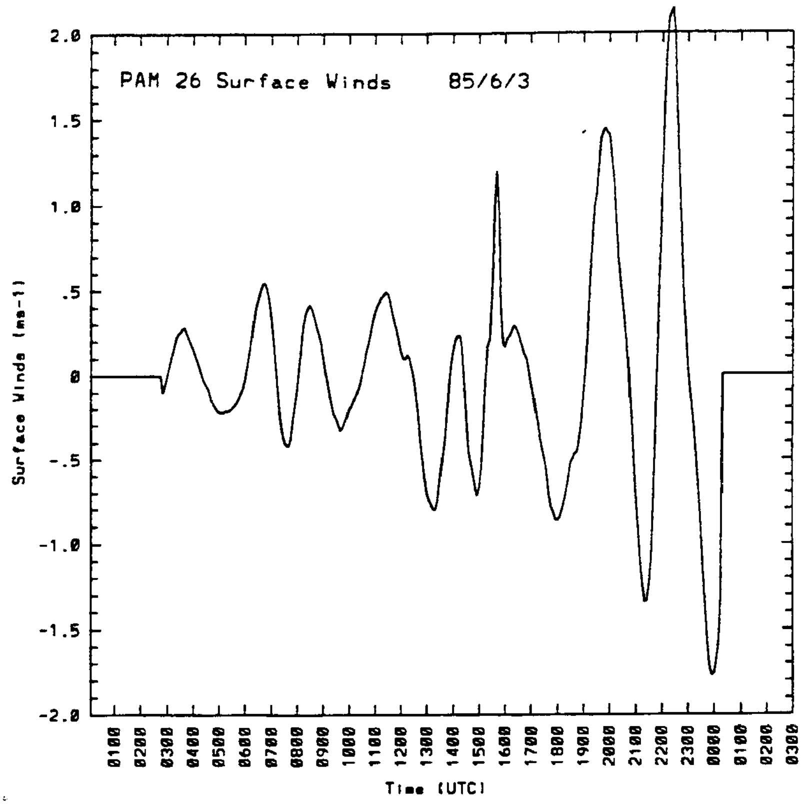

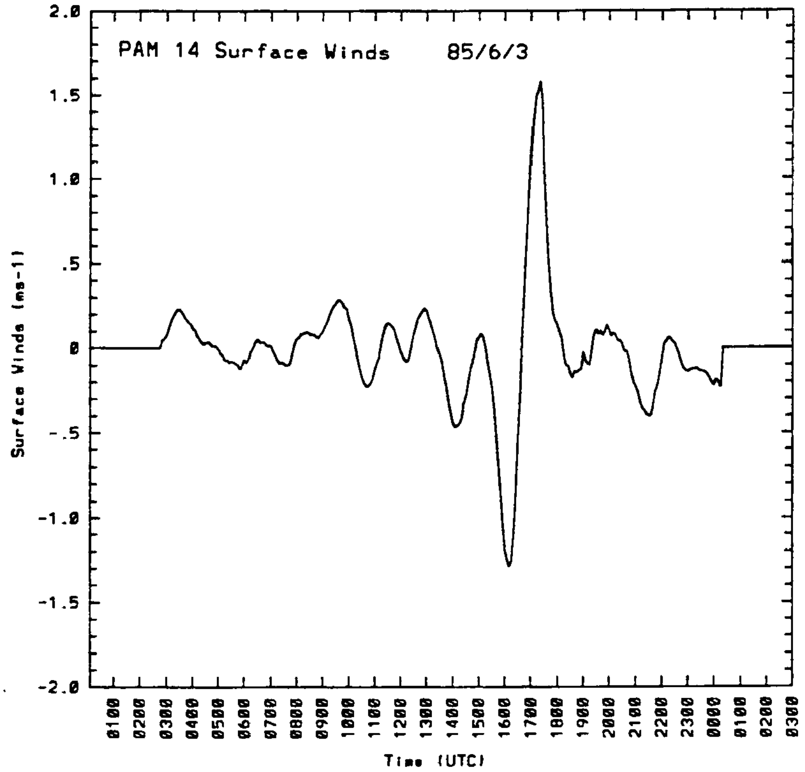

Figure 2.30: As in Fig. 2.29, but for filtered wind data (see text).

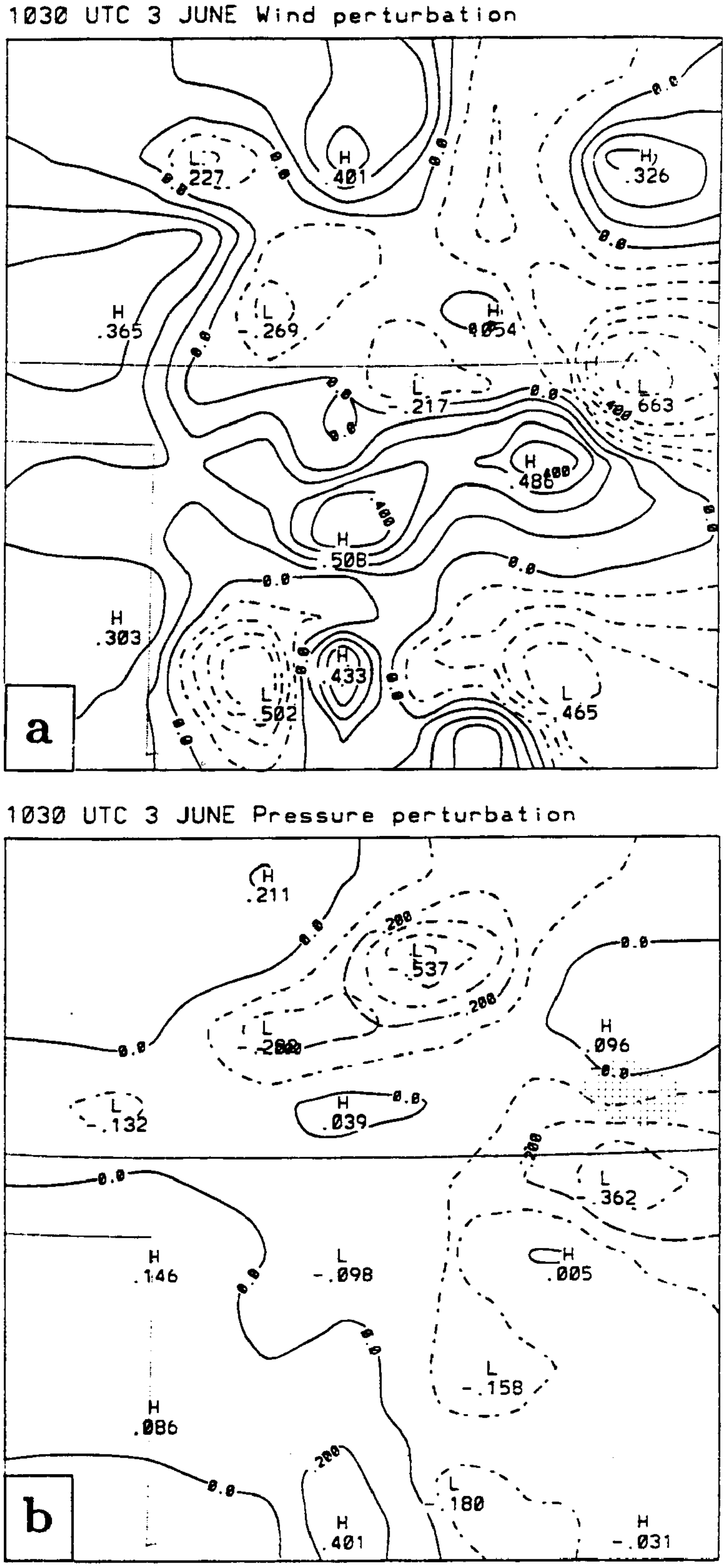

Figure 2.31: Contours of objectively analyzed surface wind (a), c), e), g), i), k), m), o)) and surface pressure (b), d), f), h), j), l), n), p)) perturbations for a) and b) 3/1030, c) and d) 3/1130, e) and f) 3/1230, g) and h) 3/1330, i) and j) 3/1430, k) and l) 3/1530, m) and n) 3/1630, and o) and p) 3/1715. Negative values are dashed and radar echo outlines are the lightly stippled areas on the pressure perturbation plots.

1130 UTC 3 JUNE Wind perturbation

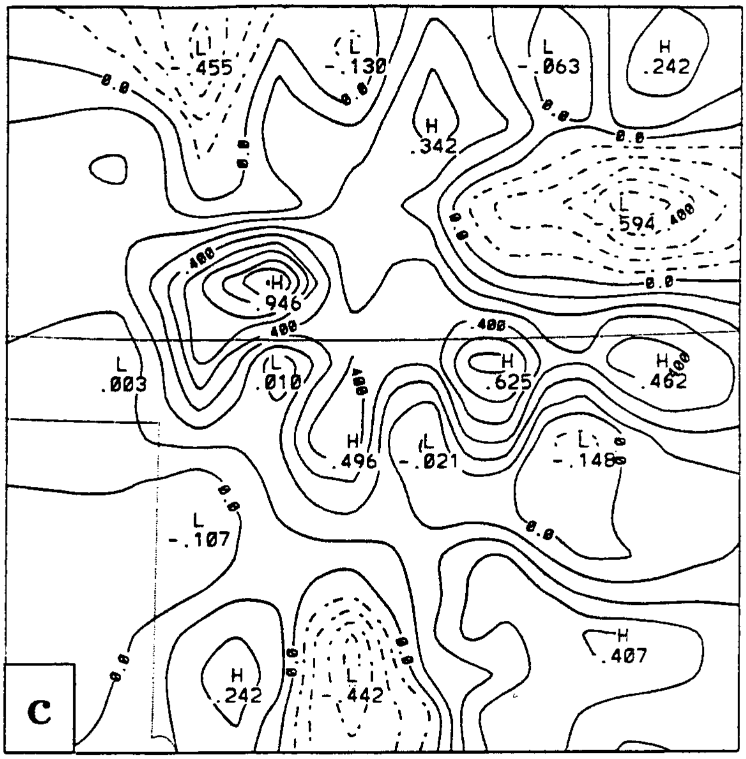

1130 UTC 3 JUNE Pressure perturbation

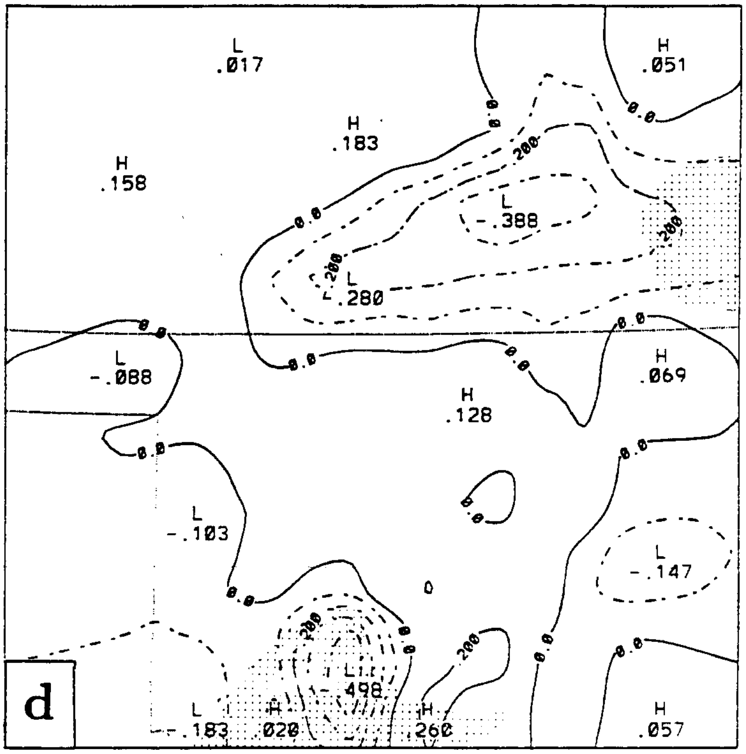

Figure 2.31: Continued.

1230 UTC 3 JUNE Wind perturbation

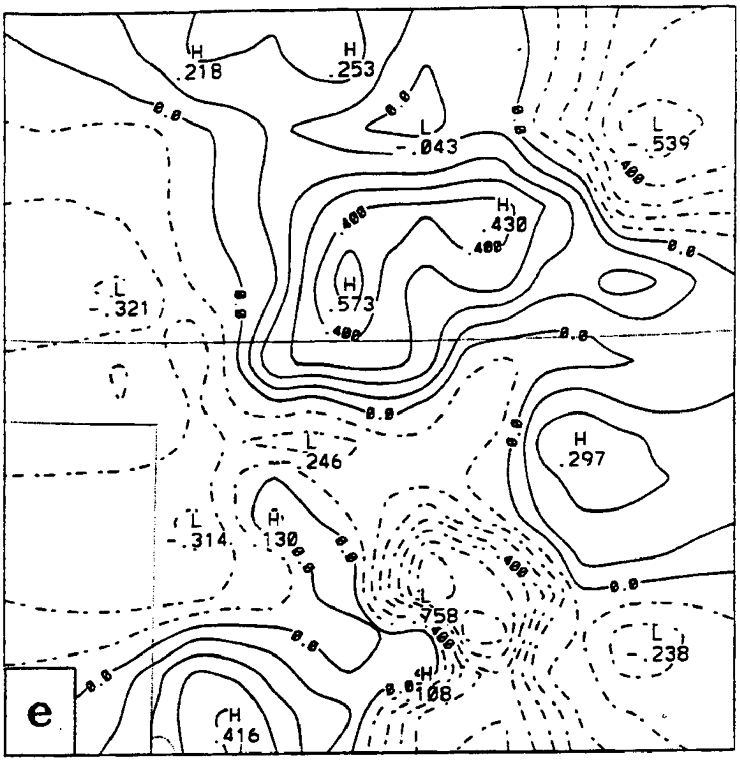

1230 UTC 3 JUNE Pressure perturbation

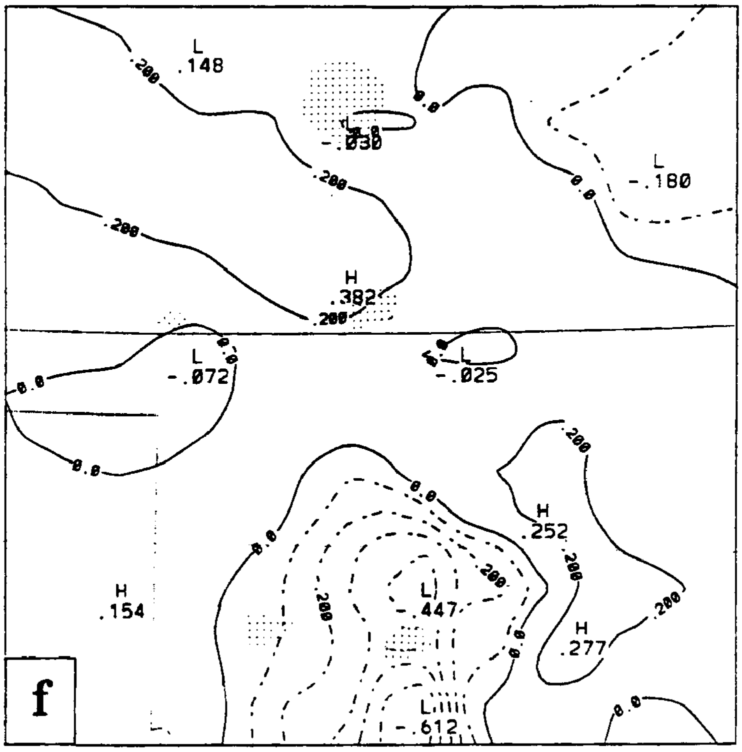

Figure 2.31: Continued.

1330 UTC 3 JUNE Wind perturbation

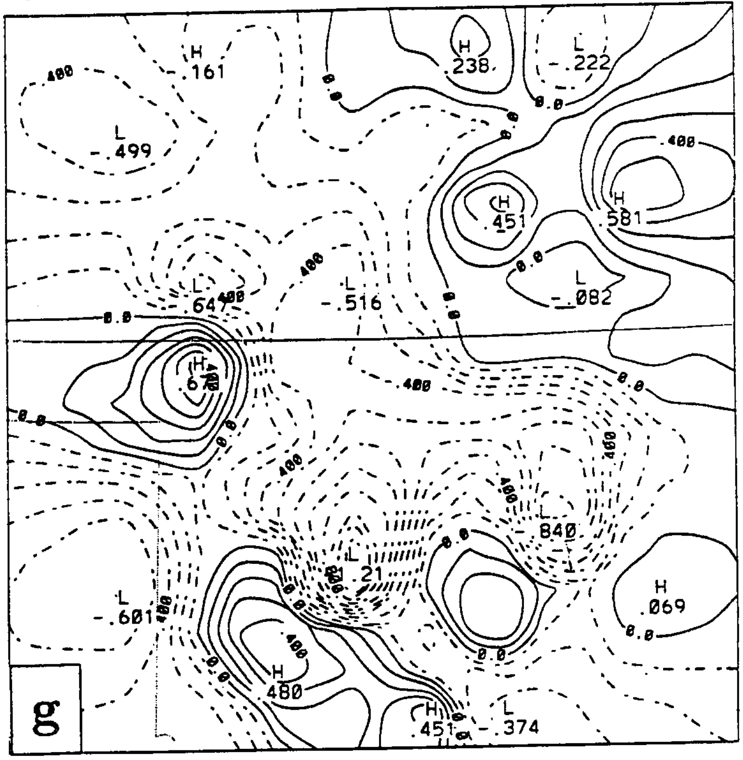

1330 UTC 3 JUNE Pressure perturbation

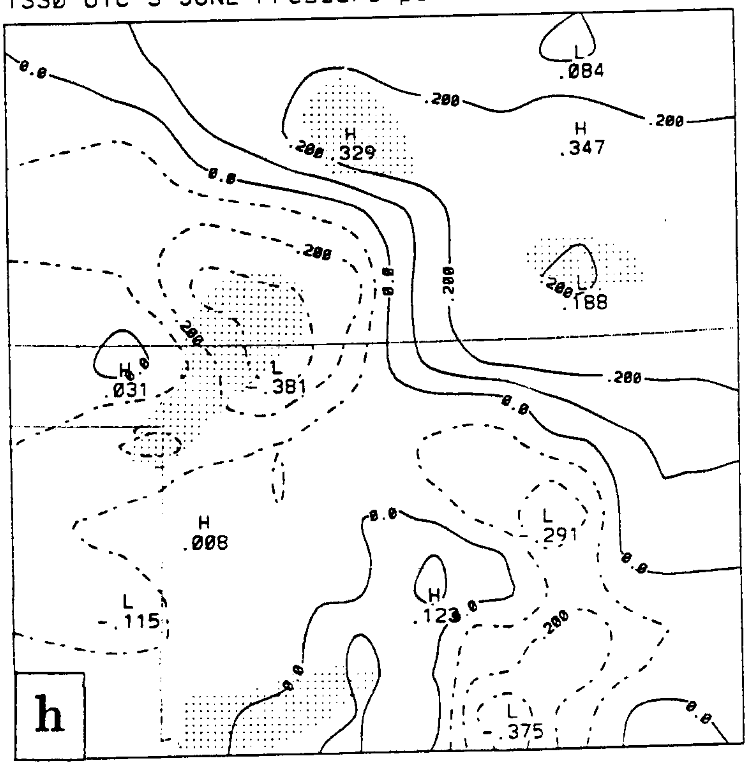

Figure 2.31: Continued.

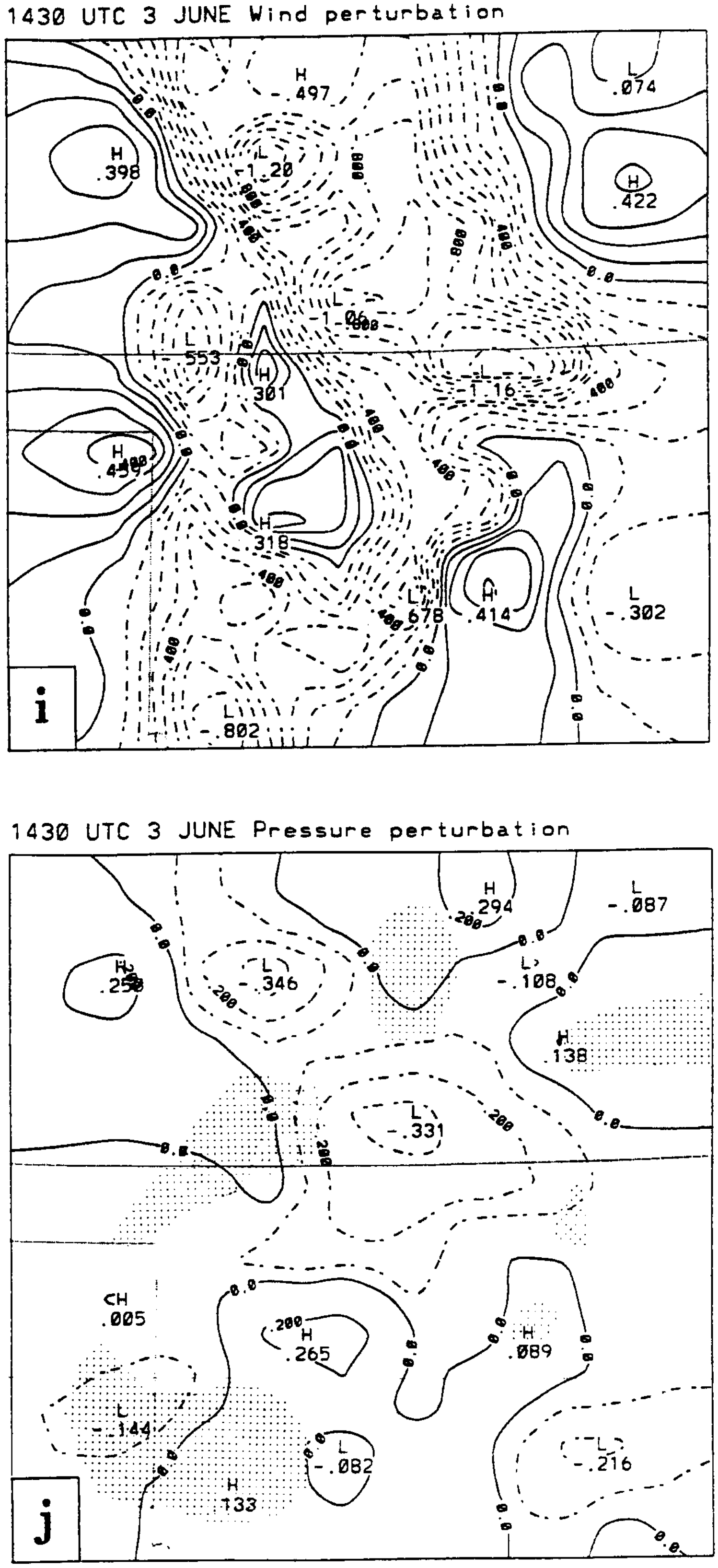

1430 UTC 3 JUNE Wind perturbation

1430 UTC 3 JUNE Pressure perturbation

Figure 2.31: Continued.

1530 UTC 3 JUNE Wind perturbation

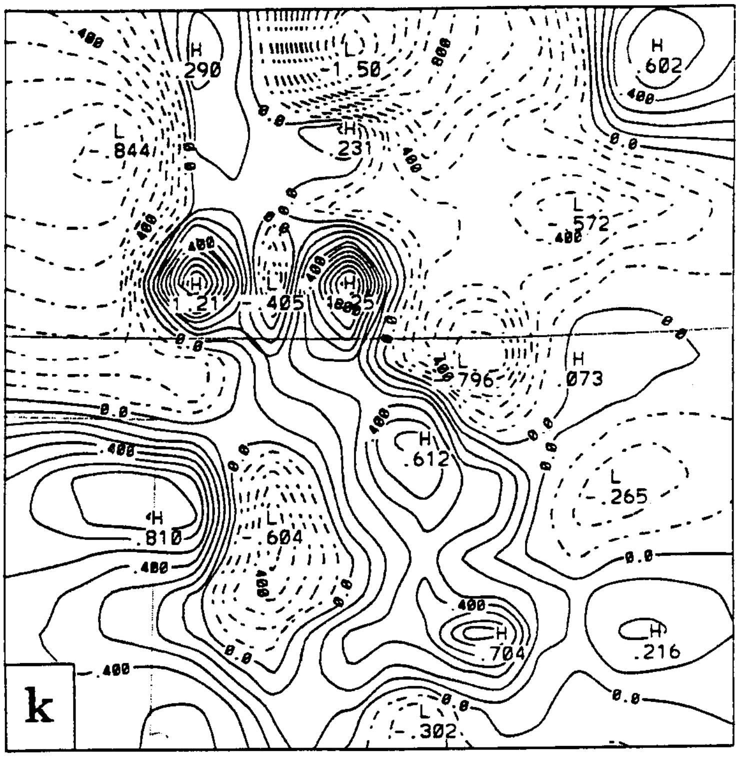

1530 UTC 3 JUNE Pressure perturbation

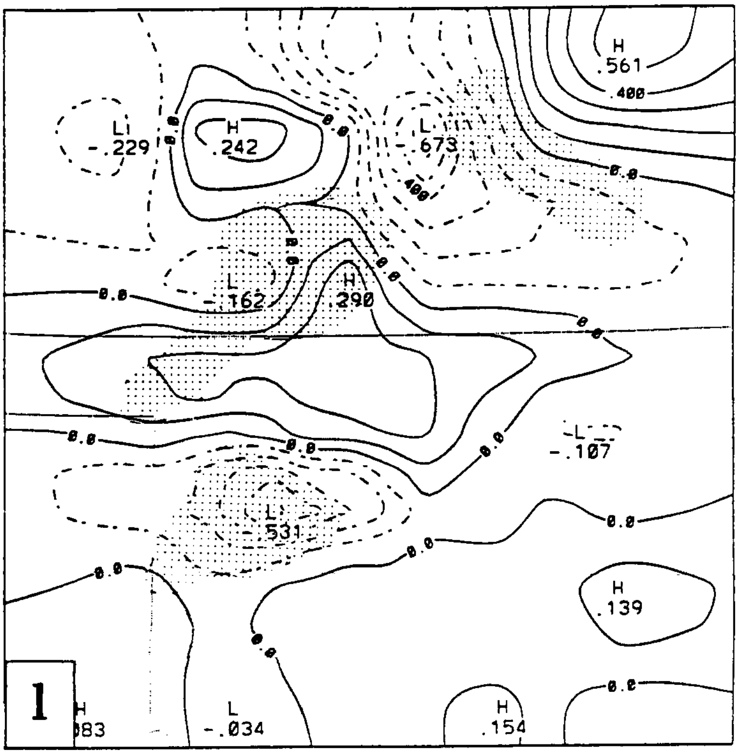

Figure 2.31: Continued.

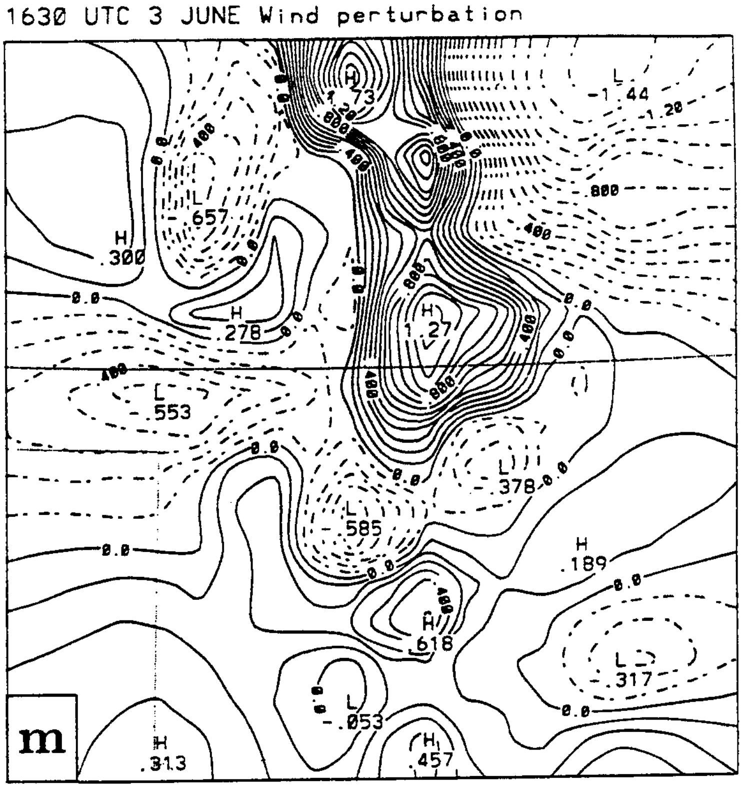

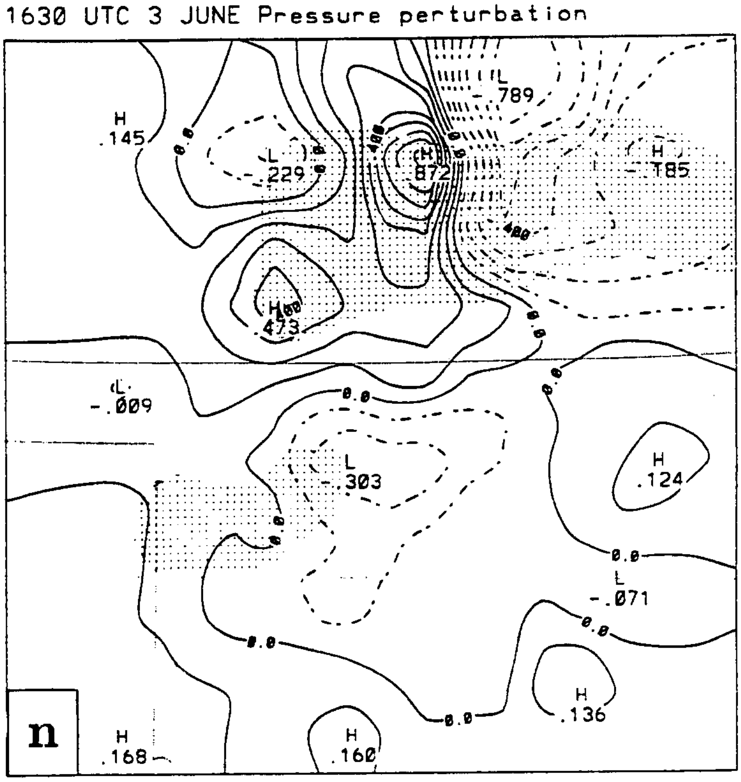

Figure 2.31: Continued.

1715 UTC 3 JUNE Wind perturbation

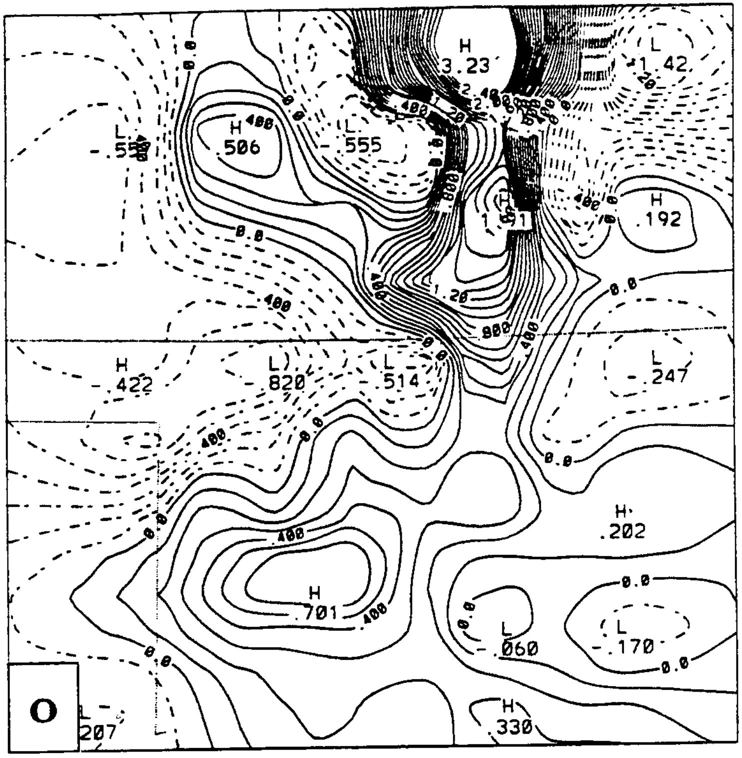

1715 UTC 3 JUNE Pressure perturbation

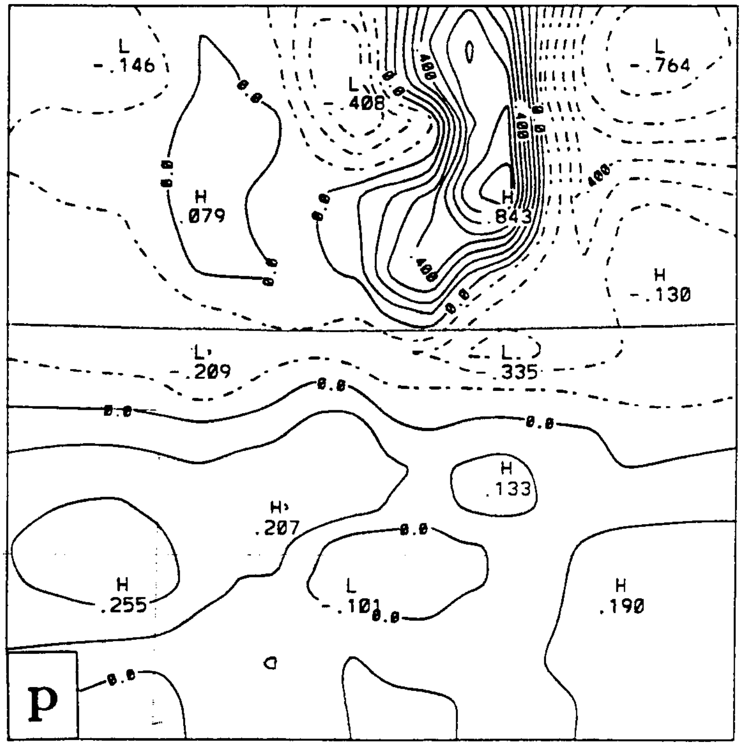

Figure 2.31: Continued.

A large area of negative p′ entered the northwestern part of the PAM mesonetwork at 0830 (not shown), tracked east-southeastward (Fig. 2.31b), crossing south central Kansas at 1130 (Fig. 2.31d) and leaving the PAM network shortly after 1230 (Fig. 2.31f). There was a corresponding positive wind perturbation with this wave which lagged the pressure perturbation (Fig. 2.31a-e). The lack of correlation of the pressure and winds with this wave is mainly because its track was nearly at a right angle to the predominant wave direction of 240° . This wave is of interest since it was associated with the surface ridge/trough and confluence line mentioned by Stumpf and Johnson (1988) and Nachamkin (1992). The wave's origin is unclear, but it may have been generated by adjustments associated with the upper level jet or by convection over Colorado well to the northwest of the PAM network. The initial convection of MCS1 (Fig. 2.31f) first appears not with this large amplitude wave, but with a rather weak feature moving from 240° . Unfortunately, the mesonetwork does not extend far enough west to allow earlier tracking of this wave. As this wave and the nascent MCS move northeast, the area of negative perturbations grows in area and intensity (becoming much larger than the convective area (Fig. 2.31h)) and moves out ahead of MCS1, becoming indistinguishable from the pre-MCS mesolow at 1630 (Fig. 2.31n). The u^* field during this time is much noisier than the p′ field, but is mostly negative ahead of the developing MCS (e.g. Fig. 2.31i and Fig. 2.31k) indicating enhanced surface northeasterlies. Dramatic changes in the wind and pressure fields occur between 1530 and 1715 as MCS1 develops a pre-MCS mesolow, a mesohigh, and a wake low. Nachamkin (1992) discusses this upscale transition in great detail, stating the dramatic surface changes occur suddenly between 1650 and 1710. However, the perturbation analyses suggest that the changes were apparent as early as 1630 (Figs. 2.31m and 2.31n) when a strong trough-ridge-trough pattern was found beneath MCS1. In addition, an area of negative wind and pressure perturbation found in the northwest corner of the mesonetwork at 1530 (Figs. 2.31k and 2.31l) tracked eastward, becoming part of the wake low. Nachamkin (1992) suggested that the wake low formed suddenly as the rear inflow jet was forced to descend behind the system. The perturbation analyses (while limited in areal extent) suggest that a negative perturbation existed prior to the sudden development.

This surface perturbation might be a reflection of the descending rear inflow jet aloft, and supports the idea (Stumpf *et al.* 1991) that the magnitude of the wake low depends upon the strength of the downward motion.

2.4.3 Conditions after 4/0000

At 4/0000, MCS2 was approaching maturity squarely in the middle of the PRE-STORM measurement network (Fig. 2.32a). Because this system was well-sampled by the observing systems and because of the resemblance of the low-level radar reflectivity pattern to a synoptic scale occluded wave cyclone, it has been the subject of several studies (see section 2.1). MCS2 tracked eastward across eastern Kansas (Fig. 2.32b-d) reaching western Missouri around 4/0430. The most vigorous convection was on the southern flank of the system in Oklahoma. By 4/0300 (Fig. 2.32c) a second line of convection began across northeast Oklahoma and northwest Arkansas ahead of the MCS2 convection and apparently intercepted the inflow to MCS2.

MCS3 had begun near GDP at 3/2130 (Fig. 2.16k) and by 4/0000 (Fig. 2.32a) was near INK. The system moved slowly northeast across the southern Texas panhandle and by 4/0600 (Fig. 2.32e) had begun to decay. Trier and Parsons (1993) discuss its behavior in more detail.

The initial convection associated with MCS4 began in northeast New Mexico at 4/0000 (Fig. 2.32a) and tracked northeastward across the Oklahoma panhandle toward southern Kansas. After 4/0600 (Fig. 2.32e) convection broke out in several places at once in southern Kansas above the frontal surface (Trier and Parsons 1993, Fig. 6b) and ahead of the initial convective system. MCS4 continued to grow and (Figs. 2.32f and 2.32g) by 4/1000 its cloud shield covered most of Kansas (Fig. 2.32h).

2.5 Summary

An observational overview during the 3-4 June MCS episode was presented in this chapter. Particular attention was paid to the conditions leading to the development of MCS1. Initial MCS1 convection began above the surface in a region of strong low-level warm advection and moisture convergence at the nose of a LLJ. While gravity waves were

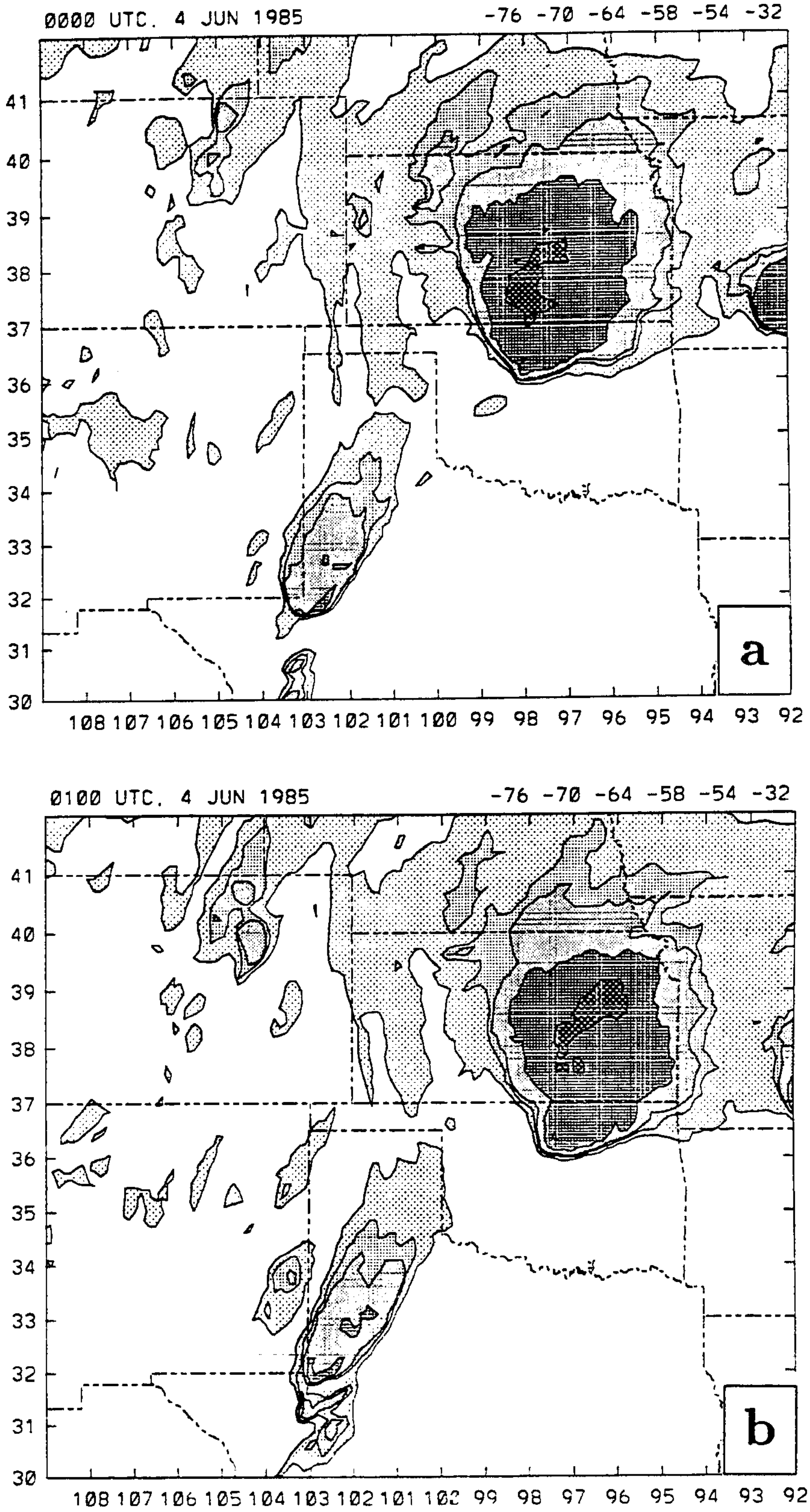

Figure 2.32: As in Fig. 2.8, but for a) 4/0000, b) 4/0100, c) 4/0300, d) 4/0400, e) 4/0600, f) 4/0700, g) 4/0900, and h) 4/1000.

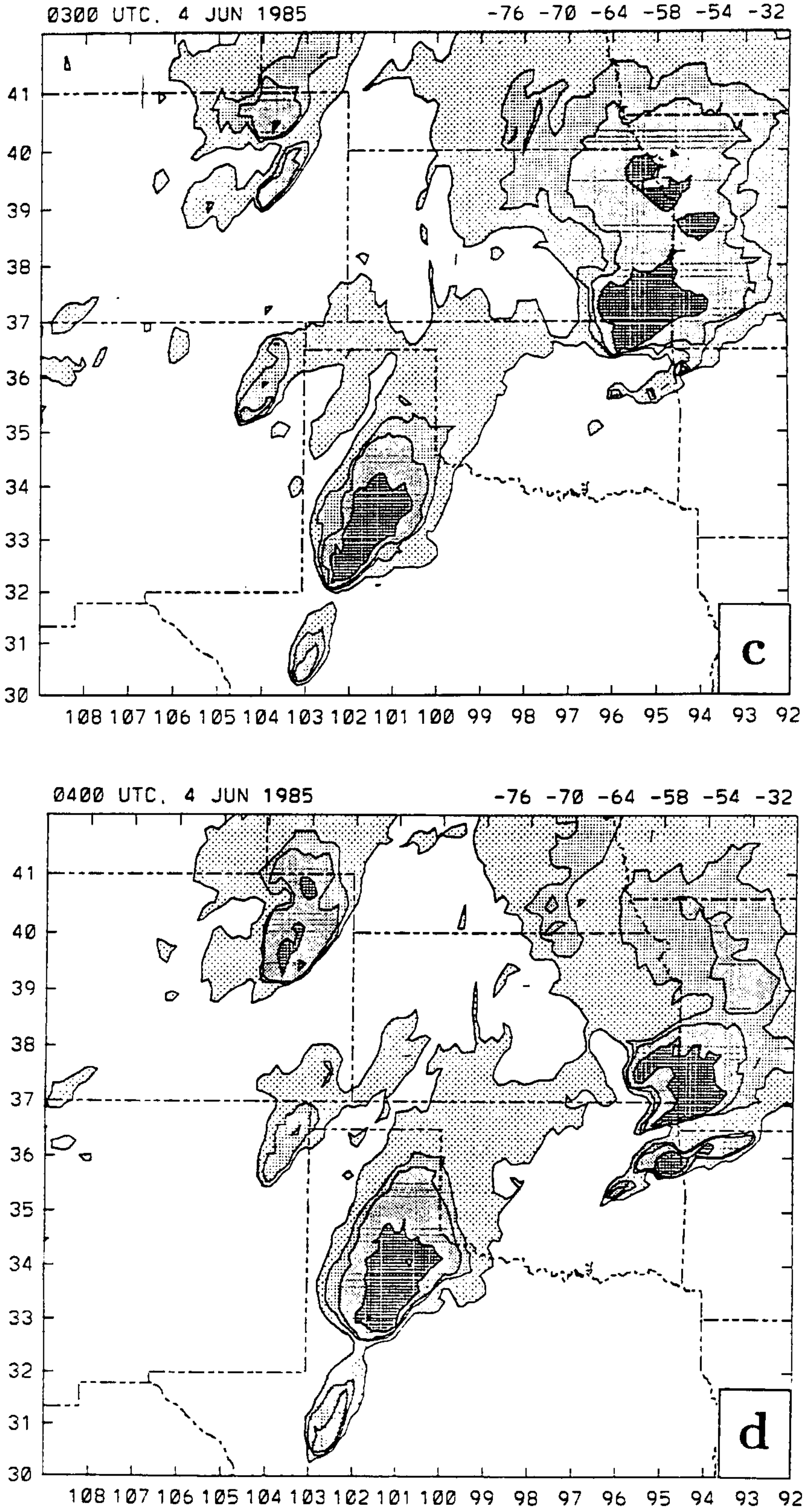

Figure 2.32: Continued.

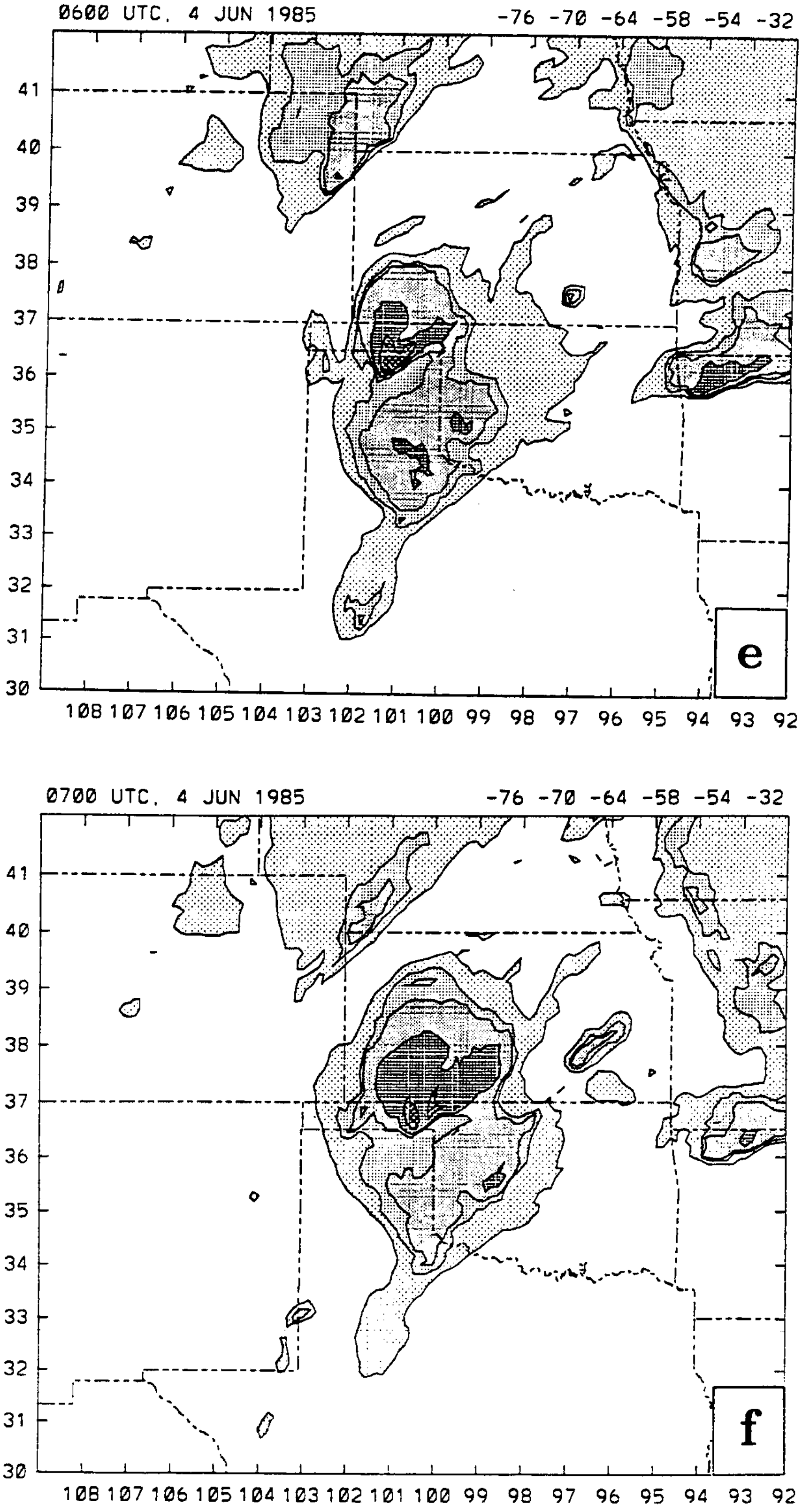

Figure 2.32: Continued.

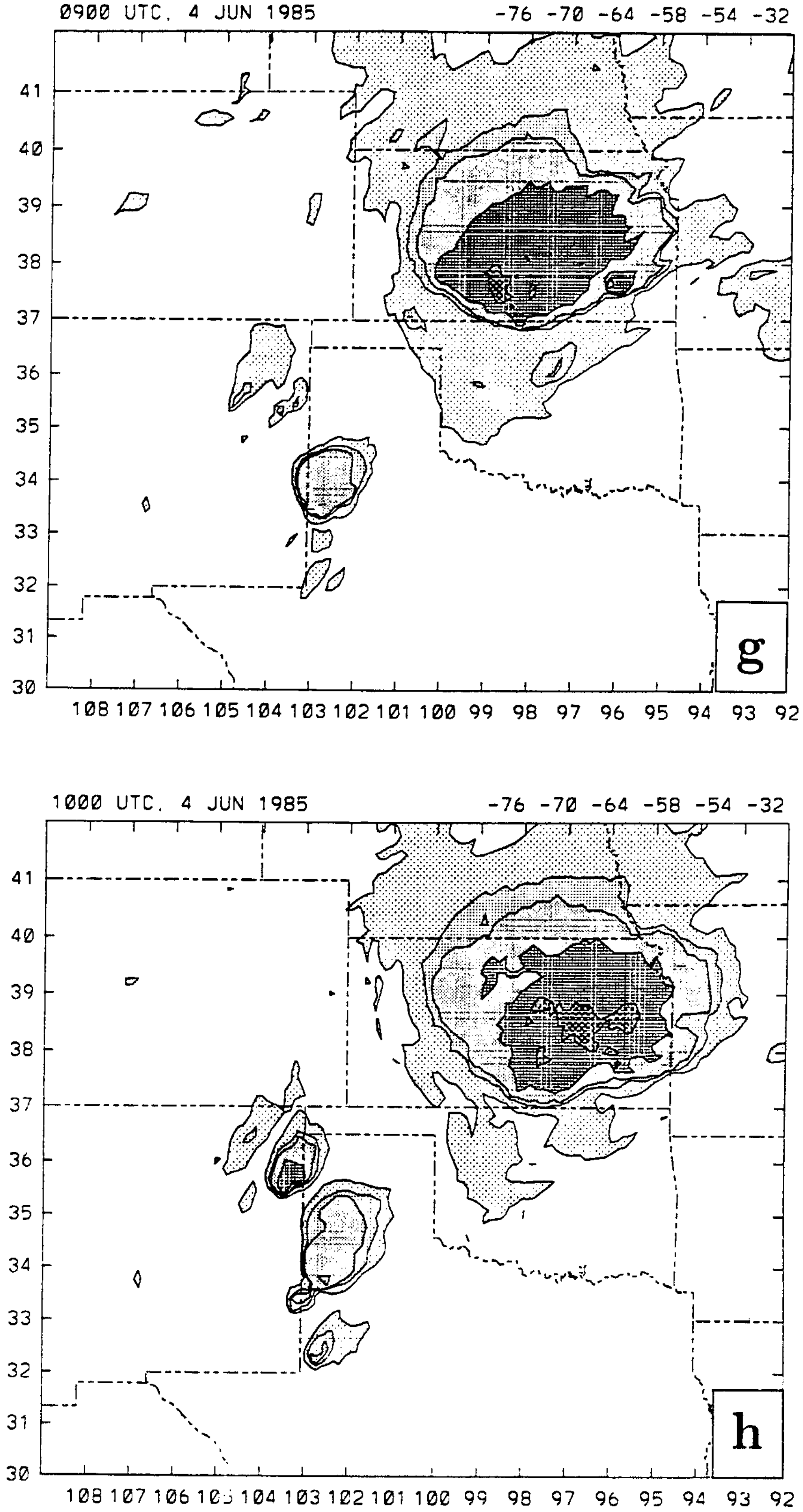

Figure 2.32: Continued.

detected in the environment, they did not appear to be linked to the triggering of MCS1. MPV analysis indicates that slantwise convective motions were possible in the MCS1 environment and may have helped trigger the upright convection. Upper-level forcing (such as lifting by a short wave or jet streak circulations) did not play an significant role in triggering the MCS1 convection.

MCS2 began near the dryline in southeast New Mexico, intensifying late in the afternoon when it neared the unstable airmass in Oklahoma and Kansas. MCS3 also began along the dryline in southeast New Mexico.

Chapter 3

DESCRIPTION OF THE MM4 MODEL

The Pennsylvania State University/National Center for Atmospheric Research MM4 model (Anthes *et al.* 1987; Anthes and Warner 1978) is a widely-used, three-dimensional hydrostatic primitive equation model. While other numerical models might be suitable for use in this study (notably CSU-RAMS (Pielke *et al.* 1992) or the NASA MASS model (Kaplan *et al.* 1982)), MM4 has been chosen because of its successful application in numerous real-data cases (see Section 1.2). Also, its relatively low computational cost (as compared to the other models) makes numerous test and sensitivity runs possible. Zhang *et al.* (1989) state that their "results indicate that the convective and boundary layer parameterization schemes and the explicit moisture physics in this model are realistic for being utilized to study the meso-beta scale structure and evolution of MCSs."

The configuration used here is similar to that used with success by Zhang and Fritsch (1986a) and Zhang *et al.* (1989). A summary of the model characteristics is presented in Table 3.1. A high-resolution, two-way interactive nested grid is contained within a coarse mesh (Fig. 3.1). The nested grid was located as far west as possible to capture upstream features which may be important for MCS initiation and propagation. Initial convection for all four MCSs began within this nested grid area. The boundaries of the coarse mesh were located as far as practical from the nest, to reduce their effects on the simulation. This grid configuration was a compromise between the need for high horizontal and vertical resolution and computational costs.

A detailed description of the model's governing equations and numerical algorithms can be found in Anthes *et al.* (1987), Zhang and Fritsch (1986a) and Zhang *et al.* (1989). The vertical coordinate is a terrain-following σ coordinate, $\sigma = (p - p_t)/(p_s - p_t)$ where p_s

Table 3.1: MM4 Version 7 nested grid model characteristics.

coarse mesh spacing	75 km
nested mesh spacing	25 km
coarse grid array size	46 x 51
nested grid array size	49 x 61
vertical levels	23 non-uniform σ levels
model top	100 mb
lateral boundary conditions	time dependent from observations
explicit precipitation	liquid and frozen (Dudhia 1989)
implicit precipitation	Kain and Fritsch (1990), Arakawa-Schubert including downdrafts (Grell *et al.* 1991), or Anthes-Kuo (Anthes *et al.* 1987)
boundary layer	high resolution (Zhang & Anthes 1982)
time step	120 s
initial data	12 h MM4 first guess enhanced by observed and bogus sounding and surface data

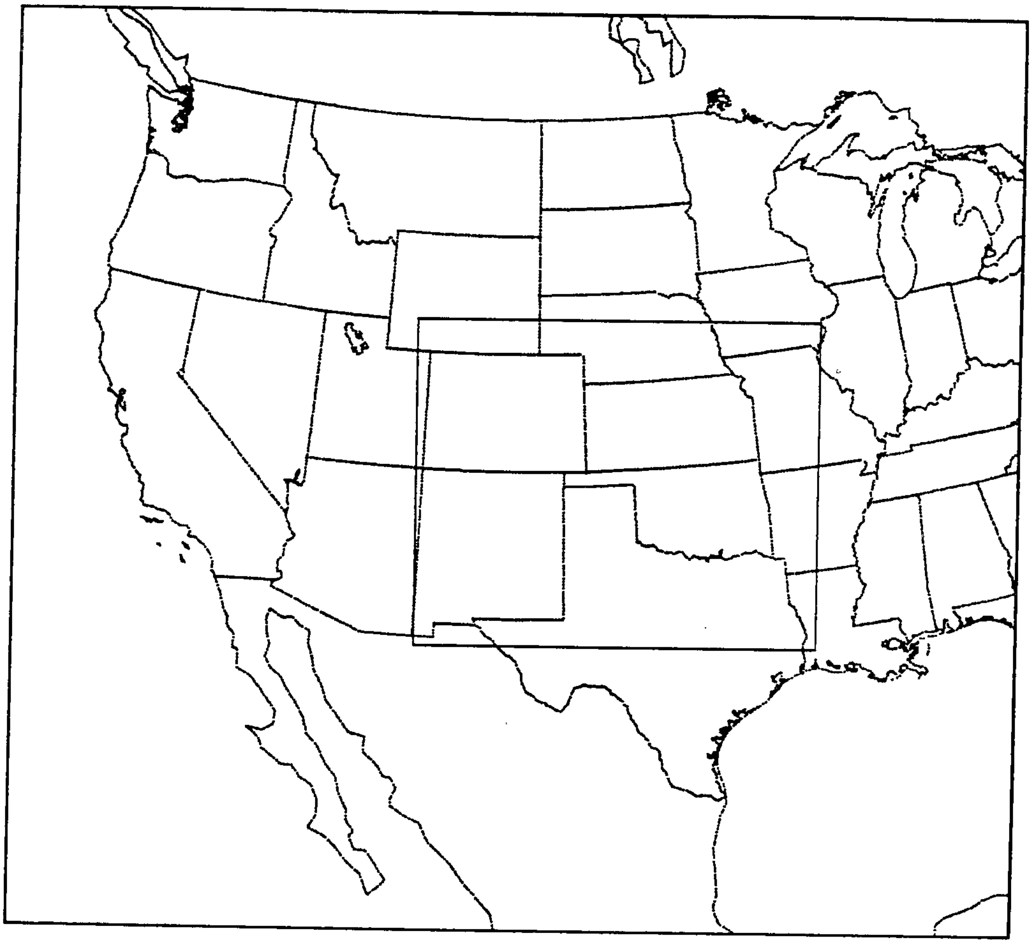

Figure 3.1: Model domain with the nested grid area indicated by the solid rectangle.

is surface pressure and p_t is the pressure at the model top and set to 100 mb. Twenty-three unevenly-spaced vertical levels were chosen with the highest resolution near the earth's surface. Model computations were carried out on the half-sigma levels as shown in Table 3.2.

Table 3.2: Model half-sigma levels. Pressure values are given for a surface pressure of 900 mb and model top of 100 mb.

K	Half Sigma Levels	Pressure (mb)
1	0.025	120
2	0.075	160
3	0.125	200
4	0.175	240
5	0.225	280
6	0.275	320
7	0.325	360
8	0.375	400
9	0.425	440
10	0.475	480
11	0.525	520
12	0.575	560
13	0.625	600
14	0.675	640
15	0.725	680
16	0.775	720
17	0.825	760
18	0.875	800
19	0.915	832
20	0.945	856
21	0.970	876
22	0.985	888
23	0.995	896

Fig. 3.2 shows the terrain fields on the coarse and fine grids. The major topographic features are captured at the resolutions used, including the gradual slope of the high plains and the steeper slopes of the Rockies. The nested grid terrain includes some smaller-scale topographic features such as the Raton Mesa (the west-east ridge in northeast New Mexico) and the Palmer Ridge (the west-east ridge in east-central Colorado).

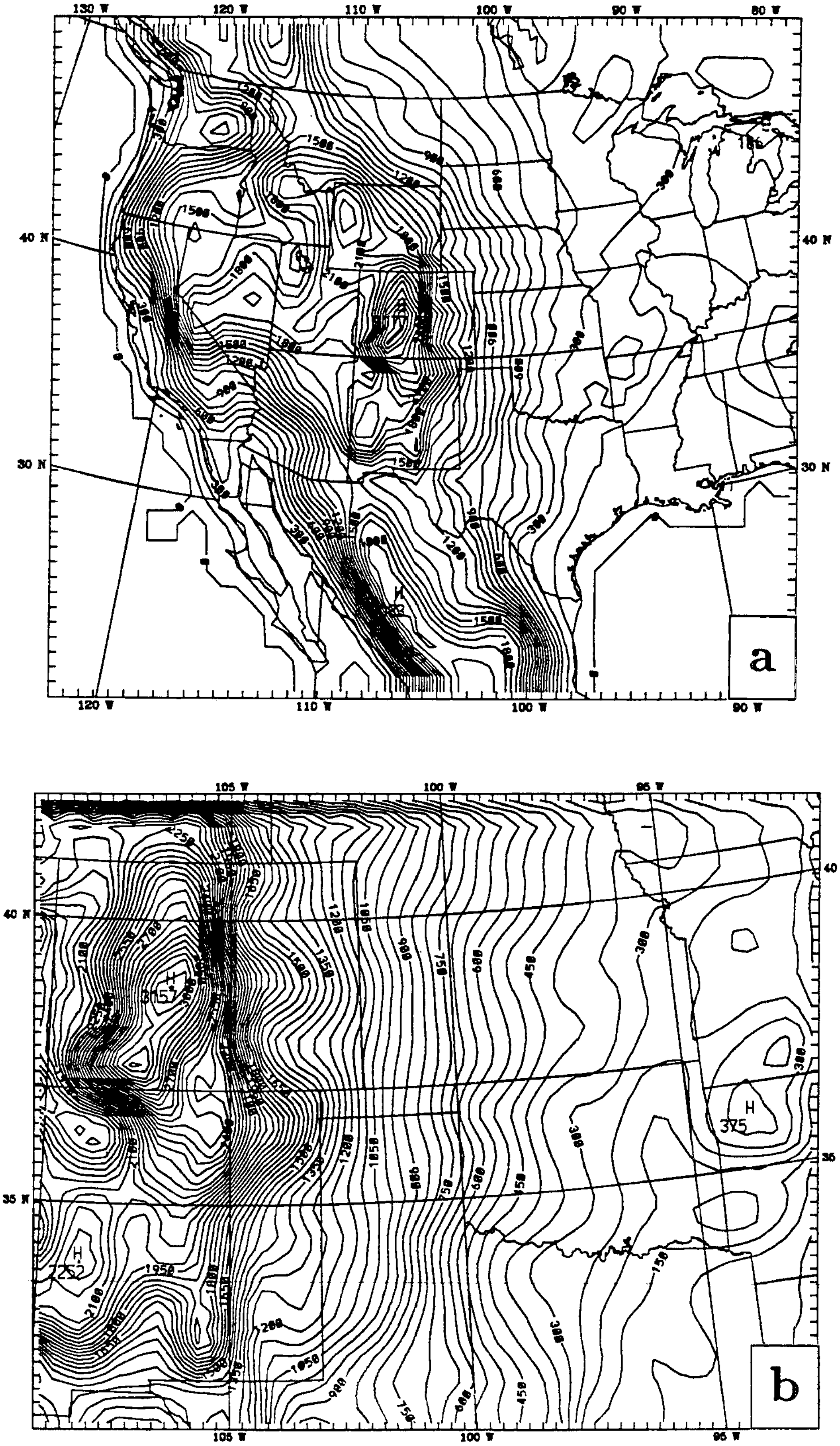

Figure 3.2: Model terrain height in meters for a) the coarse grid (contour interval of 100 m) and b) the nested grid (contour interval of 50 m) domains.

The two-way interactive nesting procedure is described in detail by Zhang *et al.* (1986) and succinctly by Dudek (1988). The coarse grid spacing is three times larger than the nested grid, so it uses a time step three times larger than the nest. The model equations are first integrated forward in time on the coarse grid. Integration then proceeds on the nested grid for three nested grid time steps using the coarse grid tendencies for the nest's lateral boundaries. When the two grids are at the same time level, the nested grid values are used to specify values at any coarse grid point within the nest using a nine-point weighted average. Therefore, smaller scale forcing is fed back to the larger grid.

Numerous physical parameterizations are available within the MM4 system. The following sections will describe the parameterizations used in this study.

3.1 Planetary Boundary Layer Parameterization

The model runs utilize a modified version of the Blackadar high-resolution planetary boundary layer (PBL) parameterization (Zhang and Anthes, 1982; Anthes *et al.* 1987) similar to that used by Zhang *et al.* (1989). The ground surface temperature is predicted using a force-restore slab model of the surface energy budget. The impact of cloud cover upon the shortwave and longwave components of the energy budget is parameterized by computing a cloud fraction based upon layer maximum relative humidities for low, middle, and high level clouds (Benjamin and Carlson 1986). Preliminary model runs of the 3-4 June case showed that in areas of observed low clouds, the model predicted surface temperatures that were too warm. Also, as compared to visible satellite images, the model over-predicted the low-cloud fraction, especially in areas with boundary-layer cumulus. Because low cloud shading effects are poorly handled by MM4, other studies have artificially altered the surface albedo in regions of low stratus clouds (e.g. Zhang and Fritsch 1986a). Here, a slight modification was made to the low cloud fraction algorithm. The lowest permissible low cloud base was reduced by one sigma level in order to help improve the simulation in regions where there was low-level moisture and fog. But, a fog and drizzle parameterization may still be needed to properly simulate those regions. Slingo (1987) considered two classes of low clouds: those associated with synoptic disturbances and those within a quiescent boundary layer. Here, a similar assumption is made – that two classes of low clouds may exist.

The standard low-cloud fraction formula used in MM4 (Anthes *et al.* 1987) is,

$$C_L = (4.0\ (RH_{max}))\ -\ 3.0.$$

where C_L is the low cloud fraction and RH_{max} is the maximum relative humidity within the low cloud layer. No clouds are assumed to exist for relative humidities less than 75%. For RH_{max}s between .75 and 1. the low cloud fraction increases linearly. Here, two low-cloud fractions are computed based on the standard MM4 formula and which use two different relative humidities. One of the low cloud fractions, $C_L(\overline{RH})$, is based on the mean relative humidity in the low-cloud layer and the other, $C_L(RH_{max})$, on the maximum relative humidity. In regions where $C_L(\overline{RH})$ exceeds 40%, the surface albedo is artificially increased as shown in Table 3.3. Therefore, in regions with a high layer-mean relative humidity and thus a high probability of thick, low clouds, shortwave insolation impinging upon the surface is reduced by increasing the albedo. These modifications yielded a much more realistic simulated ground temperature.

Table 3.3: Adjusted albedo values due to the low-cloud fraction $C_L(\overline{RH})$

$C_L(\overline{RH})$	surface albedo (%)
$\geq .8$	85
$\geq .6$	75
$\geq .5$	70
$\geq .4$	40

The low-cloud fraction used for the radiation computations was a weighted combination of of $C_L(\overline{RH})$ and $C_L(RH_{max})$ as follows:

$$C_L = (2\ C_L(RH_{max})\ +\ C_L(\overline{RH}))\ /\ 3.$$

The weights were chosen so the low-cloud fraction was similar to the standard MM4 scheme, yet includes the effect of the mean relative humidity.

3.2 Explicit Precipitation

Explicit precipitation is that which can be resolved on the grid scale. Sometimes referred to as stratiform or grid-resolvable precipitation, the scheme contains predictive equations for cloud ice and snow above the freezing level and cloud and rain water below the freezing level. For sufficiently small grid spacings, convective effects may be resolved by the explicit precipitation scheme (e.g. Bougeault and Geleyn 1989; Molinari and Dudek 1992; Rosenthal 1979), but are most successful when used within a non-hydrostatic model (e.g. Fovell and Ogura 1988). For the nested grid spacing used in this study (25 km), Zhang *et al.* (1988) recommend using both an explicit scheme and an implicit scheme to properly simulate convective systems and avoid numerical moist instability. They termed this the full physics approach.

The parameterization used here is a slightly modified version of the one used by Dudhia (1989) and is based on the models of Lin *et al.* (1983), Rutledge and Hobbs (1983) and Hsie *et al.* (1984). Neither mixed-phase microphysics nor supercooled water is accounted for in the scheme. Potter (1991) pointed out some corrections to the Rutledge and Hobbs (1983) scheme which have been incorporated here. Specifically, the density of liquid water, ρ_w, is used in the formula for the snow size distribution, and the snow fallspeed relation is based on the melted drop diameter. These corrections eliminate the need to use the arbitrary reduction in terminal fall speed used by Zhang *et al.* (1989). The Fletcher curve, which specifies the concentration of ice nuclei as a function of temperature (Fletcher 1962), produced excessive cloud ice in the cold upper levels and was replaced with the supersaturation method of Meyers *et al.* (1992). However, results from both schemes were quite similar. A temperature-dependent snow coalescence efficiency was also added (Flatau *et al.* 1989).

3.3 Implicit Precipitation

Precipitation produced by convection occurs on scales smaller than those resolved by meso-α-scale grids and so cannot be explicitly simulated. This implicit or sub-grid scale precipitation is accounted for by a convective parameterization which can be activated when the grid-scale is sub-saturated. It is assumed that the convection occupies a portion of the grid box and that the convection is modulated by the grid-scale tendencies. As the grid size decreases, these assumptions become less valid (Cotton and Anthes 1989; Molinari and Dudek 1992), but for the 25 km grid spacing used here, Zhang et al. (1988) have argued that they still hold true. Two schemes are used on the nested grid in this study – the Kain and Fritsch (1990) scheme (hereafter KF) and a modified Arakawa-Schubert scheme (Grell *et al.* 1991) (hereafter AS).

3.3.1 KF scheme

A improved version of the Fritsch and Chappell (1980a) (hereafter FC) convective parameterization scheme was developed by Kain and Fritsch (1990). A summary of the improvements is also presented in Kain and Fritsch (1994). The KF scheme uses a one-dimensional entraining/detraining plume model to more realistically represent cloud-environment interactions. The scheme permits midlevel detrainment of mass and moisture, depending upon the environment, which can be important for the development of MCSs (e.g. Gamache and Houze 1983). More detailed microphysical processes were included in the KF scheme, including the ice phase. The KF scheme was also designed to conserve mass and energy which the FC scheme failed to do (Tremback 1990).

Downdrafts, which begin at the level of minimum saturated θ_E within the cloud and extend down to the surface or where the downdraft is no longer negatively buoyant, are included in the KF scheme. A slight modification to the standard KF downdraft scheme is used here: the pressure depth over which the downdraft detrains is specified to be 50 mb.

An important component of convective parameterizations was identified by Kain and Fritsch (1992). The convective trigger function is that part of the parameterization which determines whether or not convection should start at a grid point. The KF scheme permits the use of multiple triggers. As suggested by Stensrud (1992) and shown in Chapter 5, simulations of weakly-forced cases such as 3-4 June 1985 are sensitive to the trigger function. The triggers used here include a modified Fritsch-Chappell trigger (FCT), a lifting depth trigger (LDT) and a convective inhibition trigger (CIN). The FCT is strongly based on the instantaneous grid point vertical velocity. The LDT is based on the depth over which a parcel must rise to reach its LFC, while the CIN trigger is based on the negative area which a parcel must overcome to reach its LFC. Details on the triggers are presented in Chapter 5 and in Kain and Fritsch (1992).

Following Zhang and Fritsch (1986a), 50% of the available buoyant energy is removed during the convective time scale instead of the 90% in the original KF scheme. As pointed out by Tremback (1990), this is equivalent to reducing the convective heating rates by one-half. The slower heating rates are more conducive for the development of a balanced meso-α-scale circulation (Tremback 1990). The computation of the convective time scale used by the KF scheme has also been modified for this case. The original method calculated the advective speed of convective clouds as an average of the speed at the LCL and at 500 mb, with a minimum cloud lifetime of 30 minutes and a maximum of 60 minutes. Here, the time scale is based on 80% of the pressure-weighted average wind speed from the LCL to two levels below the cloud's equilibrium level. In addition, for a 25 km grid the minimum convective time scale corresponds to an advective speed of 13.9 m s^{-1} . Because some convective elements within MCS1 were observed to move faster than this speed, and indeed faster than the wind at any level (Fortune 1989), the minimum convective time scale was reduced to 20 minutes.

3.3.2 AS scheme

A scheme designed to parameterize tropical convection was developed by Arakawa and Schubert (1974). Grell *et al.* (1991) and Grell (1993) describe a modified version of the original Arakawa-Schubert scheme which incorporates the work of Lord (1978) and includes moist downdrafts. Following the terminology of Schubert (1974) used by Grell *et al.* (1991), the dynamic control of the AS scheme is the quasi-equilibrium assumption. It is assumed that the large-scale forcing which acts to destabilize the environment is balanced by the stabilizing effects of the convection. This is a reasonable assumption for large grid areas over the tropics (Arakawa and Schubert 1974), but, as shown by Grell *et al.* (1991), may also hold over the midlatitudes, despite the evidence that on smaller scales in the midlatitudes the convective rain at a given instant may greatly exceed the synoptic scale supply (Cotton and Anthes 1989). The static control (or cloud model) used to compute the thermodynamic properties of the convection in the AS scheme assumes a constant entrainment rate – no detailed microphysics are included. The feedback from the convection to the larger scale assumes a steady-state. The convection therefore, impacts upon the environment through environmental subsidence or detrainment from the updraft top or downdraft base. The AS scheme used here includes six cloud types and a lifting depth trigger of 50 mb. Once triggered, convection is assumed to exist for 30 minutes. Semiprognostic tests of the AS scheme on an Oklahoma springtime case show that the AS scheme performed fairly well and that the inclusion of moist downdrafts was crucial (Grell *et al.* 1991). Prognostic tests of the AS scheme on the 10-11 June PRE-STORM case were also successful and provided further evidence that the quasi-equilibrium assumption may indeed be valid for springtime midlatitude mesoscale applications (Grell 1993).

3.4 Miscellaneous Parameterizations

Except where otherwise noted, the model runs utilized clear-air radiational cooling (Anthes *et al.* 1987), virtual temperature and hydrostatic liquid water loading (Zhang and Fritsch 1986a), evaporation and melting of cloud and precipitation particles, vertical mixing of momentum, and variable moisture availability. Details about these schemes can be found in Anthes *et al.* (1987).

3.5 Initial Conditions

Great care was taken to produce accurate analyses at all four synoptic times (3/0000, 3/1200, 4/0000, and 4/1200) used in this study. Model runs were initialized at 3/0000 and 3/1200, while the analyses at 4/0000 and 4/1200 were used for the time-dependent lateral boundary conditions. As shown by Anthes *et al.* (1989) the lateral boundary conditions are the most important factor upon the temporal evolution of model errors. Anthes *et al.* (1989) also pointed out that details in the initial conditions are most important during the first few hours of a simulation. Stensrud (1992) has shown that mesoscale details in the initial conditions are crucial for accurate simulation of convective systems. He also states about the 3-4 June case that "the accurate placement and slope of the frontal boundary likely would be crucial to the successful simulation of this MCC". Numerous difficulties were encountered when developing realistic initial conditions at 3/1200, and the procedures and modifications are described below.

The initial conditions for MM4 are obtained by a pre-processing system that contains three programs – DATAGRID, RAWINS, and INTERP. DATAGRID (Manning and Haagenson 1992) was used to interpolate the 2.5° NMC gridded data to the MM4 forecast grid. Part way through the current study, it was apparent from the first guess fields that the NMC data actually contained virtual temperature instead of temperature as indicated by the documentation and program code. The difference between the use of virtual temperature and temperature was apparent in low levels in the 3-4 June case because of the warm, moist airmass over the southern half of the nested grid. Modifications to the DATAGRID source code were made to properly account for the use of virtual temperature in the first guess fields. RAWINS (Manning and Haagenson 1992) uses a successive corrections objective analysis technique to enhance the first guess fields using surface and upper air observations. The successive correction procedure, using a decreasing radius of influence on each pass, produces fields that are quite close to observed at grid points close to sounding sites. However, between sounding locations, the analysis is weighted more toward the first guess field. RAWINS analyzes data on the large-scale grid, so that the smallest resolved feature is on a scale of $2\Delta x$ or 150 km. Initial conditions on the nested grid are obtained by horizontal interpolation of data on pressure surfaces - no additional enhancement is done. Therefore, even on the nested grid, the smallest resolved wavelength in the initial data is 150 km. Some modifications were made to the RAWINS source code to improve the analysis and are described in Appendix B. Vertical interpolation from the pressure surfaces to the model σ levels and from the large-grid to the nested-grid is done within program INTERP. Modifications were made to this program to develop more realistic initial conditions and are described in Appendix C.

Data from approximately 30 of the PAM/SAM sites were added to the surface data analyses at 3/0000, 3/1200, and 4/0000. Standard synoptic surface data coverage is quite good relative to the 75 km grid size, so the addition of the mesonetwork data did not yield a great improvement in the analyses. Bogus surface data (based on observations taken after 3/1200 and on the existence of low-clouds and fog seen in visible satellite images) at INK and P07 (150 km southeast of INK) were added to the 3/1200 analysis to improve the moisture field in southwest TX. Without these data, the airmass in that region was excessively dry.

Some of the PRE-STORM supplemental soundings that were available at 3/0000 were included in the RAWINS analysis (from FSI, HET, HOY, PTT, and SUL). No supplemental soundings were available at 3/1200. Many of the NWS soundings within the PRE-STORM area contained in the NMC data file at NCAR were either missing at 3/1200 or were actually 3/0900 soundings. The missing soundings were added from the PRE-STORM data files or from the NCDC archives. Supplemental soundings taken at 4/0000 were not included in the RAWINS analysis, since the model was not initialized at this time, and the supplemental data would have had no impact upon the lateral boundary conditions.

Numerous model runs beginning at 3/1200 failed to realistically simulate MCS1. These failures may be attributed to either inadequacies in the moist physics parameterizations (as discussed elsewhere) or due to unrepresentative initial conditions. Therefore, a subjective improvement of the initial data was conducted. A new first guess field at 3/1200 was obtained from a 12 h full-physics MM4 simulation which used the KF parameterization. The model first-guess field had more moisture near the origin of both MCS1 and MCS2 than provided by the 3/1200 NMC analysis. Because of the coarse 75 km analysis mesh and the location of the stationary front between sounding sites at 3/1200, RAWINS generated too much moisture on the warm side of the front in OK. This moisture led to the development of a false rain area in the model. It was decided to add several bogus soundings in OK and KS to better define the temperature, moisture, and wind fields near the front. Fig. 3.3 shows the bogus sounding locations at 3/1200. Fig. 3.4 presents the bogus soundings. These soundings were based on a subjective synoptic analysis of the available data. Unfortunately, PRE-STORM supplemental soundings were not taken

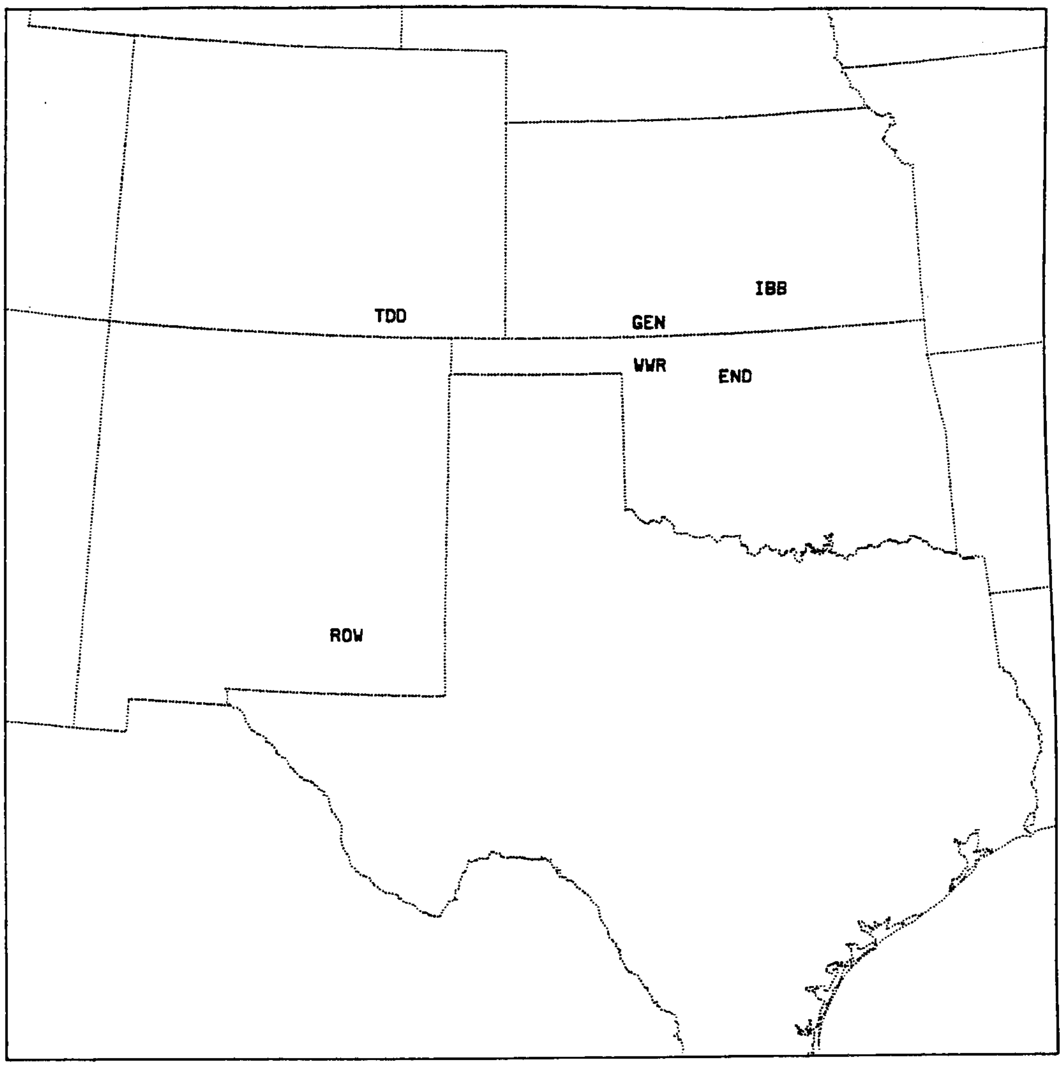

Figure 3.3: Locations of the bogus soundings added to the RAWINS analysis at 3/1200.

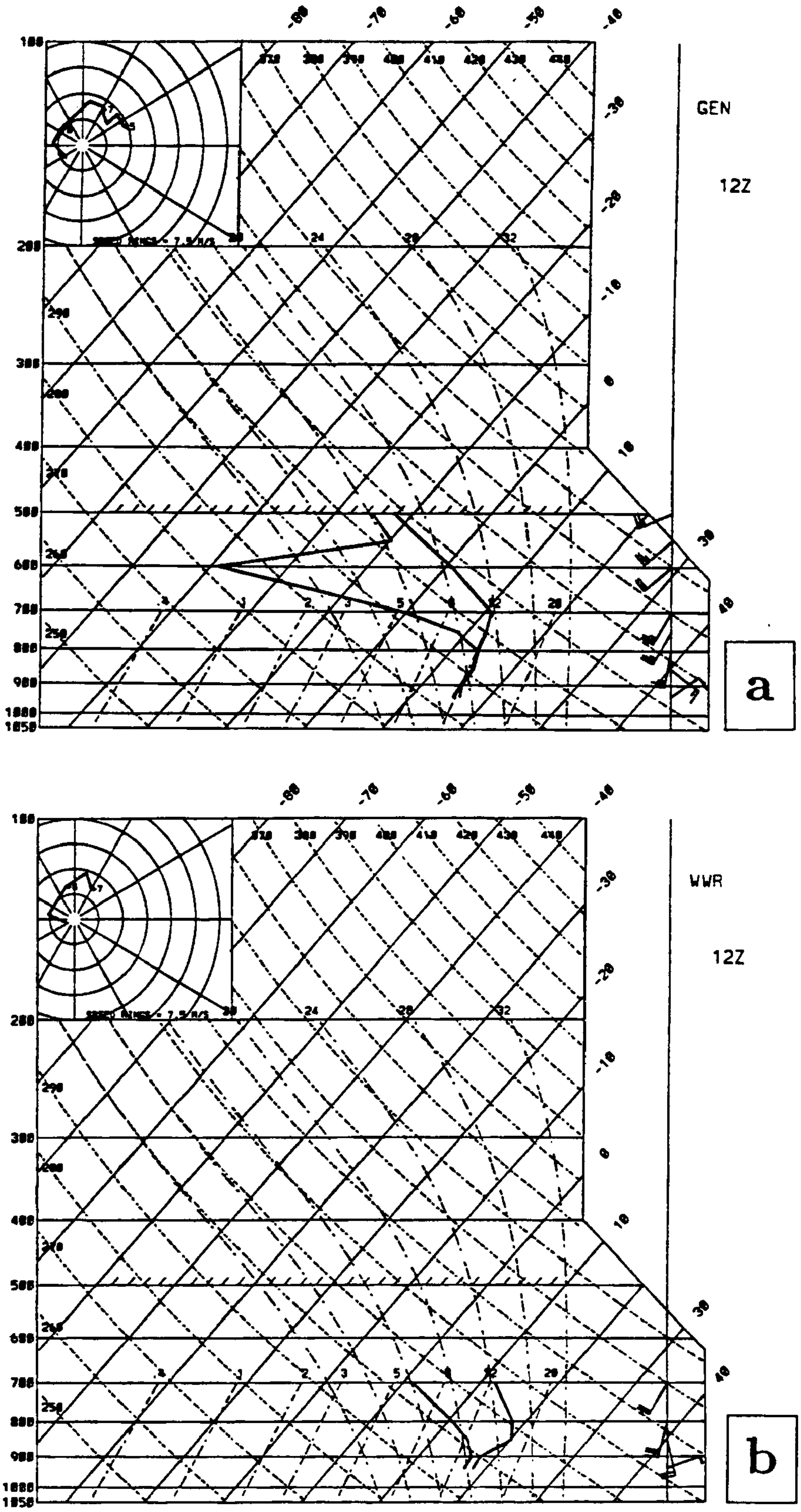

Figure 3.4: Bogus soundings added to the 3/1200 RAWINS analysis for the sites shown in Fig. 3.3 from a) GEN, b) WWR, c) IBB, d) END, e) ROW, and f) TDD.

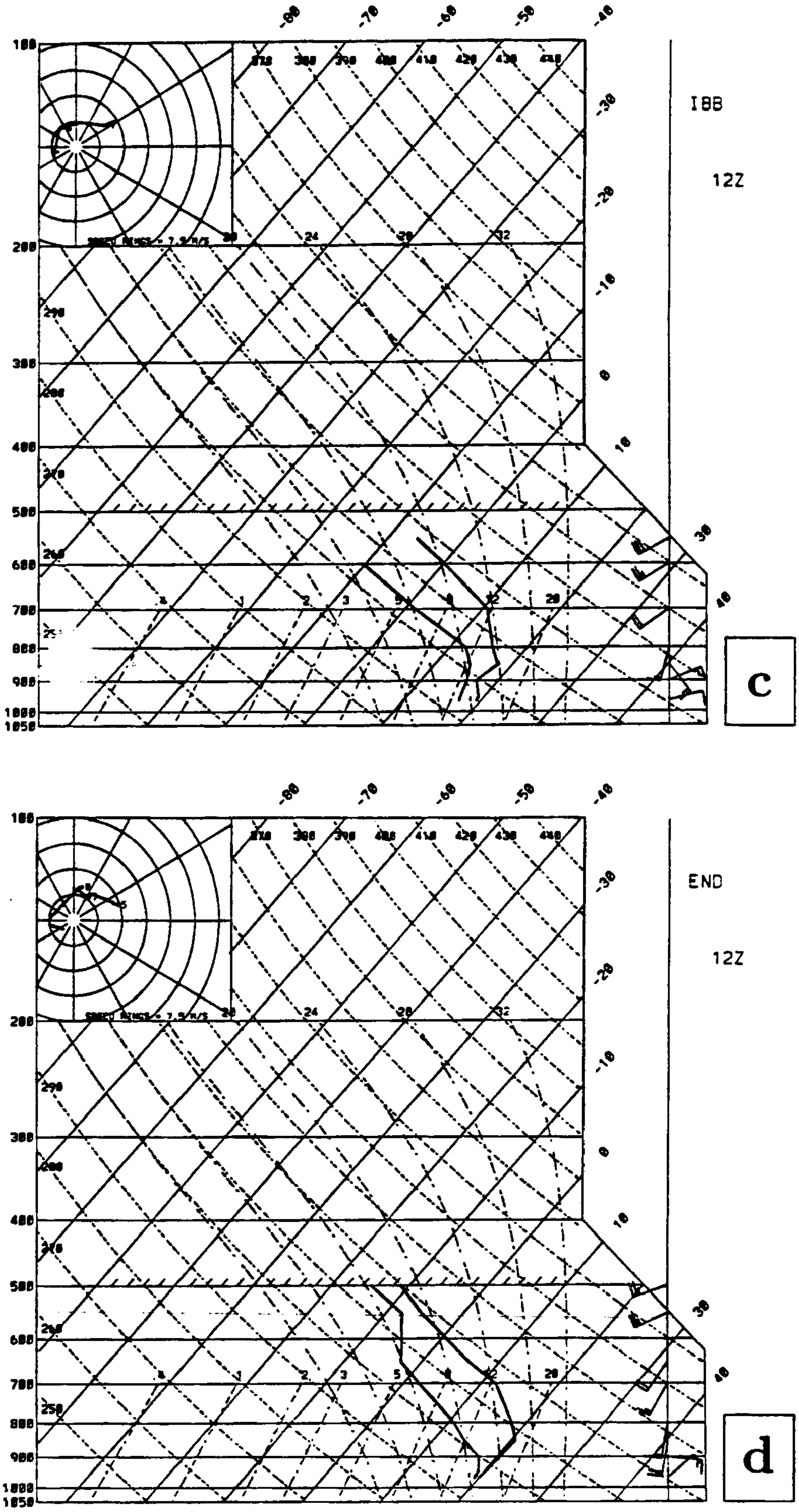

Figure 3.4: Continued.

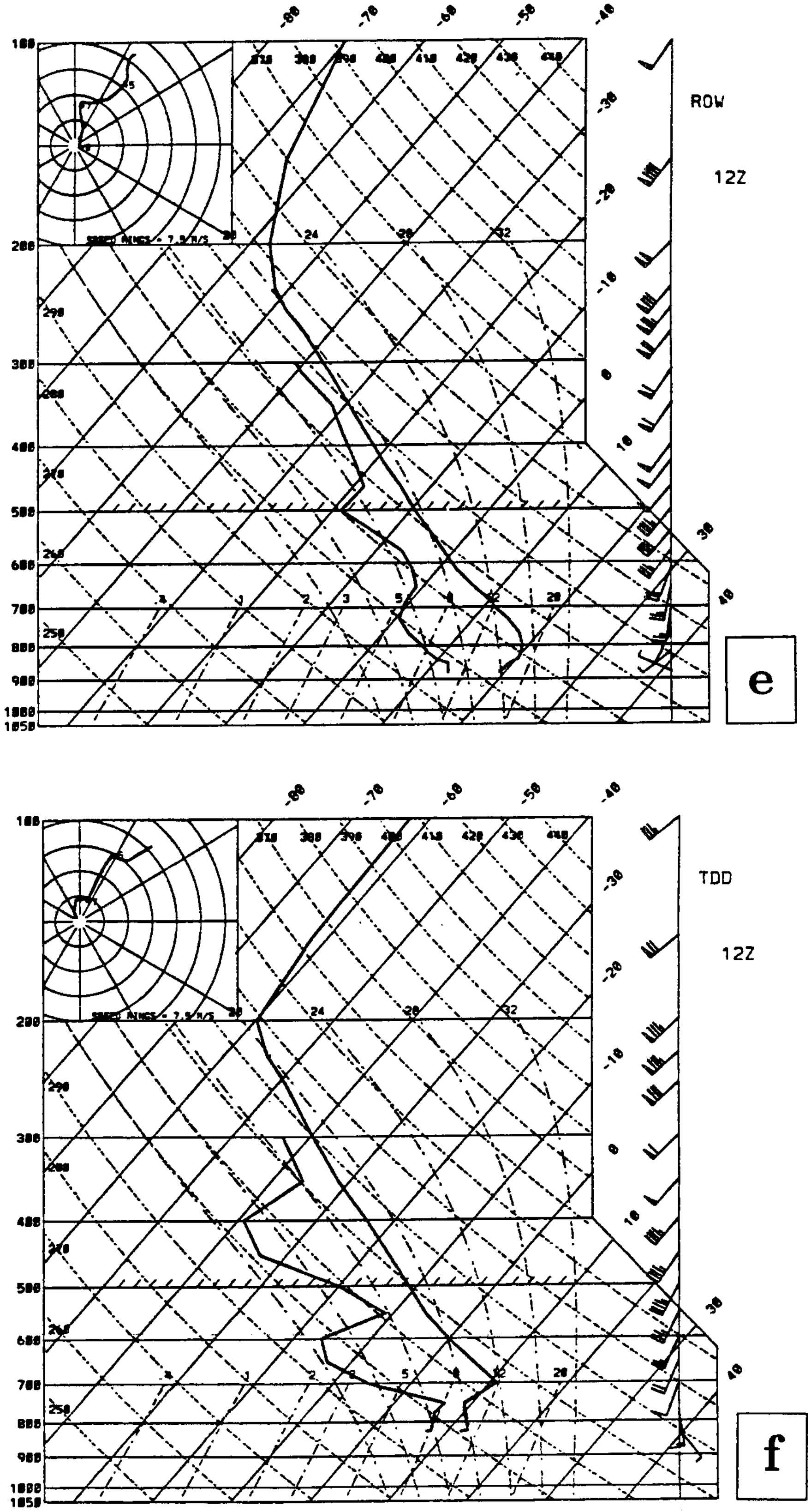

Figure 3.4: Continued.

at 3/1200 (the intensive observing period ended at 3/0900). In order to better capture the entire life cycle of MCSs, future field programs need to plan for continuing sounding releases (particularly at the synoptic observing times, 0000 and 1200 UTC). The use of the bogus soundings may be justified by the fact that soon, enhanced observing systems such as wind profilers lower tropospheric temperature profilers, and satellite sounders may become operational and would observe the features which now must be added by a subjective meteorological analysis (or that might have been captured by the supplemental soundings).

The bogus sounding at GEN (Fig. 3.4a) (near the location of MCS1 genesis) was designed to mimic the nearby DDC sounding, but with a slightly weaker 700 mb cap and a stronger south-southwesterly low-level jet. The sounding at WWR (Fig. 3.4b) which was just north of the surface front had a very shallow layer of cold air at the surface with a strong frontal inversion. Above the inversion, a low-level jet was added (as an extension to the observed LLJ at AMA). The IBB sounding (Fig. 3.4c) was constructed to have a deep cold air mass with ample moisture. The END sounding (Fig. 3.4d) (like WWR) had a very shallow surface cold layer with a strong frontal inversion.

Preliminary model runs using the modified AS scheme failed to produce convective rain associated with MCS2. The difficulty was traced back to the development of a midlevel explicit rain area (Chapter 5) which produced excessive evaporative cooling and downward motion effectively preventing convection. The explicit rain area was generated in an area of high relative humidities present in the model first guess field. A bogus sounding was added near ROW (Fig. 3.4e), in which the humidity below 600 mb was from the MM4 first guess field and the humidity above 600 mb was from the NMC first guess field. The use of the NMC first guess data at this location reduced upper level relative humidities by 10-20%.

Model simulations also diverged from reality near Trinidad, Colorado. Observations showed that the cold air mass north of the cold front had reached the southern Colorado foothills. However, because of TDD's distance from a sounding site, the RAWINS pressure-level analyses produced only a very shallow cold air mass which was quickly mixed away in the model simulation. A bogus sounding was constructed (Fig. 3.4f) to place a more realistic low-level temperature and moisture profile in this region.

Finally, the low-level divergence patterns over the TX panhandle associated with the low-level jet (Chapter 2) were unrealistic despite the incorporation of the bogus soundings in the analysis. Therefore, some of the actual nested grid point values were altered, bypassing the objective analysis. The wind fields then better resembled the concept of a low-level jet intersecting a frontal surface, but the resulting change in the model simulations was negligible.

3.6 Description of Simulations

The difficulty in realistically simulating the 3-4 June case (not only with MM4, but with CSU-RAMS as well (Tremback *et al.* 1992; Koch 1993, pg. 23) has led to a large number of model runs which were attempted to rectify possible shortcomings in the parameterizations or initial conditions. In its standard form, MM4 successfully simulated many MCS cases (section 1.2), but the highly-unstable, complex, and weakly-forced 3-4 June case tests the model's limits.

The numerical simulations described in this work are summarized in Table 3.4. The control run (CTL) was chosen since it used the most detailed initial conditions and resulted in the best overall forecast. While other experiments may have excelled with certain aspects of the event, CTL most closely resembled reality. Other experiments were the result of attempts to make a more accurate simulation or to test the sensitivities of the simulation to various changes in the model physics or input data. The experiments can be put into two broad categories: those which involve changes to the initial data fields and those that involve changes to the moist physics parameterizations. Experiment NOJS was designed to determine the impact that the omission of the upper-level jet streak near ELP from the initial data would have upon the simulation. The purpose of experiment DRY was to elucidate the dry dynamics and infer possible convective effects upon the jet streaks. Implicit convection in eastern Kansas was omitted from Exp. NOM1 in order to see what influence MCS1 might have had upon MCS2. Exp. Z0 was a simulation of the entire 3-4 June event, starting at 3/0000. Experiments CTL, LDT, and CIN permit intercomparison of the convective trigger function. Experiment MAS utilized the modified Arakawa-Schubert scheme and will be compared to the runs that used the Kain-Fritsch scheme. Experiment PEF uses the precipitation efficiency scheme of Zhang and Fritsch (1986a) within the KF parameterization and will be compared with the modified scheme employed in CTL. Finally, the sensitivity of the simulation to vertical resolution was tested by using 32 vertical levels (Exp. LV32).

Table 3.4: Summary of Simulations.

Experiment name	Initial time	duration	convective scheme	trigger function	explicit scheme	description
CTL	3/1200	18 h	KF	FCT	yes	control run
NOJS	3/1200	9 h	KF	FCT	yes	no initial jet streak
DRY	3/1200	9 h	no	no	no	no moisture
NOM1	3/1200	9 h	KF	FCT	yes	no MCS1
NMCG	3/1200	9 h	KF	FCT	yes	NMC first guess field
Z0	3/0000	27 h	KF	CIN	yes	0 UTC start
LDT	3/1200	18 h	KF	FCT	yes	KF scheme with LDT
CIN	3/1200	9 h	KF	CIN	yes	CIN trigger
MAS	3/1200	18 h	AS	LDT	yes	Arakawa-Schubert
PEF	3/1200	6 h	KF	FCT	yes	precipitation efficiency test
LV32	3/1200	9 h	KF	FCT	yes	32 vertical levels

Chapter 4

RESULTS FROM THE CONTROL EXPERIMENT

Among the numerous simulations conducted for this study, Exp. CTL exhibited the best overall performance and will be analyzed in detail. In addition to the characteristics shown in Table 3.4, CTL used the Anthes-Kuo convective scheme (Anthes *et al.* 1987) on the coarse grid. Exp. CTL was a full-physics run (Zhang *et al.* 1988) with all of the possible parameterization switches turned on.

A description of the development of convection within the simulation and how it compares with the genesis and evolution of MCS1 and MCS2 follows. First, it is important to state how an MCS can be identified within the model output fields. Koch (1985) described a simple way to identify MCCs using output from a model without a convective parameterization. Here, more explicit information is available. As an MCS evolves, it grows from subgrid-scale convection, which is parameterized, to a dynamically-large system which contains both explicitly-resolved circulations and parameterized convection. In cases with one MCS its identification is not difficult, but in the present case with multiple convective areas, some developing, some not, and occurring relatively close in space and time, it becomes more challenging. An MCS is identified as follows: A coherent (in space and time) area of explicit rain (which can be stratiform rain or explicitly-resolved convection), accompanied by an implicit rain area and mid-level (700-500 mb) rising motion. Other MCS characteristics such as anticyclonic upper-level outflow, mid-level cyclonic vorticity, and low-level divergent outflow may or may not be present. The simulated MCS has its origins in a convective rain area. While snapshots of model fields may resemble observation snapshots, it is necessary to examine the time evolution of the model fields for proper identification.

4.1 Overview of the coarse grid simulation

Because the coarse grid provides the lateral boundary conditions for the nest and contains significant meteorological features, a brief overview of its simulation will be presented. Fig. 4.1 shows the 12 h 500 mb height forecast and the corresponding verification at 4/0000. The upper low, upstream of the nested grid, would be the feature most likely to have a significant impact on the nest's boundaries. The placement of the upper low over west-central Arizona (Fig. 4.1a) matches the analysis (Fig. 4.1b). The intensity of the lows are nearly identical as well with only a 5 m difference in the minimum heights. The northern-stream flow across the Dakotas into the Great Lakes region matches observations, and the negatively tilted ridge axis across Oklahoma into Colorado is also simulated well.

The precipitation produced by the model is the end-product of complicated interactions between the simulated temperature, moisture, and flow fields. The simulated precipitation can be used as a gauge of forecast accuracy without presenting a detailed analysis of the numerous other fields. Precipitation areas can be readily compared with hourly radar summaries and raingauge data, while other observed fields are available only at twelve-hour intervals.

A series of 3 h total rain forecasts is shown in Fig. 4.2. The total rain includes both the explicit rain and the implicit (Anthes-Kuo) rainfall. Within the nested grid area, the rain produced on the coarse grid is diagnostic, since the meteorological variables are fed back from the nested grid as described in Chapter 3. At 3/1500 (Fig. 4.2a), significant rain areas are found in Indiana, South Dakota, and near the upper low in California. These areas match observed rain areas (not shown). (Observed precipitation within the nested grid region will be presented in the following section). MCS1 appears as a local maximum in Kansas, with another rain area in extreme northeast Oklahoma. By 3/1800 (Fig. 4.2b), the major rain areas are over South Dakota (as observed), western Arizona, and in eastern Kansas associated with MCS1. Virtually all of the rain was implicit. Rainfall associated with MCS2 at this time was not diagnosed on the coarse grid. By 3/2100 (Fig. 4.2c), light rain amounts were simulated over South Dakota, and in the

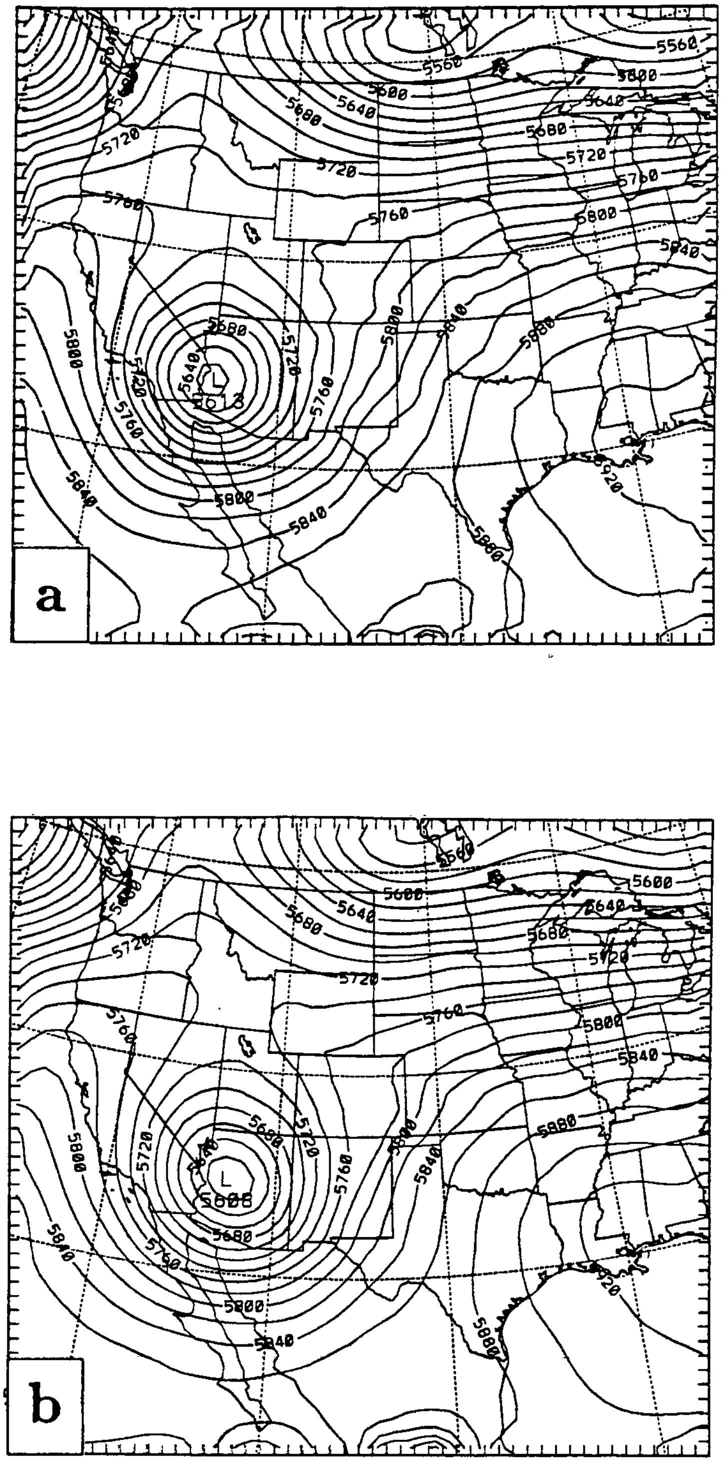

Figure 4.1: Geopotential height (m) at 500 mb contoured every 20 m valid at 4/0000 from a) CTL 12 h simulation and b) RAWINS analysis.

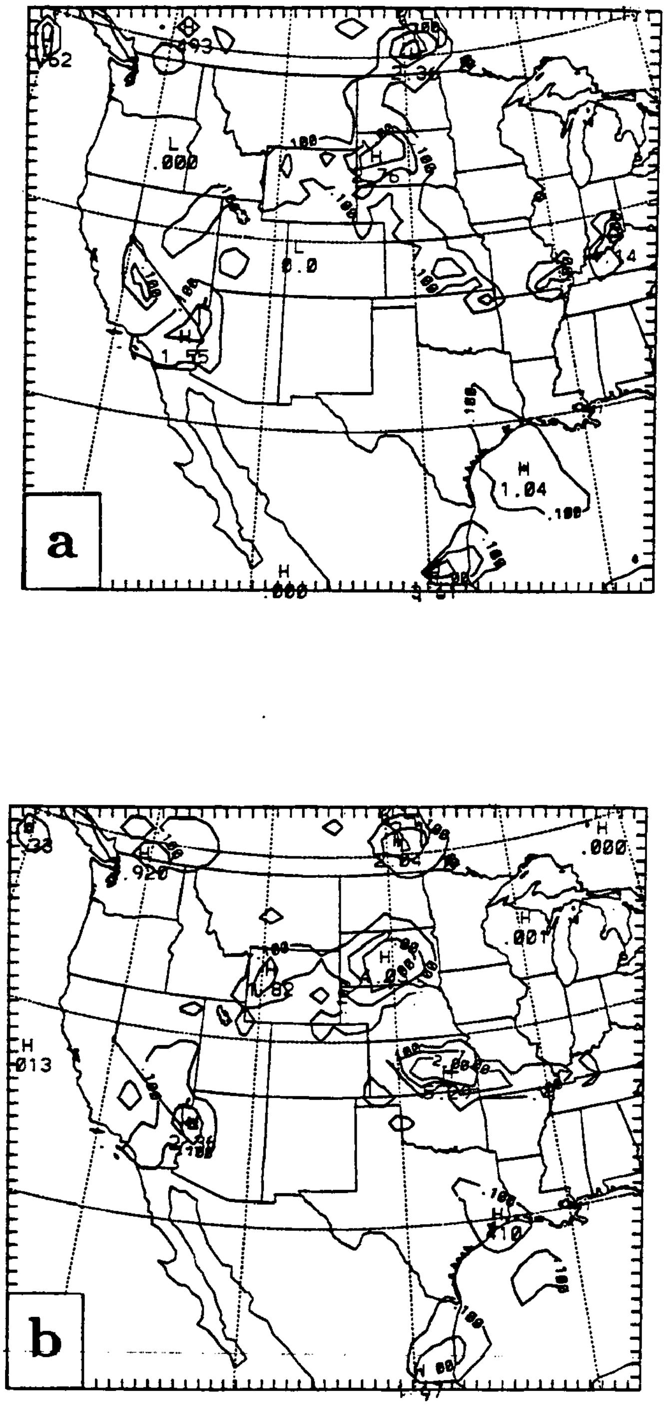

Figure 4.2: Simulated total rainfall tendency (implicit plus explicit, in mm $(3\ h)^{-1}$), on the coarse grid with an uneven contour interval 0.1, 1, 2, 5, and 10 mm valid at a) 3/1500, b) 3/1800, c) 3/2100, and d) 4/000.

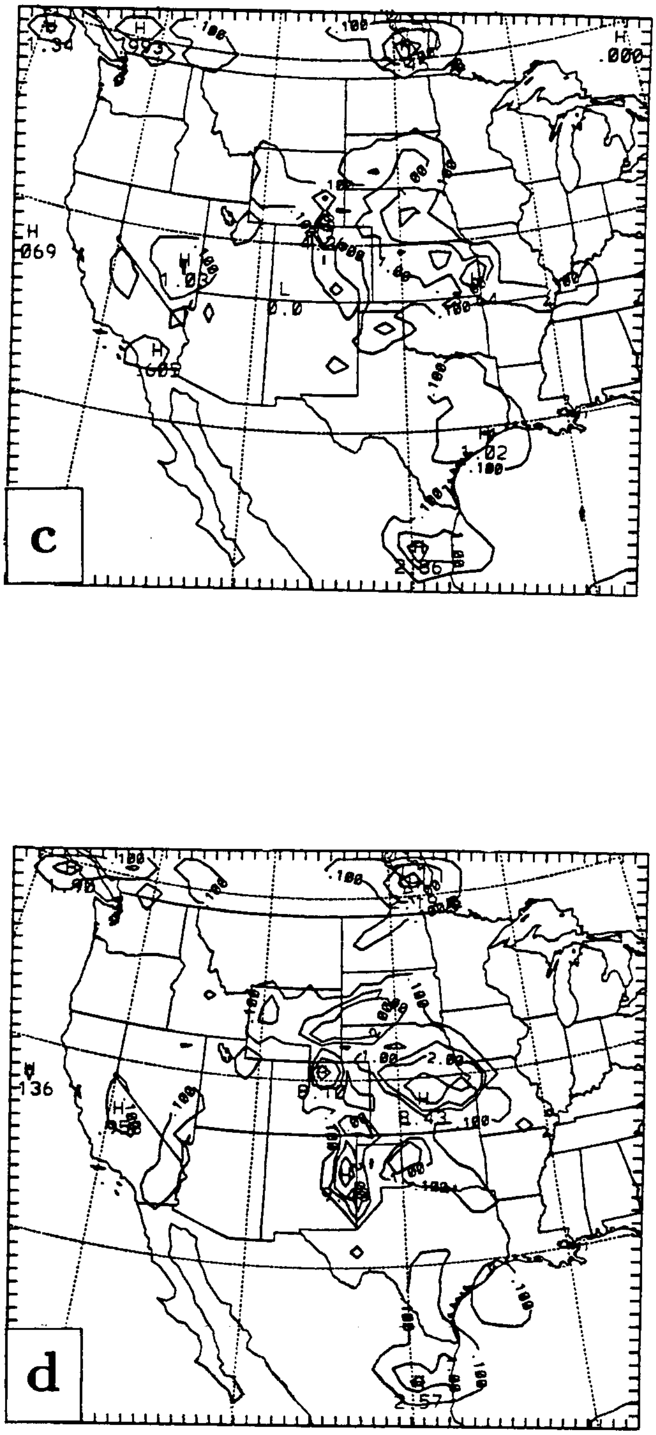

Figure 4.2: Continued.

vicinity of the upper low in Nevada. An axis of rain was along the Continental Divide in Colorado extending into Wyoming. MCS1 was simulated to be along the Kansas-Missouri border with only trace amounts extending into Oklahoma. Convection possibly associated with MCS2 was diagnosed in the Texas panhandle. These rain areas match observed rain regions quite closely except for the underprediction of strong convection in Tennessee and the overprediction of rain in eastern Texas. The 12 h forecast (Fig. 4.2d) is dominated by convection within the nested grid region. Maximum rainfall was across central Kansas, north-central Colorado, and eastern New Mexico. The Kansas rain area might correspond with MCS2 as might the detached rain area in western Oklahoma.

In general, the coarse grid simulation proceeded realistically and might be expected to provide the nested grid with reasonable boundary values. The following sections describe the evolution of features within the nested grid.

4.2 Evolution of MCS1

Model convection first developed over central Kansas at 1427 UTC. Fig. 4.3 shows the convective rainfall for the 3 h period ending at 1500 UTC along with the observed rainfall as obtained from the hourly precipitation data and PAM/SAM network. (All of the simulated rain in Kansas shown in Fig. 4.3a had fallen during the previous 33 minutes). The simulated convection began approximately 100 km northeast and 90 minutes after the actual first convection (Fig. 2.16b). Observations indicate a narrow southwest-northeast oriented area of rainfall (Fig. 4.3b).

The first model convection formed in an area of 850-700 mb convergence, north of the terminus of the LLJ (similar to the manner postulated by Trier and Parsons 1993). This was also an area with enhanced moisture as a result of the MM4 first guess field. The model run upon which the first guess was based produced a band of rain across central Kansas, leading to higher moisture contents in the CTL initial conditions then would otherwise exist based upon observations alone. Further analyses of the impact of the first guess field will be shown in the following chapter. Figure 4.4 shows the 800 mb moisture divergence at 3/1200. The maximum convergence was in south-central Kansas, along the

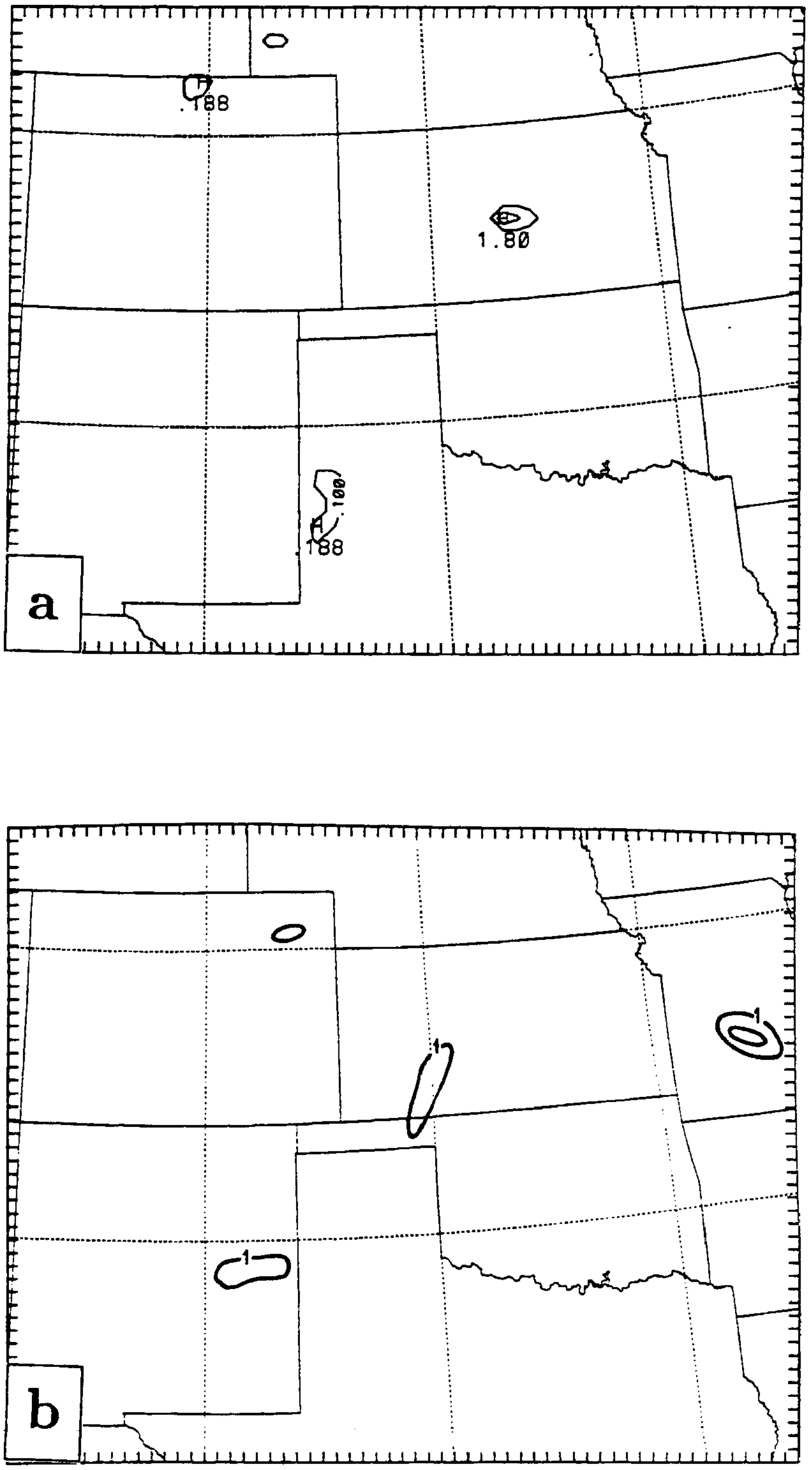

Figure 4.3: Simulated convective rainfall, with an uneven contour interval 0.1, 1, 2, 5, and 10 mm a), and observed rainfall with isopleths of 1 and 10 mm b) for the three-hour period ending 3/1500.

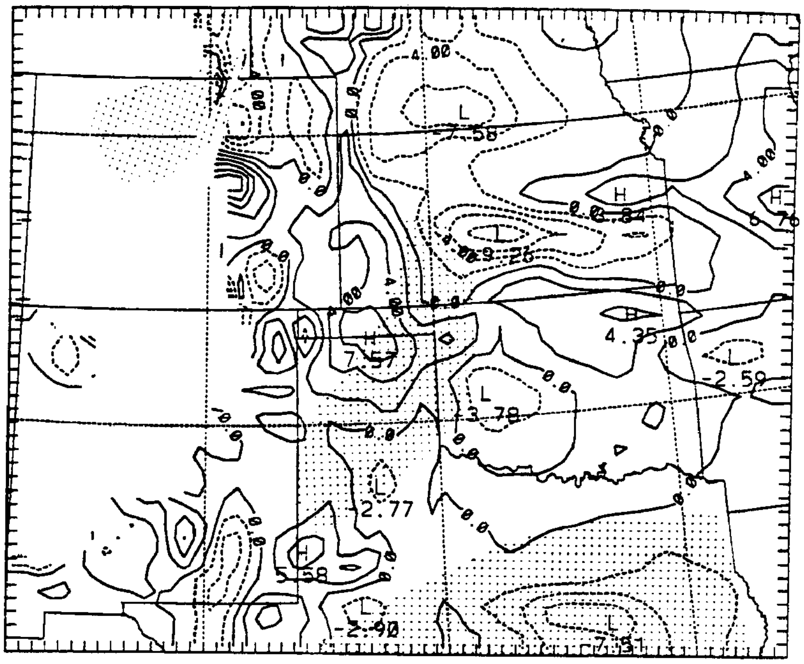

Figure 4.4: Moisture divergence (10^{-7} s^{-1}, with a contour interval of 2 x 10^{-7} s^{-1}, with negative values dashed) on the 800 mb surface at 3/1200. Areas with wind speeds greater than 10 m s^{-1} are lightly stippled.

track of the actual MCS1. Convergence in this region was enhanced by the LLJ.

For a Baiu case over Japan, Ninomiya *et al.* (1988) suggested that moist symmetric instability or slantwise convection led to local enhancement of upward motion and the triggering of upright convection above the frontal surface. Negative moist potential vorticity (MPV) (which indicates moist symmetric instability if the airmass is also saturated (Bluestein 1993)) was located along the frontal surface (Fig. 2.24b) and may have played a role in triggering the upright convection. Although Lindstrom and Nordeng (1992) developed a slantwise convective parameterization for MM4, Kuo and Reed (1988) showed that MM4 can explicitly simulate the slantwise motions. While the CTL simulation might have produced some slantwise motion, it seems most likely that convergence at the northern tip of the LLJ in a region of enhanced moisture was the most probable cause for the initiation of the modeled MCS1 convection.

Detailed output from the KF scheme showed that the Kansas convection fed on air above the surface layer. The base of the updraft source layer was at 773 mb with a Lifting Condensation Level (LCL) of 750 mb and a CAPE of 2200 J kg^{-1}. Fig. 4.5 shows profiles of the parameterized convective heating and drying for a point in Kansas with active convection at 1456 UTC. Convective heating is found from the LCL to cloud top with a maximum heating rate of 173° K day^{-1} in the upper troposphere. The heating profiles resemble those shown by Kain and Fritsch (1990, their Fig. 11). Below cloud base, considerable cooling is found along with moistening near 940 mb where the downdraft detrains. The downdraft does not extend to the surface, but ends two model levels above the surface. Strong surface outflows were not observed with MCS1 (e.g. Nachamkin 1992) – winds gradually responded to the pressure gradient between the mesohigh and the wake low (Green 1989). At this model grid point, the downdraft originated at 513 mb and became positively buoyant just below 900 mb.

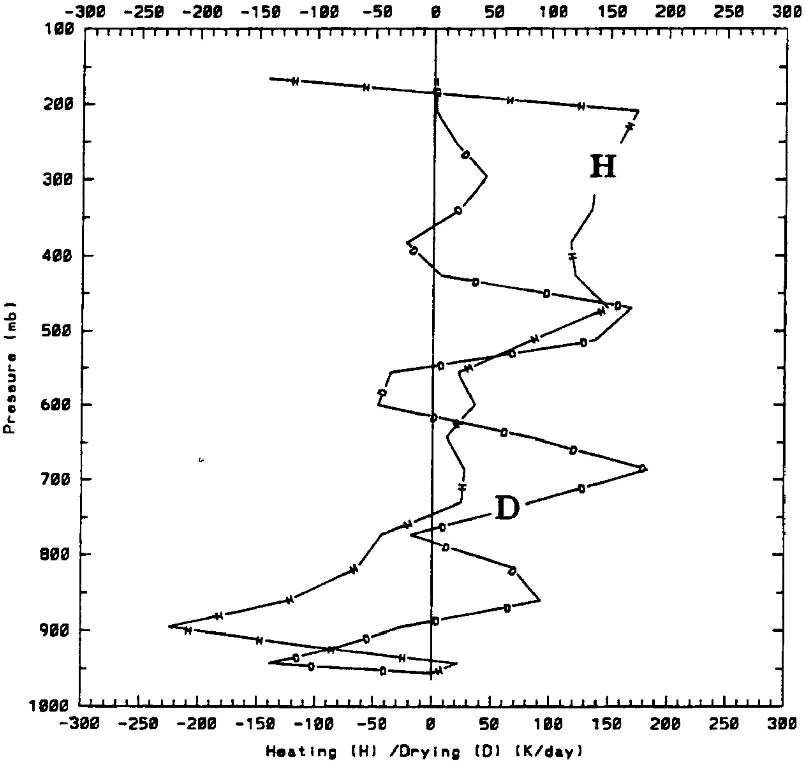

Figure 4.5: Vertical profiles of convective heating (H) and drying (D) (° K day^{-1}) from the CTL run for a point in central Kansas, 176 minutes into the simulation (1456 UTC). The solid line drawn along 0° K day^{-1} begins at the surface pressure of this grid point, 964 mb.

Between 3/1500 and 3/1600 the convective rain area across Kansas propagated or moved to the ENE at 24.4 m s^{-1} . A negligible amount of explicit rainfall was produced during this time. By 1700 UTC, the rain area began to move due east accompanied by only 0.1 mm of explicit rain. By 1800 UTC, the system was moving ESE at 15 m s^{-1} . Between 3/1300 and 3/1800 the center of the MCS1 radar echo had an average movement from 245° at 30 m s^{-1} . After 3/1900, the system was observed to turn toward the ESE. Fig. 4.6 shows the simulated rainfall for the three-hour period ending 3/1800. The location of the rainband across central Kansas (Fig. 4.6a) closely matches observations (Fig. 4.6b), but the simulated amounts are smaller than observed. Part of this discrepancy may be due to comparison of point rainfall measurements with the grid-averaged simulated rain, while there might also be a systematic under-prediction of convective rain amounts by the modified KF scheme (caused in part by the removal of only 50% of the available buoyancy (Zhang and Fritsch 1986a)). The location of the integrated rain water maximum (shown later), the integrated cloud water maximum and the one-hour convective rainfall tendency (not shown), closely matches the observed location of MCS1 (Fig. 2.16g). All convection associated with the MCS continued to be based well above the surface with LCLs between 760 and 710 mb, however there was a slight decrease in CAPEs as the system moved east, from 2200 J kg^{-1} when the system was in central Kansas to about 1850 J kg^{-1} when it was in southeast Kansas.

The circulations forced by the simulated convective system were similar to previous studies (e.g. Fritsch and Maddox 1981b) with divergent outflow above 350 mb, convergence and strong ascent in midlevels, and cool divergent outflow below cloud base (but above the surface). The 850 mb ω field at 3/1800 (Fig. 4.7) shows a narrow area of intense upward motion to the east and south of the precipitating downdraft. Downward motion was most intense within the small explicit rain area, but also extended to the west in the wake of the system. The lifting on the eastern edge of the system triggered new convection. One characteristic of the simulated MCS1 was its small area of explicit rain relative to the observations. Fig. 4.8 shows the 3/1800 integrated rain water field. While the maximum rain water mixing ratios might be expected near the core of the system, radar observations

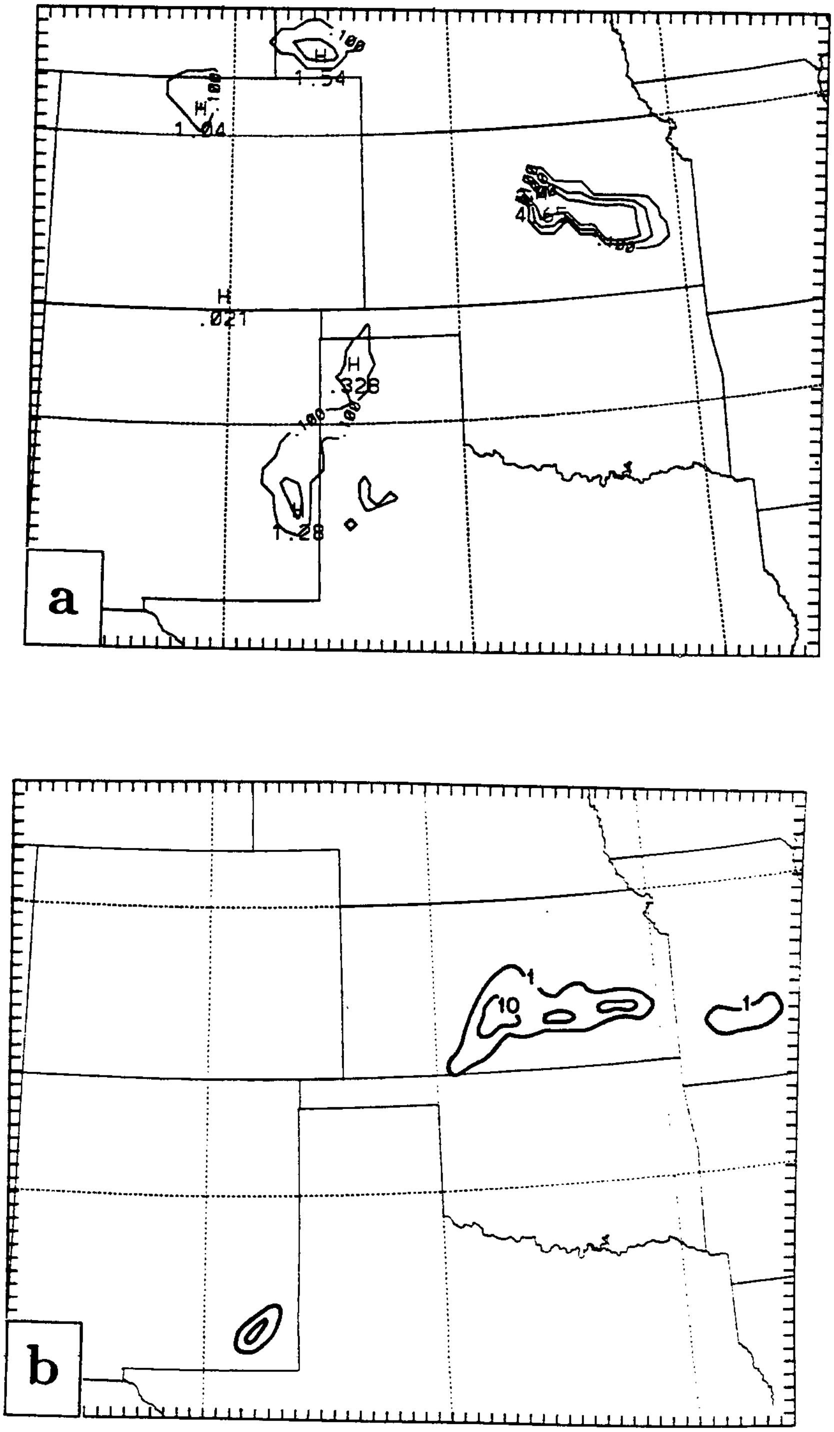

Figure 4.6: Simulated convective rainfall, with an uneven contour interval 0.1, 1, 2, 5, and 10 mm a), and observed rainfall with isopleths of 1 and 10 mm b) for the three-hour period ending 3/1800.

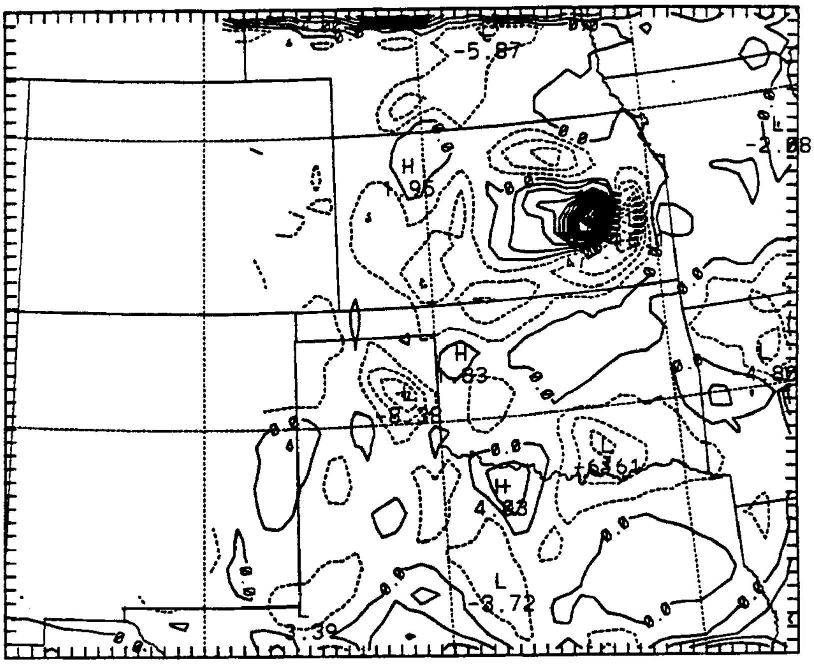

Figure 4.7: Simulated 850 mb ω (μb s^{-1}) at 3/1800. Contour interval is 2 μb s^{-1} .

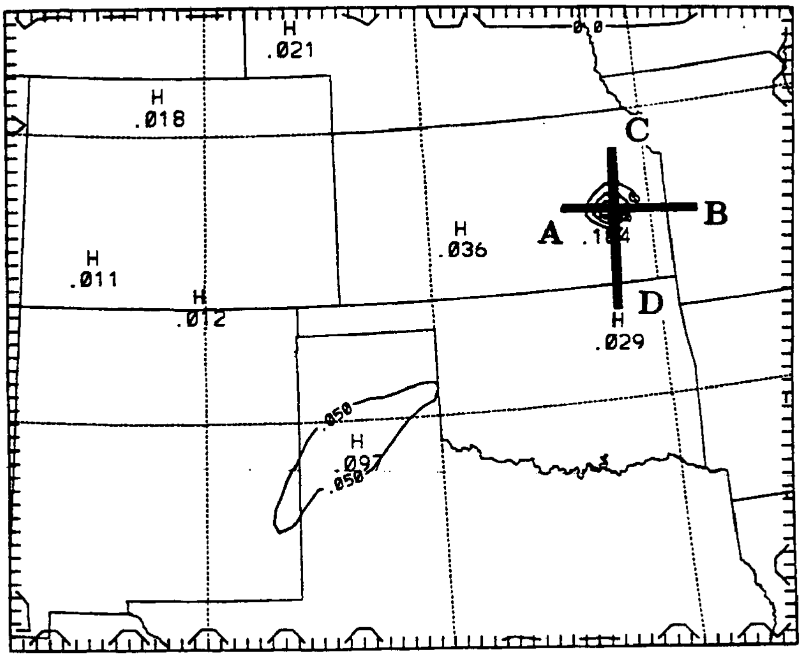

Figure 4.8: Simulated column-integrated rain water (g kg^{-1}) at 3/1800. Contour interval is .05 g kg^{-1}. Lines A–B and C–D indicate cross-section locations.

show an extensive stratiform region covering most of northeast Kansas, north and east of the active convection. The model does not produce this extensive stratiform region. Cross sections through the system were taken to examine the system's structure in more detail and to help explain the lack of stratiform precipitation.

A west-to-east cross-section of cloud and rain water fields through MCS1 at 3/1800 is shown in Figure 4.9a. The synoptic-scale processes leading to grid-scale saturation usually develop slowly so that large areas of explicit rain early in the model run occur in response to the saturation induced by the convective parameterization (e.g. Molinari and Dudek 1992). The saturation induced by the implicit parameterization takes a finite amount of time to develop, so the explicit hydrometeors lag the parameterized convection. The effects of active convection within the simulated MCS1 can be inferred by the high mixing ratios of cloud water at both upper and lower levels. (The heating due to the convective parameterization is not routinely output by the model and so wasn't directly analyzed except for selected grid points and times, however the area with active implicit convection is indicated in Fig. 4.9a). The upper cloud water maximum occurs where the parameterized convection detrains moisture and the airmass becomes saturated. The absence of cloud water near 300 mb is a result of the strong heating (and thus low relative humidities) produced by the KF scheme at that level (as shown in Fig. 4.5). The maximum rain water mixing ratios (actually snow above the 0° C level – about 650 mb) are located near 575 mb, within the active convection region. Some snow appears to have been advected downstream (toward the right of the figure) as the mixing ratios drop off slowly toward the east. Thus, it appears the simulated MCS1 has developed a leading anvil. The melting level at 650 mb can be seen as a kink in the rain water isopleths. Rain water mixing ratios decrease as the precipitation falls due to the combined effects of fallspeed separation and melting (Dudhia 1989). Explicit rain is reaching the ground through much of the core of the system (about 100 km wide), but there is little trailing anvil. Cloud water is found in low levels to the east of the system in the saturated cold airmass.

A cross-section of θ and ω (Fig. 4.9b) shows that the updraft is slightly tilted with a lower-level maximum (near 900 mb) about one grid distance (25 km) east of the upper

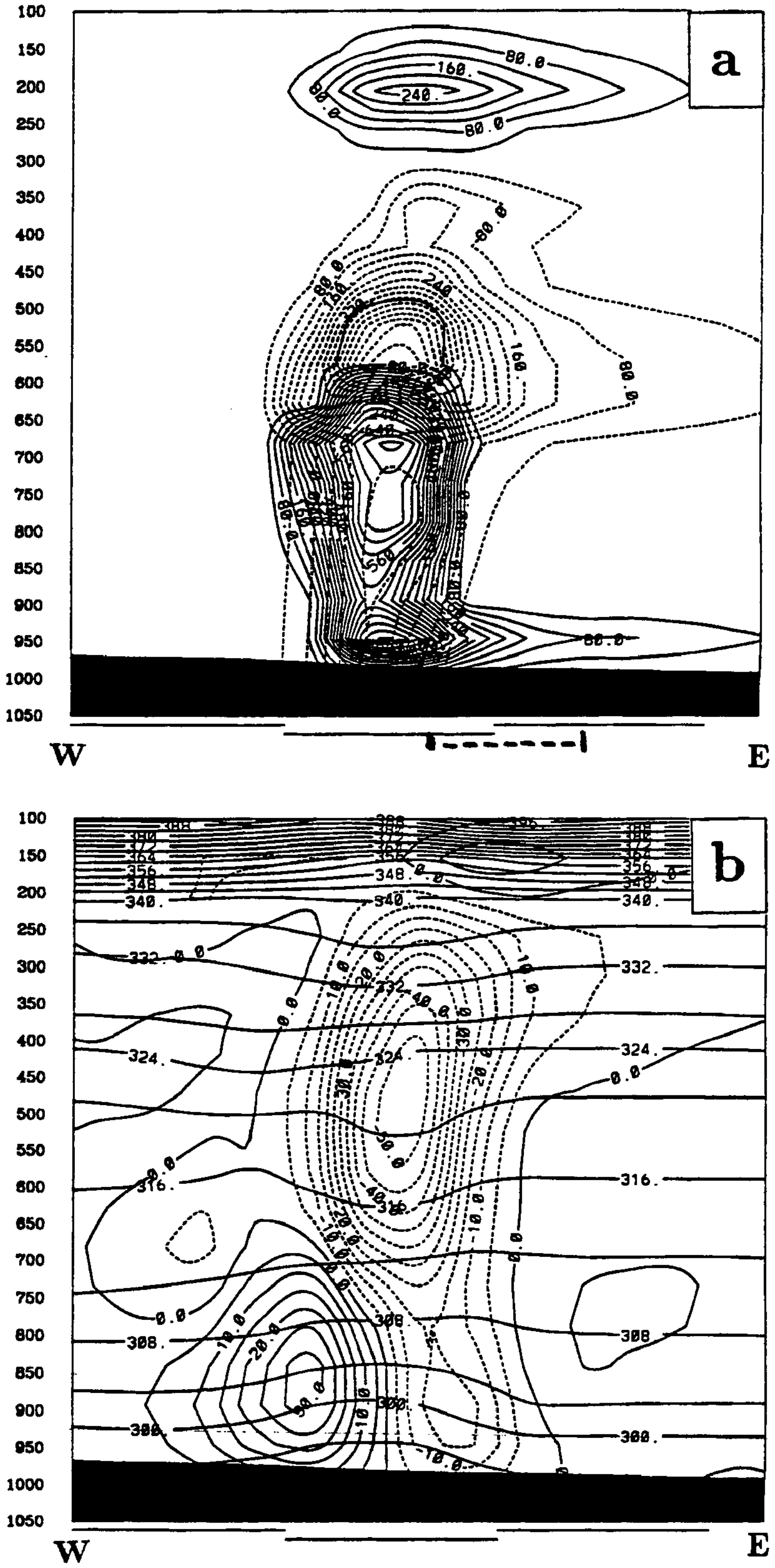

Figure 4.9: West-east cross section at 3/1800 along the line A–B in Fig. 4.8 of a) cloud water (mg kg^{-1} contoured every 40 mg kg^{-1}, solid) and rain water (mg kg^{-1} contoured every 40 mg kg^{-1}, dashed) and b) θ (° K contoured every 4° K, quasi-horizontal solid lines) and ω (μb s^{-1} , contoured every 5 μb s^{-1} negative values are dashed, positive are solid). The line segments along the bottom of the cross-section represent 100 km. The portion of the cross-section with active implicit convection is indicated by the heavy dashed line in a).

maximum. Intense heating near the -55 μb s^{-1} updraft maximum is indicated by the downward displacement of the θ surfaces. Cooling beneath the rain system is indicated by the upward bulge in the θ surfaces. The θ surfaces are also deformed near the tropopause, suggesting cooling in the lower stratosphere. The downdraft behind the system also has two maxima, one at 875 mb and one at 450 mb, farther to the west. The 450 mb downdraft maximum (near the level of the maximum updraft) may be due to blocking effects. A cross-section of the total wind speed (not shown) reveals a distinct minimum in wind speed from 400 to 150 mb just upwind of the strong updraft. Doppler-derived horizontal winds at 8.9 km above sea-level (near 300 mb) within MCS1 at 3/1716 shows maximum speeds on the northern and southern flanks of the system, suggestive of blocking (Nachamkin 1992). The lower downdraft maximum is at the back edge of the explicit rainfall. Ahead of the system is a weak area of downward motion.

A cross-section plot of the relative circulation in the plane of the cross section (calculated by subtracting out the simulated system motion of 290° at 15 m s^{-1}) along with θ_E is shown in Fig. 4.10a. Several interesting features are revealed by this plot. The cool, stable low-level air (where $\partial\theta_E/\partial p$ is < 0) does not enter into the deep circulation. Low-level air to the east of the system rises slightly, passes through the rain area and then descends to the rear, roughly paralleling the θ_E contours. This is nearly identical to the result found by Buzzi *et al.* (1991) in their 2-D modeling study of organized convection in the presence of a near-surface inversion. They found that this apparent separation of the low-level flow from the rest of the convective circulation was actually quite complex. When Buzzi *et al.* replaced the stable layer with solid ground, the convective organization was substantially different, suggesting that the low-levels play an important role, perhaps as a sink for downdraft air. In contrast to the results of Buzzi *et al.* (1991) and Zhang *et al.* (1989), MCS1 does not exhibit a front-to-rear circulation behind the system and only has the weakest of rear-to-front (rear inflow) circulations. Air entering the system from the east between 850 and 700 mb ascends and by the 550 mb level begins to turn back toward the east. All the relative winds at and above 450 mb are directed from rear to front. This result explains why MCS1 (both observed and simulated) had no significant

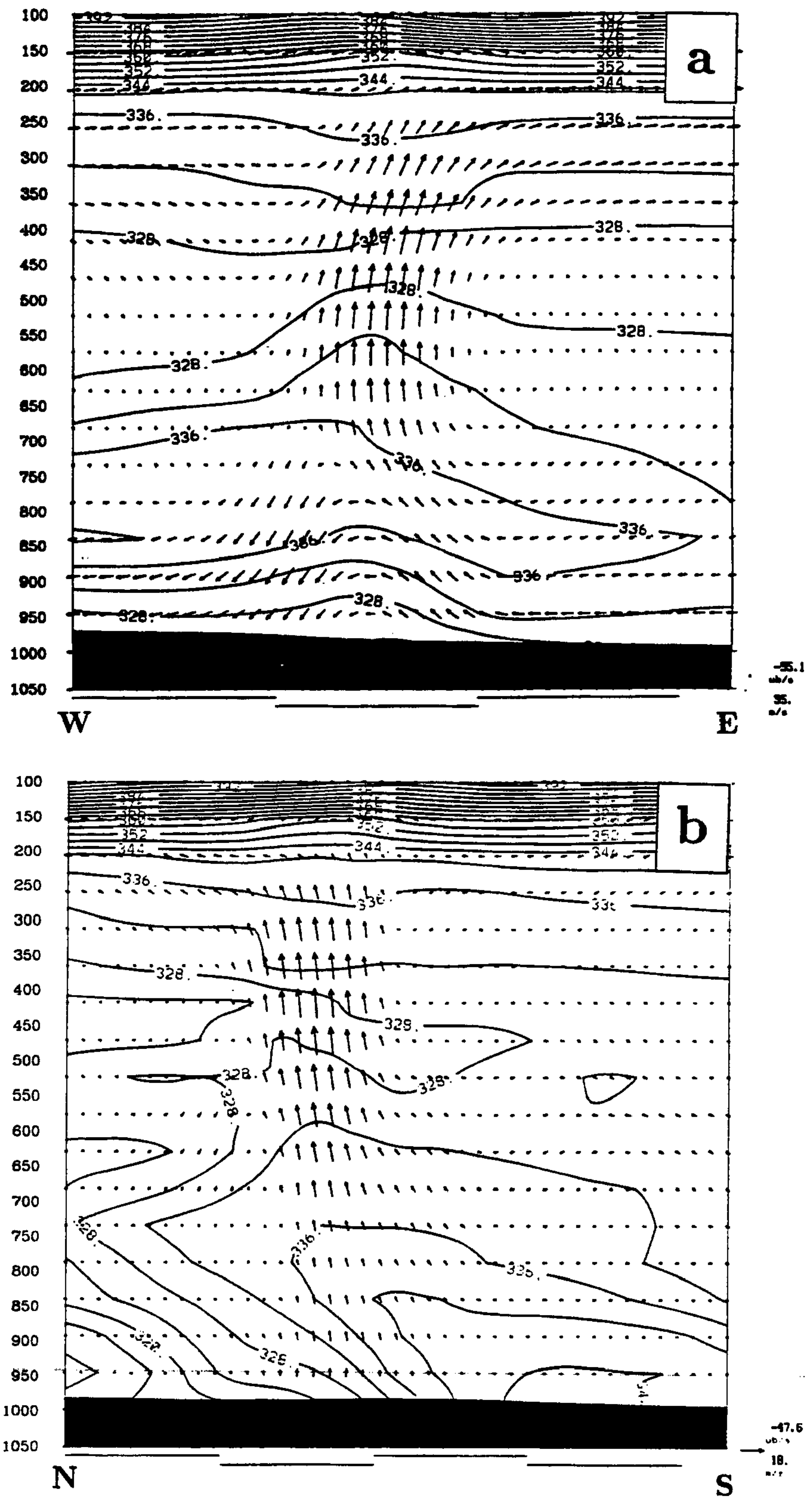

Figure 4.10: Cross section at 3/1800 a) along the line A–B in Fig. 4.8 of relative circulation in the plane of the cross section (vectors, scale at the bottom right) and θ_E (° K contoured every 4° K) and b) along the line C–D n Fig. 4.8 of actual circulation in the plane of the cross section (vectors scale at the bottom right) and θ_E (° K contoured every 4° K).

trailing stratiform region. However, the relative flow within the convective core is very small below 300 mb (where the highest hydrometeor mixing ratios are found). This helps explain the narrowness of the simulated explicit rain area. Hydrometeors produced in the saturated convective core remain there because of the weak relative flow. Thus, the explicit rain closely follows the parameterized convection. In addition, because the parameterized convection does not directly produce hydrometeors, but indirectly causes the explicit scheme to generate them after mesoscale saturation is reached (thereby disregarding the seeder-feeder process (e.g. Rutledge and Houze 1987)), hydrometeor production would slightly lag the convection. The weak rear to front flow then would advect the hydrometeors toward the convection keeping the two in lock-step (as long as the convection continued propagating in the direction of the mean shear vector). The time lag between explicit precipitation production and when it falls to the surface keeps the downdraft from interfering with the inflow to the convection.

The system-relative flow patterns are determined by the propagation of the convection and the ambient shear profile. Houze *et al.* (1990) found that systems with large leading-line/trailing stratiform regions had large cross-line shears. Asymmetric systems were found to have large along-line shear (Houze *et al.* 1990). In this case, there is little directional shear above 600 mb (e.g. Fig. 2.26a). Speeds increase greatly above 500 mb to the jet level, effectively preventing a front to rear flow from developing for any reasonable convective propagation speed. As pointed out by Dudhia *et al.* (1987) and Buzzi *et al.* (1991), the ambient shear thus exerts a subtle control on the convective dynamics.

A north-south cross-section of θ_E and circulation along the segment C-D in Fig. 4.8 is shown in Fig. 4.10b. (The circulation in Fig. 4.10b is of actual winds, but, since the cross-section is nearly perpendicular to the system propagation, these winds can be thought of as relative to the system). The figure shows that the system is feeding on high-θ_E air riding up over the frontal surface from the south. Again, as in Fig. 4.10a the system is only about 100 km wide and the strong updraft is nearly vertical. There is a slight tilt of the updraft to the north, with detrainment of cloud water to the north of the system from 350 mb to the tropopause level (near 200 mb). Downward motion is found to the north of the system (which is characteristically much weaker than the updraft, only reaching 8 μb s^{-1}). The wind cross-section plots show that inflow air enters the system from the south and east above the frontal surface, rises near vertically through the core of the system and exits at upper levels to the north and east.

Because of the relative flow through the system, it might be expected that hydrometeors produced in the convective towers would be advected to the north and east, leading to the development of a stratiform region. Observations show that while MCS1 was not highly organized, strong convection was located along the southern flank of the system with mostly stratiform precipitation with some embedded convection to the north (Nachamkin 1992). MM4's convective parameterizations do not produce hydrometeors directly, but induce mesoscale ascent and saturation leading to hydrometeor production by the explicit scheme. In the 10-11 June case (Zhang *et al.* 1989) each grid point that the squall line passed, first had deep, surface-based convection followed by explicitly-modeled stratiform rain. The MM4 simulation produced a smooth transition from the leading convective line to the trailing stratiform region. In contrast, some locations within MCS1 that observed stratiform rain never experienced deep convection. The failure of the model to develop a realistic stratiform region, therefore, might be related to deficiencies in the precipitation parameterizations as suggested by Molinari and Dudek (1992) – the most significant shortcoming being the lack of transfer of hydrometeors from the parameterized convection to the grid scale.

Through 1900 UTC, the simulated MCS1 continued to move toward the ESE, but had slowed to 14 m s^{-1} . At 1853 UTC, convection began south of MCS1, along the surface front, south of the Kansas-Oklahoma border. This convection was surface-based, very vigorous (with a CAPE of 3630 J kg^{-1}) and close to the observed convective development south of MCS1 shown in Fig. 2.16h. Convection also began southeast of MCS1 in southern Missouri at 1813 UTC. A similar band of convection was observed by radar beginning at 1829 UTC (not shown). During the next two hours, vigorous surface-based convection developed in the model along the surface front in northern Oklahoma and back-built to the southwest, south of PNC. Meanwhile, the convection associated with MCS1 in southeast Kansas weakened and died. In reality, the convection triggered near the surface front south of MCS1 expanded in size only slightly, moved northward and merged into the southern flank of the system. Fig. 4.11 shows the simulated and observed rainfall for the three-hour period ending at 2100 UTC. It can be seen that the convective rain area in northeast Oklahoma is distinct from the rain area in southeast Kansas associated with MCS1 (Fig. 4.11a). (The rain area in southeast Kansas is coherent in space and time and is identified, following the guidelines described earlier, as MCS1). No precipitation was observed during this period in northern Oklahoma (Fig. 4.11b). The erroneous development of convection in northeast Oklahoma appears to have intercepted the supply of high θ_E to MCS1, resulting in the decay of the simulated convection.

What was the origin of the convection along the surface front? Fig. 4.12 shows the vertical profile of θ_E and saturated θ_E for the point in northern Oklahoma where deep convection first developed. The LCL of the surface parcel was 920 mb, below which the air was well-mixed as indicated by the near-constant θ_E . Near 900 mb, the airmass was saturated. Higher up, a deep negative area was present extending to above 700 mb. The FCT temperature perturbation, based on the vertical velocity at the LCL, was large enough to allow the cloud parcel to be buoyant through the deep cap. A time series of the θ_E profiles shows that the cap was actually strengthening during this period, but the low-level convergence and upward motion also increased, offsetting the inhibition. Fig. 4.13 shows profiles of several variables at this grid point at 3/1840, 13 minutes before convection began. Fig. 4.13a reveals upward motion through most of the troposphere, peaking in low levels. This low-level upward motion was increasing with time (not shown). The wind speed profile (Fig. 4.13b) was unremarkable, although as mentioned earlier speeds increased significantly above 500 mb. Mid-level hydrometeors (Fig. 4.13c) were generated by lifting of a near-saturated layer over Oklahoma as shown in the OKC profile (Fig. 2.26d). Cloud water (Fig. 4.13d) was present at cirrus level as well as at low levels, where the intense lifting due to surface convergence along the front brought the airmass to saturation. The convection along the front in Oklahoma seems to be a result of the increase in convergence along the front (possibly enhanced

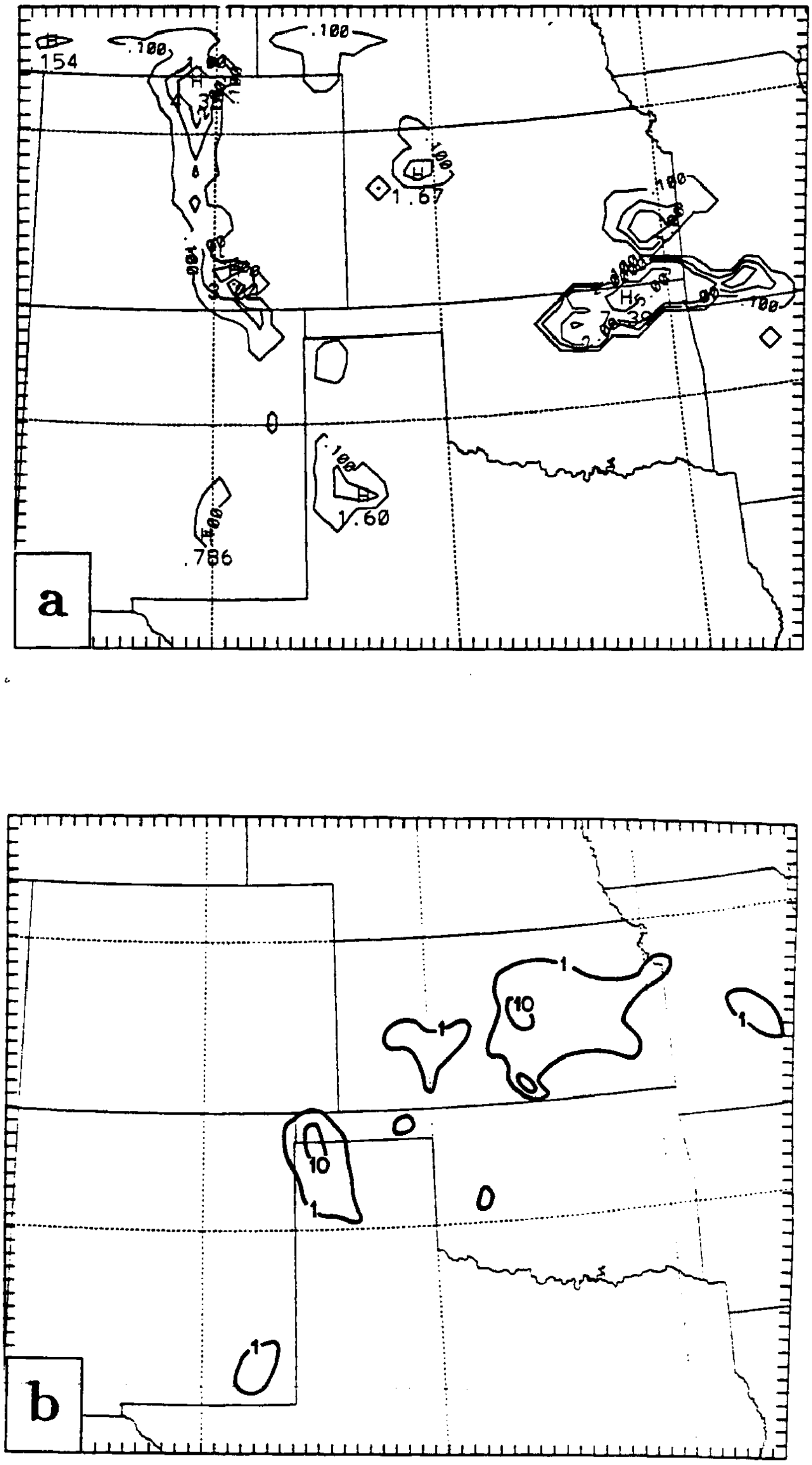

Figure 4.11: As in Fig. 4.6, but for the period ending 3/2100.

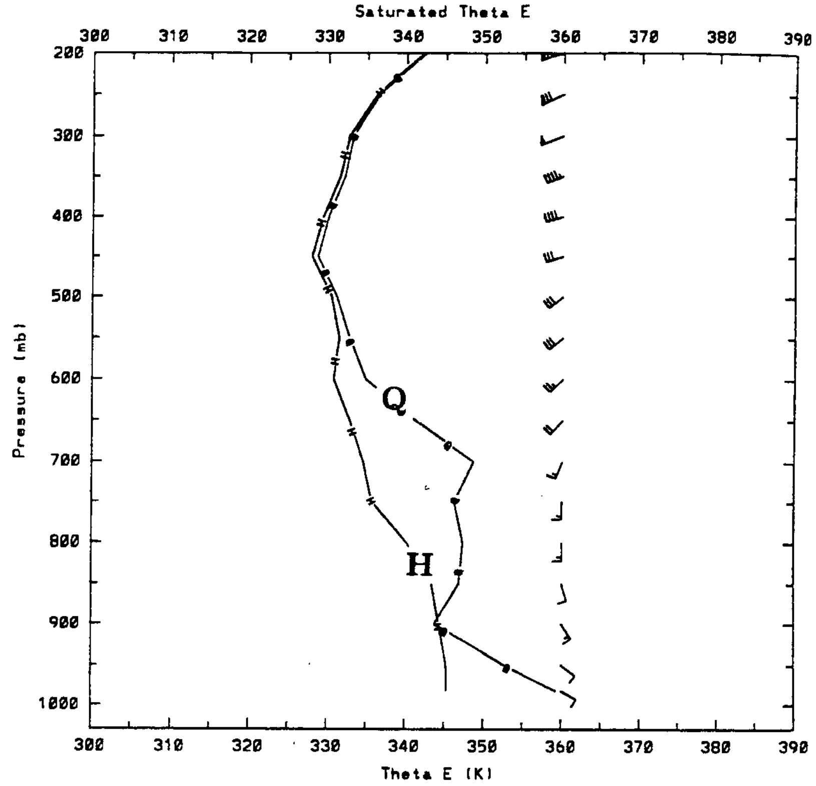

Figure 4.12: Vertical profile of θ_E (curve H) and saturated θ_E (curve Q) (in ° K) for a grid point along the surface front in northern Oklahoma at 3/1840.

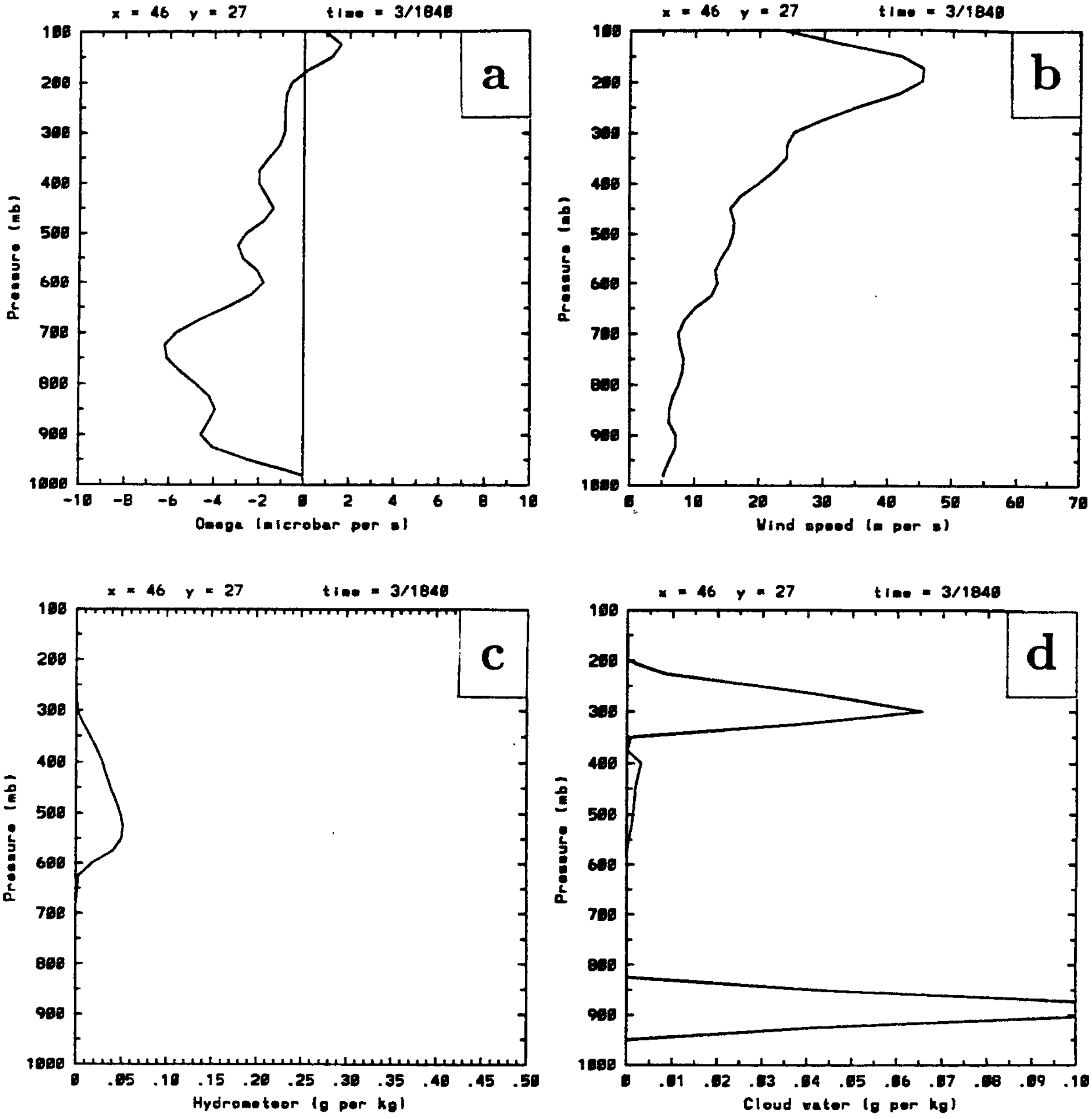

Figure 4.13: Grid point profiles from the same point as in Fig. 4.12 at 3/1840 of a) ω (μb s^{-1}), b) wind speed (m s^{-1}), c) hydrometeors (g kg^{-1}), and d) cloud water (g kg^{-1}).

by outflow from MCS1) which caused lifting sufficient to activate the FCT and overcome the cap. It is difficult to determine why actual convection did not occur in this region. Sounding observations from HOY were not available. It seems most likely that the strong cap prevented deep convection from forming. Surface observations indicated extensive low clouds (broken to overcast) were present in the region which may have reduced surface heating. In addition, the strong vertical wind shear would have tended to destroy any weak updrafts that may have started (Doswell 1985). Further tests will be described in Chapter 5.

By 2200 UTC, the precipitation area previously associated with MCS1 had dissipated, producing a maximum of only .35 mm of explicit rain in west-central Missouri (not shown). Convection continued along the surface front from S of PNC to UMN. As pointed out by Fortune (1989), MCS1 actually survived for several more hours crossing Missouri into Kentucky.

Fig. 4.14 presents a sequence of sea level pressure (SLP) plots. Initially, (Fig. 4.14a), a low was near CNM with a trough extending northeastward into Missouri. A rather smooth easterly gradient was across Kansas. The early part of the numerical simulation was characterized by large changes in the SLP as the model tried to attain a balanced state. By 3/1300 (not shown), the main SLP low was located northeast of LBB, where the warmest initial low-level temperatures were found. The warm low-levels in the AMA sounding (Fig. 2.26b) were adjusted away during the early part of the model forecast (not shown). At 3/1500 (Fig. 4.14b) the low near AMA had filled by 3 mb since 3/1300 and the true synoptic low in southeast New Mexico was apparent. The slight kink in the isobars over Kansas was in response to the new MCS1 convection. By 3/1700 (Fig. 4.14c), a closed high pressure isobar was beneath MCS1 and at 3/1800 (Fig. 4.14d) was a pronounced mesoridge. The mesohigh reached its maximum extent at 3/1900 (Fig. 4.14e). The wake low (or trough) behind MCS1 analyzed by Nachamkin (1992) or Green (1989) was not as pronounced in the model. Because the wake low is closely associated with the MCS stratiform region (e.g. Stumpf *et al.* 1991), the constricted simulated stratiform area did not force the development of a rear inflow jet and wake low.

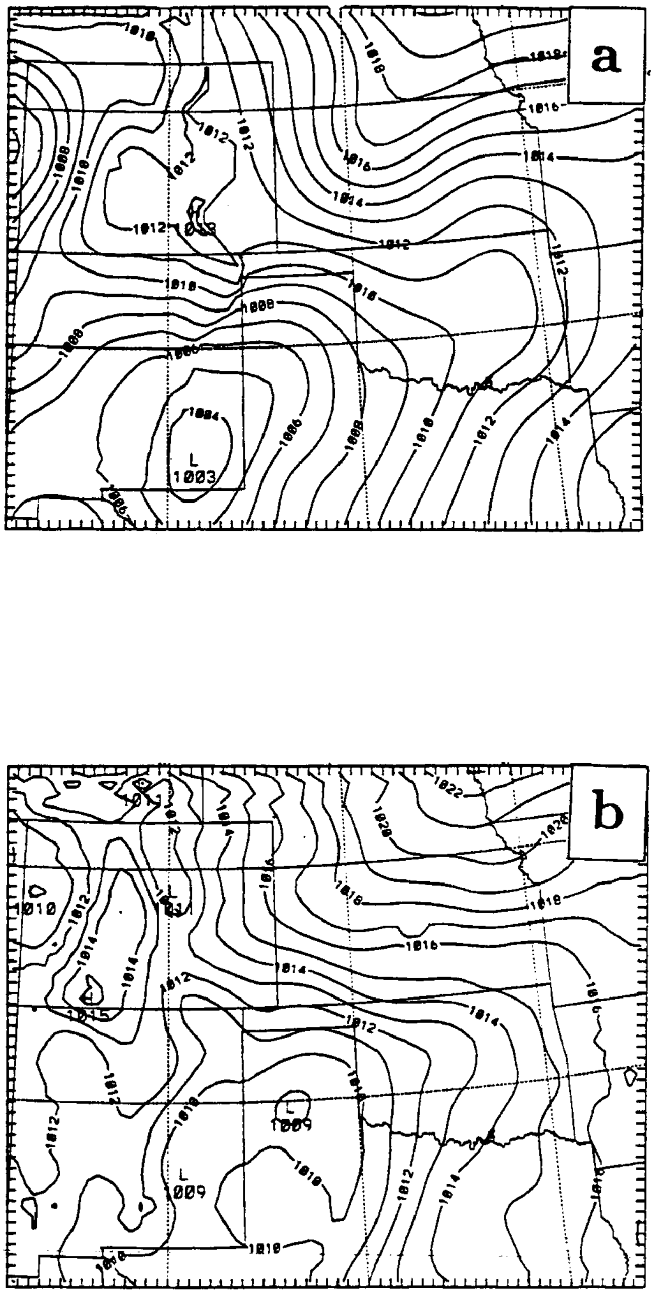

Figure 4.14: Sea level pressure (mb, contoured every mb) valid at a) 3/1200 (the initial analysis), b) 3/1500, c) 3/1700, d) 3/1800, e) 3/1900, f) 3/2100, and g) 4/0000.

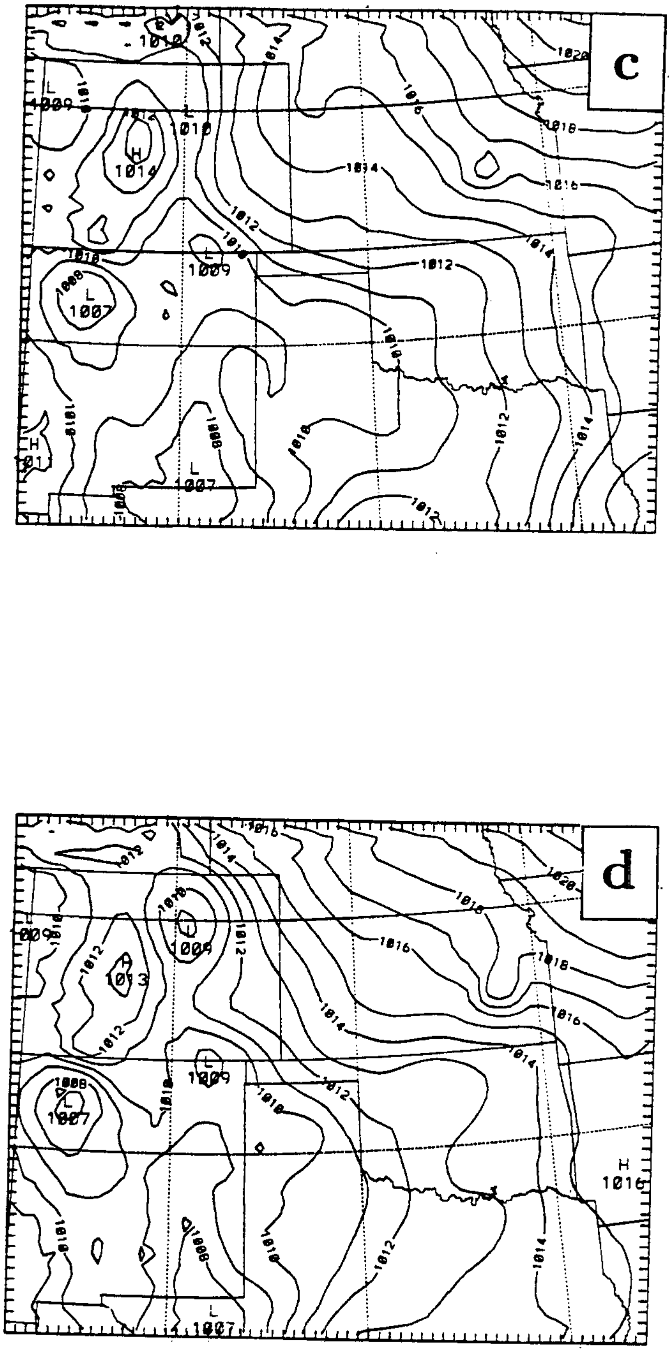

Figure 4.14: Continued.

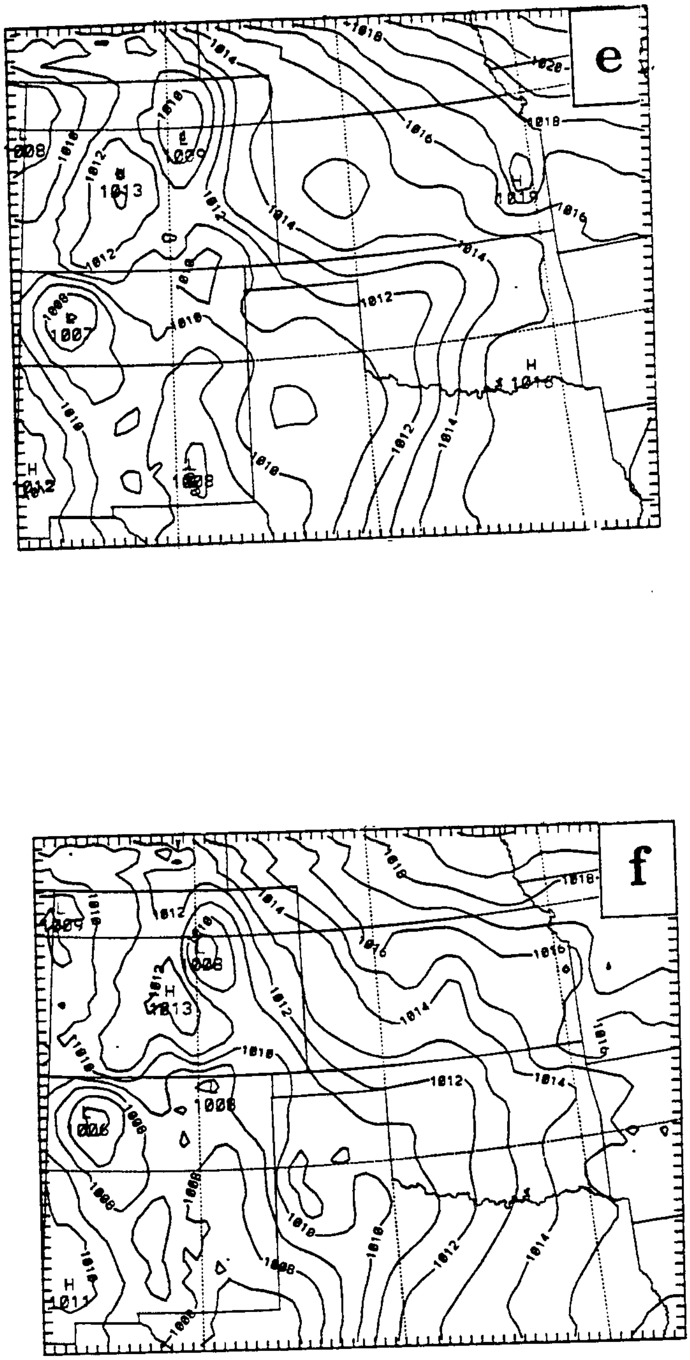

Figure 4.14: Continued.

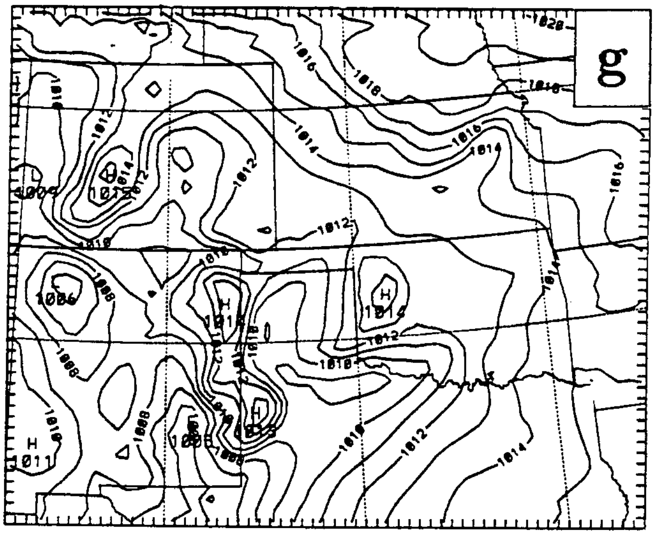

Figure 4.14: Continued.

The SLP pattern at 3/2100 (Fig. 4.14f) was rather chaotic. A tiny mesohigh and wake low along the Kansas-Missouri border was associated with the decaying explicit precipitation of MCS1. The pressure trough in central Kansas was in the wake of a mid-level explicit rain area caused by large-scale ascent. No implicit rain was associated with this feature. Strong descent and divergence was found from 600 mb to 900 mb beneath this rain area with the maximum warming at 800 mb. At 4/0000 (Fig. 4.14g) the SLP pattern contained a trough across eastern Kansas and several mesohighs beneath convective rain areas in Oklahoma, Texas, and New Mexico. Further discussion will be presented in the following section.

4.3 Evolution of MCS2

The first model convection associated with MCS2 began at 1429 UTC in west Texas. This was about 100 km northeast and one-half hour later than the observed first convection in satellite imagery (Fig. 2.16d). Figure 4.3a shows that by 1500 UTC only about .2 mm of rain had reached the surface. The LCL of this convection was modeled to be near 550 mb with CAPEs of only 240 J kg^{-1}. With such a high cloud base and weak instability, precipitation production was small and there was considerable melting and evaporation before the precipitation reached the surface.

During the first hour of the simulation (results not shown), midlevel ascent within the high-humidity airmass in eastern New Mexico and west Texas led to the production of snow and ice by the explicit moisture scheme. The explicit precipitation continued to grow in area and amount before convective rain began. It is not readily apparent what the source of the upward motion was. At 1400 UTC considerable convergence and upward motion was found between 700 and 600 mb over this region and a weak shortwave could be detected in the wind and height field at 700 mb. Divergence over this region existed between 500 and 250 mb. The speed convergence associated with the 200 mb jet streak (Fig. 2.22) led to strong convergence, downward motion and negative absolute vorticity at this level over the precipitation area. The vorticity patterns over west Texas and eastern New Mexico were also complicated. A 12 x 10^{-5} s^{-1} vorticity maximum at 700 mb was near ABI, southeast of the precipitation area. At 500 mb, a maximum vorticity axis was over the Texas panhandle, within the rain area. It appears though, that the cyclonic vorticity within the precipitation (from 600 to 300 mb) was a response to the latent heating.

During the next three hours, the model convection over west Texas drifted northeast and weakened, disappearing by 1800 UTC. A separate area of convection developed over eastern New Mexico by 1600 UTC and was in a northeast-southwest oriented line by 1800 UTC from eastern New Mexico to the Texas panhandle. Rainfall amounts were very small with this convection (Fig. 4.6a), mostly less than 0.1 mm with a maximum of 1.3 mm in eastern New Mexico. The convection continued to be based above 600 mb, with considerable evaporation occurring below cloud base.

Two factors may have led to the re-formation of convection to the west of the original rain area. First, the upper level jet streak initially near ELP moved northeast and rapidly dissipated south of LBB, re-forming over eastern New Mexico by 1600 UTC. This will be examined in detail later. Second, the explicit precipitation at midlevels led to downward motion below cloud base due to melting and evaporation. This created an environment unfavorable for convective development. Fig. 4.15 shows the integrated rain water (Fig. 4.15a) and the convective rain for the one-hour period ending at 3/2000 (Fig. 4.15b). Except for a small overlap in Texas, the convective rain was occurring to the south and east of the explicit rain. (Only .05 mm of explicit rain had reached the ground during this one hour period – the integrated rain water was mostly above 700 mb). Beneath the explicit rain area, strong downward motion was found (from 600 mb to the surface, not shown) which would prevent the trigger function from activating any implicit convection in this region.

The three-hour rain for the period ending 3/2100 (Fig. 4.11a) showed a maximum of 1.6 mm near LBB. This convective area continued to be on the southeast periphery of the explicit rain area. Fig. 4.16a shows a heating profile for a typical grid point in this rain region. Cloud base was near 600 mb, with a CAPE of only 300 J kg^{-1}. Cooling due to downdrafts extends from the cloud base down to the surface. Such weak convection with large subcloud evaporation led to small precipitation amounts.

Fig. 4.17 shows the three-hour convective rain for the period ending 4/0000. The area and amount of simulated convection increased greatly during this period (Fig. 4.17a). Other studies using the FC scheme and trigger function show a marked increase in convection near the time of maximum surface heating (e.g. Kain and Fritsch 1992; Zack *et al.* 1985). The heating of the boundary layer produces many areas where a parcel is unstable according to the FC scheme. The highest rain amounts were found in the eastern Texas panhandle extending into west-central Oklahoma, along the surface front in northeast Oklahoma, in north-central Kansas, eastern New Mexico, southeast Colorado, and in north-central Colorado. Significant, explicitly-resolved precipitation had reached the surface in north-central Kansas, north-central Colorado and eastern New Mexico (not shown). In general, the model overpredicted the areal extent of the rainfall and underpredicted the amounts. Observations indicate (Fig. 4.17b) the separate precipitation areas of MCS1 and MCS2 with almost no rainfall in Texas and Oklahoma aside from the panhandles. Rainfall

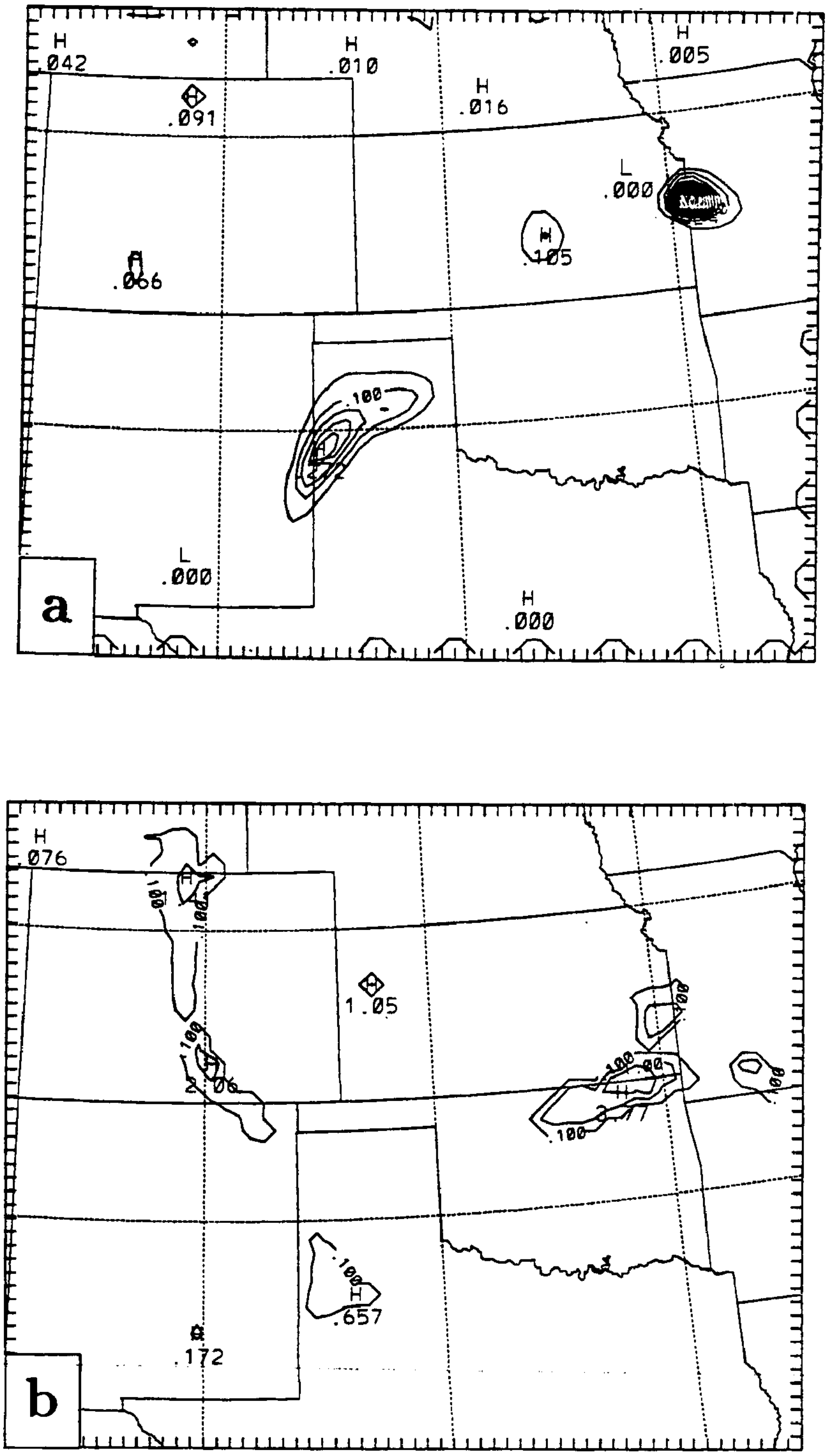

Figure 4.15: Integrated rain water as in Fig. 4.8, but for 3/2000 (a) and as in Fig. 4.3a, but for the one-hour convective rainfall tendency for the period ending 3/2000 (b).

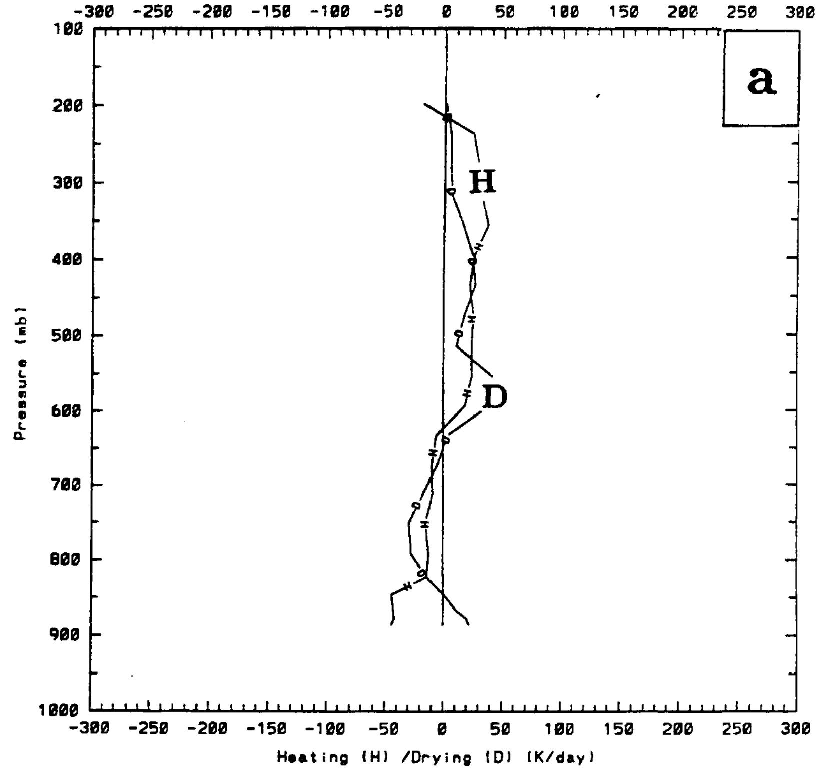

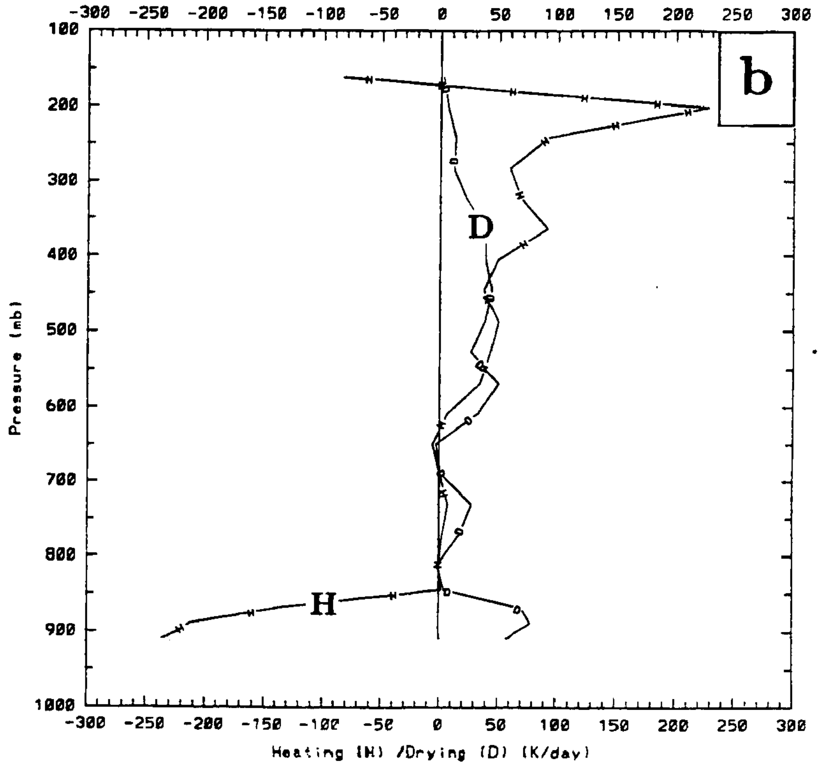

Figure 4.16: As in Fig. 4.5, but at 3/2100 for a point a) within the high-based rain area of MCS2 and b) within the deeper convection over the Texas panhandle.

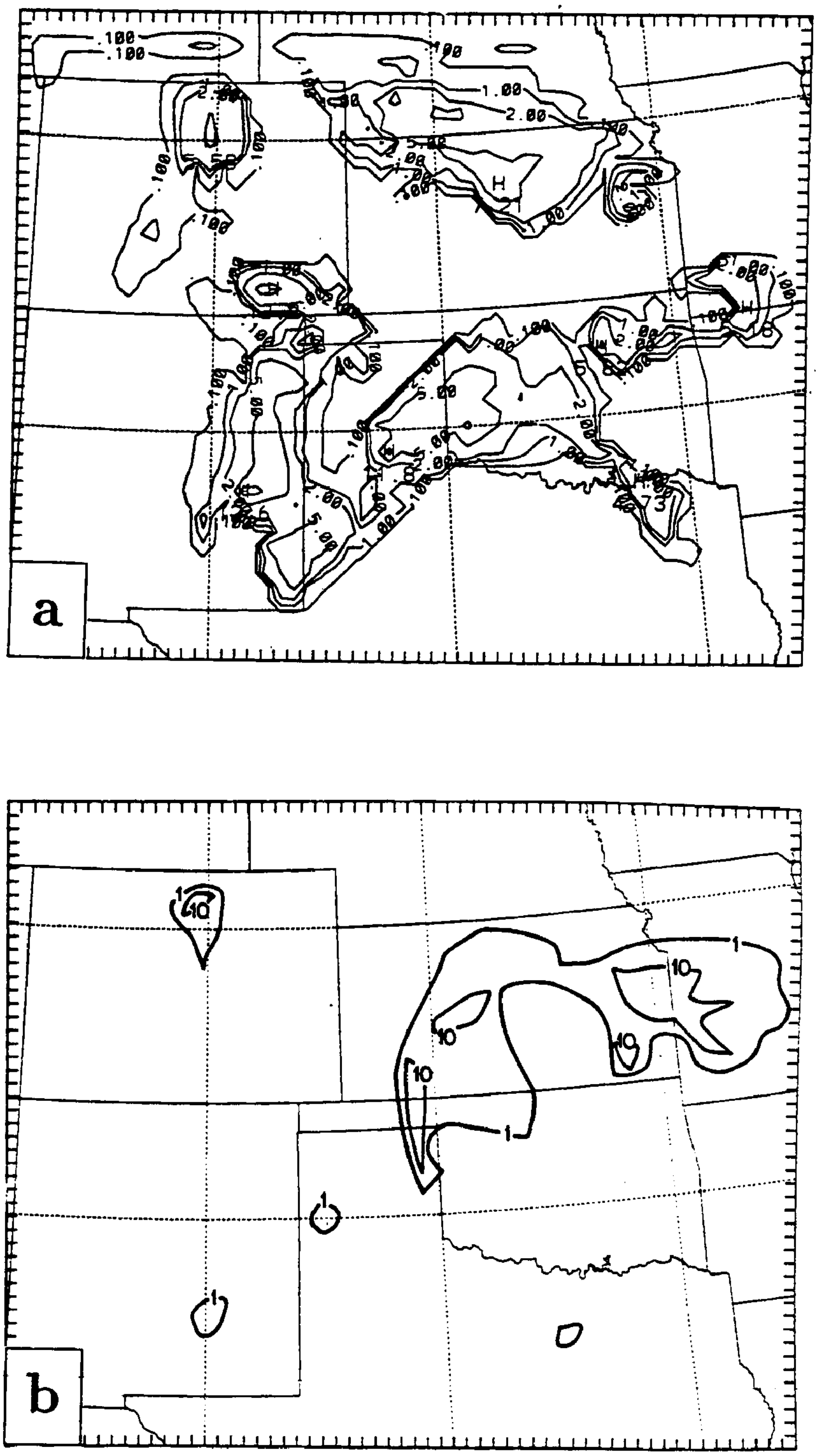

Figure 4.17: Convective rainfall, as in Fig. 4.3, but for the period ending 4/0000.

was not observed in southeast Colorado. An area of model convection occurred along the southeast New Mexico-Texas border similar to the observed convection associated with MCS3 (Fig. 2.16l). The model convection in east-central New Mexico was close to the origin of MCS4 (Fig. 2.1), but was clearly overdone. There was an east-west oriented area of simulated rain in north-central Kansas, similar to the observed ENE-WSW band. Also, the northeast-southwest band of rain in the eastern Texas panhandle and western Oklahoma was similar to the north-south observed band there, but the rainfall gap across southern Kansas is another major shortcoming of the simulation. A more detailed analysis of the simulated precipitation areas follows.

At 2100 UTC deep convection began southeast of AMA. Fig. 4.16b shows the heating profile for the first point with deep convection in the Texas panhandle. The updraft source air was the layer between 820 and 760 mb with a LCL of 776 mb. The convection was quite vigorous with a CAPE of 3625 J kg^{-1}. The heating profile is typical of those produced by the KF scheme for deep midlatitude convection, (e.g. Kain and Fritsch 1990, Fig. 11), but note the strong downdraft cooling of nearly 250 K day^{-1} at the surface. Zhang and Fritsch (1986a) and Kain and Fritsch (1990) explain that the strong warming aloft is caused by compensating subsidence of the stable layer near the tropopause. This convection appeared to be triggered as the high-based rain area moved into a region with greater instability. Ryan *et al.* (1990) show that evaporative cooling beneath high stratiform clouds (as well as evaporative and radiative cooling at cloud top) can help initiate and organize squall lines. Fig. 4.18 presents the 850 mb water vapor (q_v) and 800 mb ω fields at 2100 UTC. An upward motion area (Fig. 4.18b) (with a minimum of -11.3 μb s^{-1}) was found where the deep convection began. This was adjacent to an area where 850 moisture was pooled with q_v exceeding 14 g kg^{-1} (Fig. 4.18a). Note that to the northwest of the upward motion area was a northeast-southwest oriented band of strong downward motion. This downward motion was beneath the explicit rain area and effectively shut off the possibility of parameterized deep convection there.

During the next hour, vigorous convection spread across the eastern Texas panhandle to the Oklahoma border. Beneath this convection a strong cold pool formed and by 2300

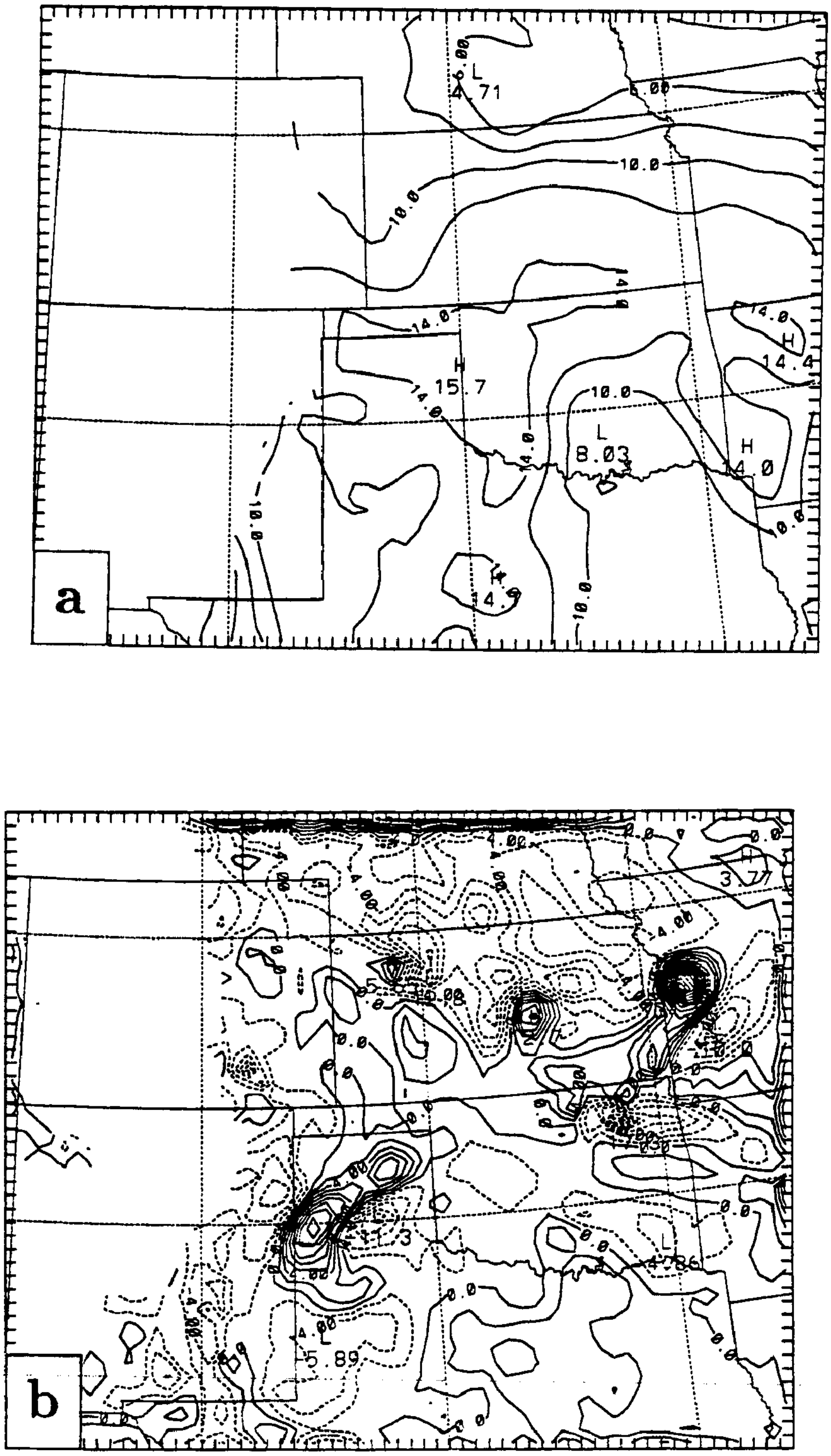

Figure 4.18: Simulated a) 850 mb water vapor (q_v, g kg^{-1} contoured every 2 g kg^{-1}) and b) 800 mb ω ($\mu b\ s^{-1}$ contoured every 2 $\mu b\ s^{-1}$, negative values are dashed) valid at 3/2100.

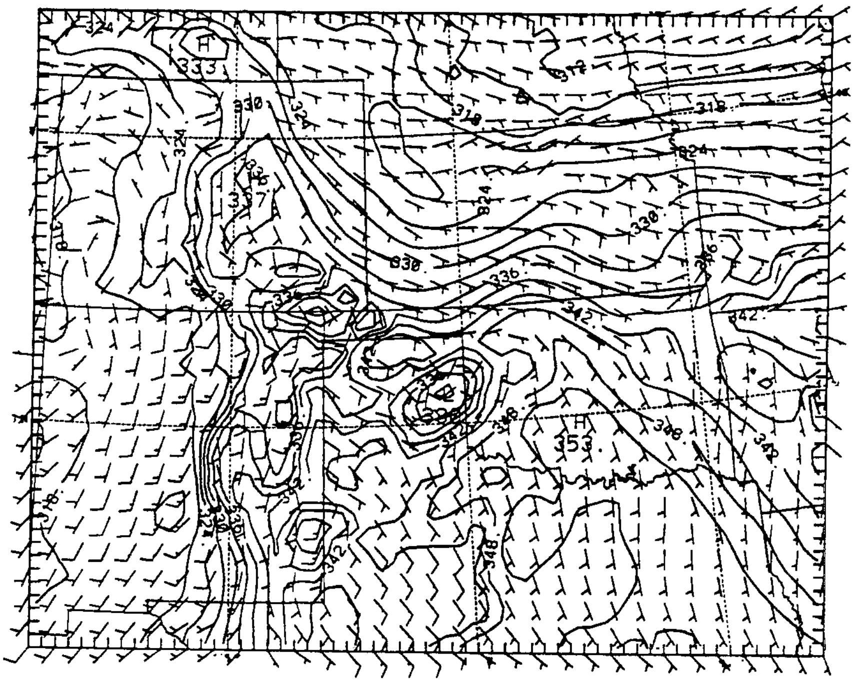

Figure 4.19: Equivalent potential temperature (θ_E , K) and winds at the lowest model layer, valid at 3/2300.

UTC (Fig. 4.19) an outflow boundary with maximum winds of 12 m s^{-1} was in extreme western Oklahoma. This is similar to the analysis presented by Stumpf (1988) (although his analyses showed more northerly surface winds with a mesohigh located just north of the Kansas–Oklahoma border). By 4/0000, the leading edge of the outflow boundary was near WWR.

Smull and Augustine (1993) found that the shear parallel and shear perpendicular rainbands within MCS2 (which merged together to resemble an occluded cyclone, Fig. 2.2) were due to a short-lived superposition of independent features and not due to dynamic processes associated with the MCS as postulated by Fortune (1989). The numerical simulation supports those results. In fact, the two rain areas in the model never intersect. The lack of simulated precipitation across southern Kansas during this time may be due to a combination of factors: the strong subsidence beneath the midlevel explicit rain area, the failure of the model to reproduce the observed northward movement of the surface front into southern Kansas (perhaps due to the deficiencies in the simulation of MCS1), the Kansas rainband and its accompanying circulation developing too far north, and the tendency for the FCT to overdevelop convection on the southern end of convective regions. Although the relative contributions of these factors are not known, the results point to the extreme difficulty in simulating SCCs with current models and observations.

Fig. 4.20 shows the minimum LI at hour 11 of the simulation. The most unstable air (with LIs less than -6° C) was ahead of MCS2 (except for a small area in southwest Kansas) along the Kansas-Oklahoma border where the most vigorous convection actually occurred. However, model convection never developed there. Fig. 4.21 shows the 850 mb ω field at 3/2300. Upward motion is within and ahead of the convective line in western Oklahoma as well as across northern and central Kansas. Downward motion is found within and behind the convective rain area, across the Oklahoma panhandle and southern Kansas. Fig. 4.22 shows the 500 mb hydrometeor mixing ratios at this time. The snow mixing ratio approaches 0.7 g kg^{-1} over the Oklahoma panhandle. Fig. 4.23 shows a grid point profile of several model variables from a point in the Oklahoma panhandle just northwest of GAG. The model never developed convection at this point, while radar observations showed that

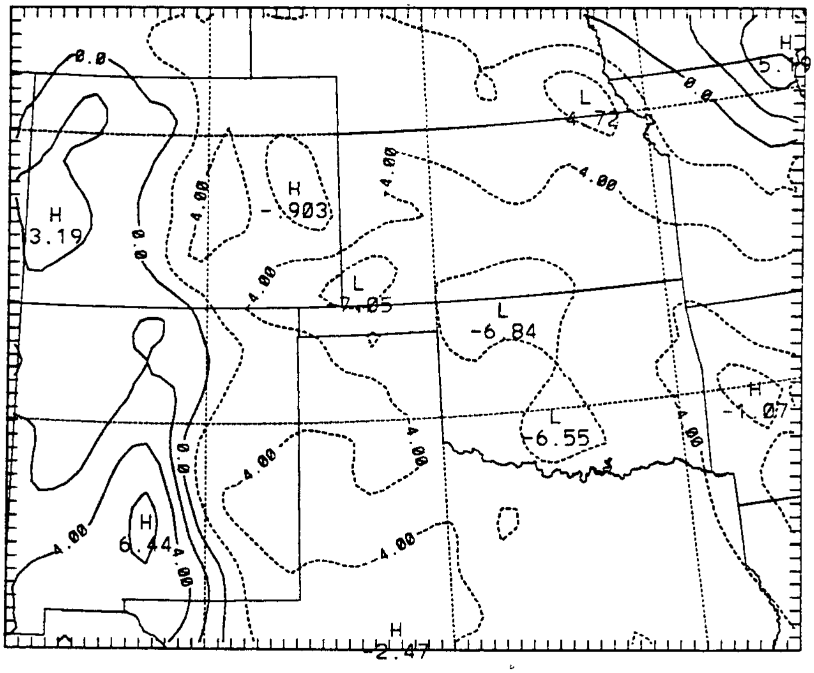

Figure 4.20: Minimum lifted index (as in Fig. 2.23a) valid at 3/2300.

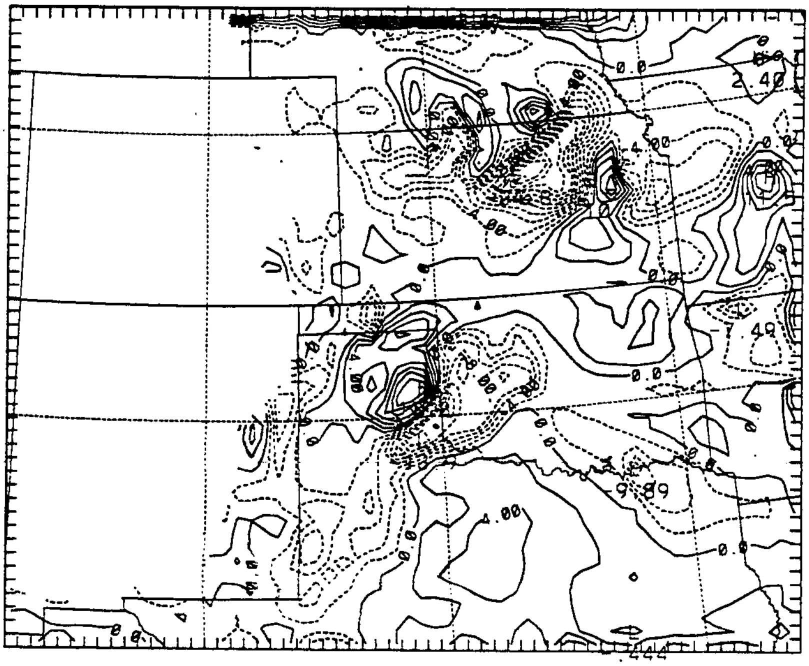

Figure 4.21: Vertical velocity, as in Fig. 4.18b but for 850 mb valid at 3/2300.

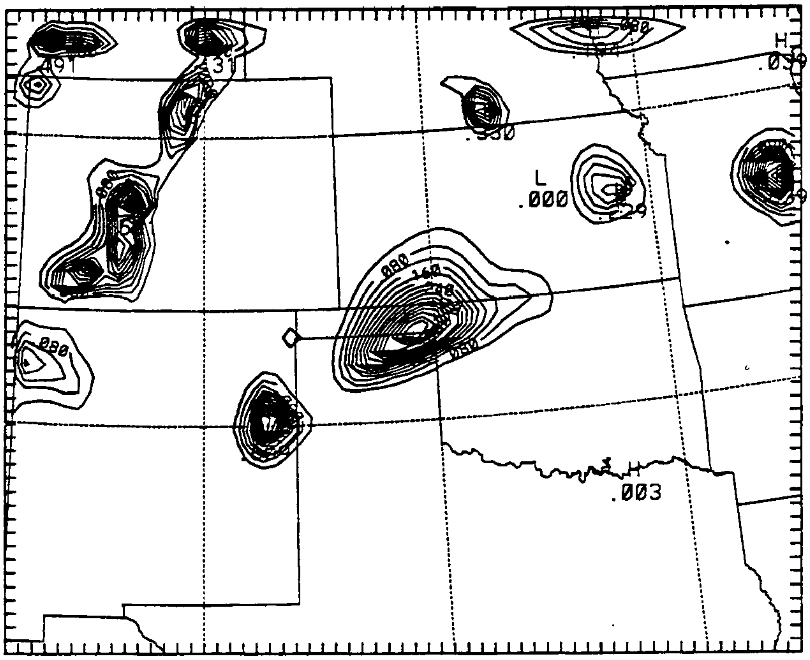

Figure 4.22: Simulated rain water mixing ratio (g kg^{-1} contoured every .04 g kg^{-1}) at 500 mb for 3/2300.

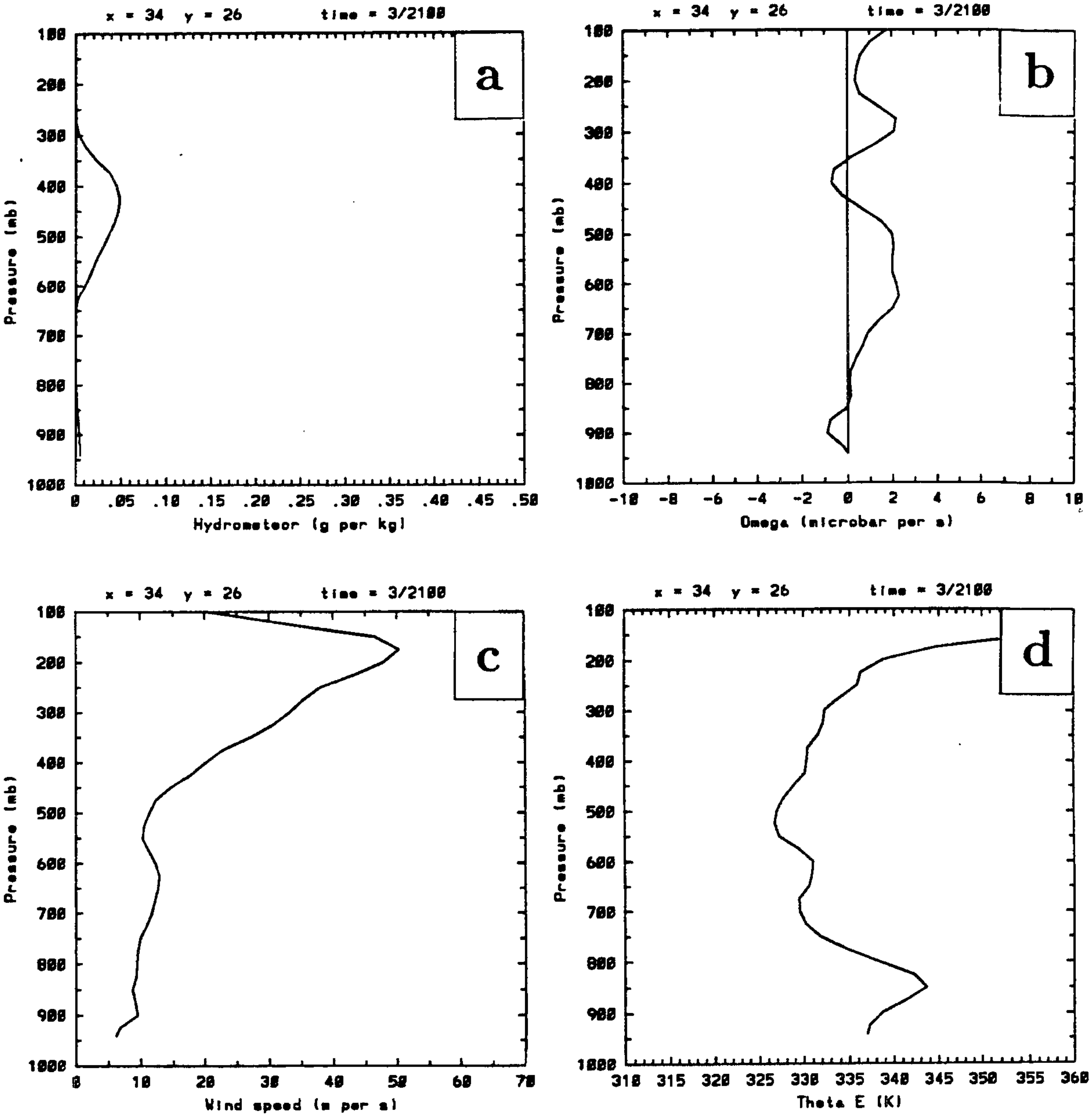

Figure 4.23: Grid point profiles from a point in the eastern Oklahoma panhandle at 3/2100 of a) hydrometeors (g kg^{-1}), b) ω (μb s^{-1}), c) wind speed (m s^{-1}), and d) θ_E (K).

strong echoes passed over this location between 2000 and 2300 UTC (not shown). At 2100 UTC (Fig. 4.23a) hydrometeor contents were low, having just begun to advect over or develop at the grid point. The corresponding vertical motions were weak (Fig. 4.23b), with a small area of upward motion near the surface and around 400 mb with sinking elsewhere. No pronounced LLJ was indicated (Fig. 4.23c). The θ_E profile suggests a considerable amount of instability was present above the low-level inversion (Fig. 4.23d). By 3/2300 (Fig. 4.24a), a large amount of snow was present all of which melted and evaporated before reaching the surface. No hydrometeors were found below 800 mb. The vertical velocities had increased dramatically along with the explicit precipitation area, exhibiting strong downward motion below 500 mb (containing near constant θ_E values between 500 and 750 mb) with strong rising motion above 500 mb (Fig. 4.24b). The low-level θ_E maximum had increased since 3/2100 and despite the slight warming near 500 mb, still exhibited considerable convective instability (Fig. 4.24d). However, the strong mesoscale downdraft prevented the convective trigger function from being activated and so the most unstable air over this region remained untapped.

By 4/0000, the 850 mb ω field reflects two separate precipitation bands (Fig. 4.25a). The north-south oriented area of rising motion across central Oklahoma was forced by low-level convergence of convective outflow. The WSW-ENE band of rising motion across eastern Kansas coincided with convergence along the precipitation band, but there was no strong cold pool there. The corresponding RAWINS analysis making use of the NMC first guess field and all available NWS and PRE-STORM supplemental observations is shown in Fig. 4.25b. It can be seen that the simulated upward motion areas are remarkably similar to the observed. The simulated peak upward motion values are more than double those analyzed, but as described in Chapter 3, the analysis is interpolated from the 75 km grid and so would have broader peaks. The model has failed to generate the strong subsidence in the wake of MCS1 in southern Missouri (since the simulated MCS1 had vanished) as well as the strong sinking behind MCS2 in western Kansas. Both of the subsidence areas are associated with the stratiform regions of the systems, which the model failed to generate. The model does have strong subsidence along the Oklahoma-Texas panhandle border and between the two upward motion centers, which was not analyzed.

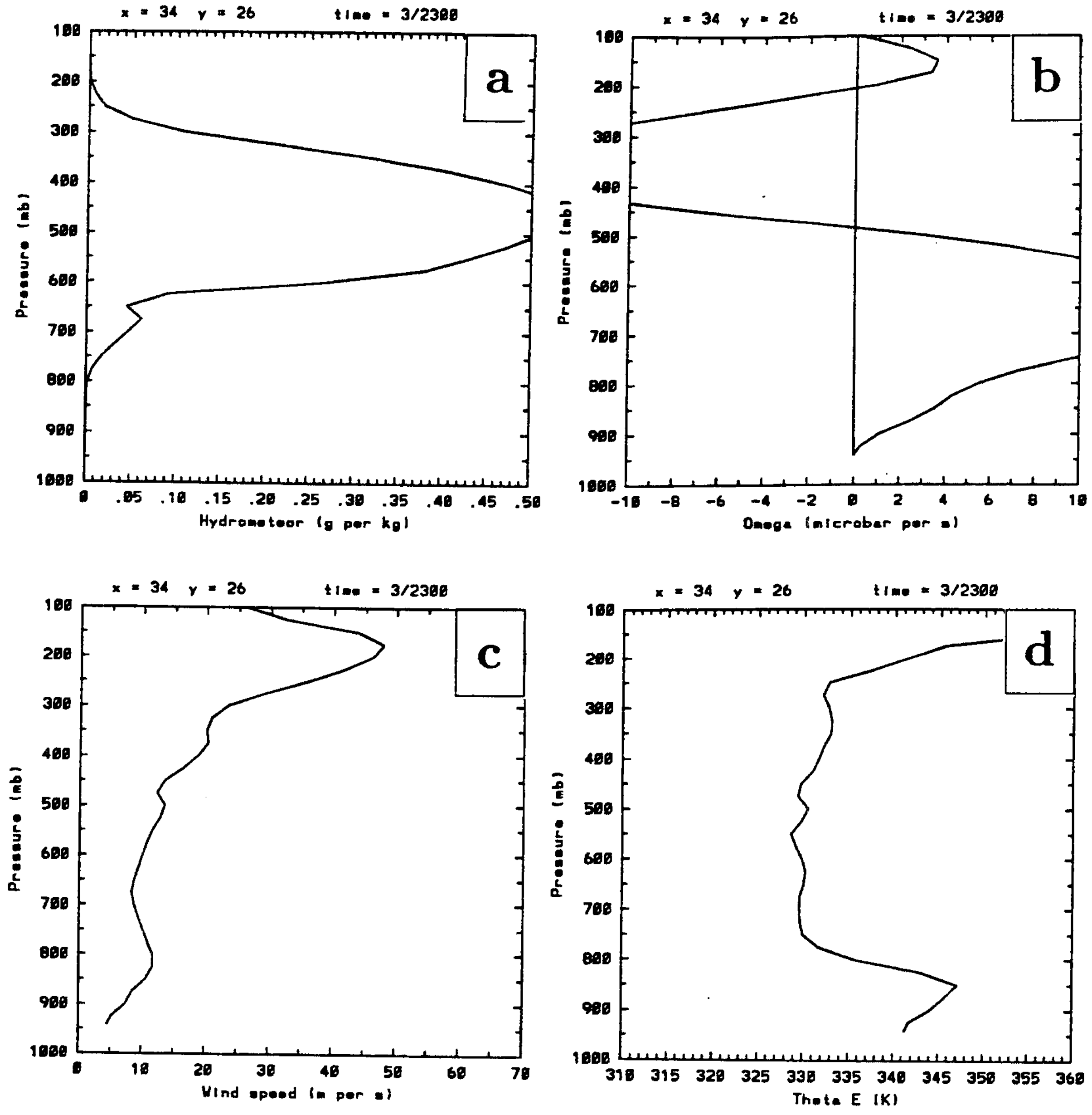

Figure 4.24: As in Fig. 4.23, but for 3/2300.

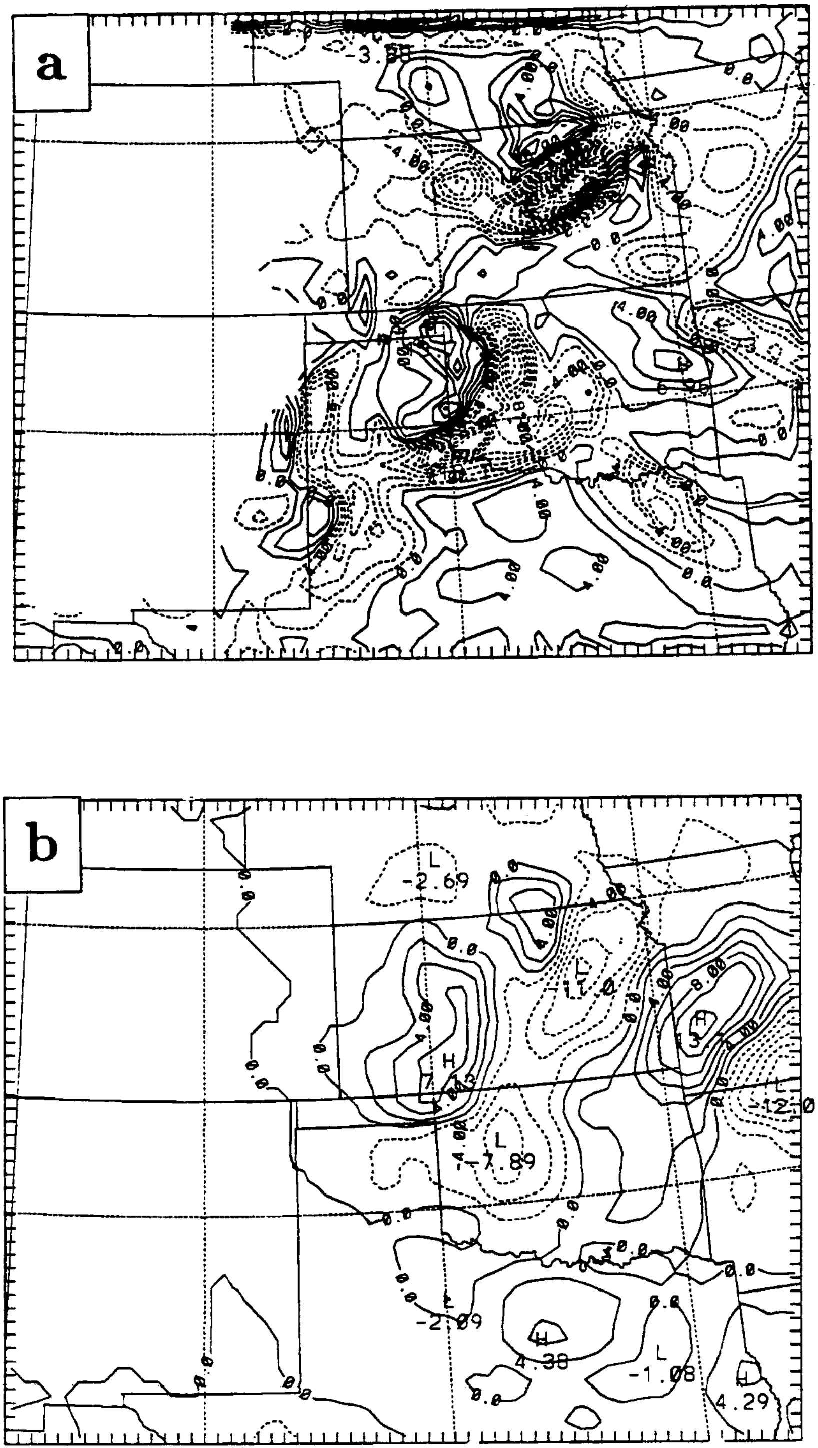

Figure 4.25: 850 mb ω (contoured every 2 μb s^{-1} , upward motion is dashed) at 4/0000 from a) the CTL simulation and b) the RAWINS analysis.

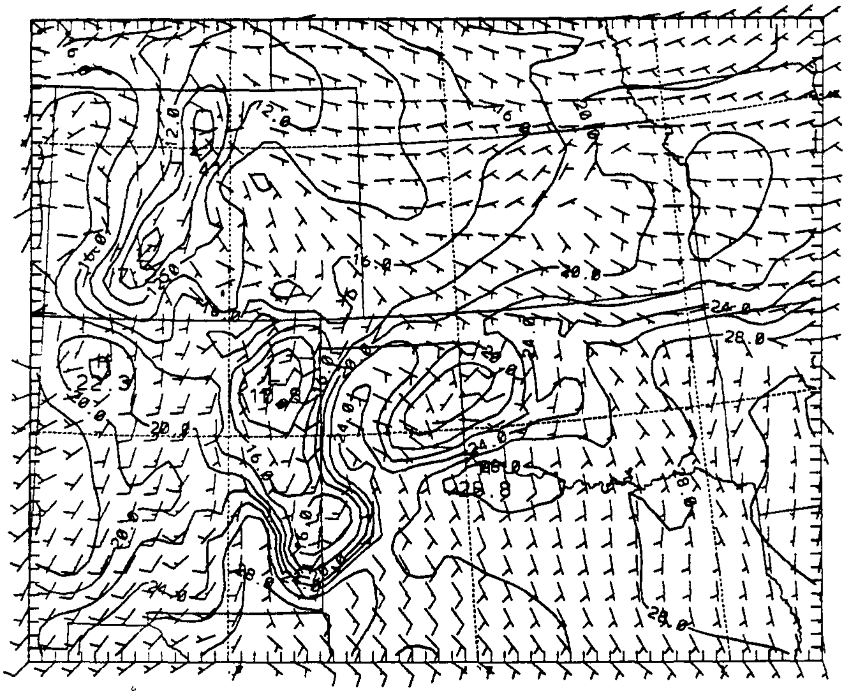

Figure 4.26: Simulated surface temperature (° C, contoured every 2° C) and winds at 4/0000.

Fig. 4.26 shows the 12 h forecast surface temperature and wind field. Fig. 4.27 shows the 4/0000 observed surface data from the regular reporting sites and the PAM/SAM network. The cold pool across the eastern Texas panhandle and western Oklahoma was similar to the observed cold pool. However, the model did not produce the northerly component to the flow behind the convective area (Fig. 4.27b). The model surface convergence in east-central Kansas was quite similar to observed, including the area of enhanced southeasterly wind speeds south of EMP. The model did not reproduce the observed warm surface temperatures across southern Oklahoma and Texas (Fig. 4.27a). In these regions, the model was 3 to 6° too cool, perhaps because of excessive cloud shading or other shortcomings in the MM4 boundary layer parameterization (Nelson Seaman, 1991, personal communication). Model surface temperatures across Kansas were quite close to observed, but the model surface front (considered to be on the warm side of the thermal gradient, south of the wind shift line) was about 75 km south of the Kansas border in northeast Oklahoma (Fig. 4.26). PAM/SAM data (Fig. 4.27b) show that the front was about 25

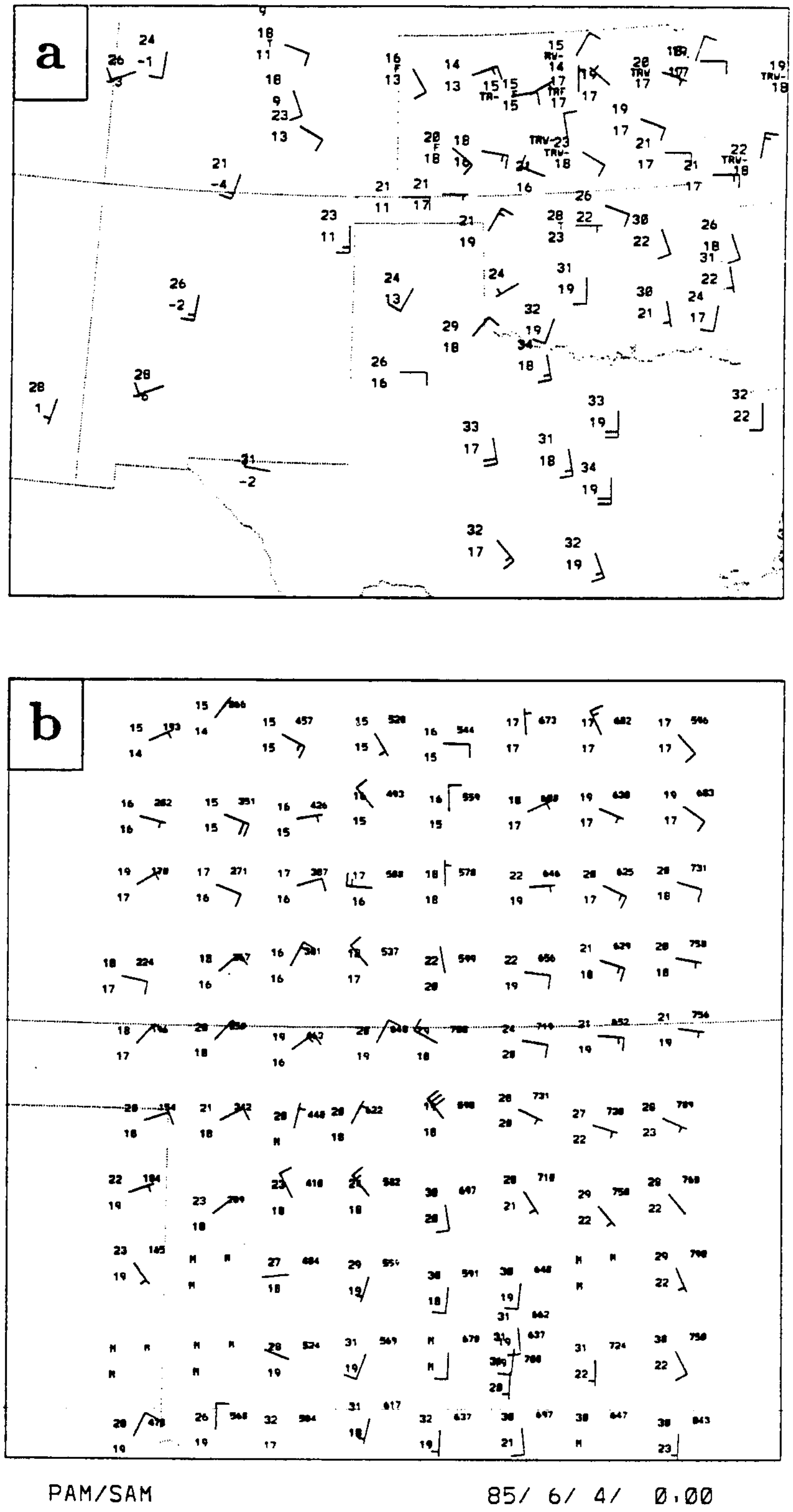

Figure 4.27: Surface observations at 4/0000 from a) the regular reporting sites and b) the PAM/SAM network. The station model is conventional (as in Fig. 2.7), but the surface pressure in tenths of mb with the leading "9" omitted is plotted to the upper right of each station in b).

km south of the Kansas border with a temperature gradient of 7° (50 km)$^{-1}$. The earlier model convection in this region may have produced too much cold low-level air, making it more difficult for the warm air south of the front to enter into the simulated MCS2.

Fig. 4.28a shows the predicted 900 mb θ_E field at 4/0000. Fig. 4.28b (from Smull and Augustine 1993) shows the corresponding analysis. The model generated properly the θ_E ridge analyzed across central Oklahoma ahead of the convective line.[1] The model also generated a strong θ_E gradient across central Kansas corresponding to the observed rain band. The analysis also shows the gradient parallel to the northeast-southwest rainband, although the gradient on their coarser analysis grid is not as strong as in the model. The strong northeast-southwest θ_E gradient suggests frontogenesis was occurring. As shown by Nagata and Ogura (1991) evaporation of precipitation in the cool air would enhance the thermal gradient. The cold pool behind the north-south convective line is quite pronounced in the simulation. The analysis has a similar θ_E trough, but the cooling is not as strong and the trough extends farther north into Kansas. Model winds were similar to observed in southeast Kansas where relative inflow to the MCS was strong. The model also generated the cyclonic shear across the northeast part of the system near FRI, but, because of the lack of convection, did not exhibit reduced speeds near DDC. The SLP field at 4/0000 (Fig. 4.14g) shows that a mesohigh coincided with the cold pool in western Oklahoma, while a trough was located across eastern Kansas ahead of the precipitation band. Mesohighs were also beneath the rain areas in eastern New Mexico and western Texas.

Feeding into the Kansas rainband was a low-level jet, shown in Fig. 4.29. The 900 mb LLJ with a maximum speed of 19.2 m s^{-1} was north of ICT, with speed divergence in its wake. This divergence led to downward motion across southern Kansas, helping inhibit implicit convection.

---

[1] A subjective analysis of θ_E derived from the 4/0000 sounding data shows no θ_E values greater than 350° K over Oklahoma. In addition, the 331° K value in northern Kansas was not observed. It appears that the objective analysis technique used by Smull and Augustine may have artificially increased the θ_E ridges.

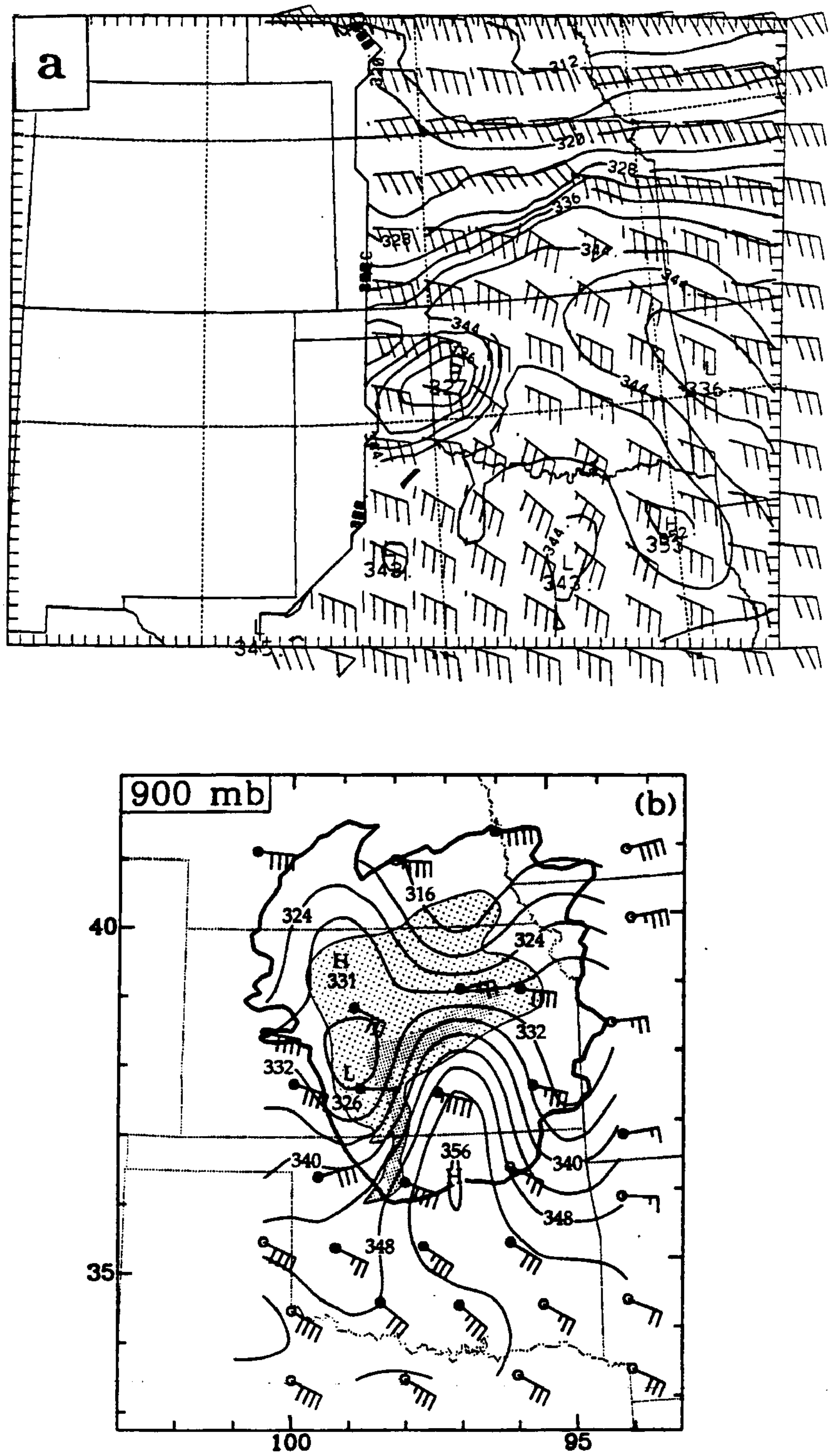

Figure 4.28: 900 mb θ_E and system-relative wind barbs at 4/0000 from a) CTL (θ_E contoured every 4° K; one full barb is 5 m s^{-1}) and b) the analysis of Smull and Augustine (1993) (θ_E contoured every 4° K). The relative winds are based on the observed MCS2 motion of 265° at 15 m s^{-1} .

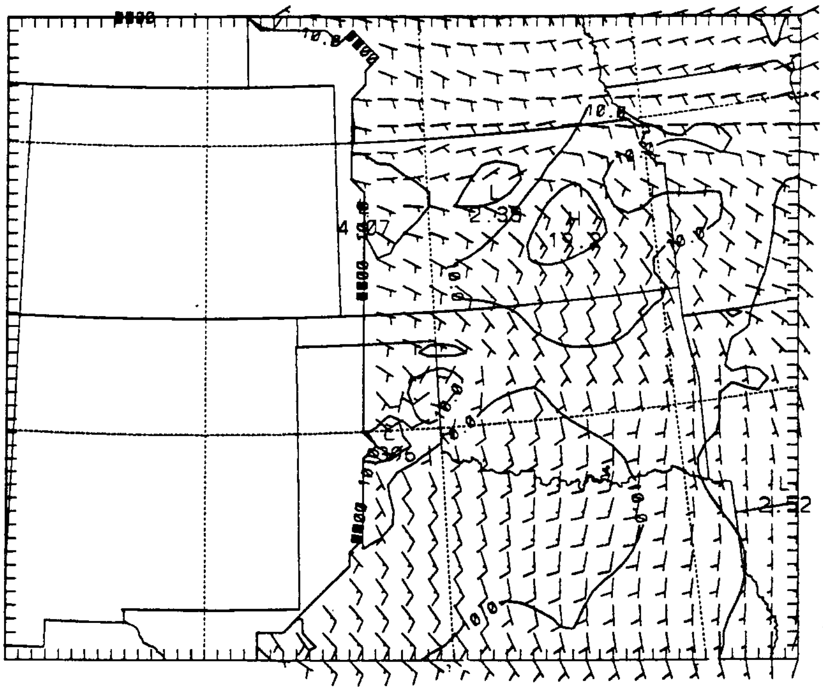

Figure 4.29: 900 mb isotachs (m s^{-1} , solid contours) and wind barbs at 3/2300.

LLJ with a maximum speed of 19.2 m s^{-1} was north of ICT, with speed divergence in its wake. This divergence led to downward motion across southern Kansas, helping inhibit implicit convection.

The Kansas rain area had its origins in northwest Kansas where convection began at 2020 UTC. By 3/2100 (Fig. 4.11a), convection was occurring at several grid points as the area expanded to the north and east. The convection was initially based near 760 mb, with CAPEs about 2200 J kg^{-1}, but cloud bases were higher (700 mb) and CAPEs lower on the north end of the rain area. The area of convection moved east-northeast across northern Kansas through 3/2200, then developed toward the southeast into central Kansas. By 4/0000 (Fig. 4.17a) the three-hour convective rain amounts resulted in a WNW-ESE oriented band across northern Kansas.

As pointed out by Stumpf (1988) and Fortune (1989), convection broke out across western Kansas shortly after 2000 UTC well ahead of the convective area moving northeast through the Texas panhandle. Fortune speculated that the storms formed as the airmass recovered in the wake of MCS1. He went on to state that, "The fact that the unstable layer was decoupled from the surface is ... important in preventing the focusing of convective activity on any outflow boundary or terrain feature. The early storms ... developed completely free of any influences from the surface and might be initiated by minor inhomogeneities in the wind or moisture fields in the elevated layer of instability. Thus the spatial pattern of the first storm cells would appear chaotic on the mesoscale". How, then, did the convection form in the simulation?

The time evolution of the vertical profile of θ_E and winds at the grid point which first had convection in northwest Kansas shows a large increase in θ_E between 3/1200 and 3/2000, near the low-level inversion. Values of θ_E at 800 mb increased from 329° K to 339° K with significant increases in both temperature and moisture. Fig. 4.30 presents profiles at this grid point at 3/2000, twenty minutes before convection began. A 17 m s^{-1} low-level jet was located within the inversion. The θ_E profile shows that parcels below 800 mb are very stable, while above that level a large amount of instability was present. Slight upward motion was present only between 850 and 750 mb, however it was sufficient, with the large amount of instability, to activate the FCT. Therefore, it appears an increase in southeasterly low-level flow advected higher θ_E air into northwest Kansas, destabilizing the grid point column.

At the initial time, an upper level jet streak was located in the southwest corner of the domain, near ELP. Fig. 4.31 shows the wind barbs and isotachs for the σ = .915 level and the 200 mb level. The σ = .915 level is about 80 mb above the surface and does not intersect the sloping terrain as a low-level pressure surfaces does. A second ULJ was over central Nebraska (Fig. 4.31b). A southwesterly LLJ was near AMA, while a band of enhanced easterlies was across northern Kansas (Fig. 4.31a). Three hours later, the ULJ over the southwest part of the domain had weakened and moved to the west of LBB (Fig. 4.32b). The Nebraska jet streak had broadened and moved eastward. The large changes in the upper level winds are associated with the adjustments during the first few hours of the model forecast. The initial data are out of balance, and the model tries to reach a balance by mutual adjustment of the mass and momentum fields. At

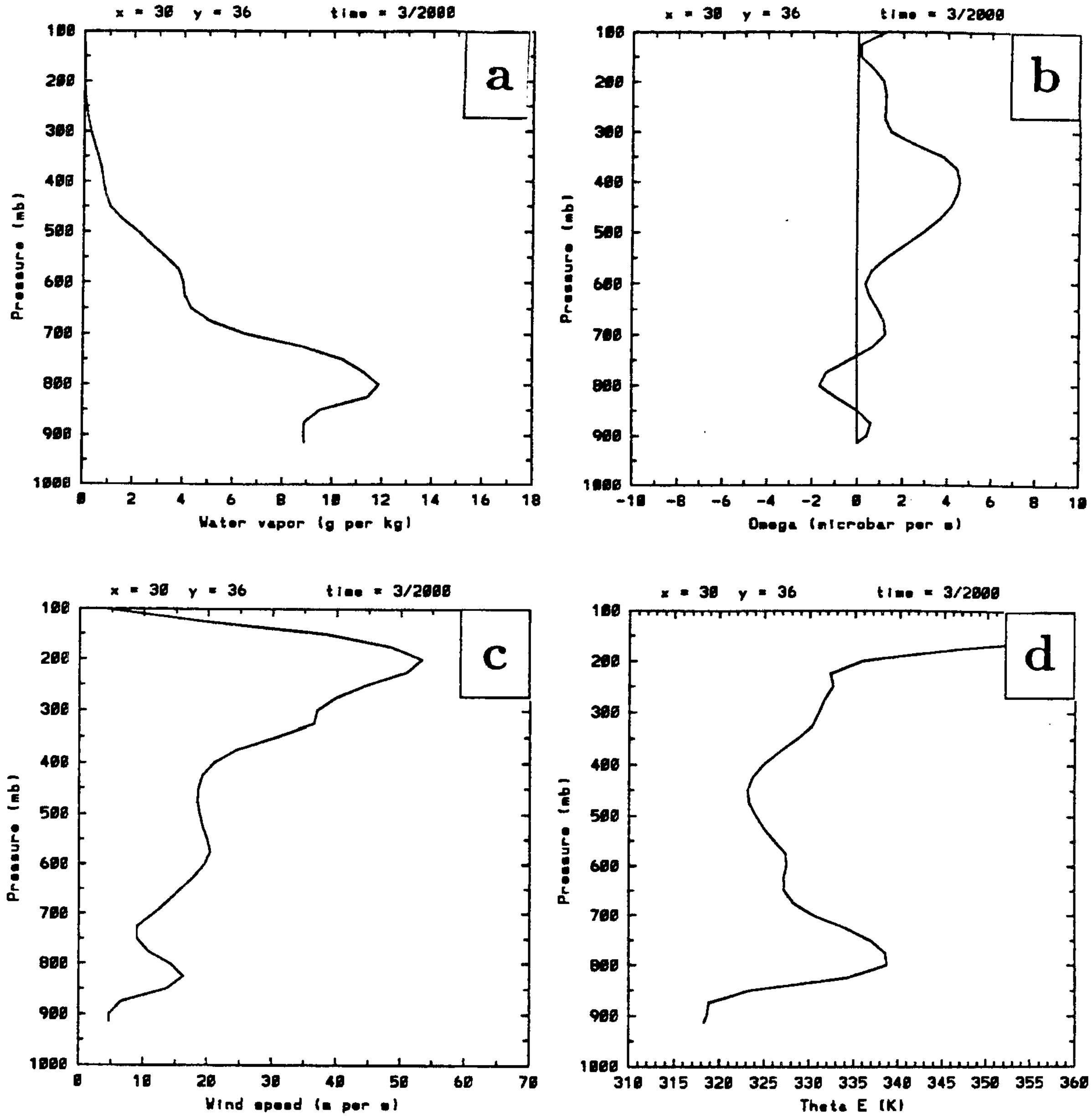

Figure 4.30: Grid point profiles from a point in northwest Kansas at 3/2000 of a) water vapor (g kg^{-1}), b) ω (μb s^{-1}), c) wind speed (m s^{-1}), and d) θ_E (K).

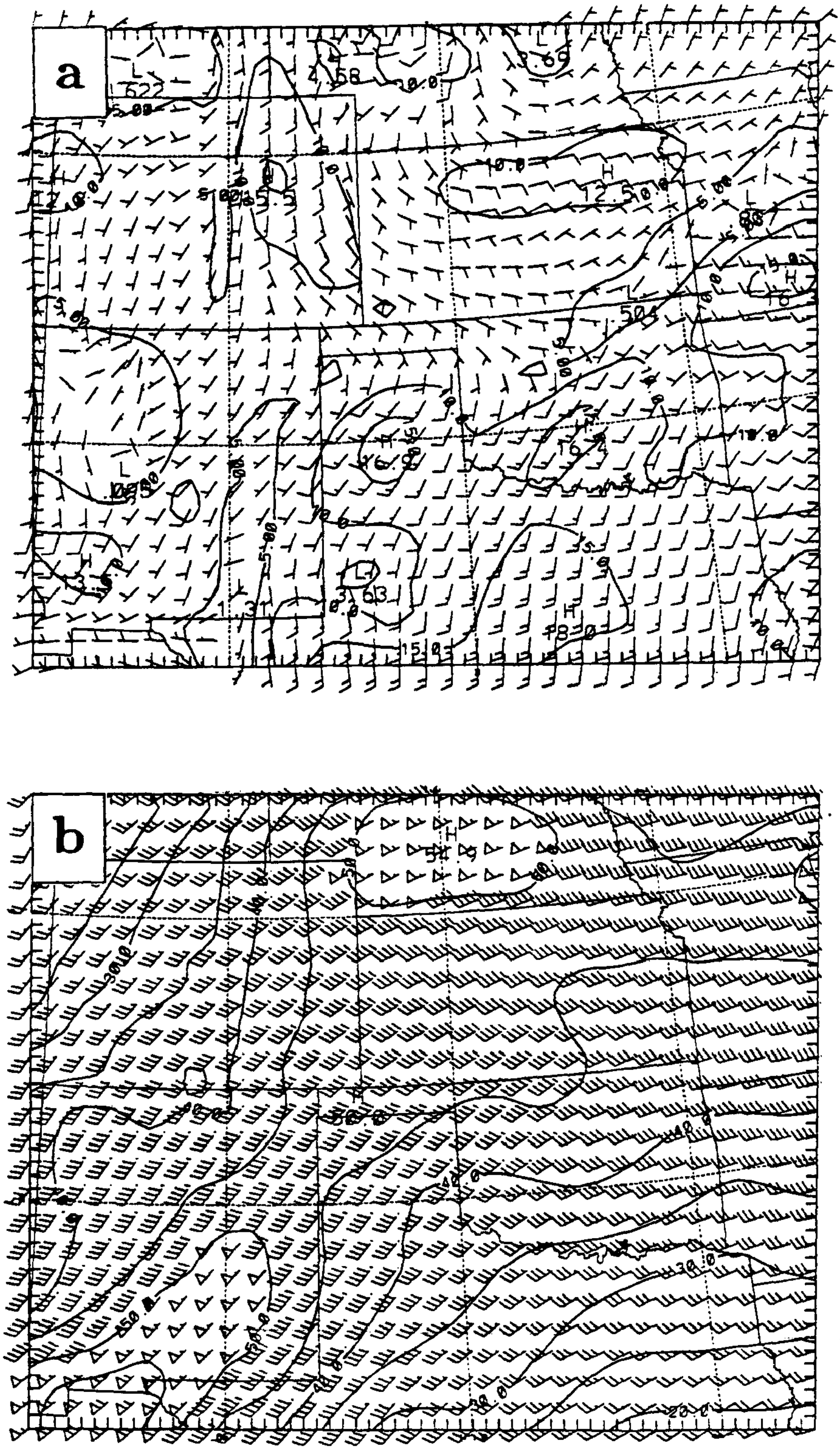

Figure 4.31: Isotachs (m s^{-1} , solid contours) and wind barbs for 3/1200 at the a) σ = .915 level and b) 200 mb level.

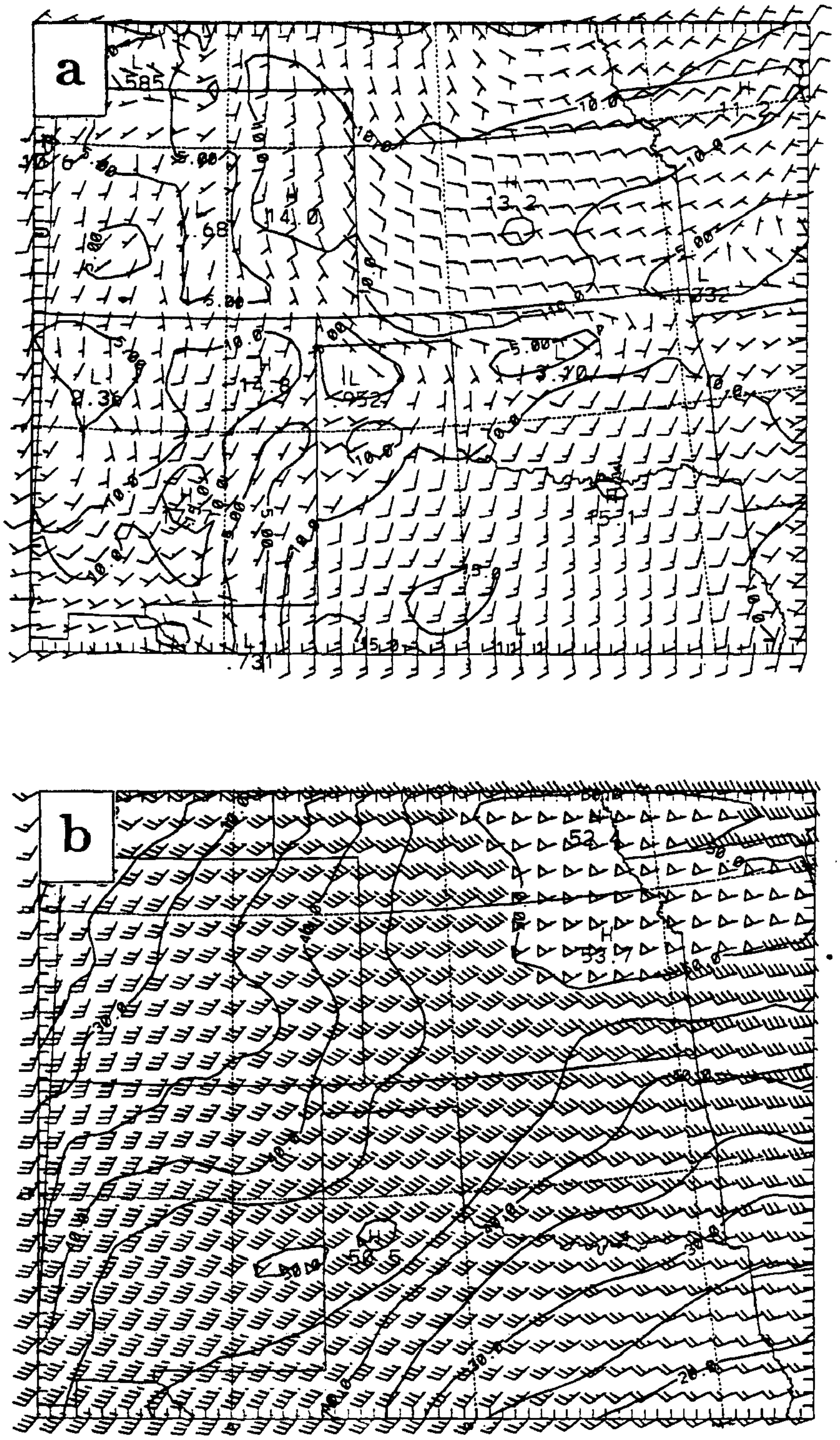

Figure 4.32: As in Fig. 4.31, but for 3/1500.

3/1500 there is no longer a LLJ over the Texas panhandle, and none is present over Kansas (Fig. 4.32a). A small area of relatively weak winds is present within MCS1 over central Kansas. By 3/1700 (Fig. 4.33b), the upper jet streak had re-formed over eastern New Mexico, west of MCS2. Examination of hourly wind fields show that the original jet streak dissipated over west Texas. By 3/1800, the new jet streak was approaching LBL on the northwest edge of the MCS2 convection and beginning to exhibit a slight anticyclonic curvature of the isotachs (not shown). At 3/1700, an area of reduced upper level flow was found over eastern Kansas associated with MCS1. At low levels over Kansas, two easterly low-level jets had formed (Fig. 4.33a). One was just north of the Oklahoma border east of DDC. A second wind maximum was along the Nebraska border. Between the two low level jets was an area of weaker winds in the wake of MCS1. By 1800 UTC the southern LLJ had grown while the northern one shrank (not shown). The nose of the low level jet was within the right exit region of the approaching upper jet streak. By 3/1900 (Fig. 4.34a), the southeasterly LLJ covered most of western Kansas. The upper level jet streak was also over western Kansas (Fig. 4.34b). An east-west cross-section of isotachs and the ageostrophic circulation in the plane of the cross-section through the point which first had convection in northwest Kansas is shown in Fig. 4.35. (As shown by Keyser *et al.* (1989) this plot only approximates the true cross-streak circulation). A transverse circulation similar to the classic indirect circulation, but displaced eastward, is present over the region. This cross-section strongly resembles the cross-section presented by Uccellini *et al.* (1987, their Fig. 4) for a developing cyclone off the east coast of the United States and the case presented by Cammas and Raymond (1989, their Fig. 22). In both those cases as well, the indirect circulation was displaced toward the anticyclonic side of the ULJ. They offer the possible explanation for the displacement as either due to weak inertial instability or warm advection along the flow (e.g. Keyser and Shapiro 1986, their Fig. 23d). Rising motion is found directly beneath the isotach maximum rather than to its left. Strong westerly ageostrophic flow is found between 300 and 200 mb. Easterly ageostrophic flow is found at low levels near a 15 m s^{-1} isotach maximum. In contrast, Cammas and Raymond (1989) show only a 4 m s^{-1} ageostrophic speed in the

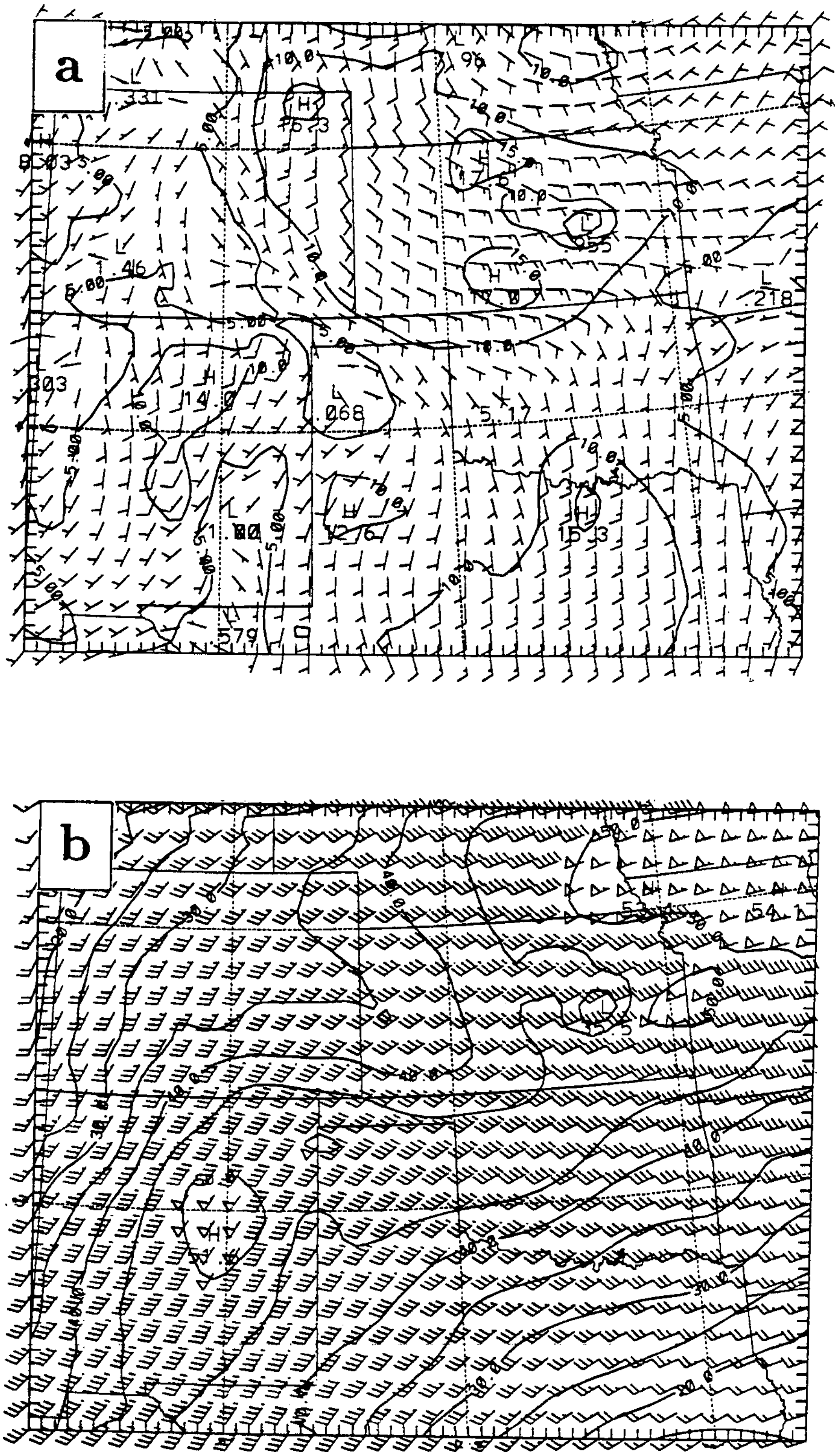

Figure 4.33: As in Fig. 4.31, but for 3/1700.

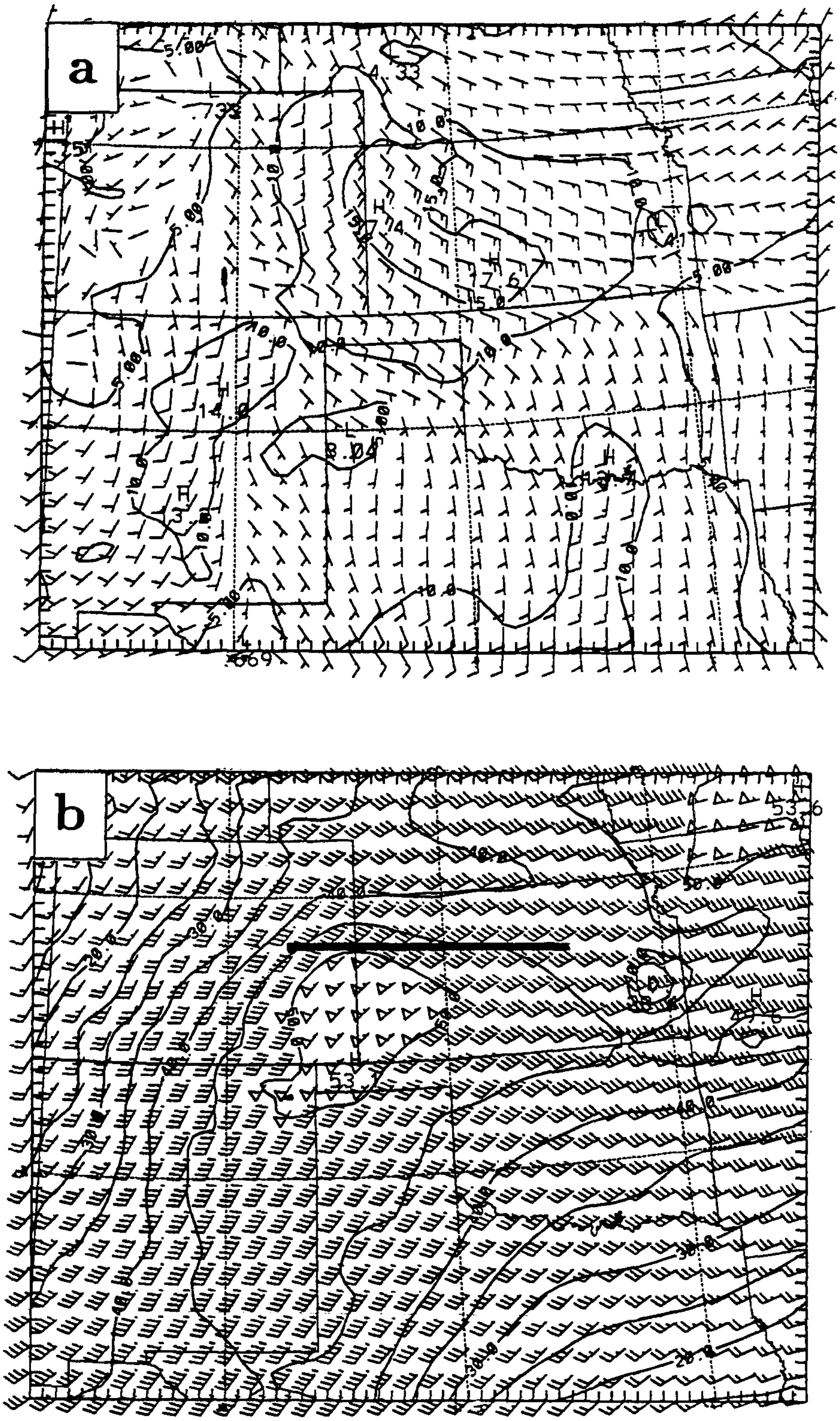

Figure 4.34: As in Fig. 4.31, but for 3/1900.

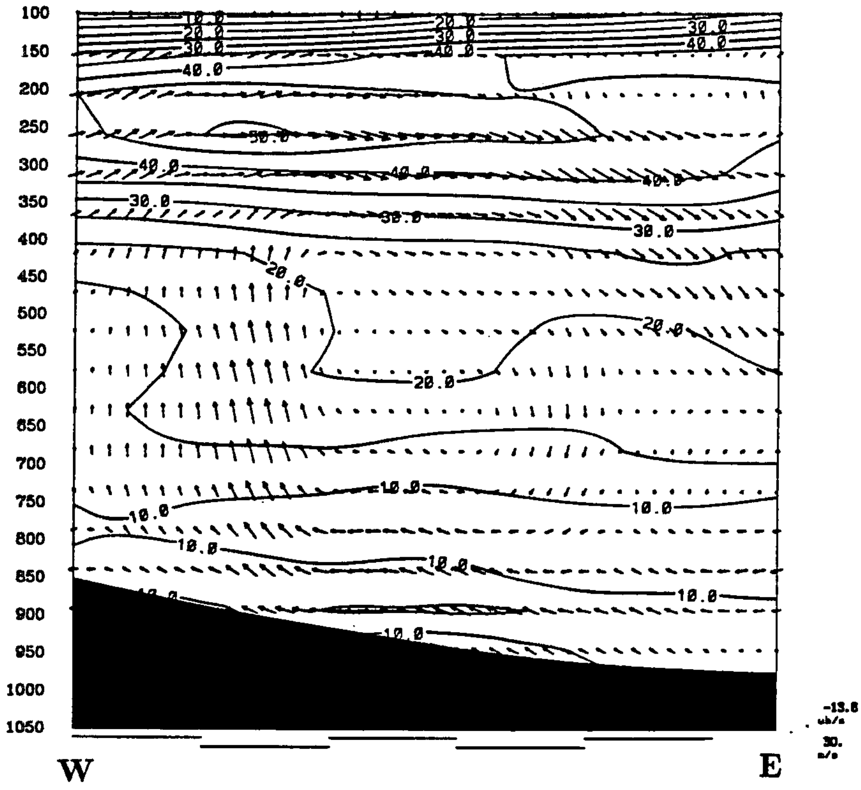

Figure 4.35: West to east cross-section along the line shown in Fig. 4.34b of wind speed (m s^{-1} , solid contours) and ageostrophic circulation in the plane of the cross-section (vectors) at 3/1900.

lower branch of the circulation in their case. The stronger low-level winds in the 3-4 June case may be a consequence of the low-level cold air which allowed the LLJ to be decoupled from the surface as is the nocturnal LLJ. This strong response of the low-level winds to the upper-level jet streak circulations is significantly different from the classic conceptual model of jet-front interactions shown by Shapiro (1982).

Fig. 4.36 shows the 850 mb ageostrophic winds at 3/1700 and 3/1900. Easterly ageostrophic winds cover Kansas, perturbed near MCS1. By 1900 UTC, the easterly flow had increased dramatically (quadrupling at some points) as the upper level jet approached. Observations show the passage of an upper jet between 12 and 13 km over LBL after 1930 UTC (Fig. 2.27b). The model results suggest that the upper level and lower level jets at this time were linked (Uccellini and Johnson 1979), although not necessarily at earlier times. It also appears that the LLJ over Kansas was influenced by the presence of MCS1. This effect will be examined more closely in the following chapter.

Unfortunately, a lack of observations prevents confirmation of the LLJ. However, the 3/2100 PTT sounding exhibits a low-level wind maximum of 11.6 m s^{-1} from 096° just below the top of the temperature inversion. The enhanced wind speeds extend from approximately 900 mb up to 880 mb. The 3/1920 RSL sounding has a low-level wind maximum between 911 and 879 mb, peaking at 9.9 m s^{-1} . Low-level winds decreased by 1 to 2 m s^{-1} on the 3/2030 RSL sounding. Data from the McPherson profiler (just north of HUT in central Kansas) were unavailable below 2.6 km (about 750 mb) and only rarely available above 9 km. No MCP data were available between 3/0600 and 3/1800. Nachamkin (1992) presents Doppler-derived winds within MCS1 and finds easterly flow below 1.9 km MSL. However, the limited time and space resolution of the data cannot resolve the simulated jet. Fig. 4.37 shows the 3/2100 200 mb wind observations. Although the number of data points is limited, the maximum winds at this level exceed 52 m s^{-1} at RSL, close to the simulated position and strength of the jet streak.

Thus, the low-level southeasterly jet which destabilized the grid columns in northwest Kansas appears to be the lower branch of the indirect transverse circulation within the exit region of an approaching upper-level jet streak. (The possible impact of MCS1 upon

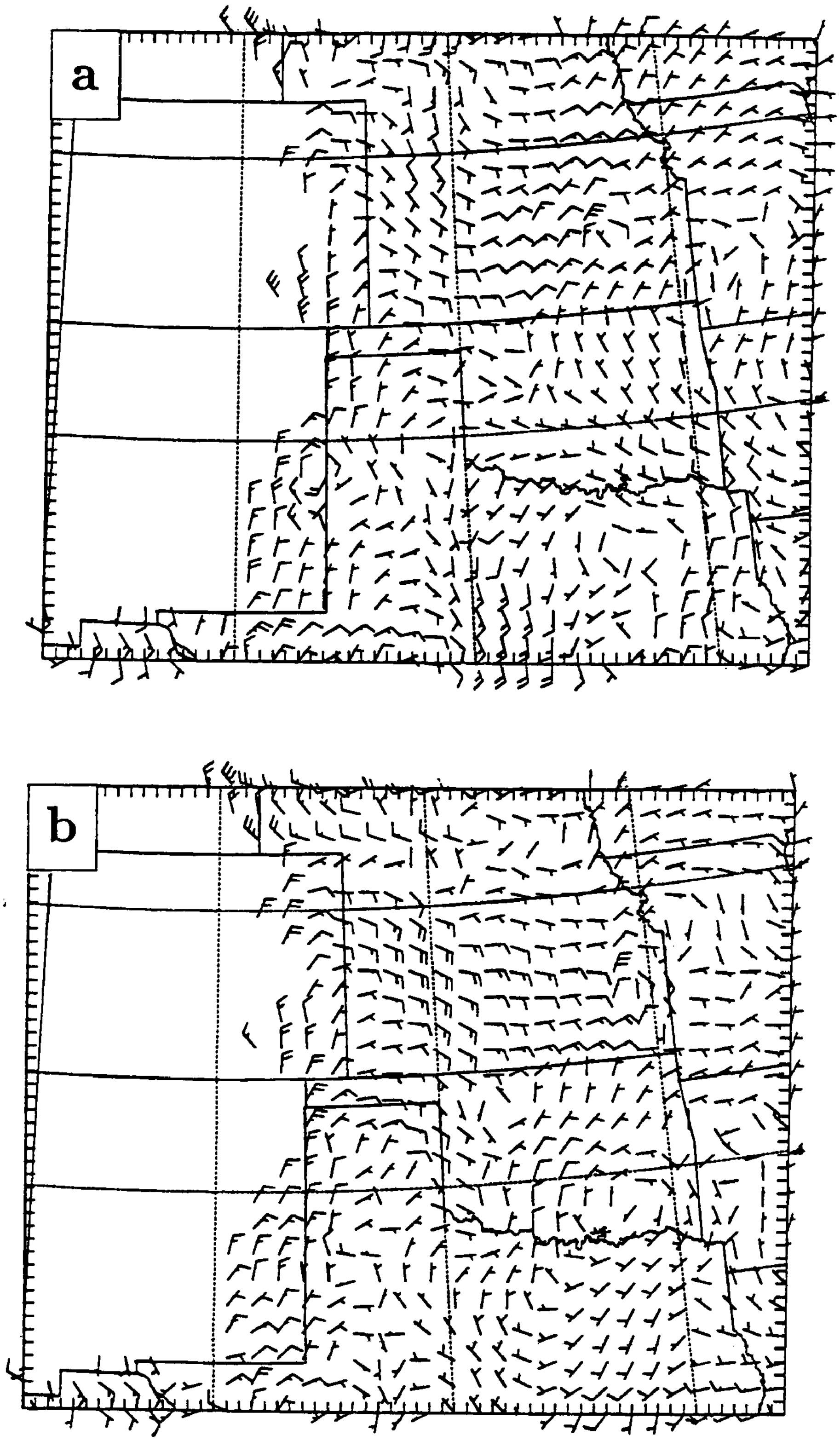

Figure 4.36: 850 mb ageostrophic winds at a) 3/1700 and b) 3/1900.

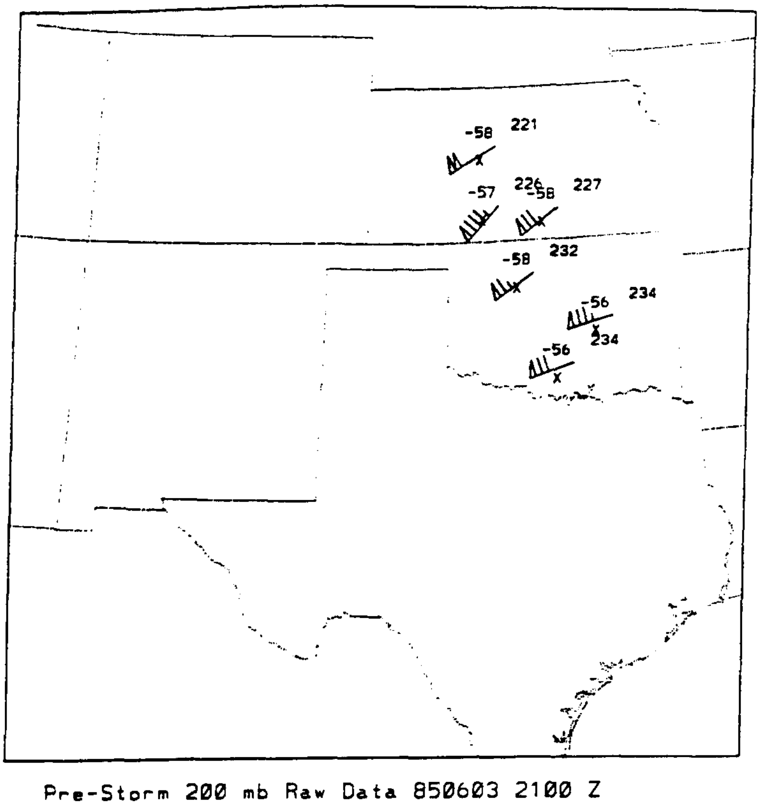

Figure 4.37: Conventional upper-air station model plot (as in Fig. 2.22) of 200 mb supplemental sounding data at 3/2100.

the LLJ will be explored in the following chapter). While the modeled northwest Kansas convection was near the location of cells shown in radar observations, the main precipitation area that was to become the northeast-southwest shear-parallel arm of MCS2 actually formed 80 km to the southeast. The simulated location of the rainband too far to the north might be the result of an incorrect placement of the upper-level jet streak. Another result of the LLJ being too far northwest was an area of speed divergence in southwest Kansas, which added to the downward motion beneath the explicit rain area approaching from the southwest. Therefore, convection was harder to trigger in southern Kansas.

In a modeling study of an autumn cold-frontal case, Sortais *et al.* (1993) found that the LLJ and ULJ were linked in a manner similar to that described by Shapiro (1982). The 3-4 June case is within a different synoptic setting with an easterly LLJ forming north of a surface front. The strong response of the low-level modeled winds to the approaching upper-level jet streak suggests that regions north of an east-west front, where the low-level winds can be decoupled from the effects of surface friction, should be a favored location for low-level jets. Advection of high-θ_E air by the LLJ could lead to rapid destabilization and the *formation of convection*.

The 3-4 June case is also complicated by the changes in curvature of the ULJ. As Moore and Vanknowe (1992) showed, the familiar four-cell pattern of a straight-line jet streak only has two cells when the streak is anticyclonically curved. Downward motion exists within and ahead of the anticyclonic jet streak while upward motion follows the core. As the straight-line ULJ approached northwest Kansas on 3-4 June, upward motion beneath the exit region helped trigger the convective system. As the ULJ approached the ridge axis, becoming more anticyclonically curved, the induced upward motion would tend to lag the jet core (e.g. Moore and VanKnowe 1992). Thus, the time that jet-induced upward motion would be maintained over the Kansas convection would be lengthened, perhaps aiding the growth of the MCS. However, the model results are complicated by many other factors (particularly the effects of latent heating) and this circulation is not apparent. In fact, the upward motion in mid-levels (700-500 mb) near the Kansas ULJ was within and downstream of the core, with downward motion within the entrance region, in opposition to the Moore and Vanknowe (1992) results for an anticyclonically-curved jet streak.

4.4 Summary

The CTL simulation was able to capture some of the observed features of the 3-4 June MCSs, although many of the meso-β-scale details remained elusive. The simulated MCS1 began at the nose of a low-level jet riding over the frontal surface into a region with enhanced moisture levels. Triggering of upright convection by slantwise motions above the front may have occurred, but cannot be confirmed by model results. The simulated MCS1 propagated to the east similar to observations, but produced less rainfall than observed. Relative flow through the system indicates that MCS1 fed on unstable air riding over the frontal surface. The low-level stable air did not directly participate in the circulation. No front-to-rear flow developed within the system and only weak rear-to-front-flow was generated. The model never developed the observed large stratiform region and consequently the surface pressure features were also weaker than observed. The simulated MCS1 died prematurely when its inflow of high θ_E air was cut off by convection which developed erroneously along the surface front to the south.

MCS2 was linked throughout its lifetime to an upper-level jet streak. The ULJ existed in the initial conditions, prior to any significant convection. Simulated, weak, high-based convection strengthened as it moved into an area with deeper low-level moisture. The ULJ induced a LLJ to develop within its exit region over western Kansas, destabilizing the air mass over the frontal surface. Convection broke out in western and central Kansas ahead of and apart from the original convective region. Strong downward motion beneath an explicit rain area and in the wake of the LLJ, prevented model convection from developing across southern Kansas. The northeast-southwest shear-parallel band across central Kansas formed along a frontogenetic low-level thermal gradient while the north-south shear-perpendicular band across western Oklahoma and the Texas panhandle was forced by low-level convergence of convective outflow.

Some possible reasons for the failure of the model to accurately reproduce the observed systems include 1) The convection was based above the surface where less mesoscale information was in the initial data. Also, the model initial fields contained no cloud or rain water – these hydrometeors had to develop during the early part of the simulation. This may have been significant over the front where MCS1 began, since the latent heating produced by the production of these hydrometeors occurred at a different time and location than observed, perhaps influencing the triggering of the convection. 2) The convective trigger function was deficient. Strongly-forced cases are less sensitive to the trigger function than this weakly-forced case. 3) The convection (particularly above the front) is not parameterizable. Parameterization implies that the larger-scale controls the character of the sub-grid-scale convection. This may not be true for some types of convection or for certain grid sizes. A full exploration of these issues is beyond the scope of this study. However, some sensitivities of the simulation to model physics and initial data will be explored in the following chapter.

TL

Chapter 5

SOME SENSITIVITY EXPERIMENTS

While the CTL run did a reasonable job of simulating the events of 3 June, several other simulations were conducted in order to determine the sensitivity of the model simulation to changes in physical parameterizations and initial data. The goal of these runs is to get an indication of critical atmospheric processes and critical parameterization components. In particular, the behavior of the upper and lower level jets and the convective parameterization will be examined.

5.1 Sensitivity to changes in the initial data

The experiments described in this section involve various changes to the initial data in order to help determine the data's impact on the development of the convective systems. Stensrud (1992) and Anthes *et al.* (1989) suggest that initial data have a significant impact on the development of convection especially during the early part of the model run. Also included in this section is a description of an experiment examining the effect of MCS1 on the Kansas LLJ.

5.1.1 No Upper-Level Jet Streak

The impact of the initial upper-level jet streak near ELP on the simulation was tested by removing this jet streak from the initial analysis. The initial jet-level winds can have a significant impact upon downstream convection (e.g. Chang *et al.* 1984; Brill *et al.* 1985). The winds above 400 mb from both the ELP observation and the ROW bogus observation were deleted from the RAWINS analysis. No change was made to the temperature or geopotential height field. Except for the change in the initial winds, the NOJS simulation was identical to the CTL run. Fig. 5.1 shows the 3/1200 200 mb wind

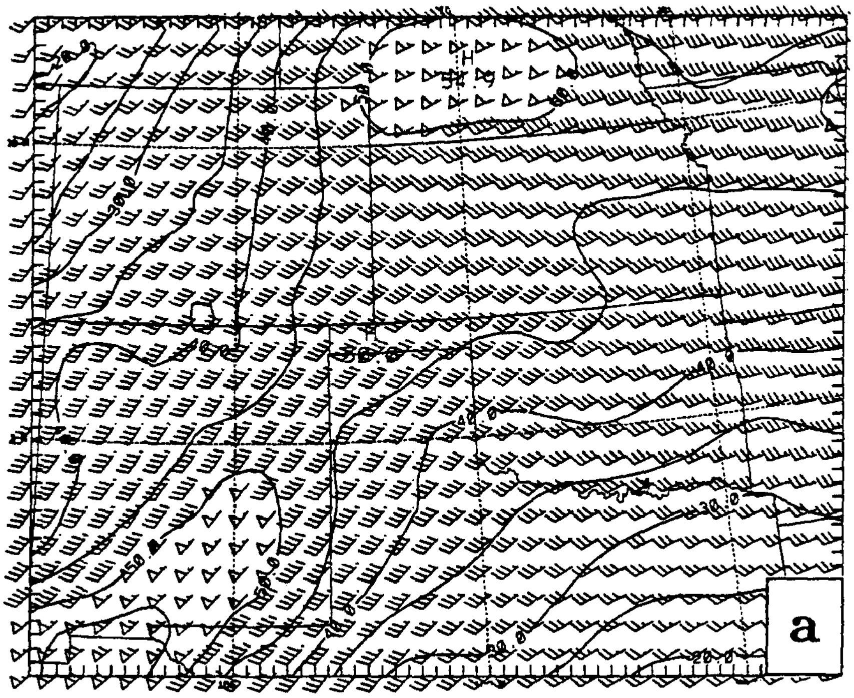

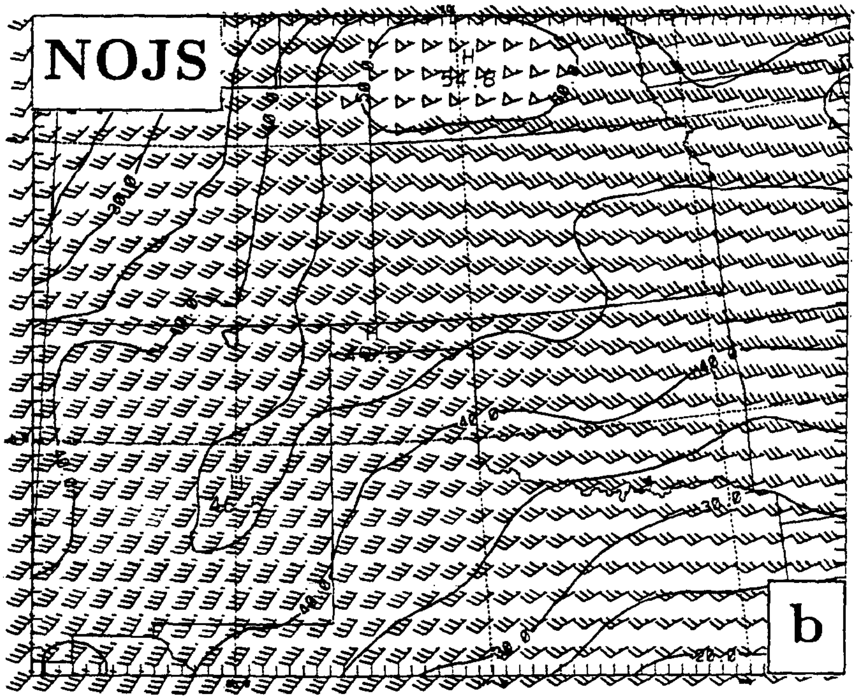

Figure 5.1: Isotachs (m s^{-1} , solid contours) and wind barbs for 3/1200 at 200 mb for a) CTL and b) NOJS.

field for the CTL and NOJS initial condition. The 58 m s^{-1} jet core over ELP has been removed, leaving a jet axis (which was present in the first guess field) with speeds less than 50 m s^{-1} across northeast New Mexico extending into Kansas. Winds over southeast New Mexico have been reduced by about 10 m s^{-1} . Model initial conditions provided by objective analyses are typically out of balance (e.g. Haltiner and Williams 1980, page 365). Since no initialization is performed for the runs described in this study (except for the removal of the mean divergence), the model initial conditions are unbalanced. However, the initial imbalance present in CTL and NOJS should be different, possibly leading to differences in the simulations.

MCS1 convection over Kansas began in the NOJS simulation (Fig. 5.2a) as in the CTL run, but by 3/1500 the maximum amount was 0.6 mm (33%) less than in CTL (Fig. 4.3a). (In nature, the jet streak near ELP would not be expected to have any impact on the MCS1 convection, but the early model adjustment processes are altered by the modified winds and consequently, the gravity wave and vertical motion patterns are altered.) The mid-level convection over the southwest Texas panhandle by this time in the CTL run was not present in NOJS (Fig. 5.2a). This suggests that the lift provided by the jet streak aided the development of this rain area. Above 500 mb there is significantly less upward motion over the southwest Texas panhandle in the NOJS simulation (not shown). However, it is difficult to distinguish between upward motion forced by the jet streak and that forced by the convective heating within the CTL run. Figure 5.3 shows that an ill-defined jet streak is present over eastern New Mexico at 3/1500 in the NOJS run. The strong initial jet streak present in the CTL run has nearly dissipated by 3/1500 (Fig. 5.3a). Three hours later the jet streak in CTL was over the extreme western Oklahoma panhandle (Fig. 5.4a). By this time the NOJS run had developed a nearly identical jet streak (Fig. 5.4b). The 3-h simulated rain in both simulations was nearly identical, with convective rain over extreme eastern New Mexico, west of LBB (Figs. 4.6a and 5.2b). The low-level ($\sigma = .915$) winds in the two runs were also identical (not shown).

By 3/2100, there were some significant differences between the simulations. Run NOJS had developed convective rainfall over the northeast Texas panhandle (Fig. 5.2c).

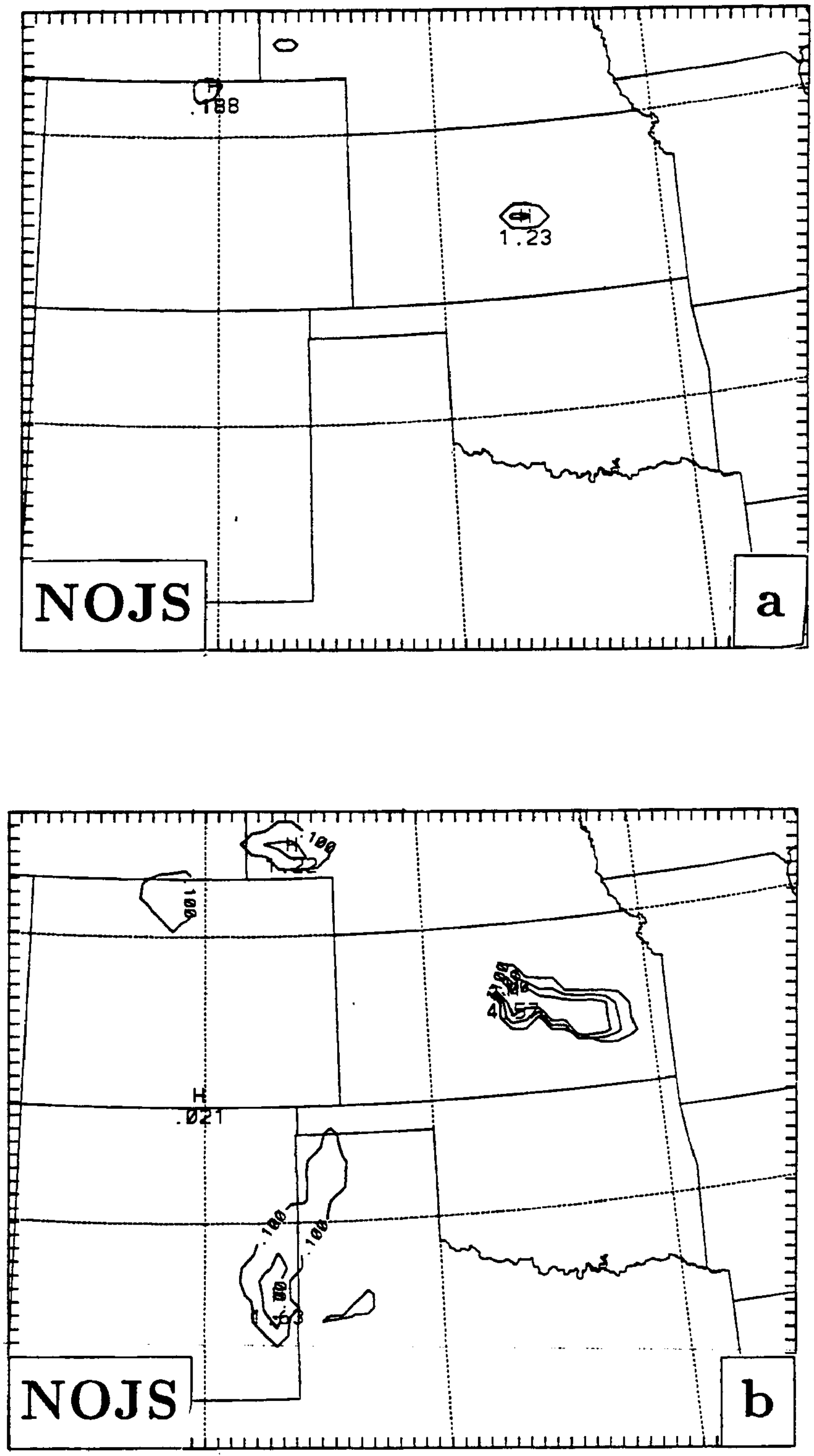

Figure 5.2: Convective rainfall as in Fig. 4.5a from NOJS for the three-hour period ending a) 3/1500, b) 3/1800, and c) 3/2100.

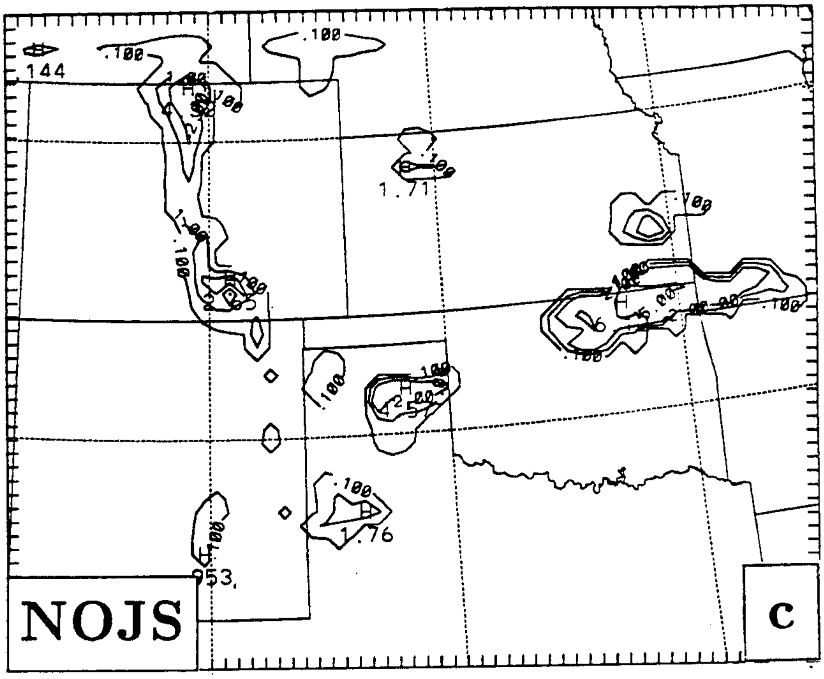

Figure 5.2: Continued.

The CTL run later developed convective rain southeast of there. The 200 mb winds were slightly different as well (Fig. 5.5). The NOJS jet streak was slightly farther east than CTL. Reduced wind speeds at this level are found in both simulations where there was deep convection.

The low-level jet over Kansas simulated by CTL developed nearly identically in the NOJS simulation (not shown). Convection developed in northwest Kansas in both runs. It was anticipated that the elimination of the upper-level jet streak in the initial conditions would alter the evolution of the LLJ in NOJS. However, since both simulations had a nearly identical upper-level wind pattern by 3/1800, conclusions about the jet coupling cannot be drawn. It can be concluded that the ULJ over western Kansas between 3/1800 and 3/2100 is not influenced as much by the initial wind field near ELP as it is by other process occurring in the model. Two other experiments were conducted to examine the development of the jets.

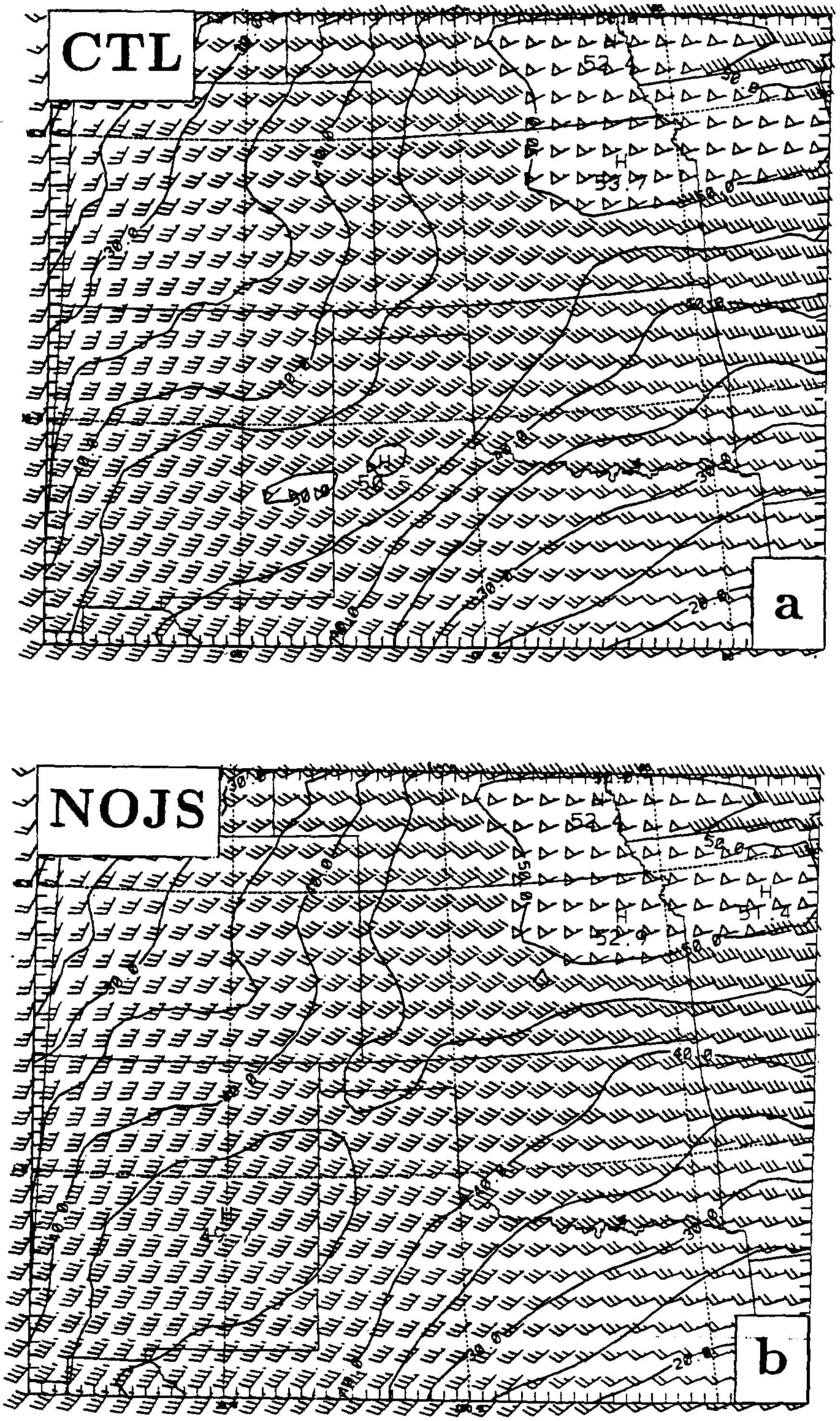

Figure 5.3: Isotachs (m s^{-1} , solid contours) and wind barbs for 3/1500 at 200 mb for a) CTL and b) NOJS.

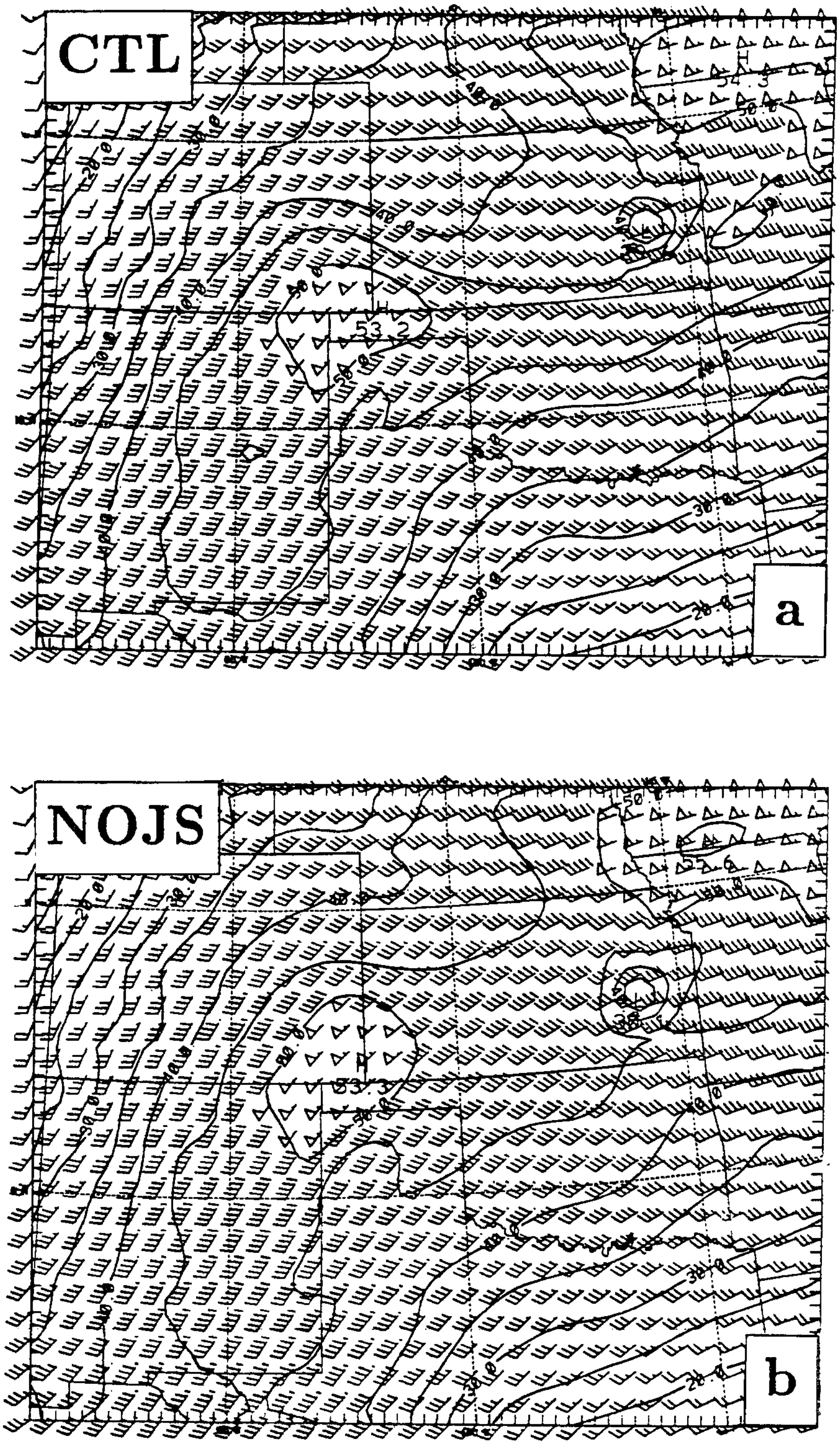

Figure 5.4: Isotachs (m s^{-1} , solid contours) and wind barbs for 3/1800 at 200 mb for a) CTL and b) NOJS.

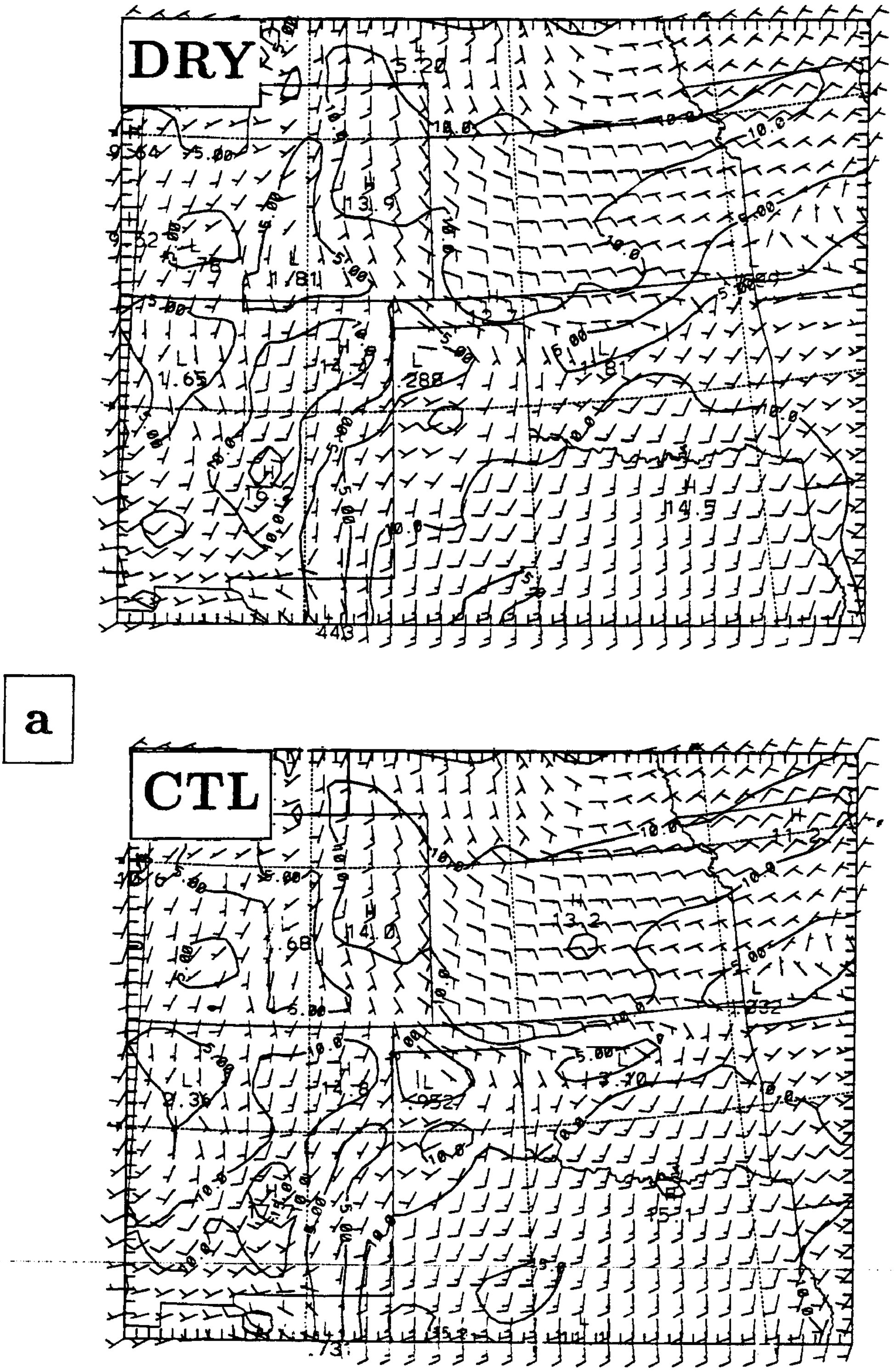

Figure 5.6: Isotachs (m s^{-1} , solid contours) and wind barbs for 3/1500 at the a) σ = .915 level and b) 200 mb level for DRY and CTL.

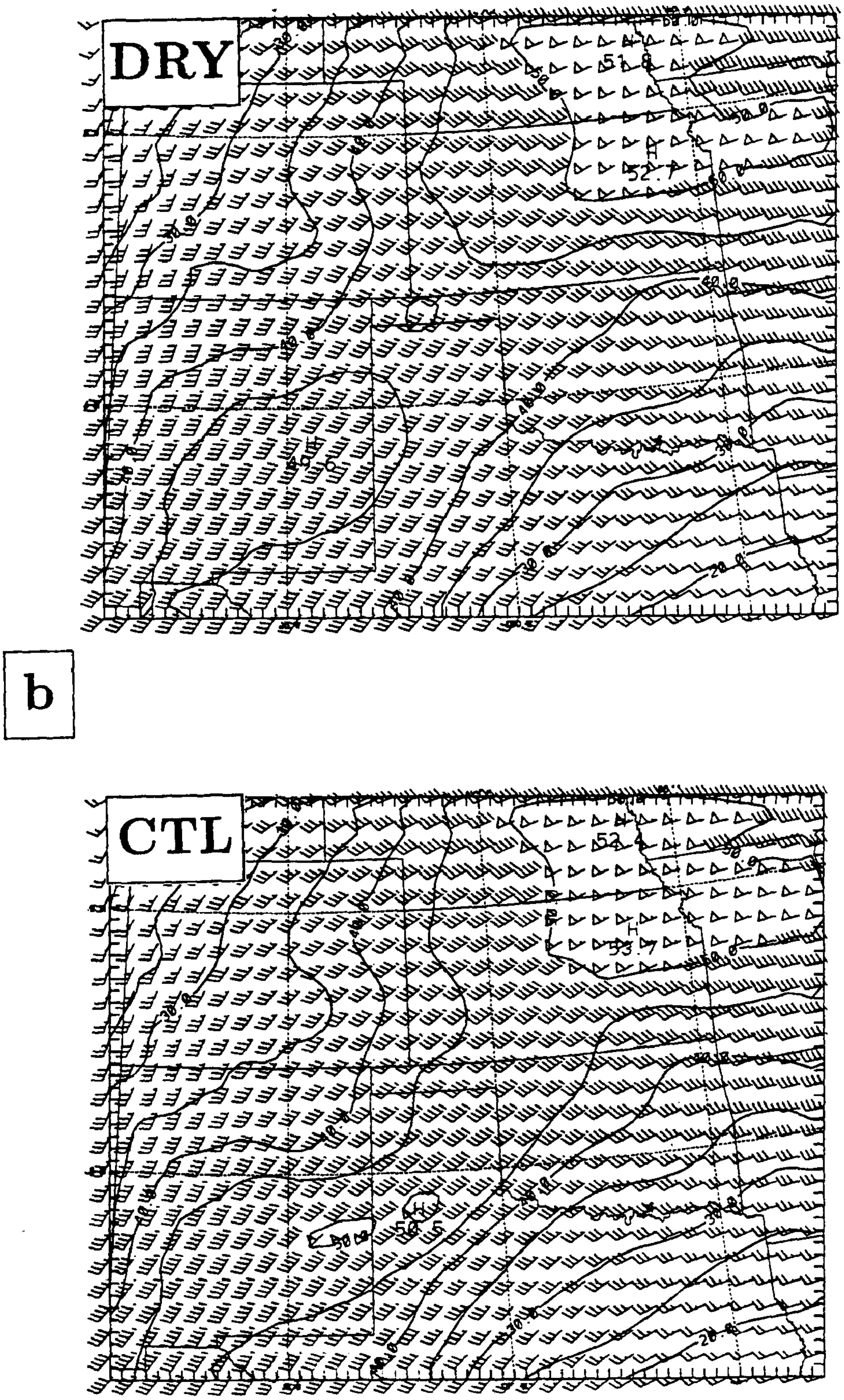

Figure 5.6: Continued.

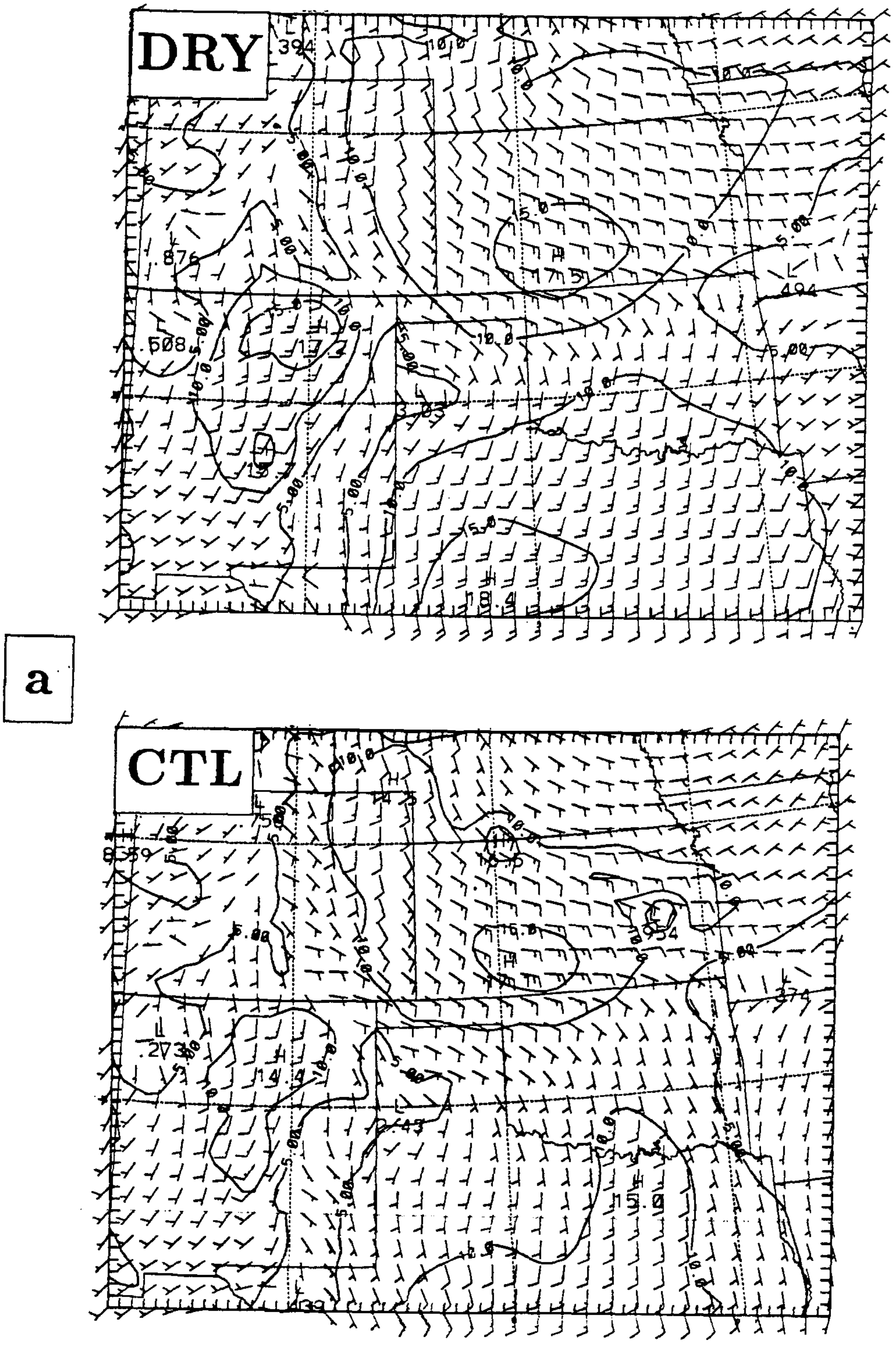

Figure 5.7: Isotachs (m s^{-1} , solid contours) and wind barbs for 3/1800 at the a) $\sigma = .915$ level and b) 200 mb level for DRY and CTL.

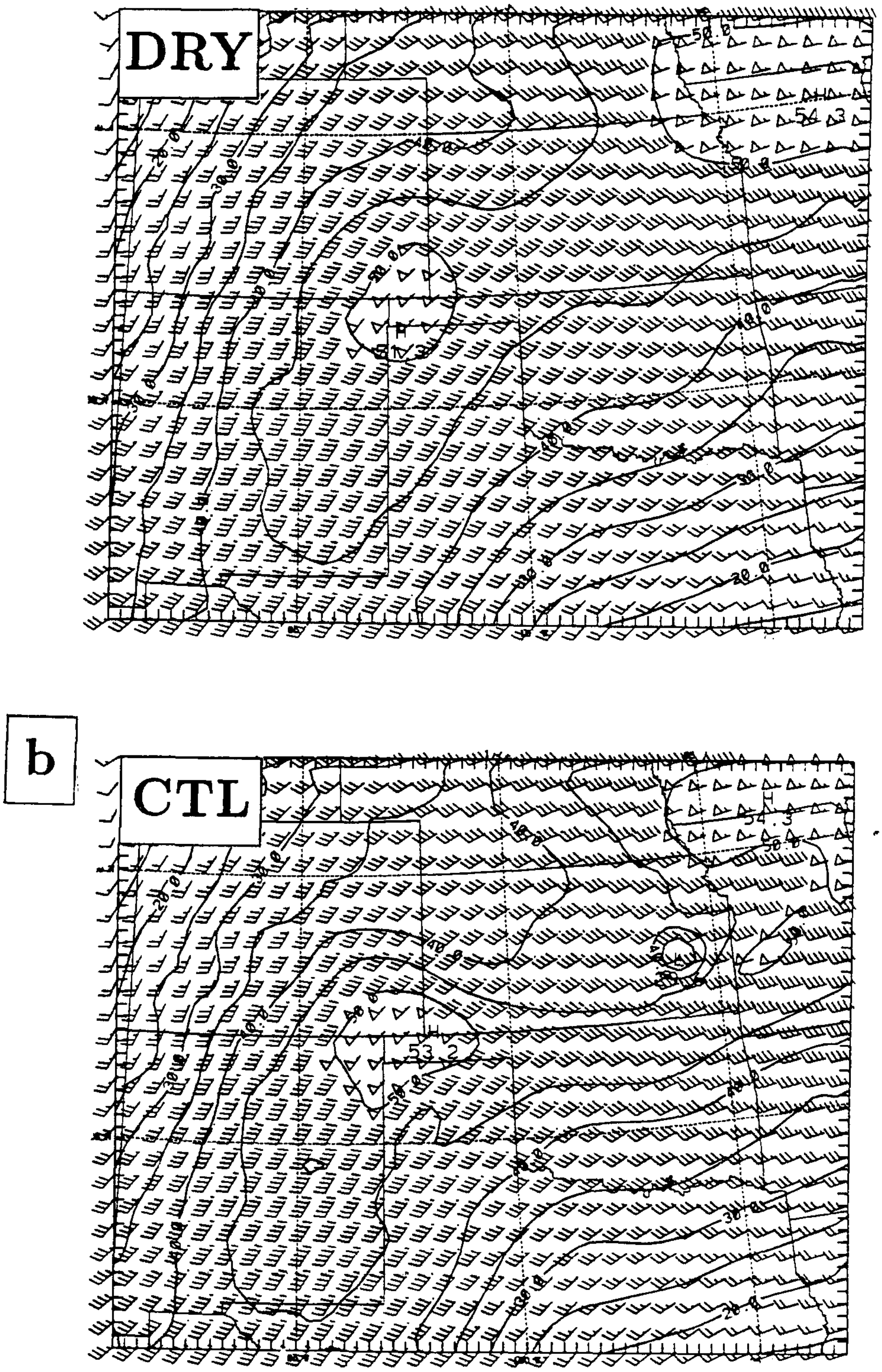

Figure 5.7: Continued.

location as DRY. It can be concluded that this LLJ is not caused by MCS1, but by dry dynamic processes. Three hours later, at 3/2100 (Fig. 5.8), the upper jet streak in DRY was elongated along the jet axis in northern Kansas. Meanwhile, CTL kept a more compact streak across western Kansas (interrupted by outflow from convection). CTL maintained strong southeasterly low-level winds across southern Kansas, with an axis from west of GLD to west of ICT. DRY had a similar low-level wind pattern, but speeds were smaller. This suggests that the moist processes associated with the low-level cloudy airmass in CTL were enhancing the low level flow, but the dry dynamics were primarily responsible for the LLJ.

Plots of isobaric potential vorticity from DRY were examined to explore the evolution of the front. Observations show large PV anomalies at fronts (Thorpe and Clough 1991) where isentropes intersect the ground and irreversible changes in PV can occur (Haynes and McIntyre 1987). Cooper *et al.* (1992) showed that surface fluxes as well as internal mixing of heat and momentum are significant sources of PV anomalies. Results from DRY are uncomplicated by diabatic effects as well as surface heat fluxes, but do include the effects of friction and diffusion. Following Hertenstein and Schubert (1991),

$$PV = g\,C\left\{\frac{\partial v}{\partial p}\left(\frac{\partial \theta}{\partial x}\right)_p - \frac{\partial u}{\partial p}\left(\frac{\partial \theta}{\partial y}\right)_p - \left[f + \left(\frac{\partial v}{\partial x}\right)_p - \left(\frac{\partial u}{\partial y}\right)_p\right]\frac{\partial \theta}{\partial p}\right\},$$

where C is a constant to convert to potential vorticity units (1 PVU = 10^{-6} m^2 s^{-1} K kg^{-1}). Initially at low levels, high potential vorticity values were located along the frontal zone (Fig. 5.9). In this region, $\partial\theta/\partial p$ is strongly negative. (The tongue of PV exceeding 1 PVU extending to the west in east-central Kansas is due to cyclonic vorticity produced by an easterly wind maximum along the Kansas-Nebraska border). By 3/1500 (Fig. 5.9b), 900 mb PV was still located along the frontal zone in northern Oklahoma with maximum values growing slightly as warm advection above 900 mb increased the vertical gradient in θ. At 3/1800 (Fig. 5.9c) higher PV values were found across central Kansas along a developing thermal gradient (not shown). The 900 mb PV maximum at 3/2100 (Fig. 5.9d) was located in central Kansas along the re-formed frontal boundary. A plot of the 900 mb temperature and winds (Fig. 5.10) shows that the maximum temperature

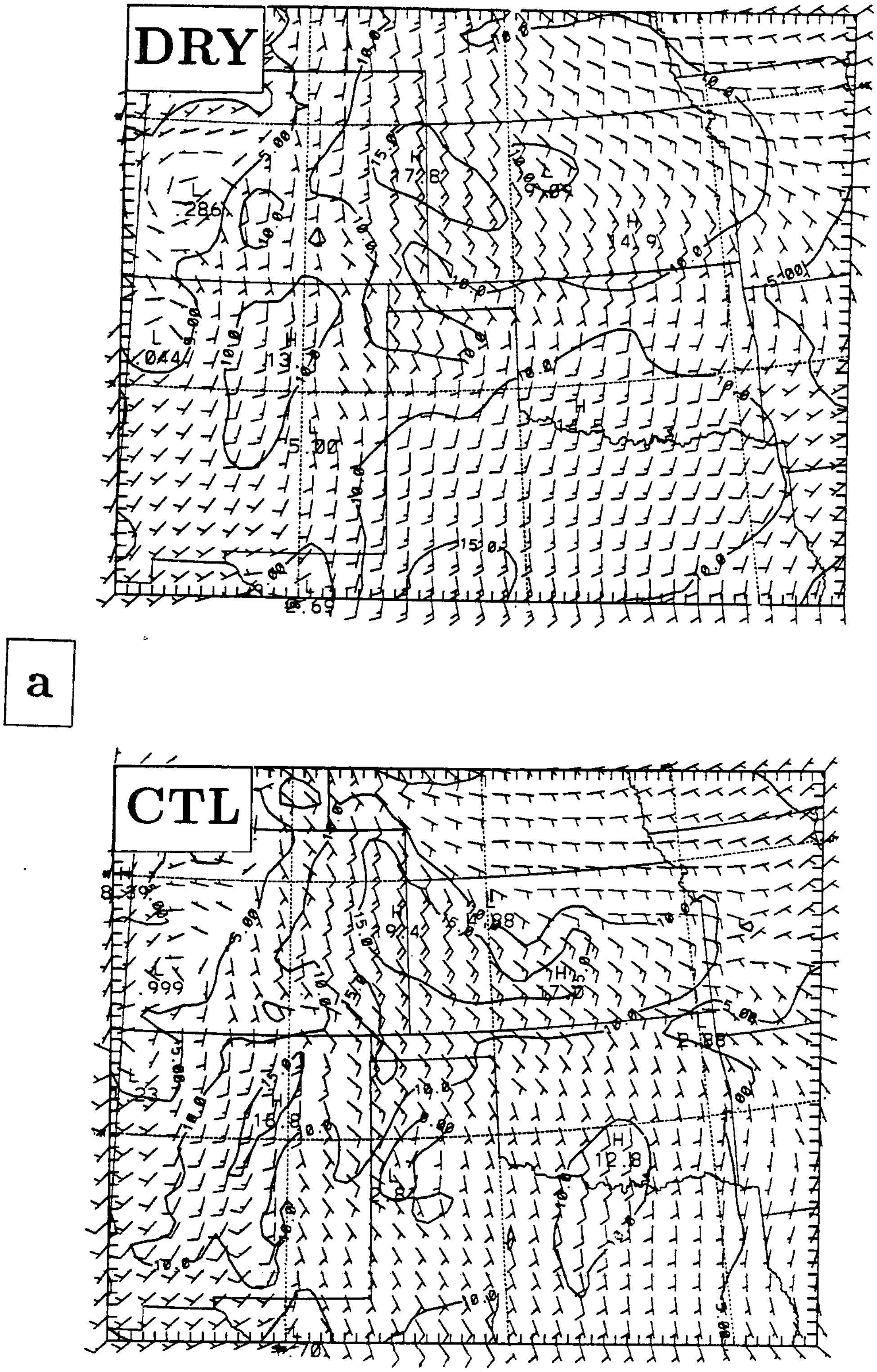

Figure 5.8: Isotachs (m s^{-1} , solid contours) and wind barbs for 3/2100 at the a) $\sigma = .915$ level and b) 200 mb level for DRY and CTL.

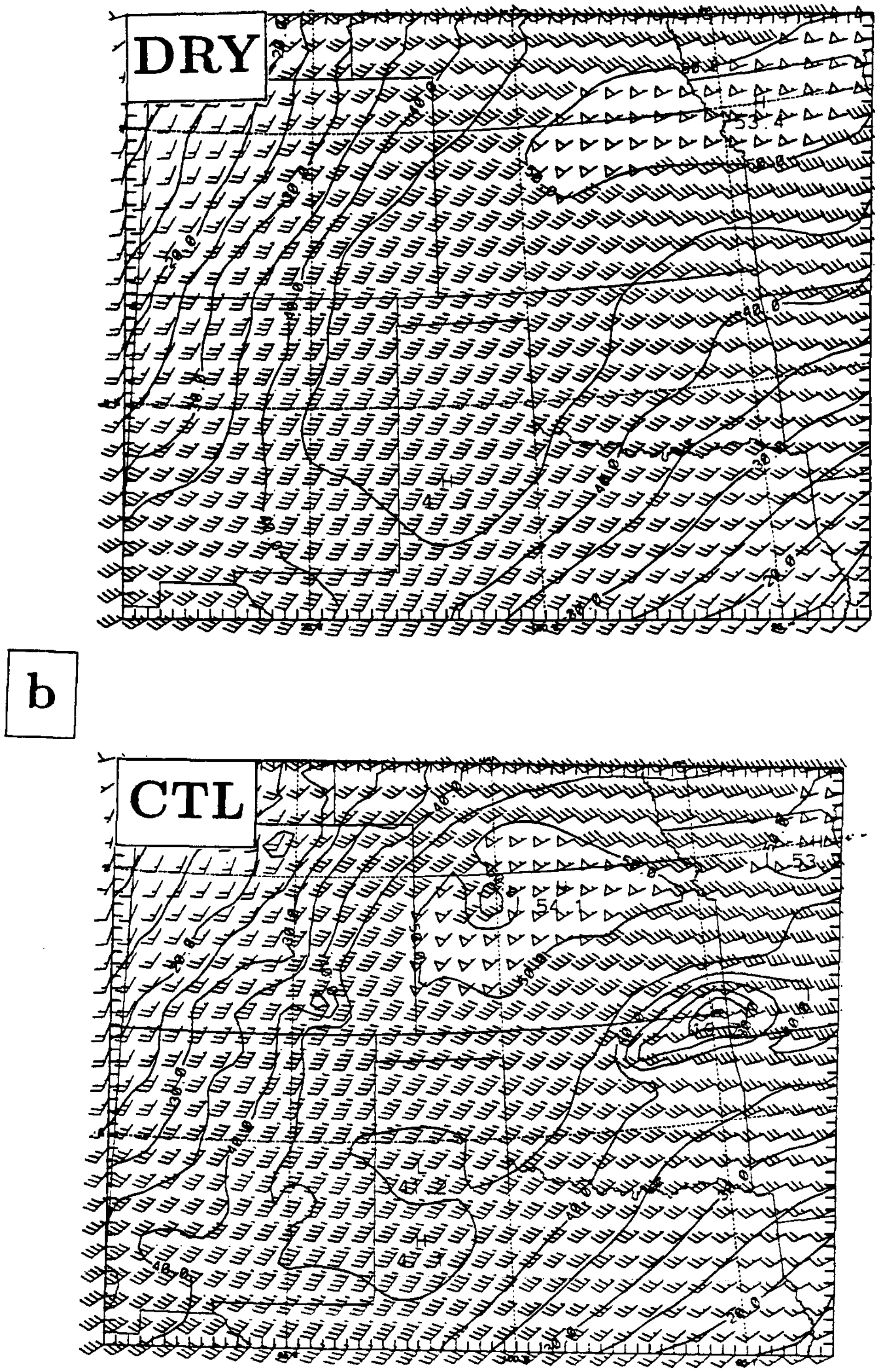

Figure 5.8: Continued.

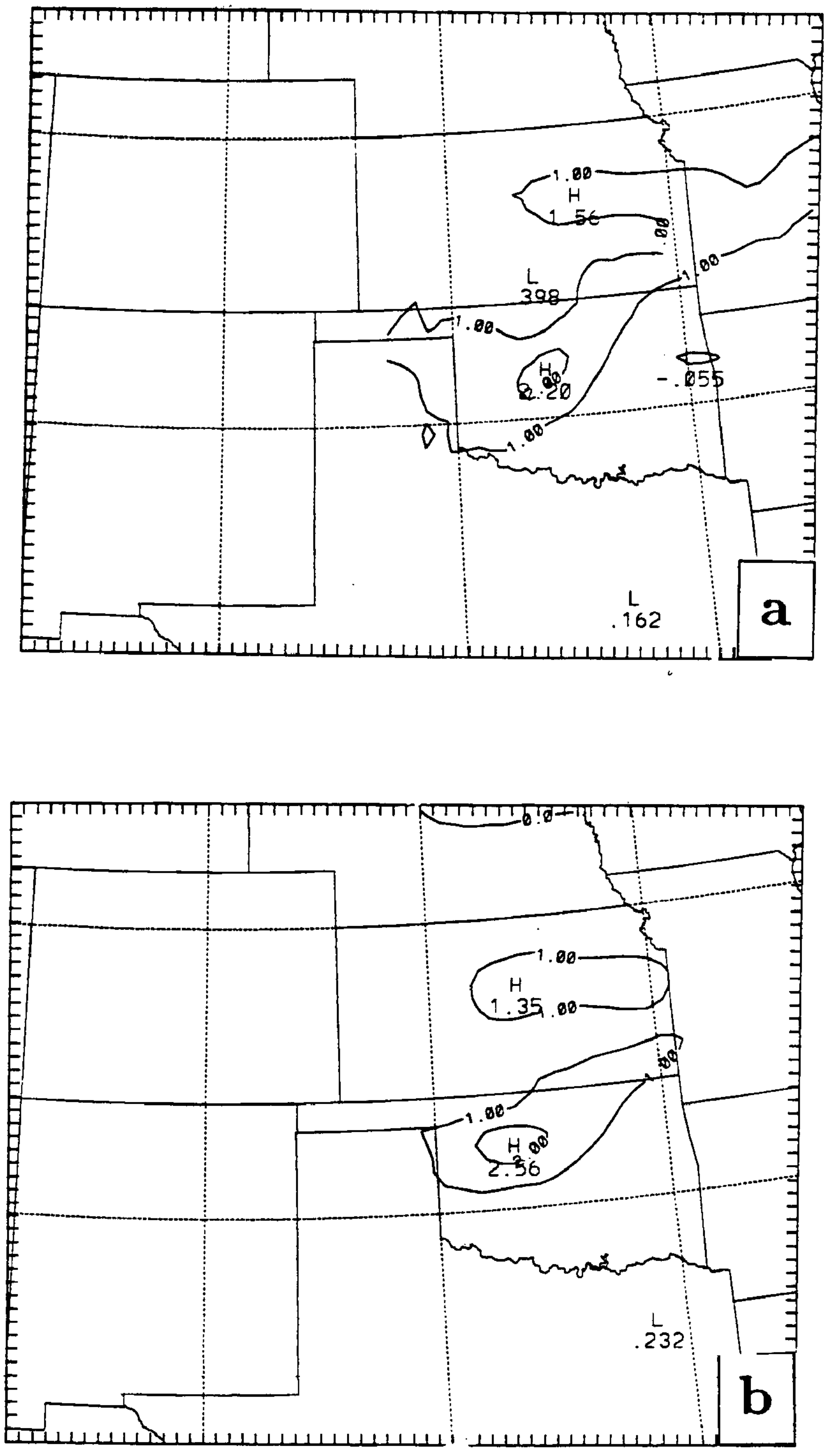

Figure 5.9: Potential vorticity (PVU, contoured every 1 PVU) at 900 mb from DRY at a) 3/1200, b), 3/1500, c) 3/1800, and d) 3/2100.

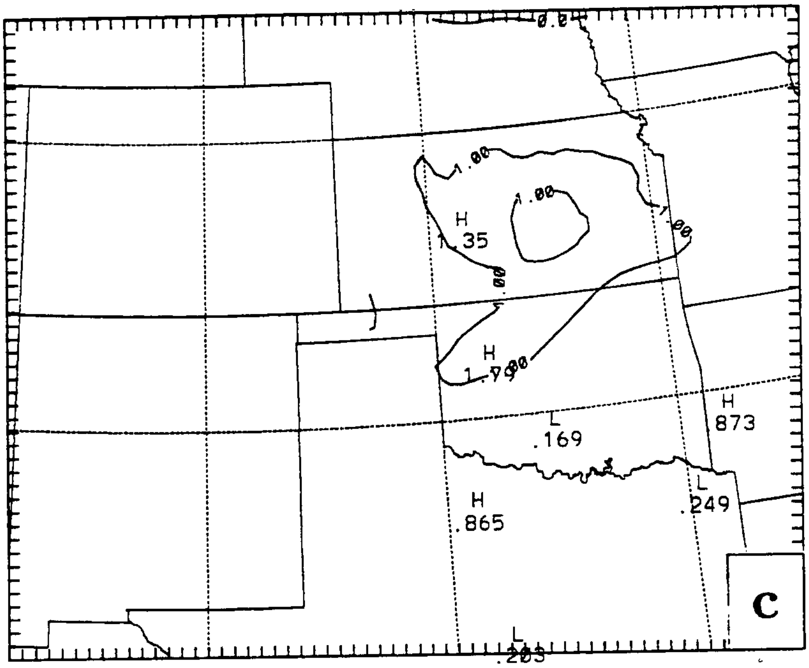

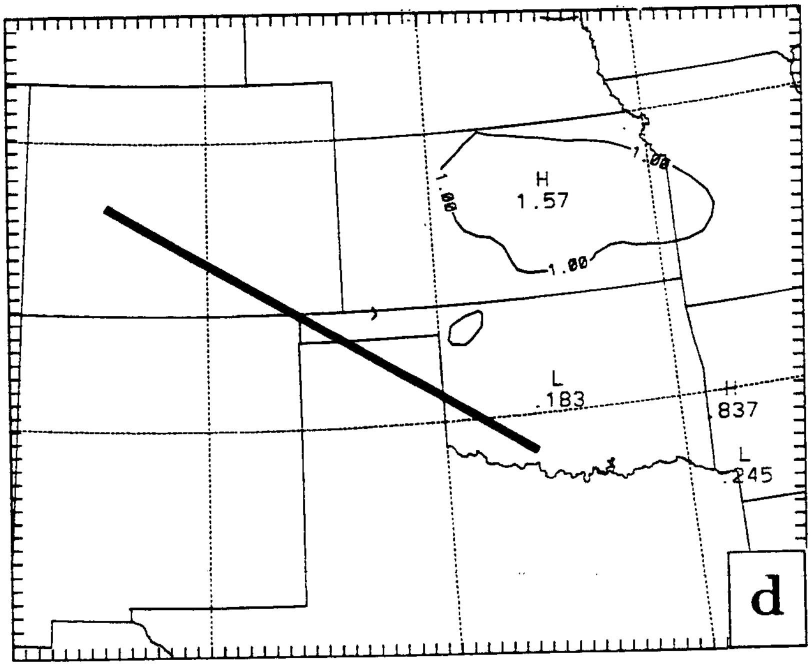

Figure 5.9: Continued.

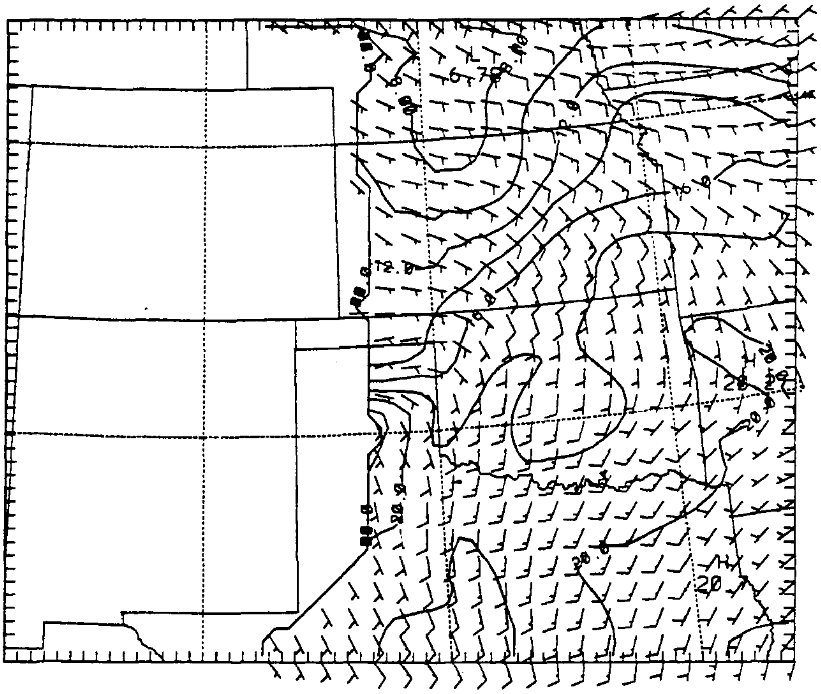

Figure 5.10: Temperature (° C, contoured every 2° C) and winds (1 full barb = 10 m s^{-1}) at 900 mb at 3/2100 from DRY.

gradient lies NE-SW across central Kansas with strong warm advection taking place. At the surface (Fig. 5.11), the front is across the Oklahoma-Kansas border extending westward into Texas. Because of the lack of surface heating, low-level temperatures are cooler than those found in CTL. However, the surface front in CTL was about 100 km farther to the south. Observations presented by Stumpf (1988) show that the surface front had moved northward into Kansas by 3/2000, before being pushed back southward at 3/2100 by outflow from MCS1 to a position between that predicted by CTL and DRY. Cloud shading and rain evaporation in the cool air north of the front may have pushed the front too far south in CTL. In DRY, low-level convergence and upward motion was centered near the PV maximum. It was along this thermal gradient in central Kansas that precipitation later formed in the CTL run. Because this area of upward motion appeared in the DRY run as well, it can be concluded that dry dynamic processes (such as frontogenesis) were responsible for its formation.

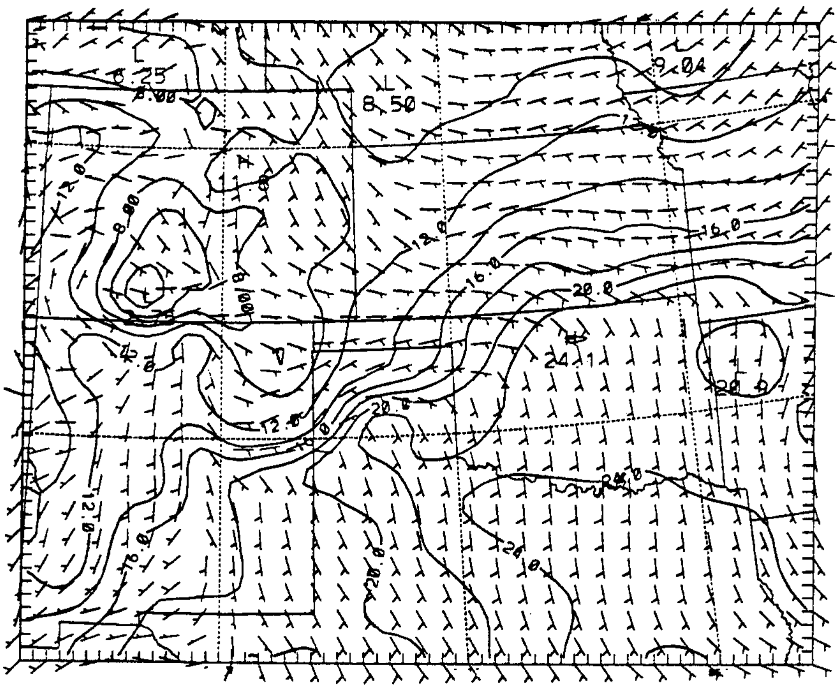

Figure 5.11: Surface temperature (° C, contoured every 2° C) and winds (1 full barb = 10 m s^{-1}) at 3/2100 from DRY.

The generation of the upper-level jet streak over eastern New Mexico and Kansas in DRY and the re-generation of the streak in CTL occurs in a region of confluent geostrophic deformation between the large-scale trough to the west and the ridge to the east. This is a region favored for the development of jets and streaks (e.g. Namias and Clapp 1949; Shapiro 1982). Cross-sections of potential vorticity taken perpendicular to the upper-level flow show that the tropopause, approximated by the 1.5 PVU surface (Bluestein 1993) was lower to the west and north of the jet axis (Fig. 5.12). (Curiously, the 1.5 PVU contour on the 200 mb surface was parallel to and just slightly poleward of the track of MCS2). The jet core straddled the tropopause in a manner similar to that shown by Reiter (1963) for the subtropical jet. While the slope and descent of the tropopause was not as great as cases described in the literature (e.g. Shapiro 1978), the processes leading to jet streak formation could be expected to be similar. The re-generation of the streak in CTL (and its existence in NOJS and DRY) suggest that the initial upper-level wind field may not be as important as the initial thermal structure for simulating the placement

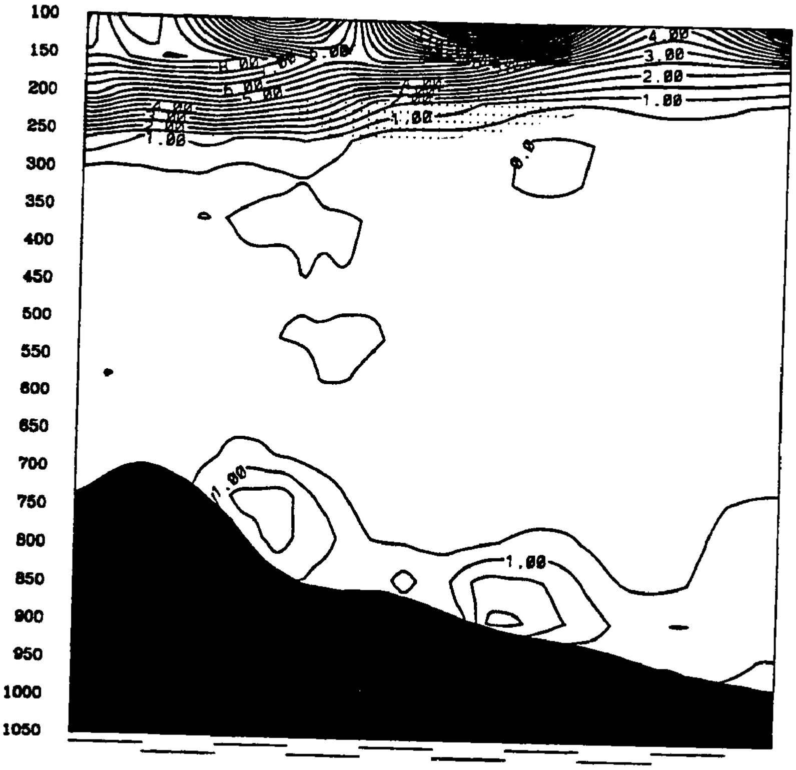

Figure 5.12: Northwest-southeast cross section along the line shown in Fig. 5.9d of potential vorticity at 3/1800 from DRY. Regions with wind speeds greater than 45 m s^{-1} are shaded.

and strength of the jet streak in this case. A more detailed diagnosis of this streak was not performed because of difficulties with the calculation of the geostrophic wind by the back-end programs. Computation of geopotential heights are very sensitive to the surface pressure and the results were quite noisy in regions with complex terrain. The geostrophic and ageostrophic winds (and their gradients) were quite noisy and any results were not meaningful. An additional simulation could be conducted with initial conditions that contain a smoothed thermal field and the actual wind field (similar to the approach of Hoke and Anthes 1976).

The 800 mb vertical velocity fields at 3/2100 from DRY and NOJS are shown in Fig. 5.13. Since both of these runs use the same initial data, differences in the results can be attributed to the omission of moist processes and, to a lesser extent, surface sensible heating from DRY. As described earlier, the results from NOJS are similar to those from CTL. Both DRY (Fig. 5.13a) and NOJS (Fig. 5.13b) (as well as CTL (Fig. 4.17b)) have upward motion across northern Kansas along and north of the frontal surface. Both runs have a band of upward motion extending from central to southeast Oklahoma in a region of speed convergence at the terminus of a broad low-level jet (Fig. 5.8). Both runs have upward motion maxima across western Texas near MAF. Finally, both runs have downward motion across southwest Kansas and the northern Texas panhandle. The largest differences occur in the regions of simulated convection. DRY (Fig. 5.13a) has a region of sinking in northeast Oklahoma and southeast Kansas while NOJS (Fig. 5.13b) has strong upward motion associated with the erroneous frontal convection there. Strong sinking at 800 mb is found beneath MCS1 and MCS2 (Fig. 5.13b) which is not present in the DRY simulation. While DRY has some sinking over the Texas panhandle, the sinking is two to four times stronger beneath the explicit rain area in NOJS. This suggests that it is the downdrafts beneath the explicit rain area in NOJS (and CTL) that are predominantly responsible for suppressing the simulated MCS2 convection, although speed divergence behind the low-level jet across western Kansas and eastern Colorado (Fig. 5.8) also contributes to the sinking.

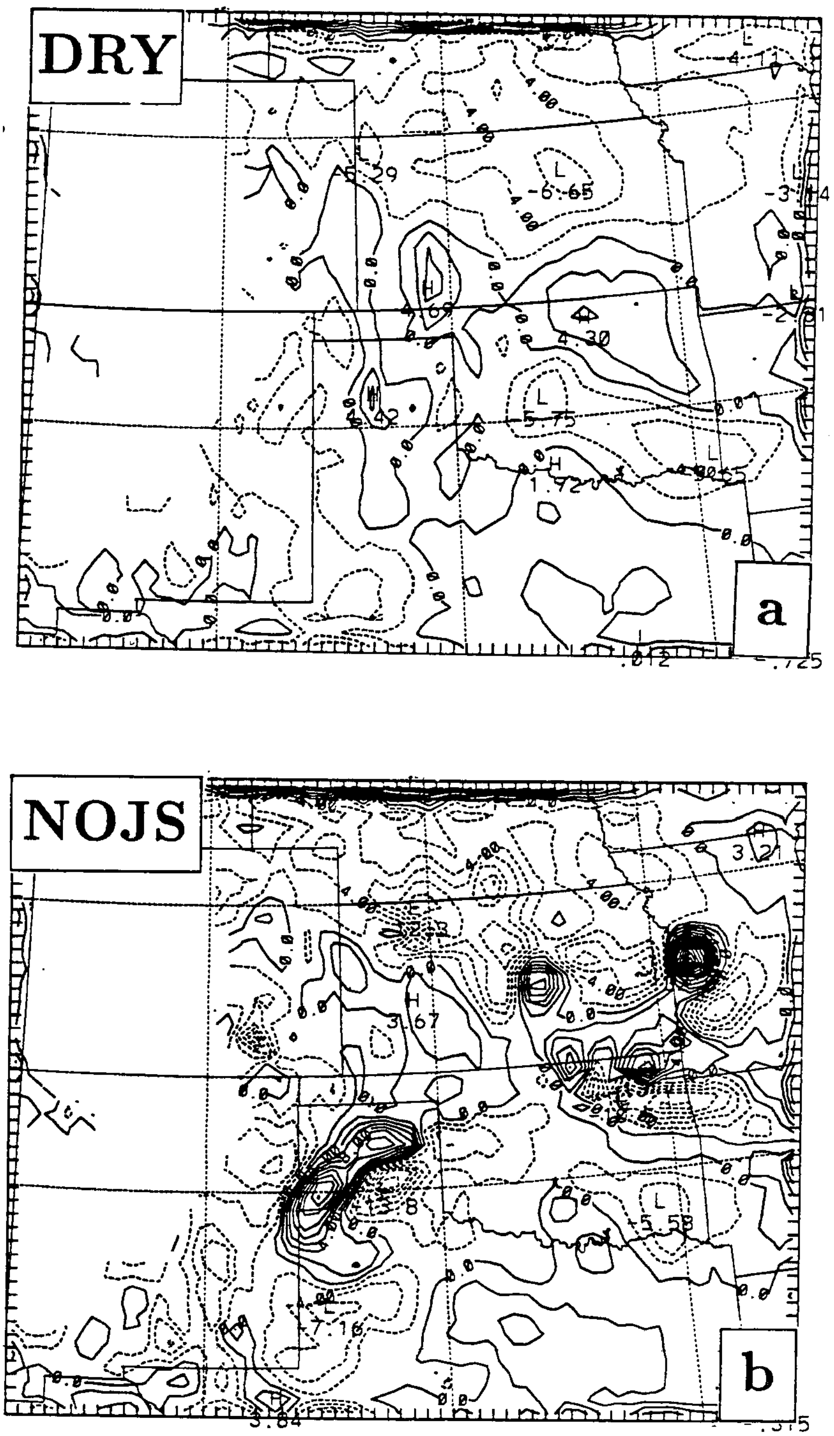

Figure 5.13: Vertical velocity, ω (μb s^{-1} , contour interval of 2 μb s^{-1} with negative values dashed) on the 800 mb surface at 3/2100 from a) DRY and b) NOJS.

5.1.3 No MCS1

As described earlier, a LLJ developed over Kansas in the vicinity of and in the wake of MCS1 in both CTL and NOJS, as well as in the DRY run. A simple test to determine what role the MCS might have played in the development of the jet is described in this section. In NOM1 parameterized convection over the eastern two-thirds of Kansas was not permitted between 3/1200 and 3/1900. In all other respects the model run was identical to CTL. The artificial suppression of the convection leaves only the explicit moisture scheme to remove the instability. And, as has been demonstrated in other studies (e.g. Dudek 1988) the explicit-only runs have a large spin-up time for developing MCS precipitation on a relatively large 25 km grid. The effect of eliminating implicit MCS1 convection is to remove the thermodynamic effects that MCS1 may have had on the atmosphere over eastern Kansas.

Fig 5.14 shows the time evolution of the total rain tendency (implicit plus explicit) at three-hour intervals. At 3/1500 (Fig. 5.14a), no precipitation was simulated over Kansas. A small area of convective rain was over west Texas. By 3/1800 (Fig. 5.14b), an area of convective rain over the Texas panhandle and eastern New Mexico was very similar to the MCS2 development within the CTL run. The only simulated rain in Kansas was in the southwest corner where some very small amounts of explicit rain were produced in the saturated low-level airmass. Fig. 5.14c shows the 3 h total rain ending at 3/2100. Convection along the Colorado mountains and in the southern Texas panhandle develops as in CTL. There is no rain area in eastern Kansas and western Missouri that corresponds to the rain area identified as MCS1 in CTL. However, there are a couple of other interesting similarities to CTL. The convective rain area in northwest Kansas attributed to the LLJ in CTL has also developed by this time in NOM1. In addition, the erroneous convection along the surface front in northern Oklahoma has also developed in NOM1. It can be inferred that the simulated MCS1 in CTL was not responsible for the development of the convection in northwest Kansas or northern Oklahoma.

The time evolution of the upper and lower wind fields are shown in Fig. 5.15. At 3/1500 (Fig. 5.15a) both the 200 mb and $\sigma = .915$ NOM1 wind fields are similar to CTL

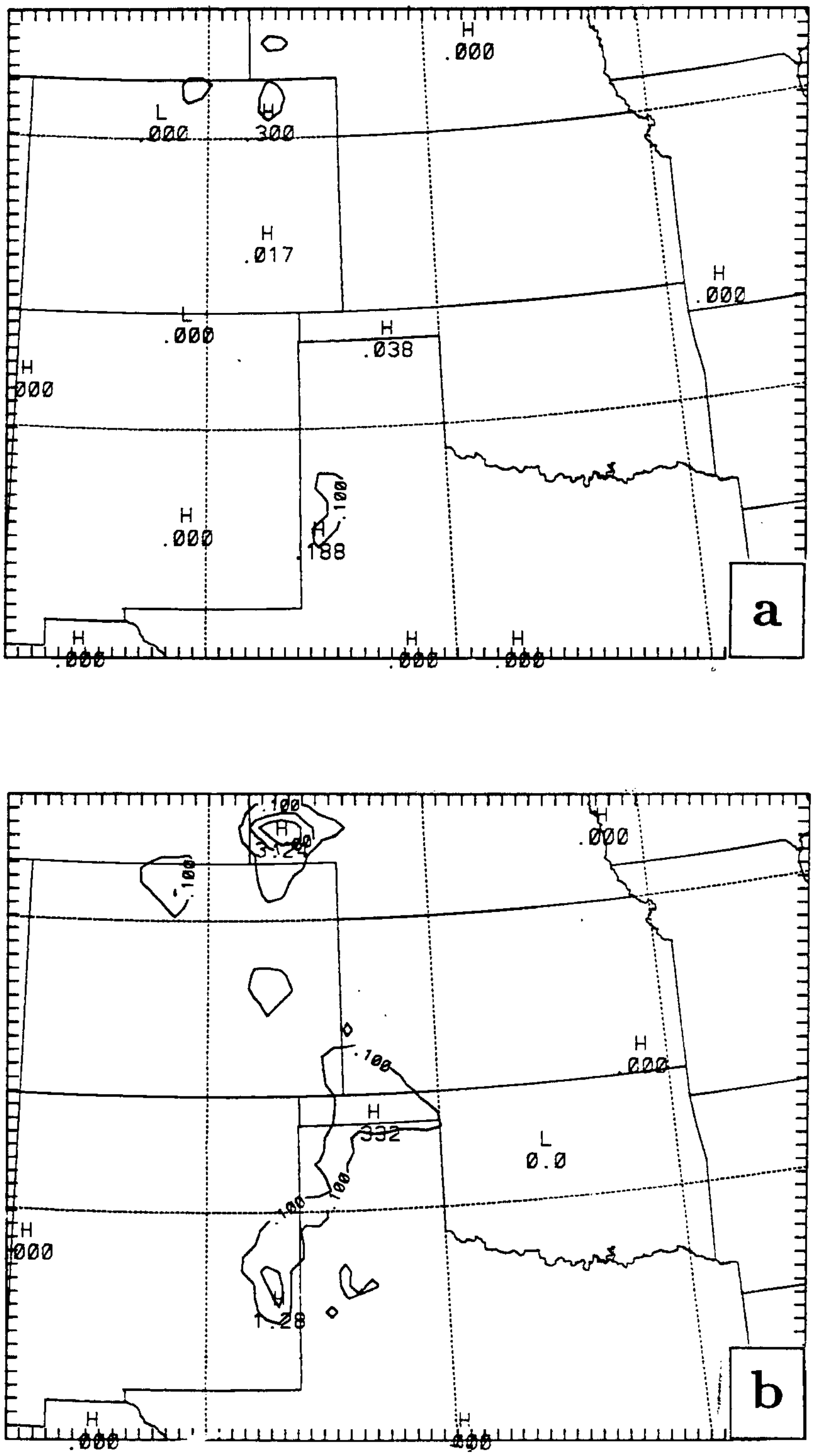

Figure 5.14: Three-hour total rainfall tendency (implicit plus explicit, in mm $(3\ \mathrm{h})^{-1}$ from NOM1 contoured as in Fig. 4.5a) at a) 3/1500, b) 3/1800, and c) 3/2100.

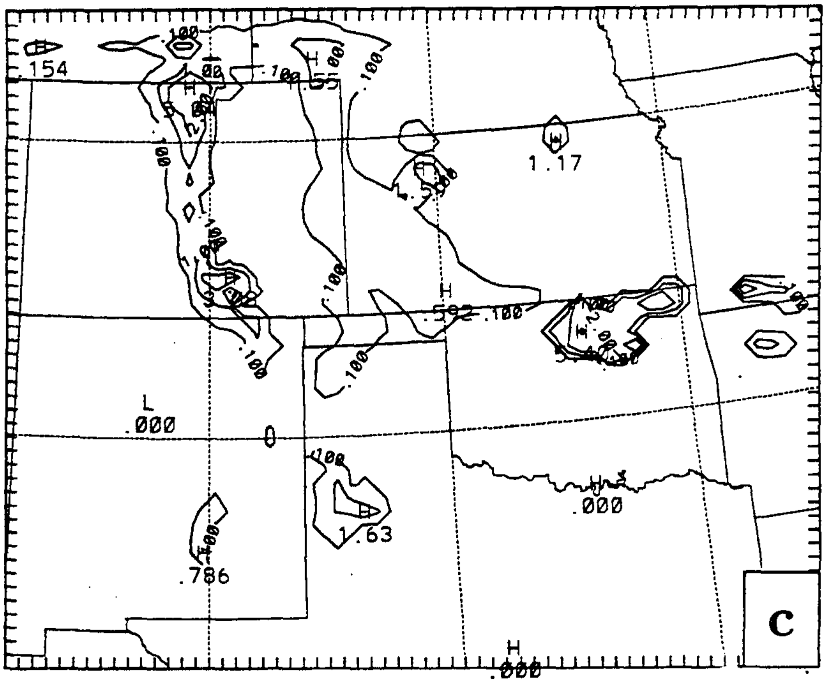

Figure 5.14: Continued.

(Fig. 4.32) with an upper-level jet streak over eastern New Mexico and the southern Texas panhandle and another upper jet streak over northeast Kansas and with a broad area of easterly low-level flow across Kansas. The small area of reduced low-level winds near MCS1 in CTL is not present in the NOM1 field. A Doppler wind analysis by Nachamkin (1992) also indicates reduced low-level easterly speeds to the rear of the MCS with stronger speeds on the north and south edges (his Fig. 6.8). At 3/1800 (Fig. 5.16b), the upper winds are similar to those in CTL (Fig. 5.4a) except over eastern Kansas where the MCS1 convection in the CTL simulation had reduced the wind speeds. Plots of 200 mb divergence (not shown) indicate an area of broad, weak divergence in the NOM1 simulation, while CTL exhibits strong divergence over MCS1 with a bow-wave-shaped area of convergence immediately upstream of the MCS1 convection. The low-level easterly winds in NOM1 (Fig. 5.16a) have increased and exceed 15 m s^{-1} over a broad area of central Kansas. The dual speed maxima are similar to CTL (Fig. 5.7a), but the low-level winds in CTL have an area of reduced speeds in the wake of MCS1 not found in the NOM1 simulation. Plots of divergence on the σ=.915 surface show little difference between the CTL and NOM1 runs,

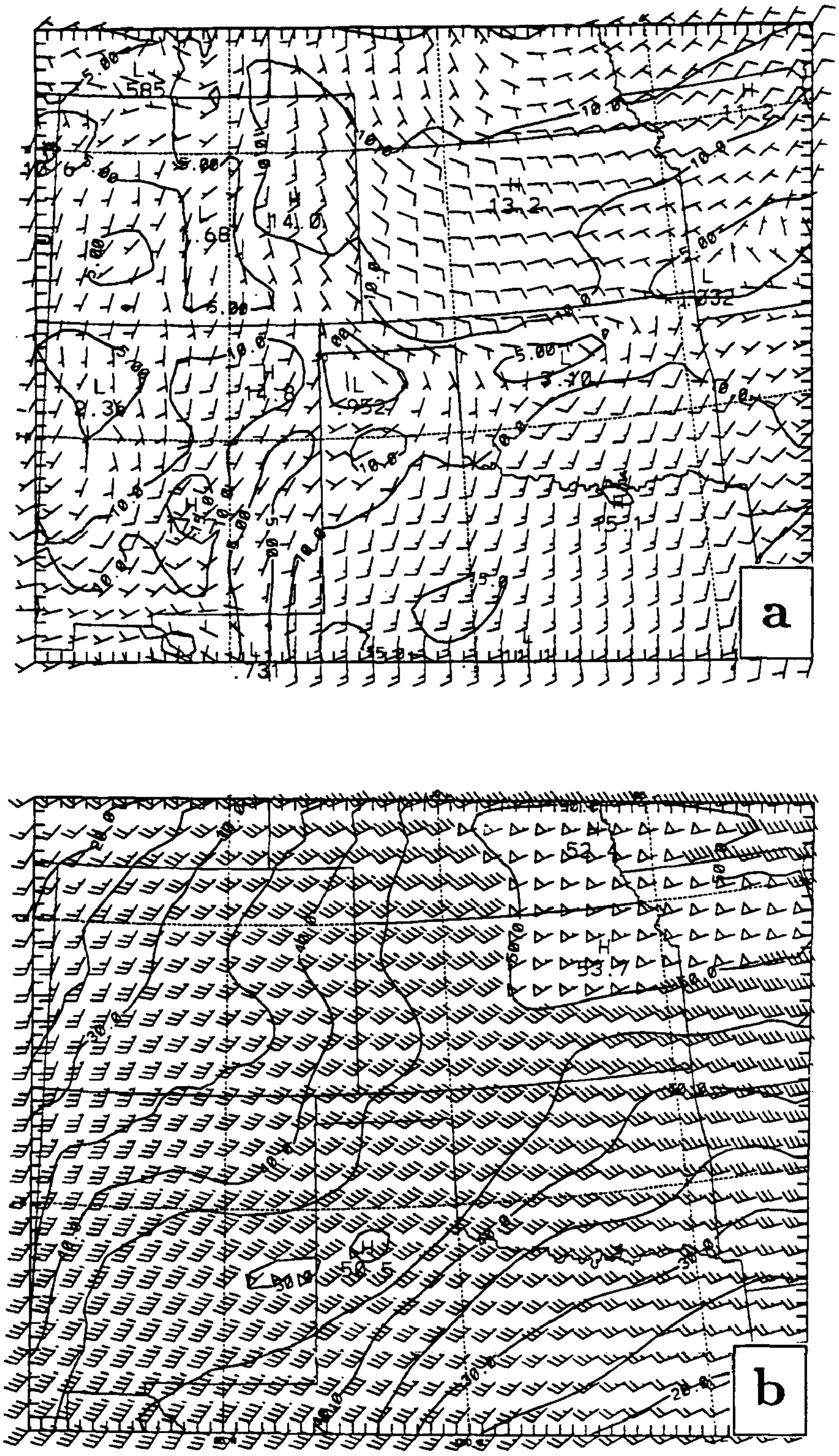

Figure 5.15: Isotachs (m s^{-1} , solid contours) and wind barbs for 3/1500 at the a) σ = .915 level and b) 200 mb level from NOM1.

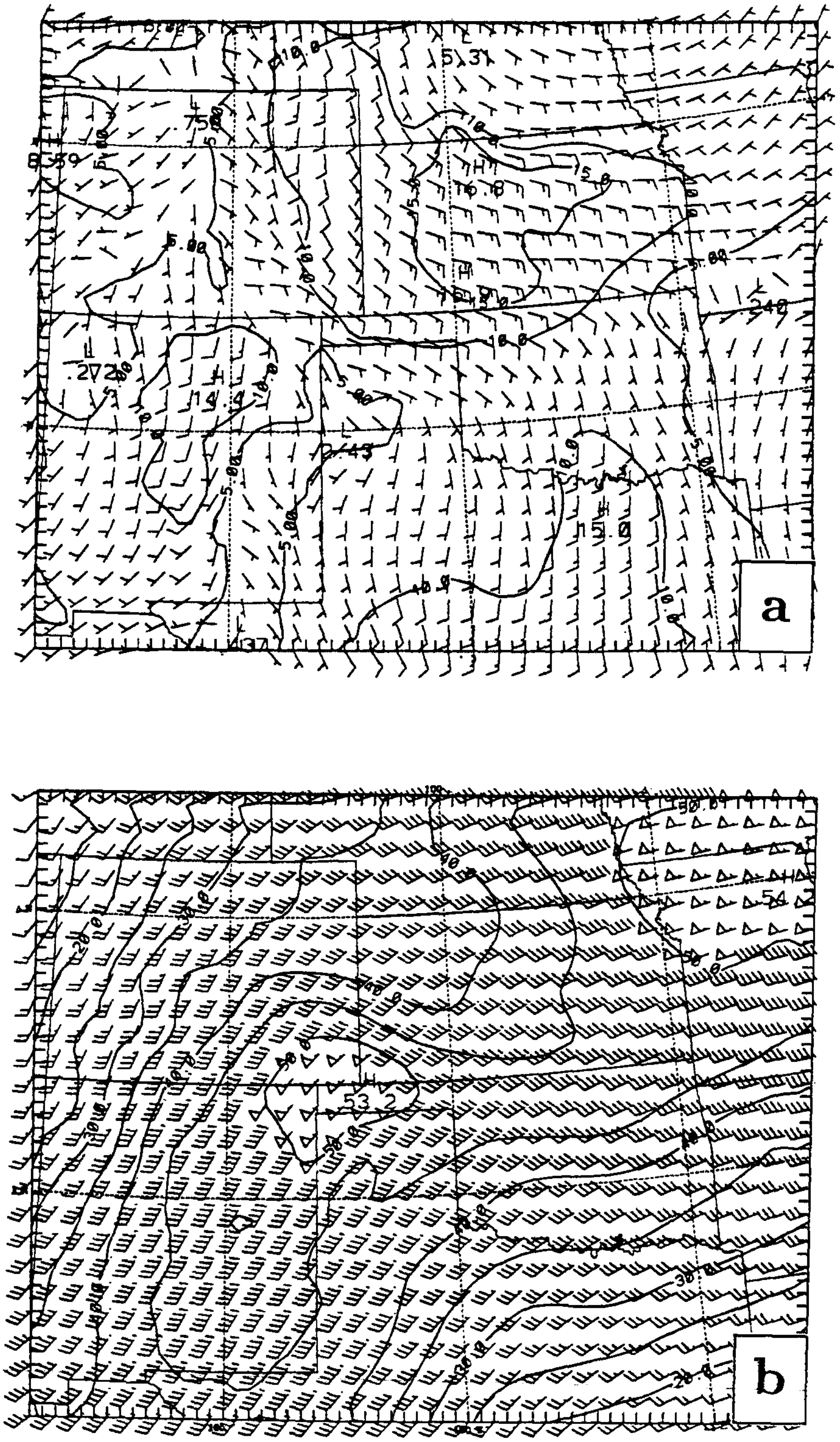

Figure 5.16: Isotachs (m s^{-1} , solid contours) and wind barbs for 3/1800 at the a) σ = .915 level and b) 200 mb level from NOM1.

except in the immediate vicinity of MCS1 (not shown). The 3/2100 NOM1 upper-level winds (Fig. 5.17) contain an area with speeds exceeding 50 m s^{-1} across northern Kansas into Missouri. The CTL run has reduced 200 mb speeds near the Kansas-Oklahoma-Missouri border and extending northward along the Kansas-Missouri border (Fig. 5.8b). At the σ=.915 level (Fig. 5.17a), winds exceeding 10 m s^{-1} were across the southern half of Kansas, extending northward along the Kansas-Colorado border. A nearly identical pattern was found in the CTL simulation (Fig. 5.8a). These enhanced winds led to a WNW-ESE convergence band at this level extending from north of RSL to northeast of CNU (Fig. 5.18). It can be concluded that this band (which in the CTL run, was likened to the observed WNW-ESE band within MCS2) was not influenced by MCS1, but was due to other dynamic processes as discussed in the previous sections.

In summary, comparison of runs without MCS1 (DRY and NOM1) with those that include the system (CTL and NOJS) shows that the simulated MCS1 had a minimal impact upon MCS2. An easterly LLJ developed over Kansas in all four runs as an upper-level jet streak approached the region. Reduced low-level easterlies were found in the immediate wake of the system. Any enhancement of the easterlies by low-level outflow from the system was obscured by the larger-scale processes. At upper levels, the effect of MCS1 was to create divergence and reduce the wind speeds keeping the jet streak over the northeast portion of the domain separate from the one approaching from the west.

5.1.4 NMC First Guess

To demonstrate the importance of the first guess field upon the evolution of the simulated convective systems, some results from NMCG will be presented. Experiment NMCG was identical to CTL, except for the initial conditions. The first guess field provided to RAWINS was the NMC 2.5° analysis rather than the MM4 first guess field used in CTL. The bogus soundings were included in the NMCG analysis.

The major difference between the initial fields was the moisture distribution. The difference in 700 mb specific humidity (MM4 first guess minus NMC first guess) is presented in Fig. 5.19. The biggest difference is in central Kansas, where the MM4 first guess field had 1.5 g kg^{-1} more moisture than the NMC first guess field. The 12 h MM4 simulation

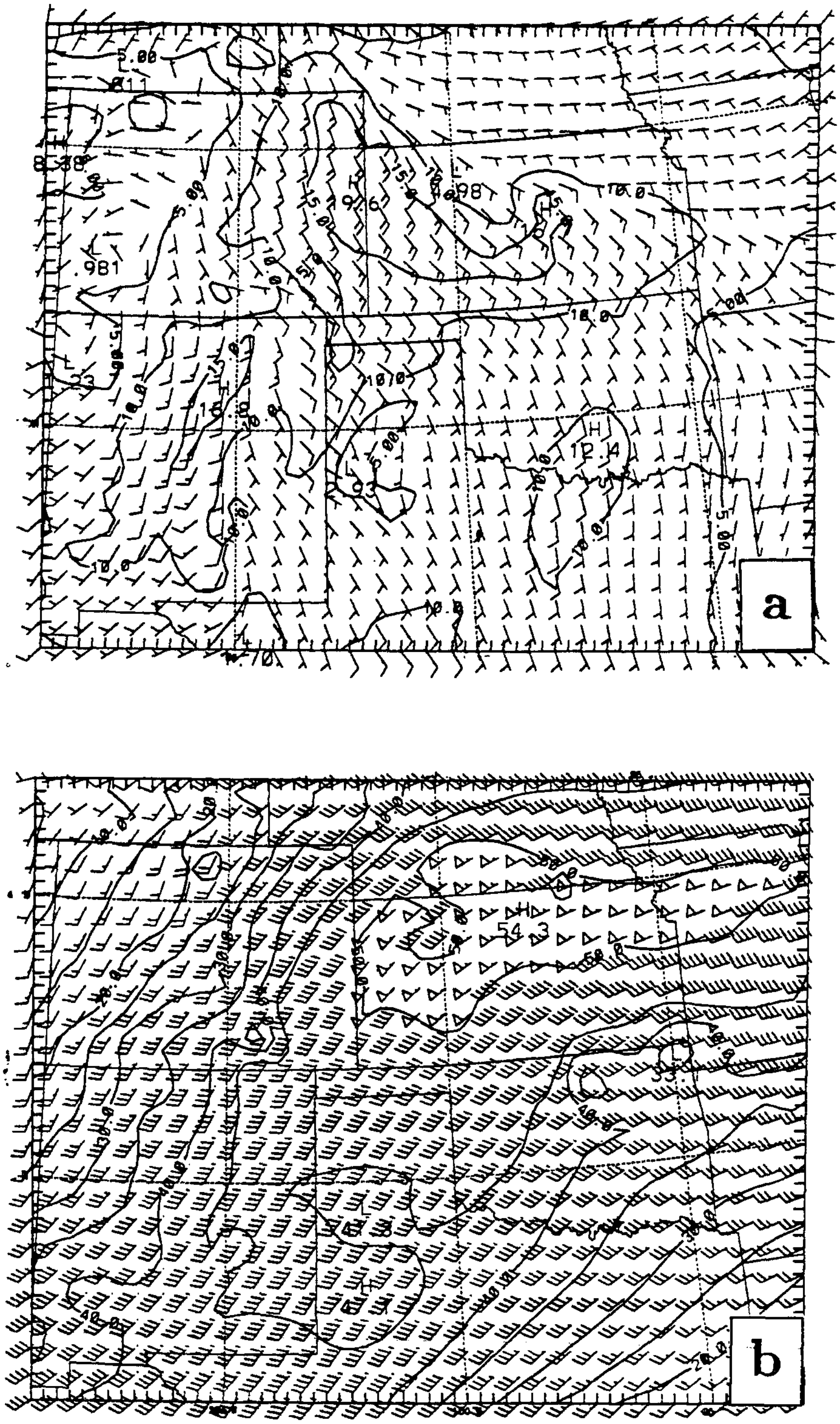

Figure 5.17: Isotachs (m s^{-1} , solid contours) and wind barbs for 3/2100 at the a) σ = .915 level and b) 200 mb level from NOM1.

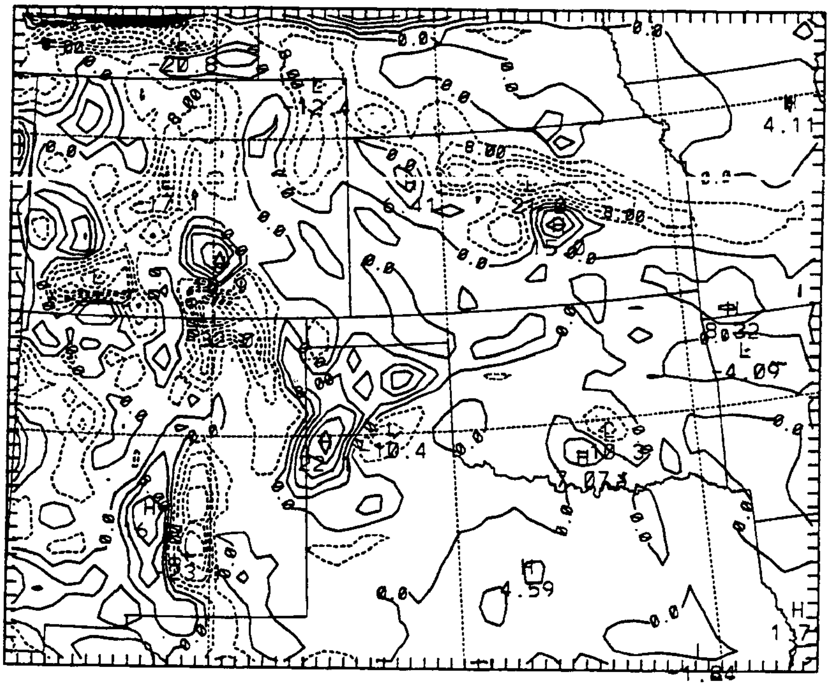

Figure 5.18: Divergence (10^{-5} s^{-1}, contoured every 4 x 10^{-5} s^{-1} with negative values dashed) on the σ = .915 level at 3/2100 from NOM1.

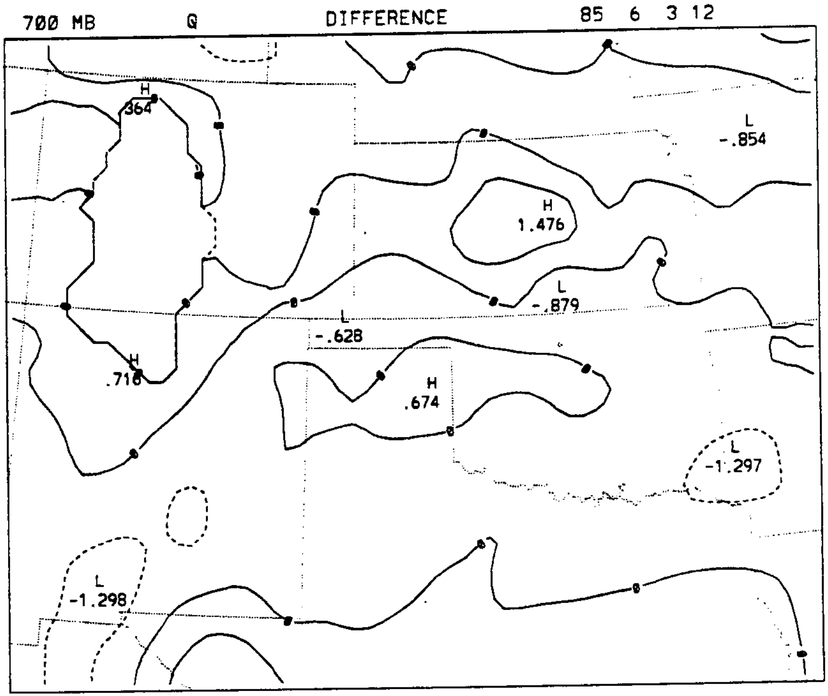

Figure 5.19: Difference in the 700 mb mixing ratio (g kg^{-1}) between the MM4 first guess initial condition and the NMC first guess initial condition at 3/1200. Contour interval is 1 g kg^{-1} with negative values dashed.

valid at 3/1200 had produced a rain area in central Kansas, so that the resulting first guess field had high humidities there. The NMC analysis had no corresponding area of high humidities and since the area was between observation sites, the NMC initial conditions were drier. The moist region in the MM4 first guess field was close to the cloud base in the region where simulated MCS1 convection began in CTL and so had a significant impact on the triggering of the convective parameterization. Differences in the other fields (T, U, V) were not as pronounced as the moisture differences, although the MM4 first guess field had more low-level convergence across central Kansas.

Fig. 5.20 shows the simulated convective rainfall for NMCG. No convection was found over Kansas at 3/1500 (Fig. 5.20a) as there was in CTL (Fig. 4.3a). The small convective amounts along the New Mexico-Texas border and in Colorado were different from CTL as well. By 3/1800 (Fig. 5.20b) NMCG had developed convective rain along the Oklahoma-Kansas border, south and east of the observed location of MCS1. There was more convection over the Texas panhandle than in CTL, which agrees better with observations (e.g. Fig. 2.16g). Due to the difference in initial moisture distribution, NMCG produced much less explicit rain water over E New Mexico and Texas than CTL (not shown), so there was less suppression of surface-based convection in the Texas panhandle. This resulted in a better (though not perfect) simulation of the early MCS2 convection. By hour nine of the simulation (3/2100, Fig. 5.20c), the area of rain over northern Oklahoma had grown, but had moved only slowly eastward. Areas of convective rain extended into southeast Kansas and back toward the west near DDC. The rain area over the Texas panhandle had moved eastward to along the Oklahoma border. Both of the major rain areas (over northern Oklahoma and along the Oklahoma-Texas border) had developed strong cold pools and the attendant low-level moisture convergence (not shown). As in other runs using the FCT, convection developed too far south, propagating with the low-level convergence.

In summary, the evolution of the convective systems in this weakly-forced case during the early part of the simulation is quite dependent on the initial conditions and the first guess field in particular. The initial moisture distribution influences the timing and

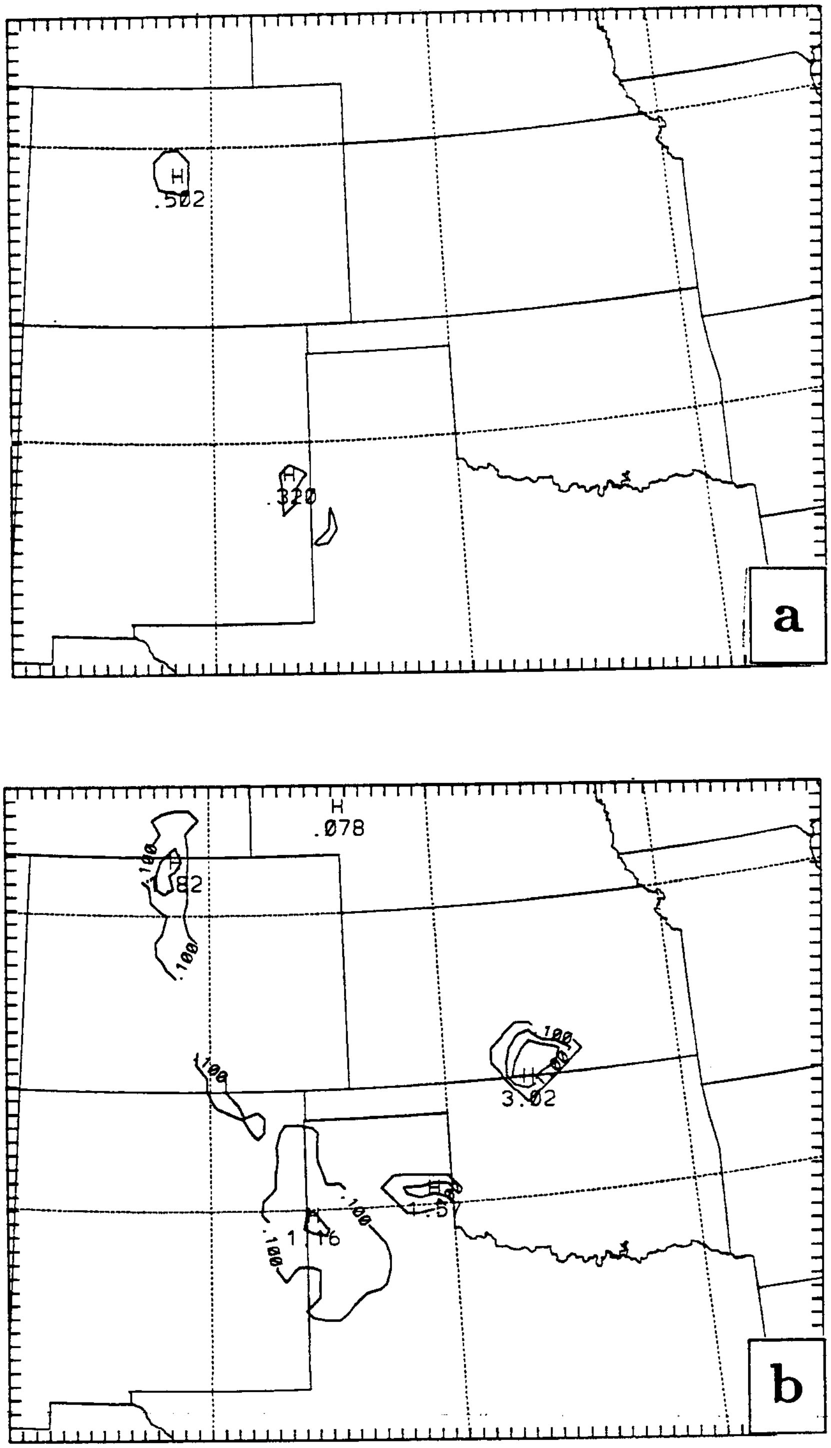

Figure 5.20: Three-hour convective rainfall tendency for NMCG at a) 3/1500, b) 3/1800, and c) 3/2100.

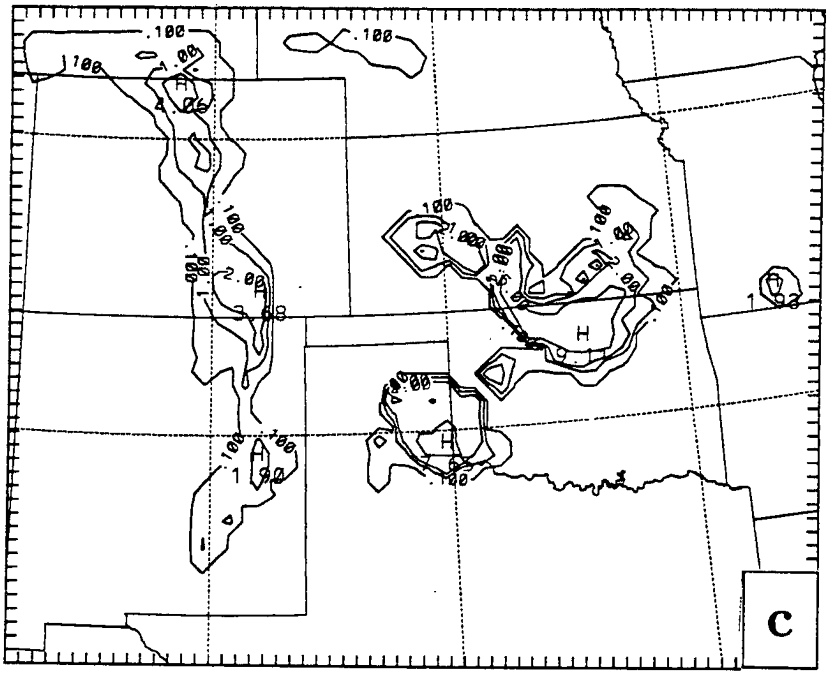

Figure 5.20: Continued.

location of the development of both implicit and explicit rain. Subsequent evolution of the implicit rain over the Texas panhandle is related to the circulations produced by the explicit rain. When less explicit rain is present and the mesoscale downdrafts are weaker or nonexistent, surface-based convection develops in a more realistic manner. While Stensrud (1992) argued that mesoscale surface features are important in weakly-forced cases, the results here suggest that features aloft, particularly the moisture distribution, are important for the simulation of some cases. While simulations of some cases may develop realistic meso-β-scale convective features from initial data that includes only the standard synoptic-scale soundings (as in Zhang *et al.* 1989), simulations of other cases are unable to develop realistic results even with several mesoscale bogus soundings. As Anthes *et al.* (1989) stated, some cases are harder to forecast than others. A future challenge will be to determine *a priori* the forecastability of a given case.

5.1.5 3/0000 Initial Time

The purpose of Z0 was to simulate the mesoscale conditions leading to the formation and evolution of MCS1. The model runs initialized at 3/1200 were not in a state of internal balance at the time of MCS1 initiation and the undersampling of the atmosphere by the standard rawindsonde network may have led to inadequate initial conditions (e.g. improper moisture distribution along the front). By hour thirteen of a model run started at 3/0000, the model would have reached a state of internal balance and might be expected to have produced a reasonable simulation of the MCS1 environment.

Unfortunately, there are difficulties in initializing a model run at 3/0000 as well. A small area of vigorous convection had developed along the surface front by initial time (Fig. 2.8a) which grew and moved eastward (Fig. 2.8d). Initializing a model containing diabatic heating is still a research topic (e.g. Wang and Warner 1988). The actual model initial surface temperature and wind field (Fig. 5.21) contained a frontal temperature gradient much broader than reality (Fig. 2.7) due to the coarse analysis grid. In addition,

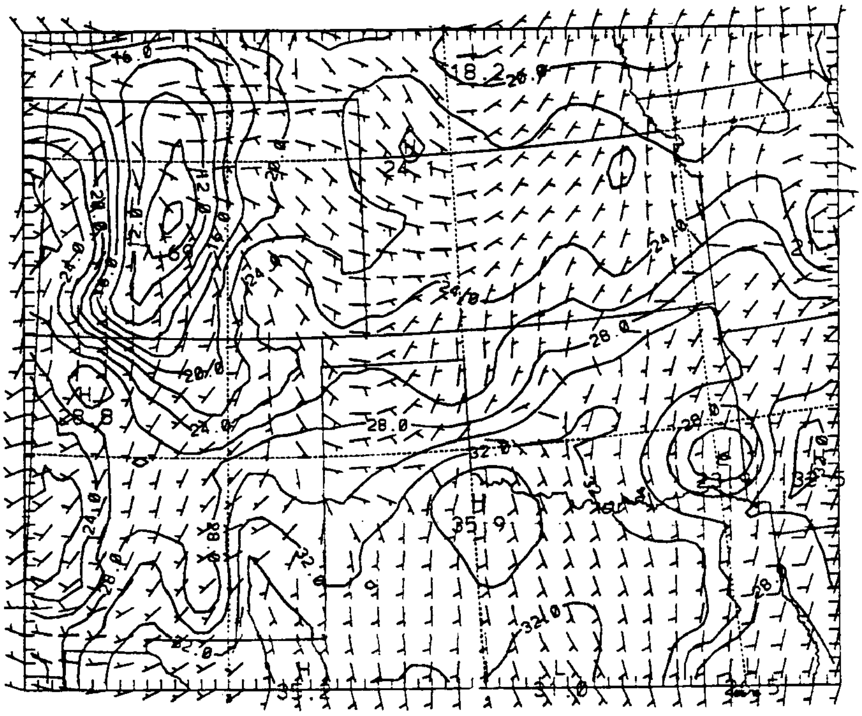

Figure 5.21: Initial analysis of surface temperature and winds, as in Fig. 5.11 at 3/0000.

the region of surface convergence along the front was weaker and broader than might be expected (Fig. 5.22) although there was a maximum in surface convergence near the

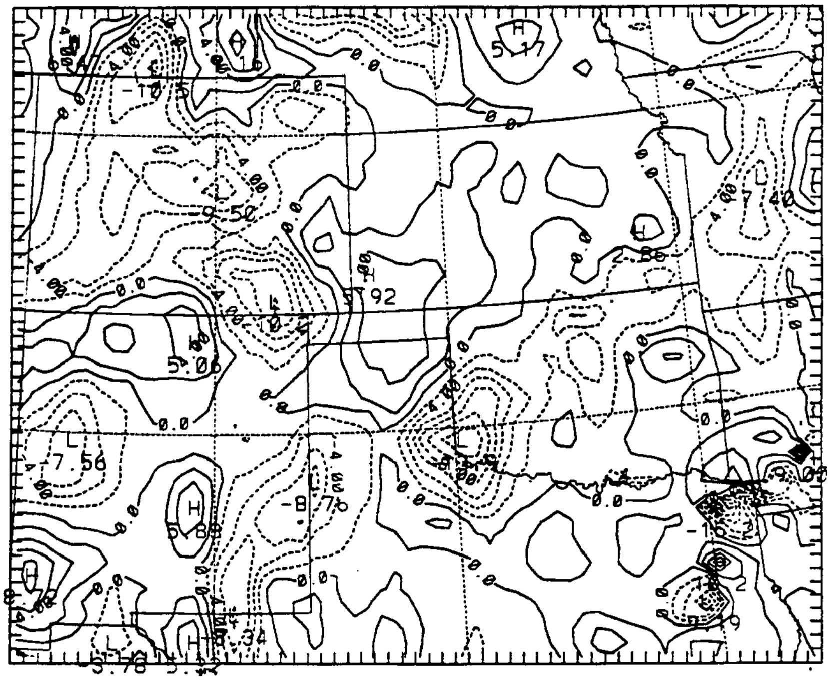

Figure 5.22: Initial surface divergence (as in Fig. 5.18) at 3/0000.

observed convection. Plots of surface and minimum LI (not shown) indicate the most unstable parcels were at or just above the surface as might be expected in a well-mixed late afternoon boundary layer. The most unstable area (minimum LI) was co-located with the maximum surface convergence near LTS in southwest Oklahoma. However, the CIN trigger did not initiate convection there, as the negative area was substantial due to the subsaturated subcloud layer. Fig. 5.23 shows a skew-T plot from a model grid point near LTS. Considerable lifting would be needed to overcome the negative area found between 800 and 700 mb. During the first couple of hours of the simulation, the model tightened the temperature gradient and increased convergence along the surface front (Fig. 5.24). However, the diurnal cooling during this time reduced the instability of the surface parcels so that convection did not begin in southwest Oklahoma despite the increasing convergence. Minimum LIs over southwest Oklahoma increased from -9.3° at

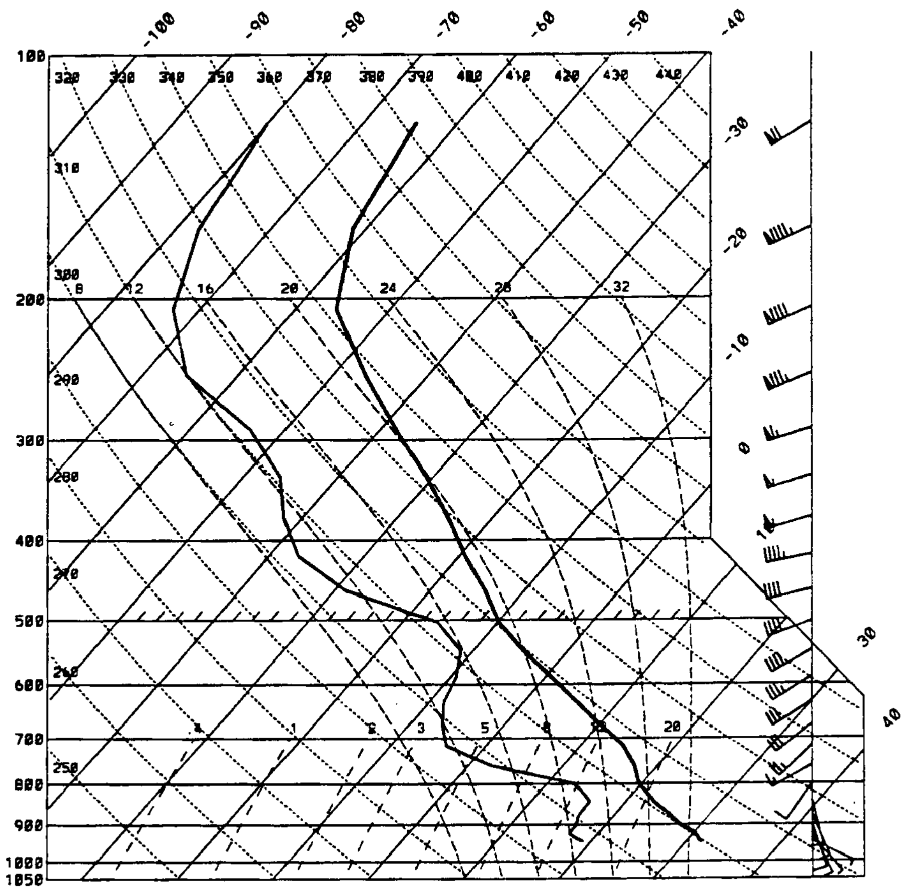

Figure 5.23: Skew-T plot of the model initial data from a point near LTS in southwest Oklahoma at 3/0000.

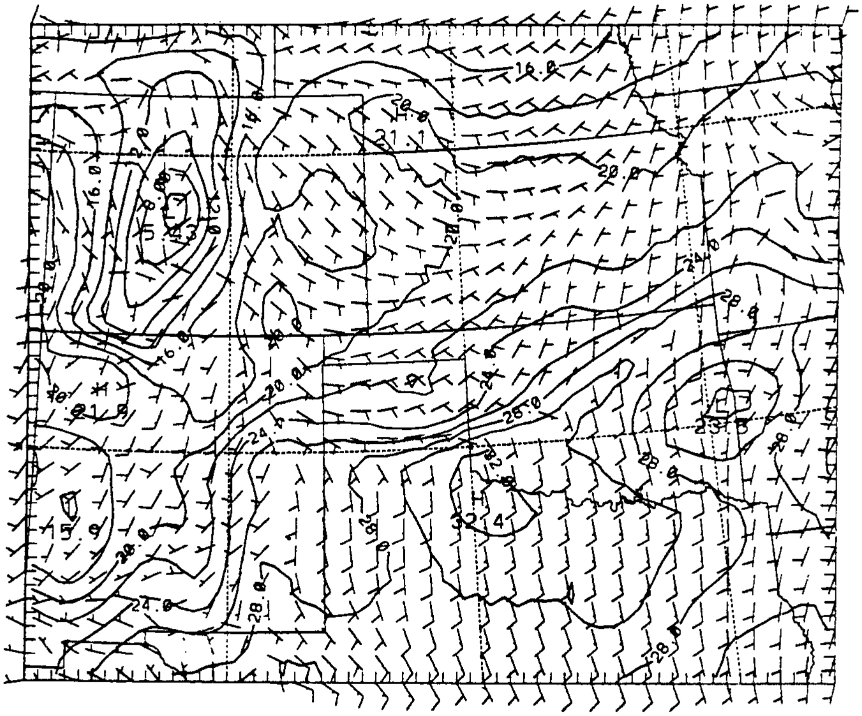

Figure 5.24: Surface temperature and winds at 3/0300 (as in Fig. 5.21) from Z0.

0000 UTC to -6.0° . In order to improve the gradients in the initial condition, the first guess field was taken from a three hour simulation of a previous MM4 run started at 3/0000. While the first guess field was from a future time, it was hoped that the improved gradients would offset any errors introduced due to the off-time. However, there were only slight differences in the initial fields when the MM4 first guess was used. It seems that problems with using a coarse analysis grid to represent tight surface gradients cannot be offset by an improved first guess field.

Fig. 5.25a shows the 3 h simulated convective rainfall ending at 3/0300. The two convective areas over Missouri were similar to observations (Fig. 2.8d), while the Colorado convective area was also observed although the strong radar echos there suggest that the model underforecast this convection. Observed convection was east of the simulated rain in southeast New Mexico. Small, but intense convection was observed across most of Oklahoma along the surface front. The model only produced convective rain at one gridpoint in Oklahoma. Three hours later at 3/0600 (Fig. 5.25b), the model produced convection

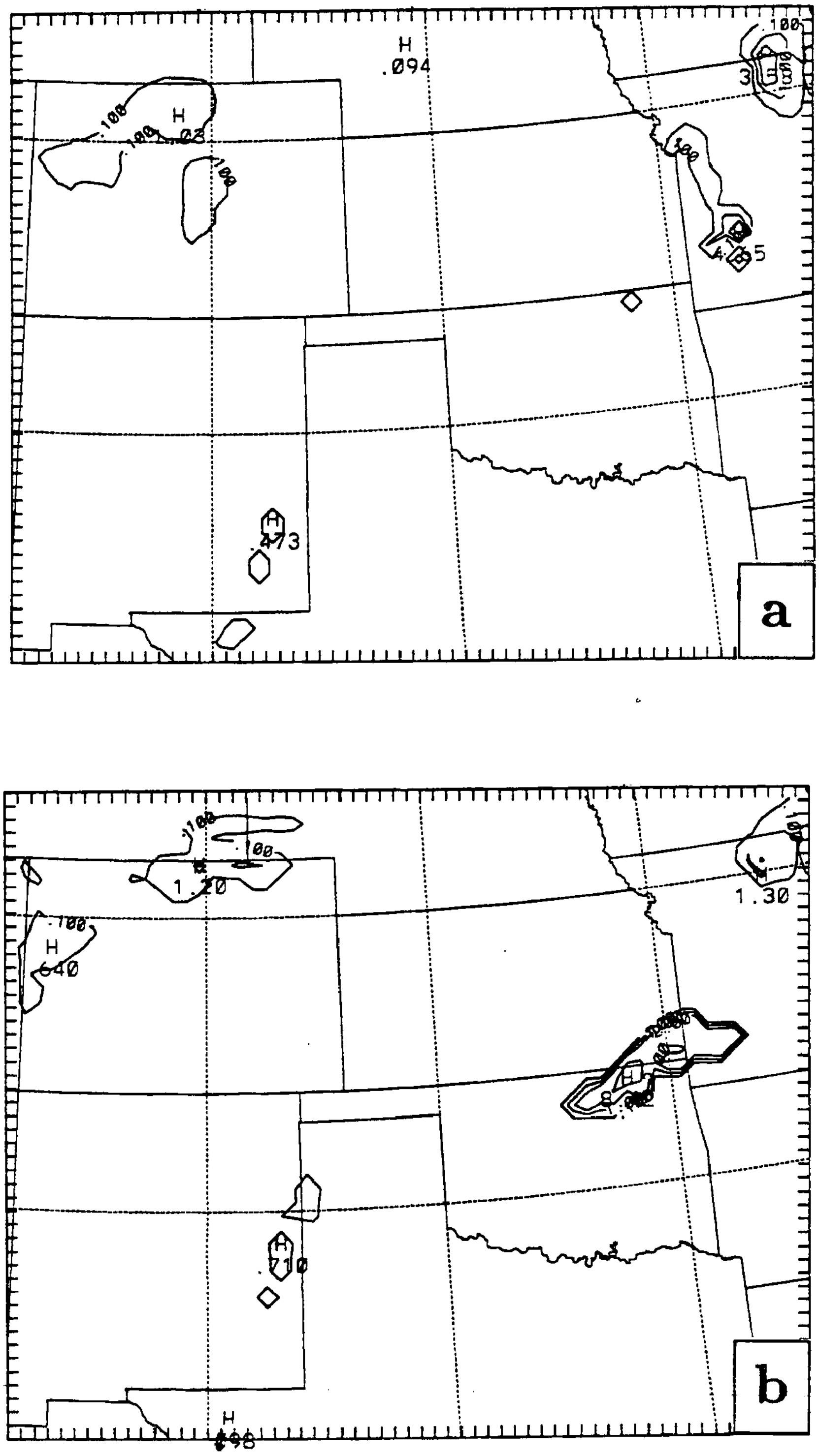

Figure 5.25: Three-hour convective rainfall tendency from Z0 (as in Fig. 4.5a) for the period ending a) 3/0300, b) 3/0600, and c) 3/0900.

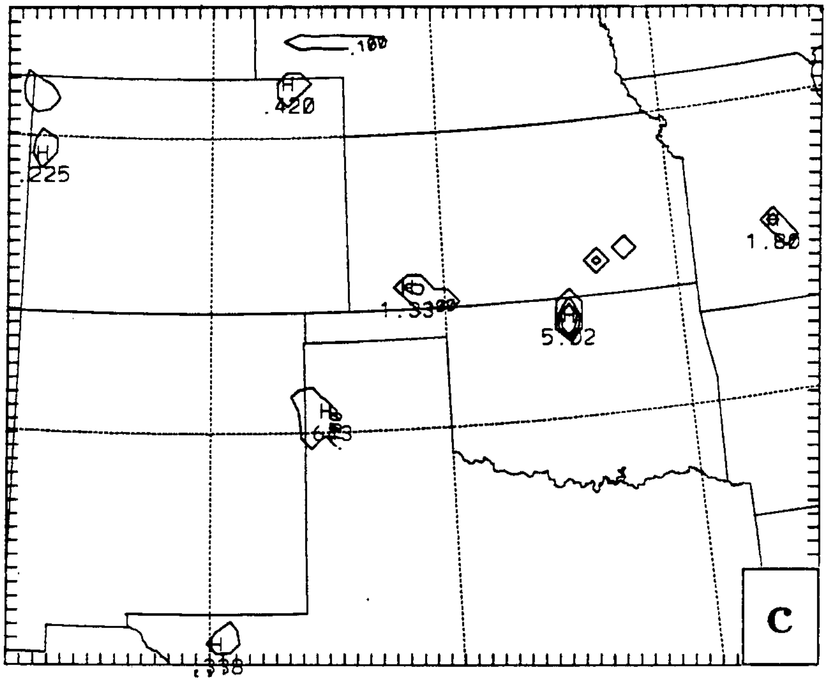

Figure 5.25: Continued.

in northeast Oklahoma extending into southwest Missouri. Actually, the convective areas during this time were over south-central Missouri and across the Texas panhandle extending into western Oklahoma. By 0600 a LLJ had formed in the simulation across the Texas and Oklahoma panhandles north of the observed convection. The LLJ was present at the 850 mb level and was a maximum at the 800 mb level. Strong warm advection was occurring above the frontal surface. The minimum LI was now decreasing across southern Kansas and northern Oklahoma and was lower than the surface LI, indicating increasing potential for elevated convection.

At 3/0700 elevated convection began near LBL quite close to the observed initial point of MCS1 convection, but nearly six hours too soon. This convection was based near 700 mb and by 3/0900 (Fig. 5.25c) covered several gridpoints in southwest Kansas. Other convection began across southeast Kansas similar to the isolated observed echos there between 3/0900 and 3/1200. The northern Oklahoma convection in Fig. 5.25c was the remnants of the line shown in Fig. 5.25b and had died by 3/0700. The southwest Kansas convection began in a region of strong low-level warm advection, upward motion, and near-saturated air (not shown). Slantwise convection may have been occurring as saturated air and negative MPV was present across southern Kansas at 700 mb (not shown).

Fig. 5.26a shows a backward trajectory for an air parcel located at 800 mb over southwest Kansas at 3/1200 (calculation procedures can be found in Gill 1992). Twelve hours earlier, this parcel was 15 mb above the surface over northern Texas. The time history of pressure along the parcel trajectory (Fig. 5.26b) shows that the parcel rose steadily along the frontal surface. This parcel would have encountered the convection along the front in SW Oklahoma had that convection been simulated properly, possibly delaying the parcel's arrival in southwest Kansas or altering its thermodynamic properties. Because this trajectory arrived in southwest Kansas unimpeded, model convection may have started there too soon. A group of backward trajectories originating at 3/1200 in southern Kansas at the 750 mb level (within the updraft source layer for the parameterized convection), shows that the parcels were located over northern Texas and southern Oklahoma twelve hours earlier (Fig. 5.27). A representative trajectory is shown in Fig. 5.28a. The parcel was about 50 mb above the surface at 3/0000, rose sharply when it encountered the front around 3/0300 and then rose more gradually (Fig. 5.28b). It can be concluded that (barring excessive mixing) the air that fed the elevated convection over Kansas, originated within the heated boundary layer over northern Texas and southern Oklahoma the previous afternoon.

By 3/1200 (Fig. 5.29) an east-west band of convection extended across central Kansas, parallel to the 850-300 mb shear vector (Fig. 2.25). Rainfall amounts were greater than 2 mm in a narrow band. Less than 1 mm of explicit rain was produced within this region (not shown). Fig. 5.30 shows a north-south cross section through the rainband. High θ_E air rises over the frontal surface, until reaching its LFC where it rises abruptly in the narrow convective rainband. Directly beneath the rain, downward motion is found. Strong convergence from 800 mb to 500 mb is found along the band with divergence at higher levels (not shown). Explicit cloud and rain water are confined primarily to levels below 700 mb in the band (Fig. 5.30b). No extensive stratiform region had yet developed. The strong upward motion in the band is a response to only the implicit convective heating.

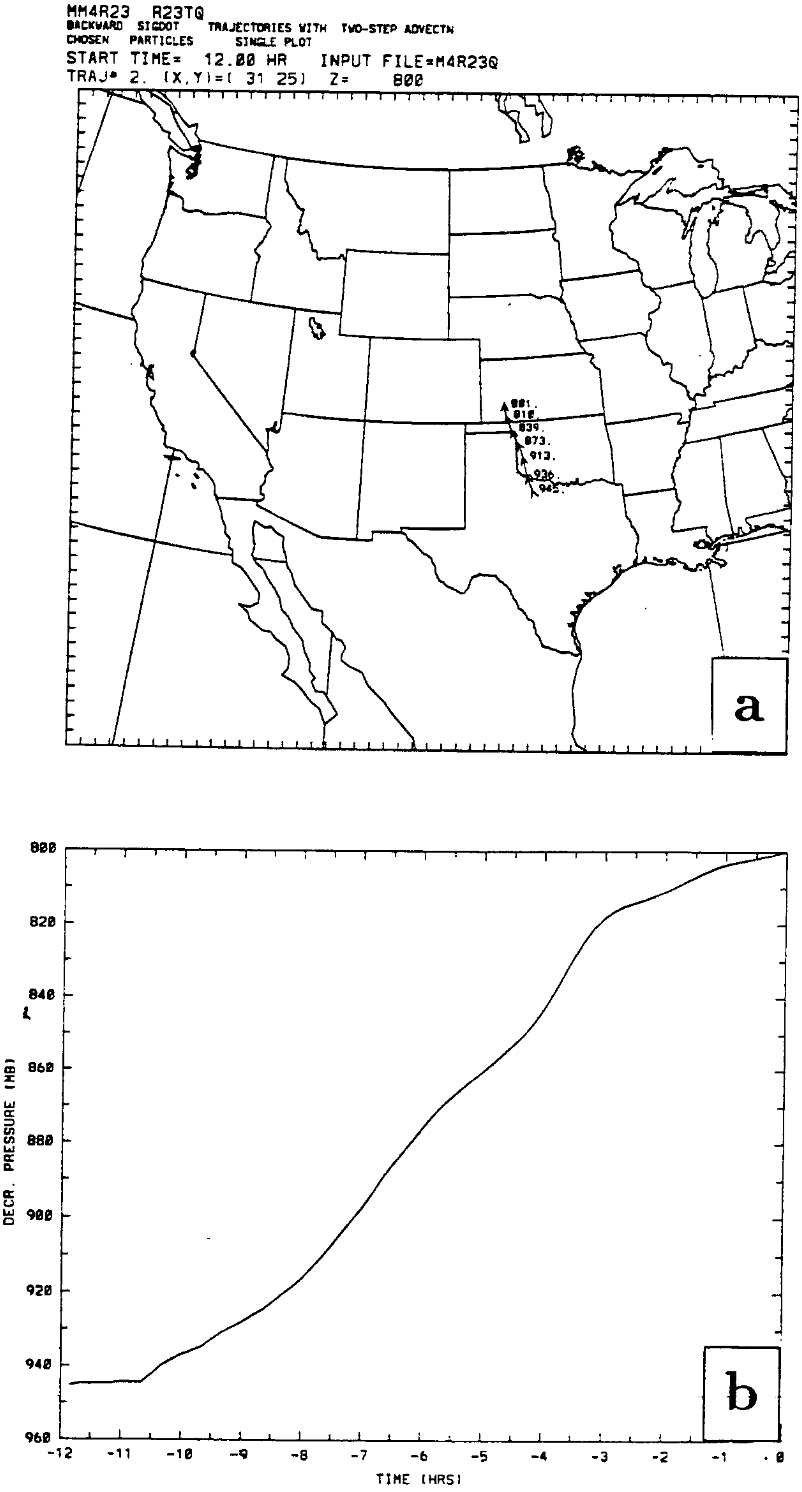

Figure 5.26: Backward trajectory from Z0 for a parcel over southwest Kansas at 800 mb at 3/1200. The two-hourly position of the parcel is indicated by the arrows along with its pressure (mb). The pressure of the parcel as a function of time is shown in b).

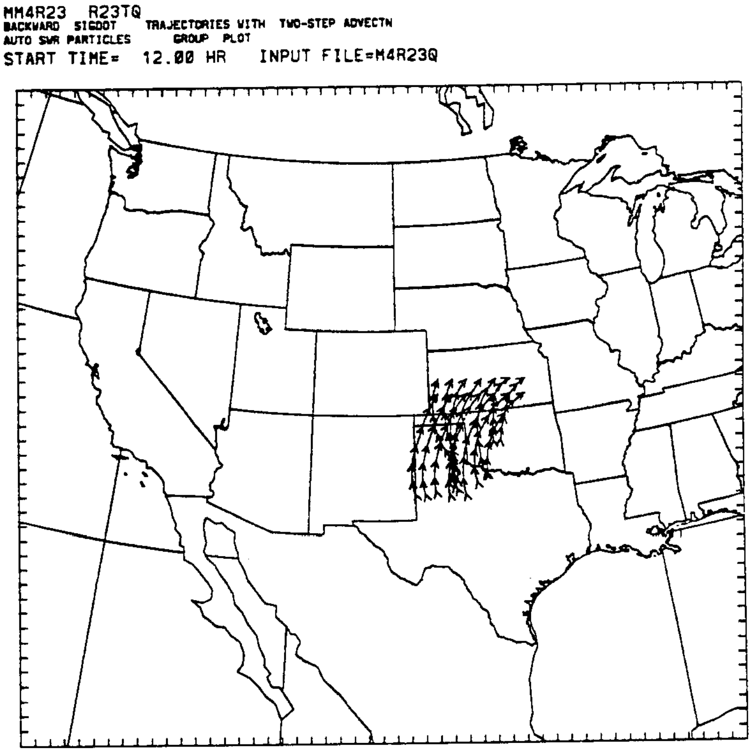

Figure 5.27: As in Fig. 5.26a, but for several parcels over central Kansas at 750 mb at 3/1200.

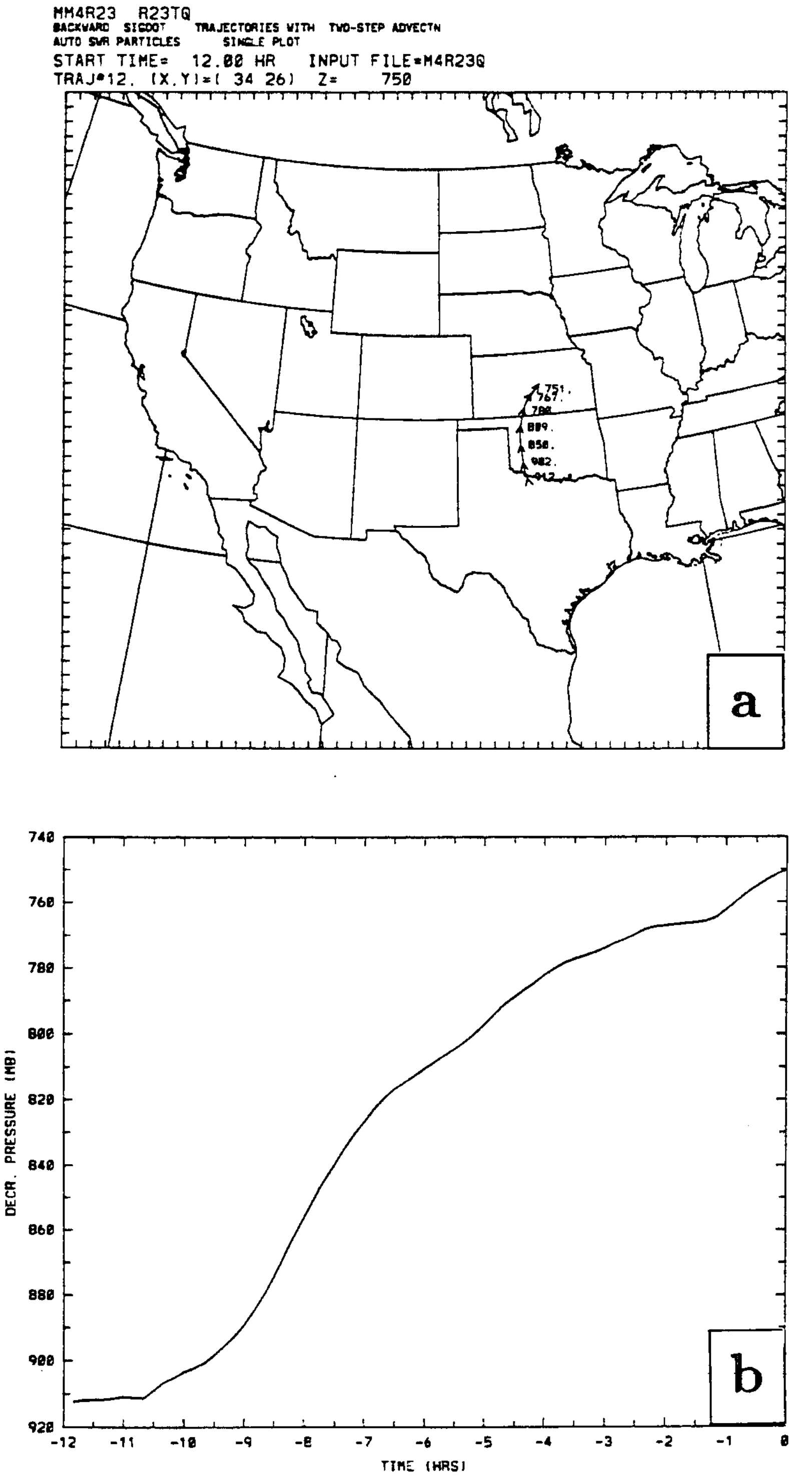

Figure 5.28: As in Fig. 5.26 but for a representative parcel in Fig. 5.27.

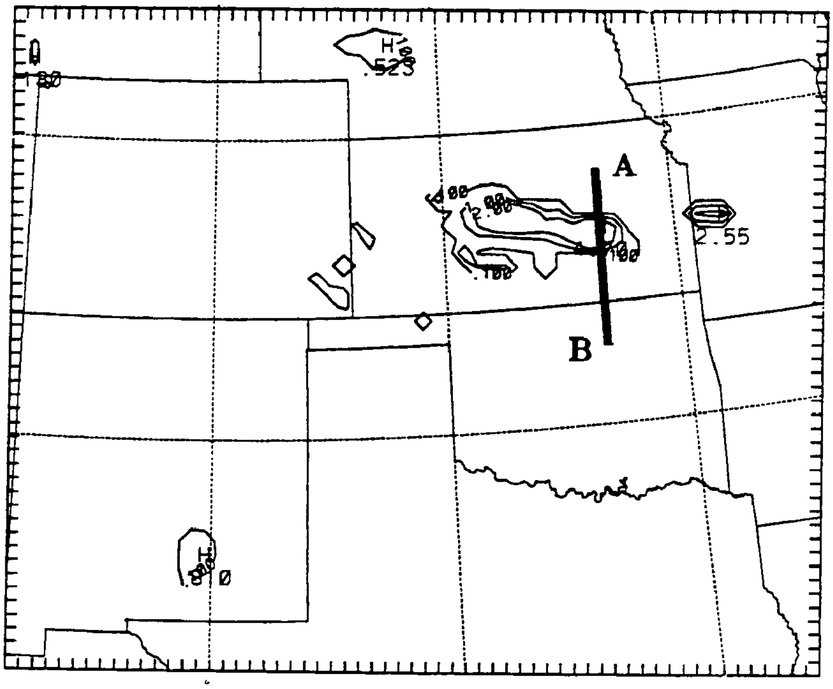

Figure 5.29: Three-hour convective rainfall for the period ending 3/1200 from Z0.

Three hours later (Fig. 5.31) the main portion of the rain area was over southeast Kansas, moving parallel to the 850-300 mb thickness contours. While a narrow band of implicit rain was across central Kansas, the eastern portion of the band was broader with more than 10 mm of both implicit and explicit rain. As in the CTL simulation, there was no trailing stratiform region – the implicit and explicit rain maxima were located at the same grid point. Hydrometeors were now found in midlevels (700-500 mb), similar to a stratiform region. A mesohigh (without any wake low) was found beneath the rain area (not shown). This mesohigh (seen most clearly in the geostrophic wind field, not shown) extended from 850 mb to the surface. A strong mesovortex (revealed in the geostrophic wind field and absolute vorticity field) occupied mid-levels (from 800-500 mb). Above the mesovortex was another mesohigh. A layer of constant θ_E was found within the mesovortex (not shown) with a maximum upward motion of -168 μb s^{-1} at 500 mb.

By 3/1800 (Fig. 5.32), the simulated MCS was fairly representative of the real MCS1, although approximately three to four hours too early. The east-west convective band was

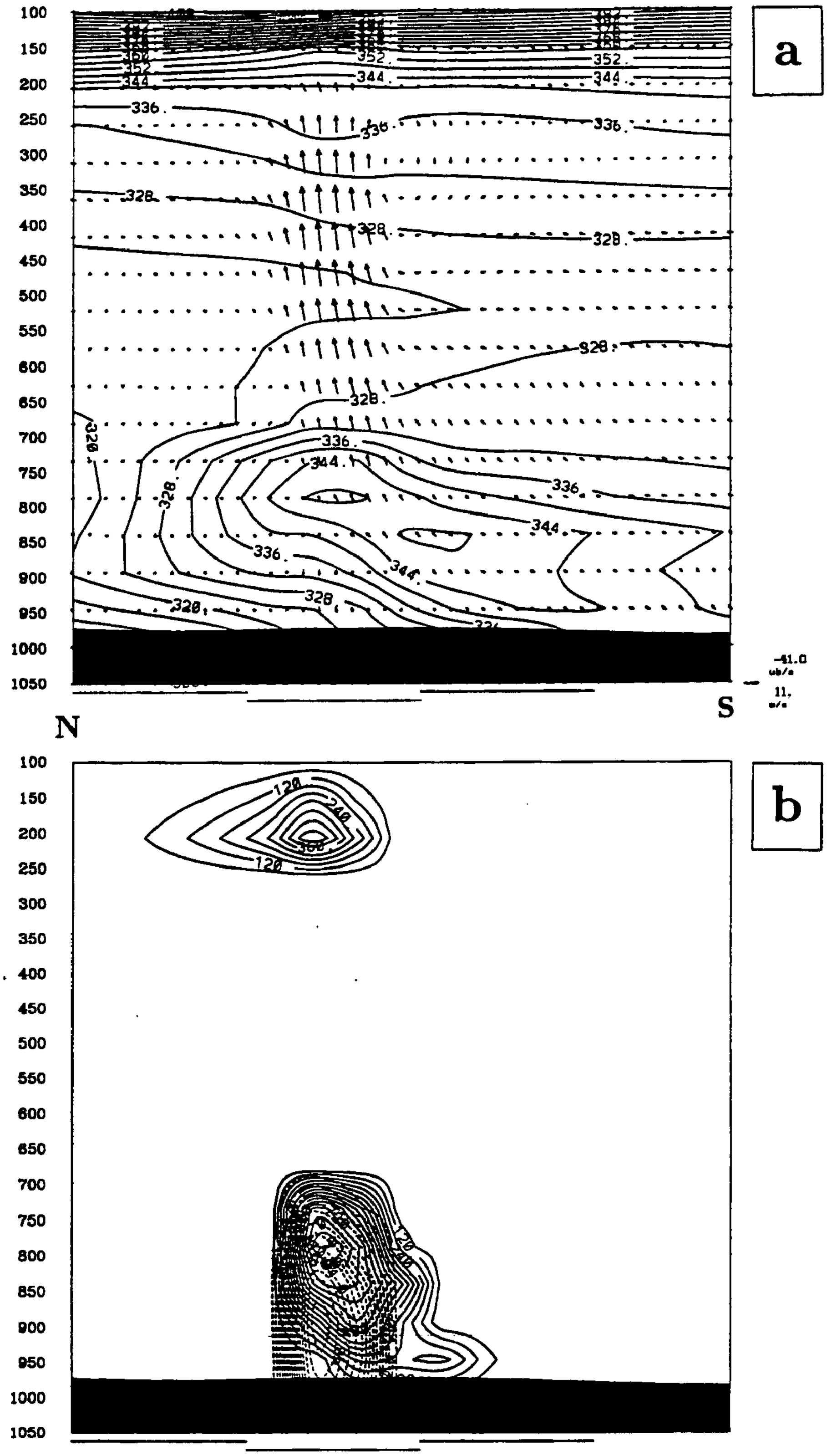

Figure 5.30: North-south cross-section along the line A-B in Fig. 5.29 of a) θ_E (K, contour interval of 4 K) and winds in the plane of the cross-section and b) cloud water (mg kg^{-1} contoured every 60 mg kg^{-1}, solid) and rain water (mg kg^{-1} contoured every 7 mg kg^{-1}, dashed) at 3/1200 from Z0.

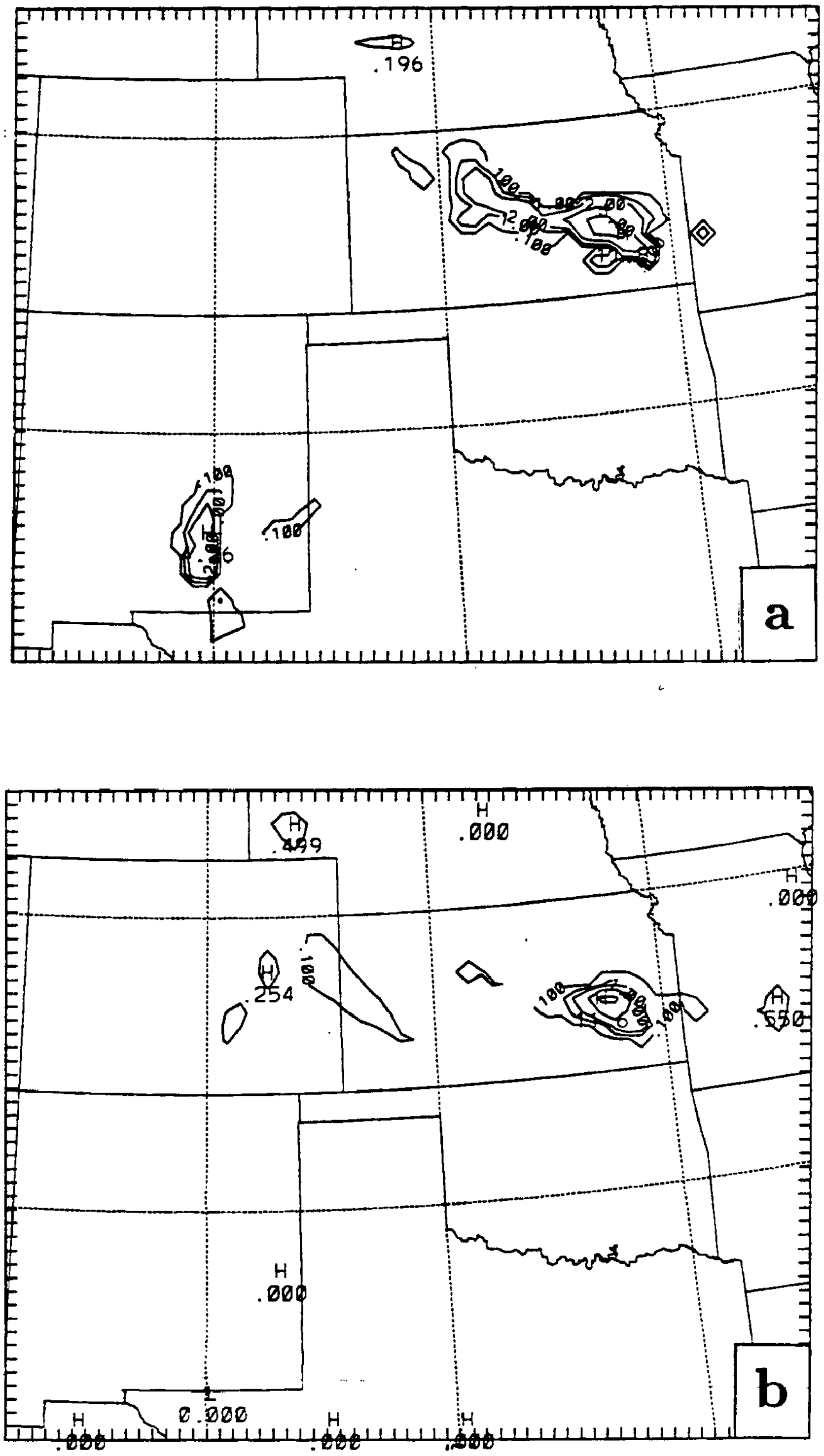

Figure 5.31: Three-hour rainfall for the period ending 3/1500 from Z0 of a) implicit rain and b) explicit rain.

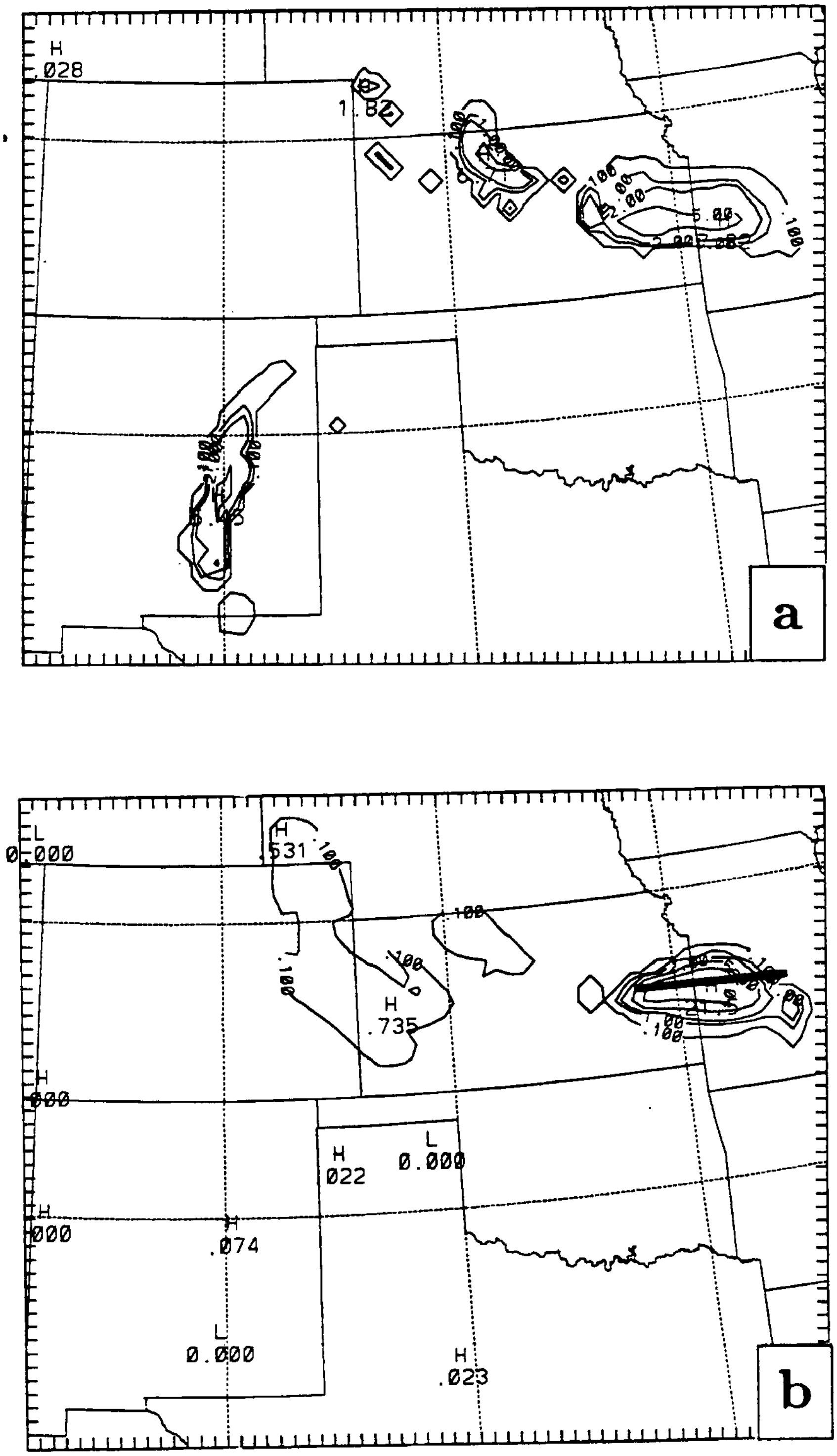

Figure 5.32: Three-hour rainfall for the period ending 3/1800 from Z0 of a) implicit rain and b) explicit rain.

along the southern flank of the system (Fig. 5.32a), while the maximum explicit rain was to the north and east of the convective band (Fig. 5.32b). The broad explicit rain area was accompanied by realistic pressure features. Fig. 5.33 shows the SLP field for 3/1800. A strong mesohigh is beneath the rain area (with a mesotrough to its east), while a wake low with one closed isobar is along the Kansas-Missouri border. Updrafts within the rain area continued to exceed -100 μb s^{-1} within midlevels. An west-east cross-section through the MCS is shown in Fig. 5.34. The relative flow features within the Z0 MCS1 (Fig. 5.34a) are similar to those found in CTL (Fig. 4.10), except that the updraft core (from 700 to 300 mb) is much stronger and is a region of constant θ_E indicative of a mesovortex (Zhang and Fritsch 1988c). Rain water mixing ratios are much larger in the Z0 MCS (Fig. 5.34b) than in the CTL simulation (Fig. 4.10b). While no rear inflow circulation can be seen (Fig. 5.34a), strong downward motion near the 875 mb level (> 50 μb s^{-1}) at the back edge of the rain area led to warming and drying (indicated by the higher θ_E values at the back edge of the rain area, but more pronounced in the θ and relative humidity fields, not

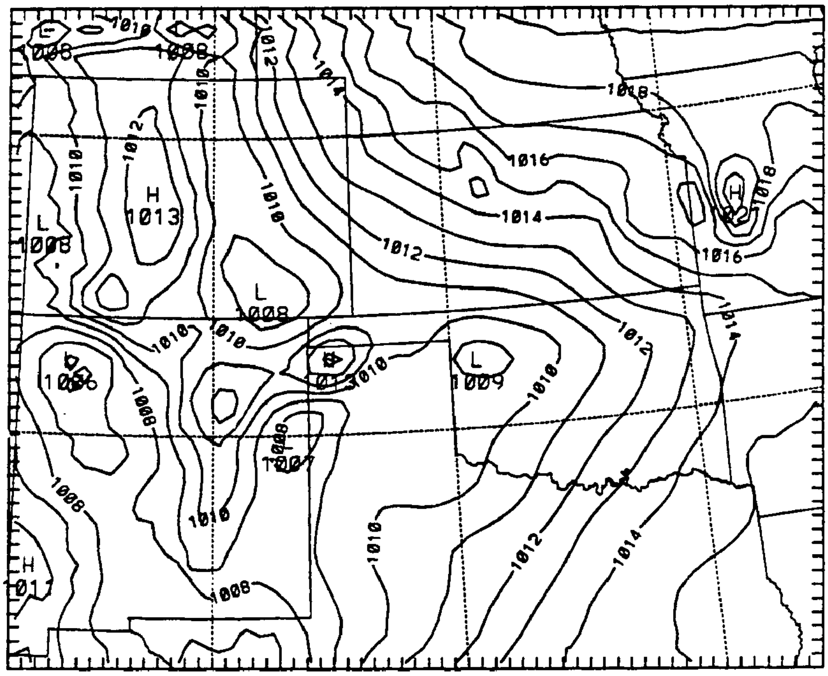

Figure 5.33: Simulated sea level pressure (mb, contour interval of 1 mb) from Z0 at 3/1800).

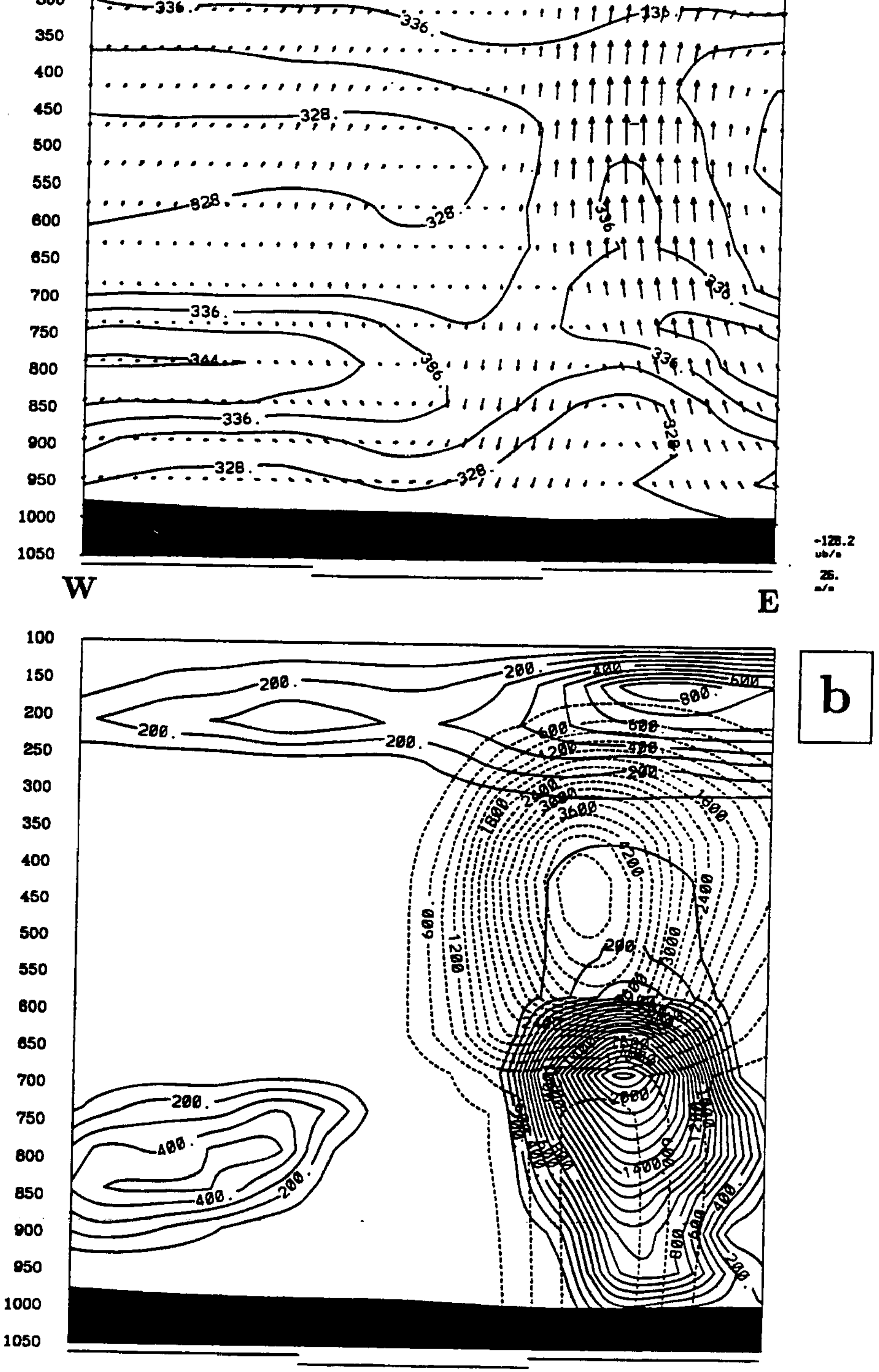

Figure 5.34: East-west cross-section along the line shown in Fig. 5.32b at 3/1800 from

shown) and resulted in the wake low. The low-level sinking and resulting warming behind MCS1 were less pronounced in the CTL run (Fig. 4.8b). While Z0 was too early with MCS1, the wider and more intense explicit rain area led to the development of some of the observed dynamic features of the MCS, such as the wake low. While the wake low is the end product of a chain of complicated processes (Zhang and Gao 1989), it is primarily the result of the explicit precipitation parameterization. In runs without large and intense explicit rain areas (as in CTL), a wake low does not form. These results are consistent with those found by Zhang and Gao (1989).

As can be seen in Fig. 5.32a, Z0 does not reproduce the evolution of MCS2 very well. One area of convection was over north-central Kansas, west of MCS1, along the 800-700 mb front. A second area of convection was over eastern New Mexico, similar to the CTL run, farther west than observed. By hour 24 of the simulation (Fig. 5.35a), implicit rain was widespread but rather disorganized (Fig. 5.35a). A band of rain was across northern Kansas along the 800 mb front. A large area with some local rain maxima was across eastern New Mexico, the Texas panhandle, and northern Oklahoma. The explicit rainfall (Fig. 5.35b) shows an interesting pattern over New Mexico. The rain was dispersed along a narrow path paralleling the 850-300 mb thickness contours. The integrated rain water (Fig. 5.36) shows that hydrometeors have been advected downstream in a narrow plume from an intense core of explicit rain. This core is an example of a Numerical Point Storm (NPS, Giorgi 1991) or grid point instability (Zhang *et al.* 1989). Molinari and Dudek (1986; 1992), Kalb (1987) and Dudek (1988) also describe the occurrence of NPSs. NPSs are characterized by large precipitation amounts, strong updrafts and large amounts of latent heating. Zhang *et al.* (1989) show that a mesolow forms due to the excessive heating, leading to further low-level convergence of high θ_E air. The downdrafts produced by the explicit scheme are insufficient to keep the positive feedback between convergence, rising motion and release of latent heating from continuing to grow. Kalb (1987) demonstrated that the NPS is a convective overturning of an entire grid column with the compensating descent occurring in adjacent grid points. Zhang *et al.* (1989) point out that NPSs can develop because the explicit scheme neglects important subgrid scale processes such as

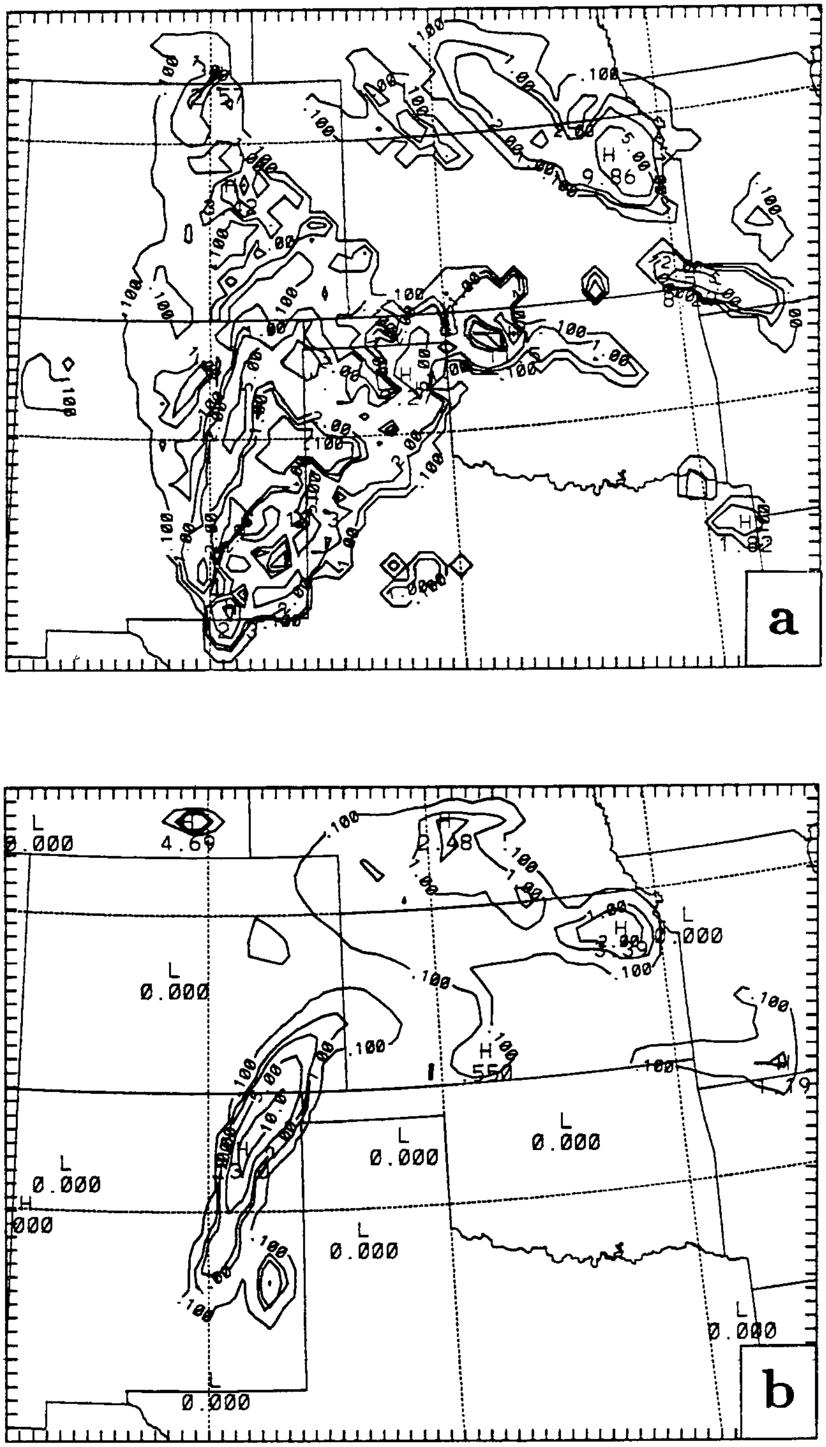

Figure 5.35: Three-hour rainfall for the period ending 4/0000 from Z0 of a) implicit rain and b) explicit rain.

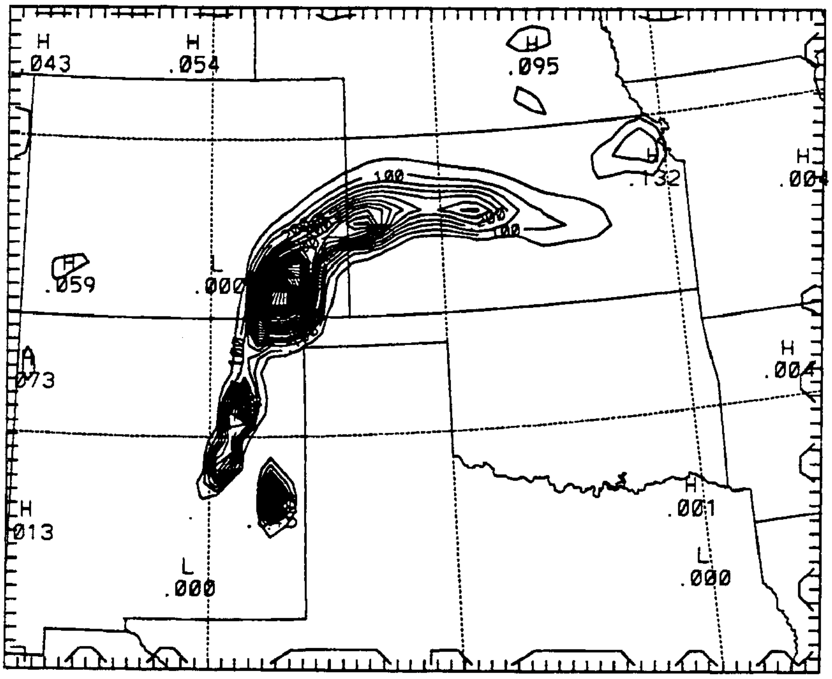

Figure 5.36: Simulated column-integrated rain water (g kg^{-1}) at 4/0000 from Z0. Contour interval is .05 g kg^{-1}.

lateral detrainment. They suggest that the simultaneous use of an explicit scheme which includes ice physics with an implicit convective parameterization can prevent development of the NPSs. In the present case, NPSs develop in northeast New Mexico after 3/2200 in the Z0 run as well as in the other simulations despite the use of both an implicit and explicit scheme. Experiments with changes to the implicit parameterizations are described in the next section.

In summary, Z0 simulated MCS1 reasonably well, although the system developed too early. In both Z0 and CTL, MCS1 convection began above the frontal surface as air was lifted over the cold surface airmass. Strong warm advection and moisture convergence was occurring in the region of initial convection. Both runs started convection north of the terminus of the LLJ, although the Z0 LLJ was not as pronounced as in CTL. Slantwise convection may have played a role, as both model runs exhibited negative MPV with saturated air near cloud base. The mature MCS1 in Z0 was more intense than in CTL, producing more precipitation and stronger surface pressure features.

5.2 Sensitivity to changes in the moist physics parameterizations

The experiments described in this section involve modifications to the moist physics parameterizations, particularly the convective schemes. Also included in this section is an analysis of a simulation with increased vertical resolution.

5.2.1 Convective Trigger Function Tests

Kain and Fritsch (1992) pointed out that simulations of the 10-11 June 1985 squall line case is sensitive to the convective trigger function. The convective trigger function is that part of the parameterization which decided whether or not deep convection exists at a grid point. Tests of three different triggers will be described in this subsection.

Fritsch-Chappell Trigger

The FCT as used by Kain and Fritsch (1992) attempts to account for the subgrid nature of the triggering of convection by adding a temperature perturbation to a rising parcel based on the grid-scale vertical velocity. Zhang and Fritsch (1986a) and Kain and Fritsch (1992) point out that observational and numerical studies show that these temperature perturbations are linked to the low-level convergence.

The trigger proceeds as follows. Starting with the lowest model layer (and continuing upward until either a cloud is started or the layer 300 mb above the surface is reached), a 60 mb source parcel is constructed by mass-weighted mixing of an appropriate number of model layers above the starting level. The 60 mb-deep mixed parcel is lifted to its LCL, where a temperature perturbation is added based on the relation,

$$\delta T \ = \ C_1 \, w_0^{1/3}$$

where δT is the temperature perturbation, C_1 is a unit constant and w_0 is the grid-scale vertical velocity at the LCL. The one-third exponent is an attempt to account for the volumetric relationship between forcing and thermal bubbles (Fritsch and Chappell 1980a; Zhang and Fritsch 1986a; Kain and Fritsch 1992). If the temperature of the parcel plus the temperature perturbation is greater than the grid scale environmental temperature, the cloud computation proceeds. If the parcel temperature is less than the environment, the trigger fails and the procedure is repeated for the next highest model layer.

The updraft vertical velocity above the LCL is calculated using the buoyancy equation:

$$w_U^2(k+1) = w_U^2(k) + 2g \int_{z(k)}^{z(k+1)} \frac{\overline{T}_U(k) - \overline{T}_E(k)}{\overline{T}_E(k)} dz,$$

where w_U is the updraft vertical velocity, $\overline{T}_U(k)$ is the mean saturated updraft parcel temperature, $\overline{T}_E(k)$ is the mean environmental temperature, z is height, and g is the gravitational constant. At the LCL it is assumed that $w_U^2 = 1 \text{ m}^2\text{s}^{-2}$ and T_U is linearly interpolated between the temperature at the bottom of the source layer and $T_U(LCL)+\delta T$.

The buoyancy of the parcel is based partly on the temperature perturbation and thus indirectly on the grid-scale vertical velocity. Therefore, the trigger is doubly dependent on the grid-scale vertical velocity. Of course, the trigger is also dependent on the parcel thermodynamics and the environmental temperature profile.

Zhang and Fritsch (1986a) found that the FCT was activated too easily during the afternoon when the boundary layer was most unstable, generating spurious airmass convection. They added an arbitrary time-dependent damper to reduce w_0 and so reduce the temperature perturbation.

The FCT has performed well for many strongly-forced cases (i.e. when there is organized, strong upward motion). However, the FCT has several deficiencies. Kain and Fritsch (1992) point out that the FCT over-predicted convection occurring in the 10-11 June 1985 case. Indeed, every published study using the FC parameterization (and thus the FCT) has too much convection, especially on the southern and southwestern flanks of convective systems where there tends to be strong convergence between the cold low-level outflow and the unstable environmental inflow (e.g. Zhang and Fritsch 1986a; Zhang and Fritsch 1988c; Stensrud 1992). While this is a preferred area of an MCS for convection (Loehrer 1992), the FC studies over-develop such convection. Because the 3-4 June case was only weakly forced and the deficiencies in the FCT more noticeable, it was necessary to modify the FCT.

The FCT was modified for use in the CTL run as follows. First, it is required that θ_E must decrease with height at the bottom of the 60 mb mixed layer. For well-mixed boundary layers, this is not a necessary requirement. For warm-sector air riding over a cold air mass (as over Kansas in the present case), θ_E increases with height. It can't be assumed that such a parcel could be well-mixed. The original FCT would mix the high values of θ_E downward, resulting in a lower cloud base than should exist.

The coefficient for the temperature perturbation, C_1, is reduced to 0.5. Tremback (1990) states that the temperature perturbation is arbitrary. No hard evidence exists for the coefficient or the one-third power relationship, although Zhang and Fritsch (1986a) and Kain and Fritsch (1992) argue that this is a reasonable approach. Sensitivity tests for the temperature perturbation (not shown) revealed that reducing C_1 to 0.5 eliminated some of the spurious convection while maintaining the MCS1 convection over Kansas. In fact, no temperature perturbation was needed for some of the MCS1 convection.

Where strong upward motion was occurring near the surface front in northern Oklahoma, the corresponding δT was large, allowing parcels to break through the existing cap. In lieu of using a time-averaged vertical motion in the temperature perturbation expression, it is required that the updraft parcel temperature must exceed the environmental (grid-resolved) temperature for five consecutive timesteps. This approach eliminates triggering convection by a sudden spike in the vertical motion, perhaps caused by a transient gravity wave. Instead, the trigger is activated by persistent forcing.

The computation of the parcel vertical velocity from the buoyancy equation uses a parcel temperature which includes the temperature perturbation. Thus, a large temperature perturbation due to a large grid-scale vertical velocity can lead to an excessively buoyant updraft which can overcome a substantial negative area. Observations show that cloud base updrafts are typically about 1 to 6 m s^{-1} (e.g. Kessler 1986). The cloud base vertical velocity was therefore fixed to be 1 m s^{-1} . Finally, the time dependent damper for w_0 (Zhang and Fritsch 1986a) was retained.

The following subsections describe two other triggers used in the KF parameterization. The rest of the KF scheme (and other model components) was left identical to the CTL run.

Lifting Depth Trigger

As used by Kain and Fritsch (1992), the lifting depth is the pressure depth between the level of maximum θ_E and that parcel's LFC. If the computed lifting depth is less than some arbitrary value, the cloud computations continue. A reasonable value for the lifting depth is 50 mb (Kain and Fritsch 1992). As those authors pointed out and which is also true for the 3-4 June case (results not shown), there is great sensitivity to the lifting depth. Smaller values result in less convection, while greater, less-restrictive values (e.g. 250 mb) produce too much convection.

The LDT was implemented here as follows: starting at the level of maximum θ_E and continuing upward to 300 mb above the surface, the parcel's deep lifting depth was computed. The deep lifting depth was defined as the pressure difference between the source level and the highest level below 500 mb where the θ_E of the source air exceeds the saturated θ_E of the environment. The original lifting depth method used the pressure depth between the source level and the next highest level where θ_E of the source air exceeded the saturated θ_E of the environment. Figure 5.37 illustrates a sounding where the original scheme would fail. The unstable surface parcel needs 40 mb of lift to reach the LFC.

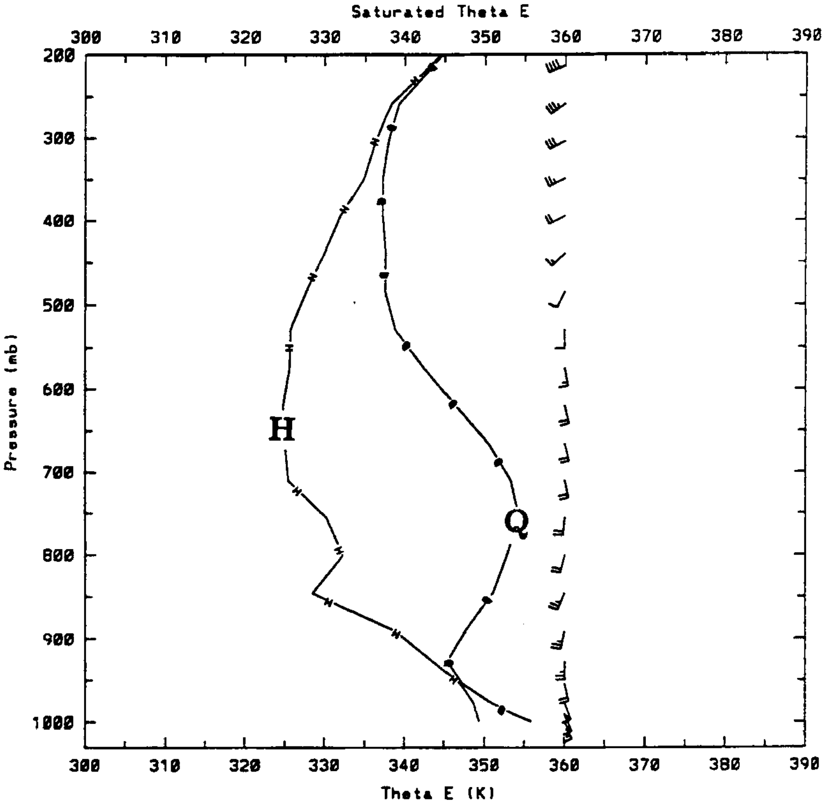

Figure 5.37: Vertical profile of θ_E (curve H) and saturated θ_E (curve Q) (in ° K) for a grid point in southeast Texas at 3/1340.

But, this is overlaid by a strong cap, which the parameterization would easily overcome. This profile should support only shallow, boundary layer cumulus. If the lifting depth is computed downward from 500 mb, the needed lift is much larger and the trigger would not be activated.

To make it easier for surface-based convection in dry regions to be triggered, the lifting depth was set to 175 mb if the source parcel was close to the surface (less than model level 6), there was greater than 3 cm s^{-1} upward motion at 500 mb, and the absolute value of the difference between the source layer θ_E and the surface θ_E was less than 2° (i.e. a well-mixed boundary layer with no low-level inversion). Otherwise, the lifting depth was kept at 50 mb. In addition, upward motion was required at all levels between the source level and one model level below the LFC. For the 50 mb lifting depth, the upward motion of the LCL must exceed 1.5 cm s^{-1} while for the 175 mb depth, the upward motion at the LCL must exceed 5 cm s^{-1}. (The original LDT had no vertical motion constraints). The vertical motion requirements were needed to restrict convective development where there were strong, but shallow caps (as in southeast Texas; see also section 5.2.2). The larger requirement for the surface-based convection is to allow that to occur only where there is organized lift taking place. The cloud base vertical velocity for the updraft computations was set to 1 m s^{-1} as in the modified FCT.

Convective Inhibition Trigger

The theoretical basis for both the FCT and LDT can be questioned and they both have obvious deficiencies. Convective inhibition, meanwhile, has been shown to be a reasonable predictor for the development of deep convection (e.g. Colby 1984; Ziegler and Hane 1993). Kain and Fritsch (1992) describe a simple negative area trigger used in their study which had similar deficiencies as the LDT. A different convective inhibition trigger (CIN) is used here. Computations proceed as in the LDT, but instead of testing for a lifting depth, the negative area (in J kg^{-1}) is computed for the source parcel. If the convective inhibition is less than 55 J kg^{-1}, the trigger is activated. The only upward motion requirement is 1.5 cm s^{-1} at the LCL. The value of 55 J kg^{-1} is, like the 50 mb lifting depth, a rather arbitrary value, but based on the author's forecasting experience, it is a reasonable one. Recently, Ziegler and Hane (1993) have shown using observations that a threshold of 50 J kg^{-1} was the best predictor for initiation of convection along the Oklahoma dryline. The CIN trigger should be expected to outperform the LDT in regions with a strong, but shallow cap and where there is a weak, but deep cap. Like the LDT, the CIN should have difficulties in dry regions with large negative areas. Sanders and Blanchard (1993) describe a case in which a small area of convection was triggered within a large area that was favorable for development. The problem remains that in nature a negative area may be overcome only in a small subgrid region by subgrid processes.

Comparison of the trigger function simulations

Fig. 5.38 shows the 3 h simulated convective rainfall for the three different trigger function runs. At 1500 UTC, all three triggers had activated convection at very nearly the same location in central Kansas with the least amount of rain produced by the LDT. The CIN trigger initiated high-based convection over north-central Oklahoma. The LDT and CIN trigger runs had produced more convection over southeast New Mexico by this time in slightly better agreement with observations than the FCT. By 3/1800, all three runs had convection in eastern Kansas, in a WNW-ESE band. The narrowest band was in the FCT run with a peak rainfall amount of 4.6 mm which was slightly more than half the maximum amount produced by the other two triggers. The CIN trigger had the broadest area of MCS1 rain. The mid-level convection at hour three of the CIN forecast had diminished in area and amount and had moved northward into the southern flank of MCS1 not unlike the visible satellite observations. Both the LDT and CIN had developed some convection in southwest Missouri. All three runs handled MCS2 similarly, with the CIN trigger again producing the most rain across the largest area. All three runs also produced convection (possibly prematurely) over the northern Colorado mountains.

By 3/2100 the results from the three runs begin to diverge significantly. As discussed in Chapter 4, the FCT produced vigorous surface-based convection along the front in northern Oklahoma. Both the LDT and CIN runs produced convection in northern Oklahoma, but not as extensively as in FCT. The predominant rain areas in LDT and CIN remained in Kansas. The simulated MCS1 moved east quickest in FCT perhaps slightly

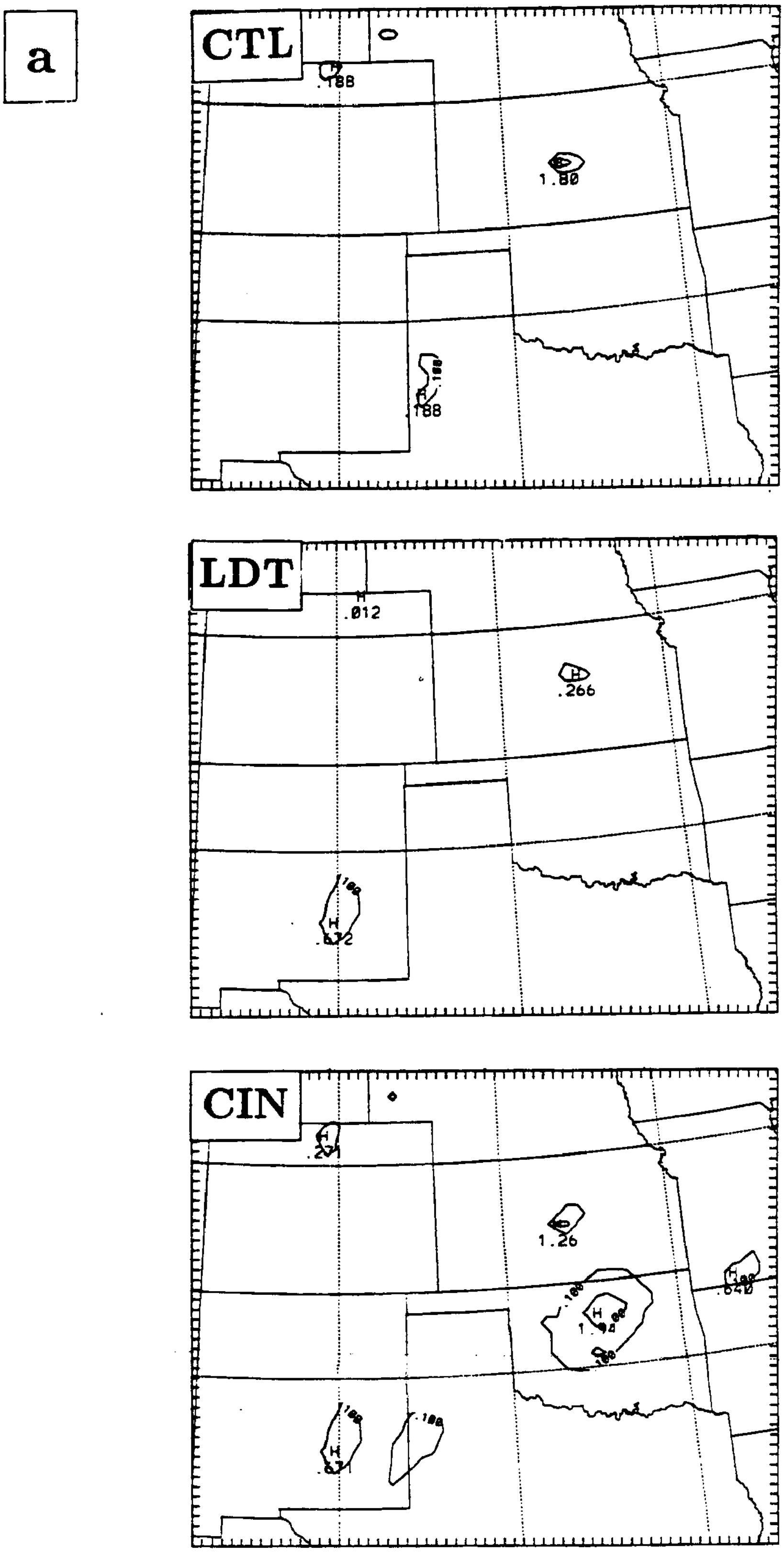

Figure 5.38: Implicit rainfall from the three trigger function runs (FCT, LDT, and CIN) at a) 3/1500, b) 3/1800, c) 3/2100, and d) 4/0000 (except for CIN).

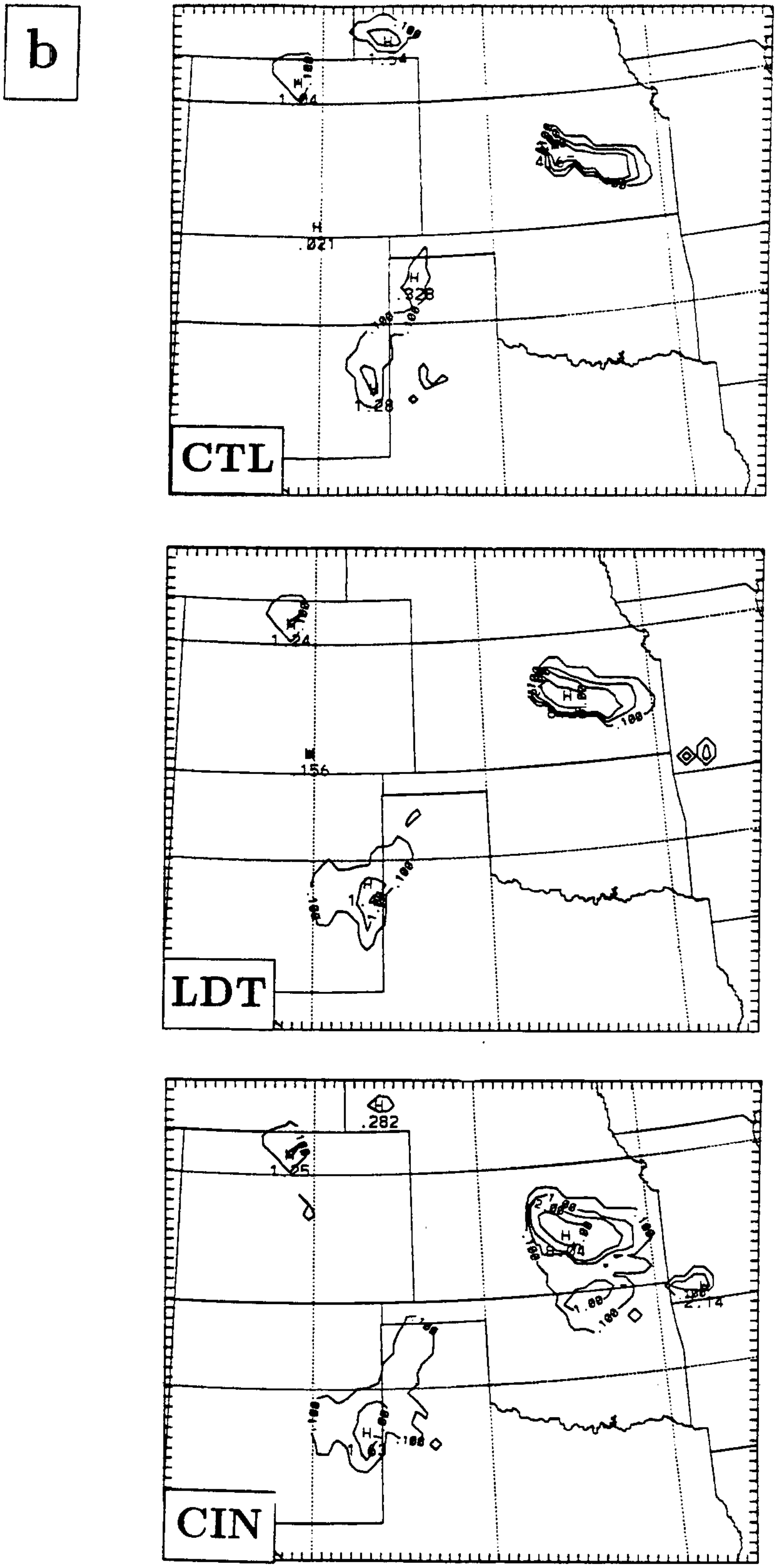

Figure 5.38: Continued.

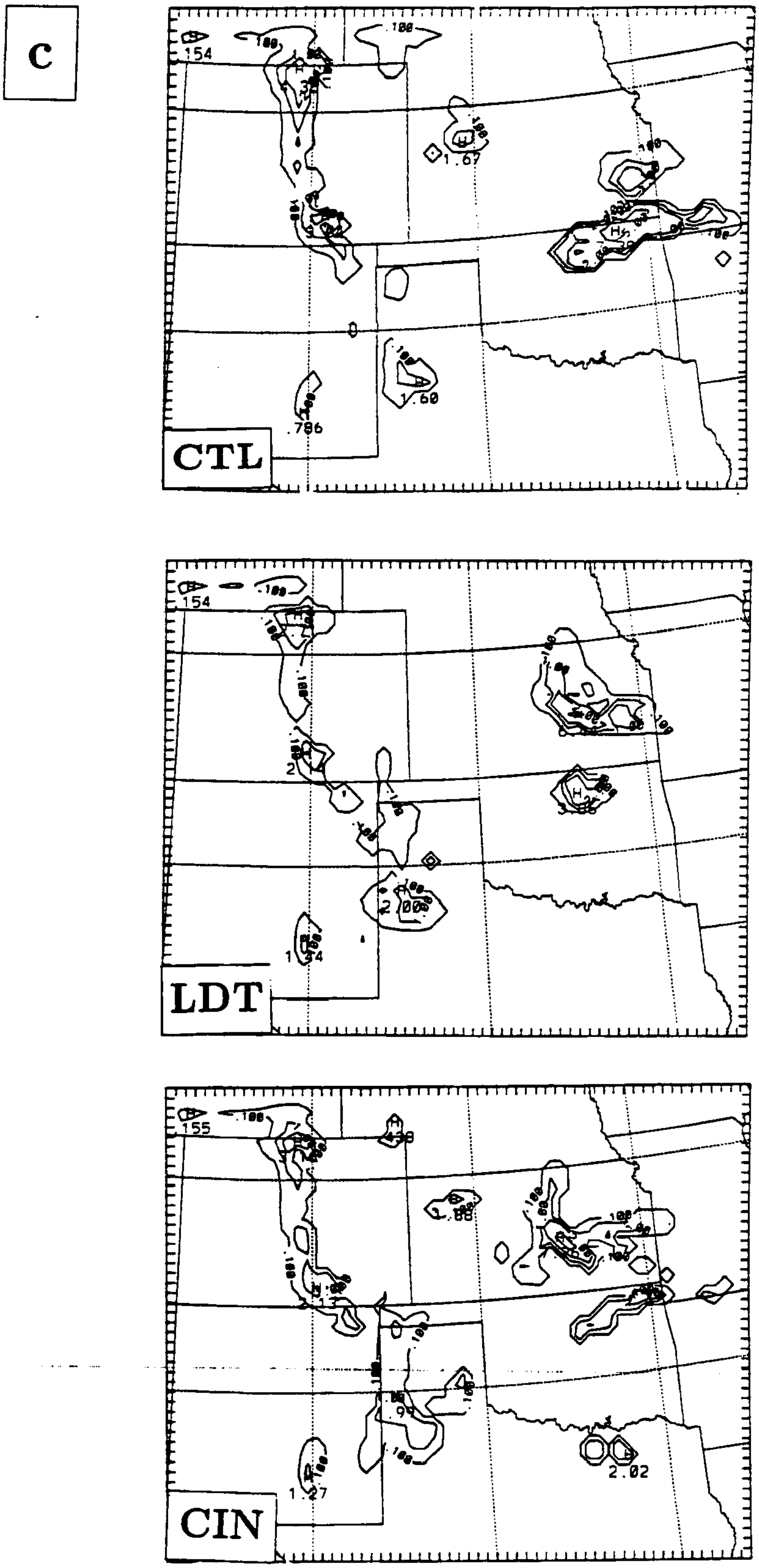

Figure 5.38: Continued.

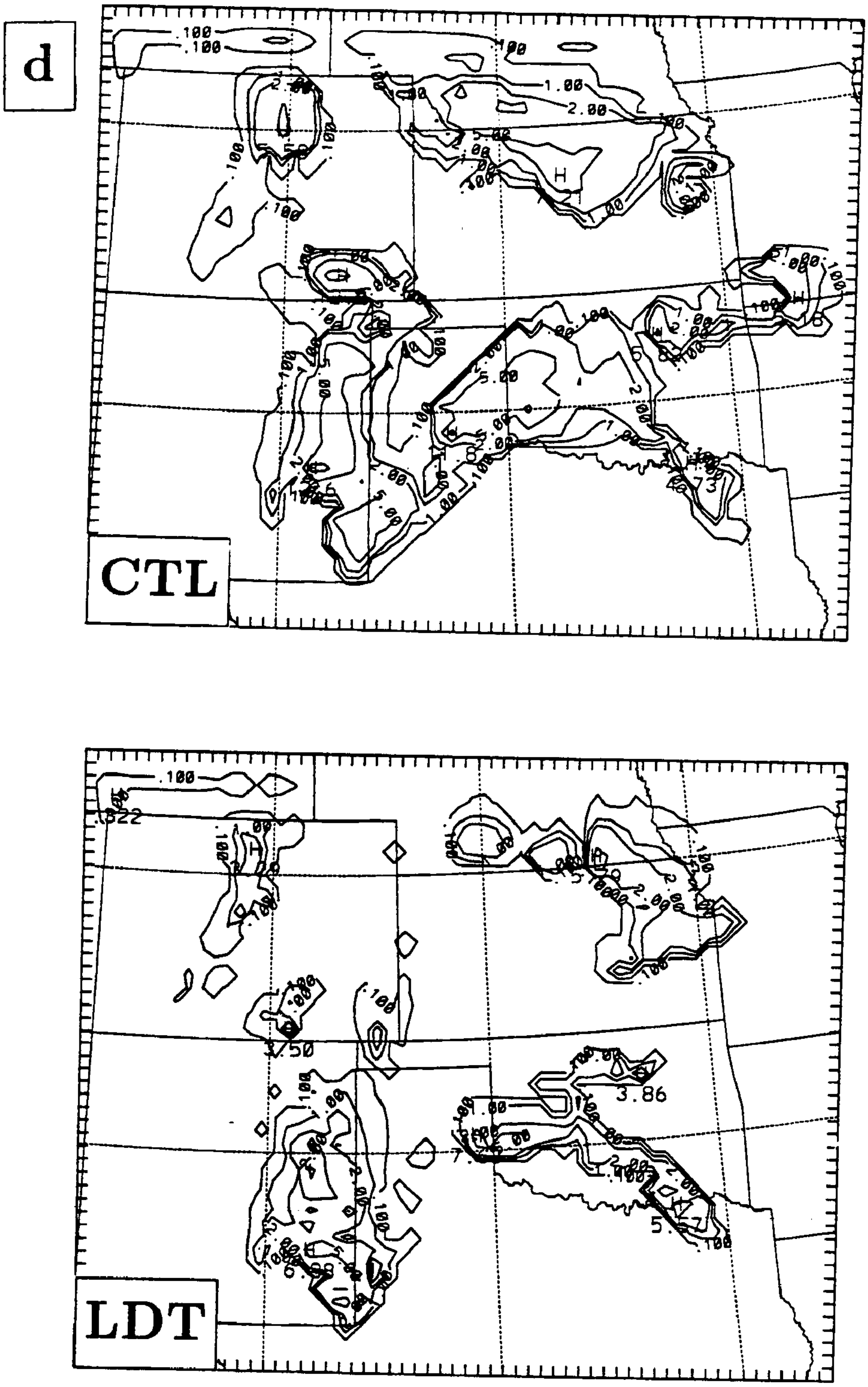

Figure 5.38: Continued.

faster than observations. The maximum rain area in LDT during the 3 h period ending at 2100 UTC, moved to the southeast only 50 km. In the CIN run the maximum rain area was stationary and other convection had back-built to the west. Radar observations show that widely scattered convection did develop by 2000 UTC in the wake of MCS1 and in advance of MCS2. Therefore, the back-building in the model may not be entirely untrue. However, radar also shows that MCS1 was highly organized and straddling the Kansas-Missouri border by 2100, while LDT and CIN have little convection in Missouri at this time. Both FCT and CIN developed convection in northwest Kansas (which in the CTL run became the northern portion of MCS2), while LDT failed to generate this area. (This will be discussed in the following subsection). All three runs again handled the MCS2 convection similarly, slowing its progress across the Texas panhandle in contrast to reality. The FCT run again had the lowest rain amounts in this region. The CIN run by this time had erroneously developed rain in the capped region in northeast Texas. All three model runs developed too much convection along the Colorado mountains, especially in the southern half of the state. In summary, by 3/2100 all three runs began having difficulty with simulating MCS1. The FCT developed too much convection along the surface front which choked off the θ_E supply to MCS1, while the LDT and CIN developed convection over the same area of Kansas as the supply of high θ_E air continued to be lifted over the frontal surface.

The LDT and FCT simulations continued beyond 4/0000. Between 3/2100 and 4/0000, the FCT produced significantly more implicit rainfall than LDT. As mentioned earlier, the FCT tends to generate too much convection near the time of maximum surface heating. The LDT had less convection in Colorado than FCT, but completely missed the development of MCS1 convection into Missouri. The LDT also missed the development of convection across western and central Kansas. As discussed in Chapter 4, the CTL run developed convection in a band across Kansas that resembles the actual MCS2 precipitation. The LDT results bear little resemblance to MCS2, especially considering that the LDT rainfall area in eastern Kansas had moved little during the previous six hours. Both runs had convection across southern Oklahoma where only shallow cumulus was observed.

Slightly different amounts of explicit moisture were produced by the three simulations (not shown) with the FCT generally producing the most hydrometeors and CIN the least. None of the simulations produced an extensive, realistic MCS1 stratiform region.

For the weakly-forced 3-4 June case, model results are quite sensitive to changes in the convective trigger function. These results back up the findings of Kain and Fritsch (1992) and suggest more investigations (particularly observational studies) are needed before convective systems can be accurately simulated. It will likely be necessary to parameterize the trigger function, using different triggers in different meteorological regimes. For example, using the FCT in areas of surface-based convection within a well-mixed boundary layer and using the LDT or CIN where there is frontal overrunning. Currently, all the triggers are based on low-level conditions – changes aloft are assumed only to effect the temperature and moisture profiles. Stensrud and Maddox (1988) and Miner (1992) have shown that deep convection can be suppressed in regions with strong low-level forcing by circulations aloft.

The development of convection in northwest Kansas

As shown in Chapter 4, convection began in the CTL simulation over northwest Kansas at 3/2020. No corresponding convection developed in LDT. Fig. 5.39 shows a profile of θ_E and saturated θ_E from the CTL run at the grid point where convection developed in northwest Kansas at 2020 UTC. The minimum deep lifting depth for parcels on this sounding was 81 mb – much larger than the 50 mb depth needed to activate the LDT. Animation of the grid point profiles shows that while θ_E was increasing with time at 800 mb due to advection by the low-level jet, warm advection at 700 mb was increasing the cap at a faster rate. The parcel vertical velocities attained from the positive buoyancy within the unstable layer between 750 and 700 mb were sufficient to overcome the overlying cap in the FCT. Activation of the LDT was not possible at this grid point and became more difficult with time. So, aside from the small differences in evolution of the variables between the two simulations, the difference in trigger function alone was the cause of the different evolution in the Kansas convection after 2000 UTC.

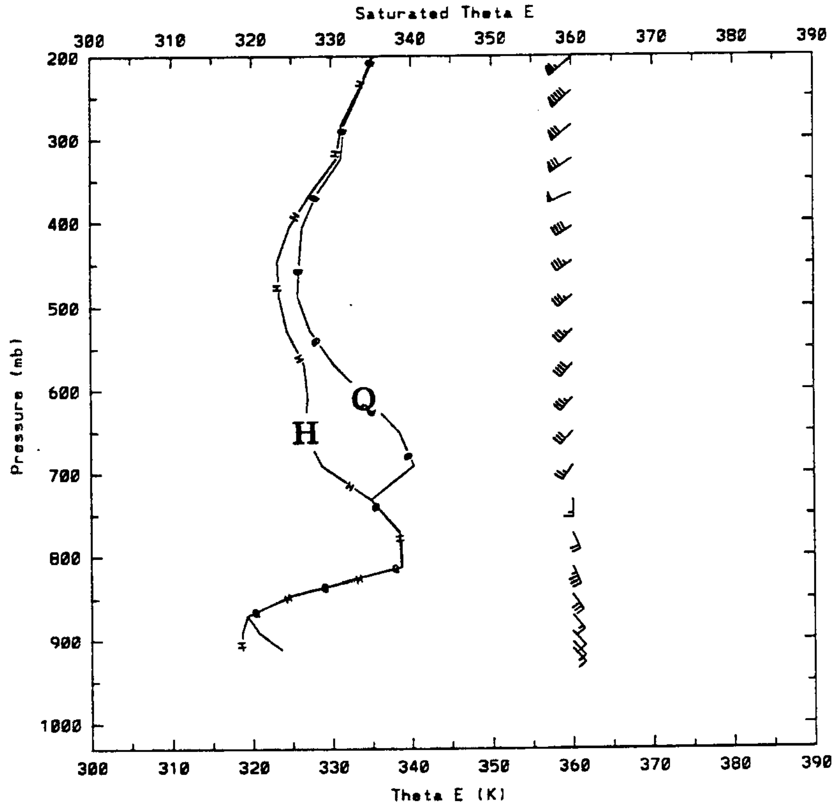

Figure 5.39: Vertical profile of θ_E (curve H) and saturated θ_E (curve Q) (in ° K) for a grid point in northwest Kansas at 3/2020.

5.2.2 Arakawa-Schubert Scheme

Grell *et al.* (1991) and Grell (1993) demonstrate that an Arakawa-Schubert parameterization with downdrafts can successfully simulate midlatitude MCSs. Simulations of the 3-4 June were conducted using this AS scheme.

The lifting depth trigger function used with the AS scheme tests for the removal of a restraining inversion as follows. Starting at the level of maximum moist static energy, each source parcel is lifted to determine if an LFC exists. If one does, the LFC is computed 30 minutes into the future based on the instantaneous tendencies. Then, if the pressure difference between the source level and the future LFC is less than 50 mb, the cloud computations proceed. If the trigger is not activated, the next highest source parcel is checked, up to about the 500 mb level.

Fig. 5.40 shows the three-hour simulated convective rain at 3/1500 from a run using the AS scheme. While convective rain is predicted near the origins of MCS1 and MCS2,

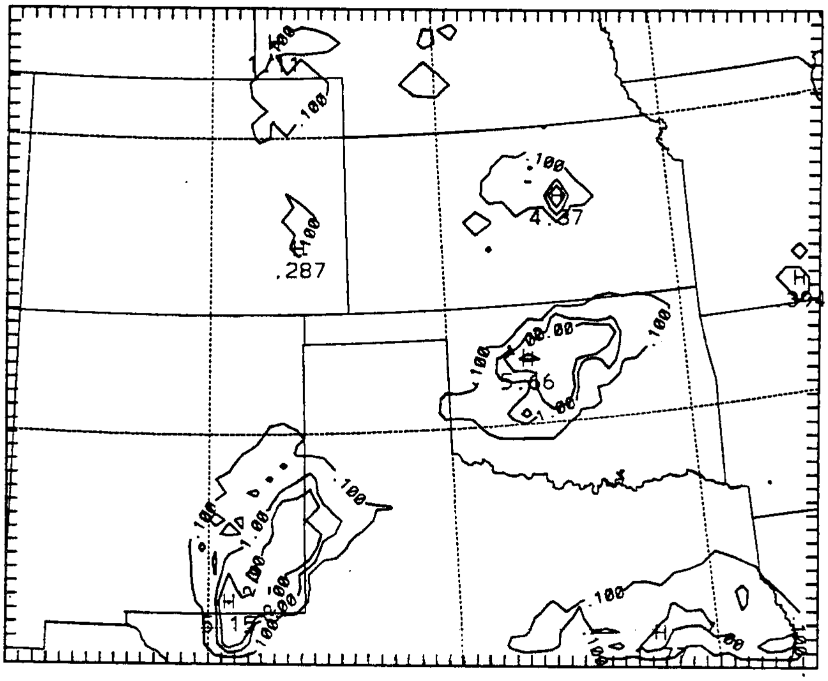

Figure 5.40: Convective rainfall for the 3 h period ending 3/1500, as in Fig. 4.3a, but from the unmodified AS run.

convective rain is produced over Oklahoma where only trace amounts were observed and over southeast Texas where none was observed. The airmass over southeast Texas was very unstable, but was also strongly capped (Fig. 2.26e). The LDT disregards the strength of a cap and only considers the depth that a parcel must rise to its LFC. Therefore areas with strong, but shallow caps are prone to activating the trigger. Vertical velocities over southeast Texas were weak (not shown), seldom exceeding -2 μb s^{-1} in low levels. Therefore, an additional trigger test was added that required upward motion to be greater than 2 μb s^{-1} at the source level and at the next highest model level. This rather weak requirement reduced the southeast Texas convection, without affecting other convective areas which usually had upward motion easily exceeding the 2 μb s^{-1} threshold. The over-predicted rain in Oklahoma and the excess amounts in southeast New Mexico required more analysis.

The Arakawa-Schubert scheme was designed to parameterize tropical convection and contains some assumptions which are not applicable to the mid-latitudes. The downdraft scheme (Grell 1993) is based on the work of Houze *et al.* (1980) who developed a diagnostic scheme for GATE convective systems. Over the GATE region, cloud bases are comparatively low (below 1 km) and so, evaporation below cloud base is not very great. Over the mid-latitudes, cloud bases can be very high (> 6 km) and the sub-cloud layer can be very dry (e.g. Fig. 2.26d OKC sounding). Complete evaporation of the cloud's rainfall can occur (except for a few of the very largest raindrops). The 3/1200 OKC sounding was used to initialize the parameterized microphysical model of Gallus (1993). A simulation based on this sounding developed weak, high-based convection which produced precipitation that evaporated before reaching the surface (not shown).

Following Johnson (1976), the AS downdraft scheme assumes that the downdraft mass flux is a function of the updraft mass flux and reevaporation of convective condensate (Grell 1993),

$$m_0(\lambda) = \frac{\beta(\lambda) I_1(\lambda) m_b(\lambda)}{I_2(\lambda)} = \epsilon(\lambda) m_b(\lambda).$$

where $m_0(\lambda)$ is the mass flux of the downdraft origin (the level of minimum saturated moist static energy within the cloud), $m_b(\lambda)$ is the updraft base mass flux, $I_1(\lambda)$ is updraft condensate, $I_2(\lambda)$ is the evaporation of condensate in the downdraft, $1-\beta(\lambda)$ is the precipitation efficiency and λ is the spectral cloud type. The precipitation efficiency is computed based on the cloud layer mean wind shear (Fritsch and Chappell 1980a). The deficiencies of the FC precipitation efficiency formula are discussed elsewhere in this chapter, but even assuming a perfect foreknowledge of a given cloud's precipitation efficiency, this downdraft scheme is inadequate. For the OKC sounding,

$$I_2 \gg I_1, \quad \beta \sim 1 \quad and \quad \epsilon = 0.1.$$

The downdraft mass flux is adjusted so that it evaporates the amount of condensate produced in the updraft. Using the example of the MCS1 convection with a high precipitation efficiency,

$$I_2 \simeq I_1, \quad \beta \sim 0.1 \quad and \quad \epsilon = 0.1.$$

In both cases, m_0 is an identical percentage of m_b despite a very different environment.

Johnson (1980) states that ϵ may be a function of wind shear, relative humidity, and convergence/divergence patterns. Fankhauser (1988) discussed the wide variety of factors which influence precipitation efficiency and the difficulties in determining a general relationship based on limited observations. He suggested further investigations require a detailed cloud model. Determination of a relation for ϵ is equally difficult. Here, modifications were made to the downdraft computations to improve the low-efficiency, high-based cases rather than to determine a general formulation for ϵ.

Rather than automatically extending the downdraft to the surface as in the Grell (1993) AS scheme, the downdraft was stopped at the level where the evaporation equaled the available condensate (i.e. where $I_2 = I_1$) and ϵ was fixed to be one. The downdraft then detrains at the next lowest level. This modification would mostly affect clouds with little precipitation production (weak or shallow clouds) with high bases or very dry subcloud layers.

Fig. 5.41a shows the three hour simulated rain at 3/1500 using the modified AS scheme (MAS). Experiment MAS is identical to the CTL run, except the modified AS scheme is used on both the large and nested grids. The erroneous rain areas over Oklahoma

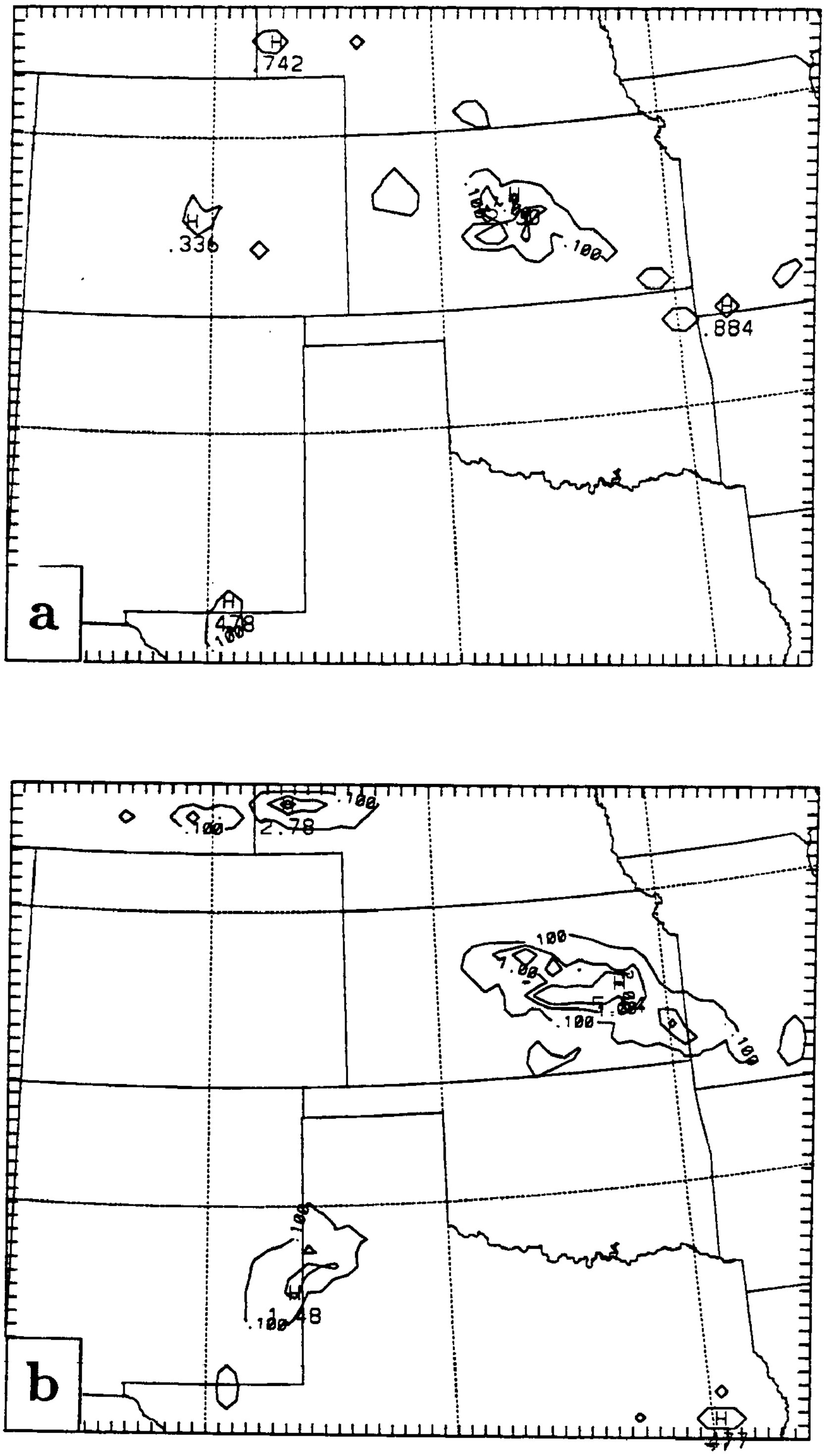

Figure 5.41: Convective rainfall as in Fig. 4.5a, but from the MAS run at a) 3/1500, b) 3/1800, c) 3/2100, and d) 4/0000.

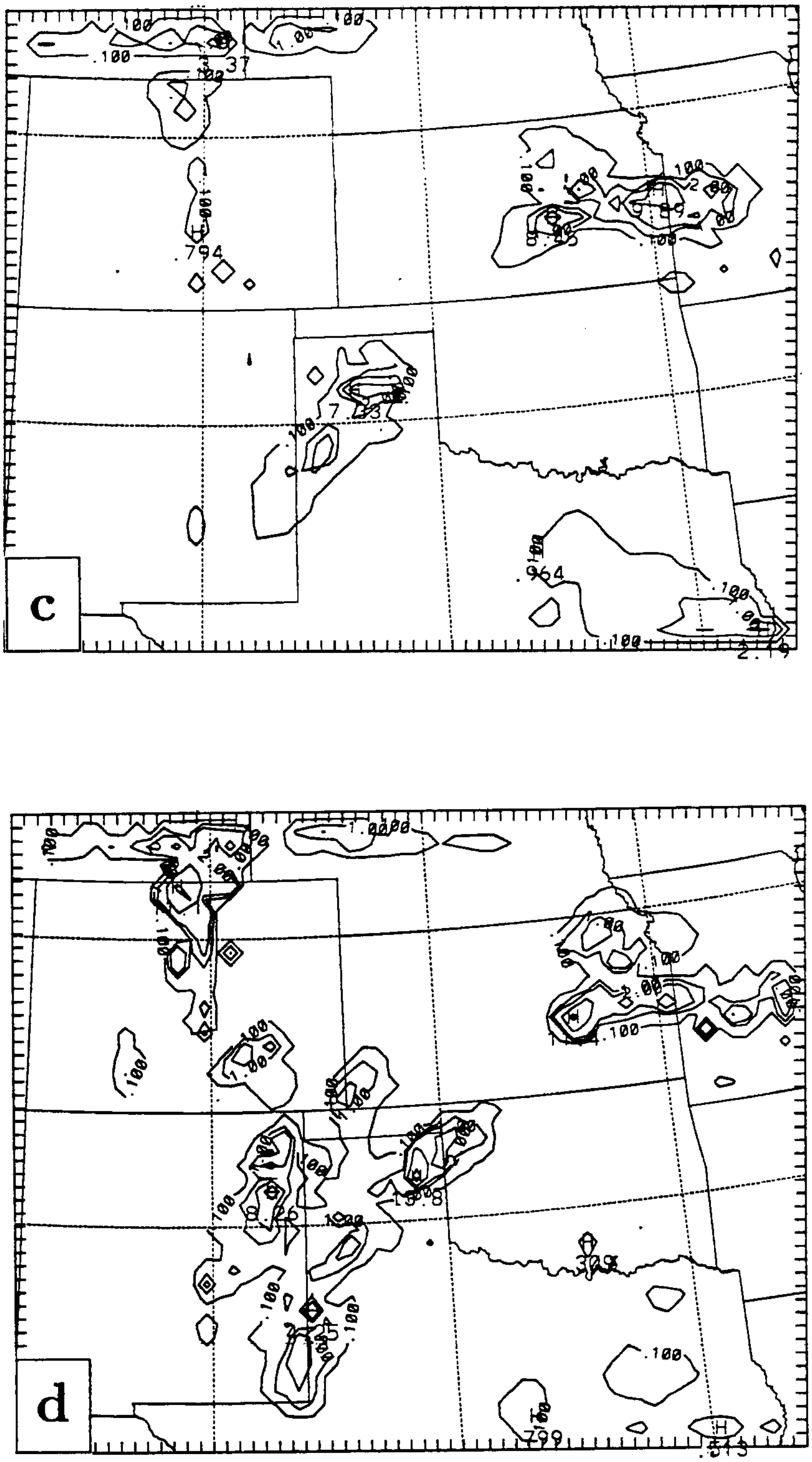

Figure 5.41: Continued.

and Texas in the unmodified AS scheme have been eliminated. The excess precipitation previously found with MCS2 (Fig. 5.40) has also been reduced. Meanwhile, the simulated convective rain associated with MCS1 is quite reasonable. As compared to CTL, by 1500 UTC the AS scheme has produced more rainfall over a larger area. By 3/1800 (Fig. 5.41b) MCS1 is developing toward the east and southeast. A rain area is along the New Mexico-Texas border, similar to the actual MCS2. A small amount of rain is forecast over southeast Texas.

A one-dimensional version of the MAS scheme was constructed in order to conduct some simple tests with the parameterization. The 1-D version was used to investigate the triggering of MCS1 convection. Input to the routine is a grid point sounding and temperature and water vapor tendencies. Fig. 5.42 shows an input profile from a point west of PTT at 3/1200. Source parcels between 800 and 700 mb need considerable lift to reach their LFC. Over this depth warm advection is implied by the veering of the winds. So, the input temperature tendency to the 1-D routine consisted of warming in the 800-700

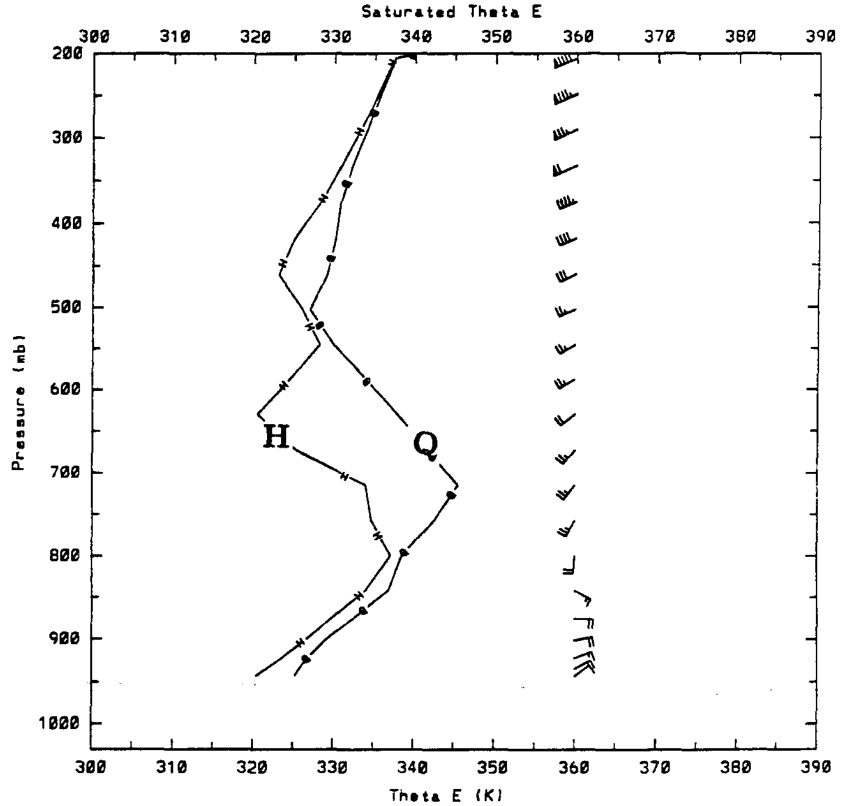

Figure 5.42: Vertical profile of θ_E (curve H) and saturated θ_E (curve Q) (in ° K) at 3/1200 for a grid point west of PTT near the origin of MCS1.

mb layer and slight cooling aloft. The moisture tendency was similar to that computed by the model. No convection was triggered with these tendencies. Convection was triggered when cooling was introduced near the cloud base. Convection also started when moistening near cloud base was large. In both cases, the effect was to more easily saturate the updraft parcel. It seems then, that in areas of warm advection, it is not the de-stabilization of the sounding by low-level warming which triggers convection, but cooling due to upward motion or moisture advection which eventually triggers the convection. The low-level jet can provide strong moisture advection and enhanced upward motion can be found near the the jet's terminus. Thus, the nose of the LLJ should be a favored region for triggering of convection within a warm advection pattern (Trier and Parsons 1993).

During the next three hours of the simulation, MAS simulates very well the motion of MCS1 to the east into Missouri (Fig. 5.41c). Unlike the CTL run, convection does not develop along the surface front in northern Oklahoma. The development of MCS2 across the Texas panhandle is also simulated well. There is, also more realistically, less convection along the steep slopes in Colorado than in the KF runs. Deficiencies in the forecast are the excess convection over southeast Texas (reduced by the modifications to the trigger function, yet still present) and the re-development of convection north of ICT, behind MCS1. The wind fields evolve similarly to CTL (not shown) producing both the upper and lower level jets over Kansas. However, as with the LDT run, convection does not develop in northwest Kansas. Through the first 9 h of the simulation, the AS scheme performs fairly well, perhaps outperforming CTL in terms of location and amounts of rain. During the rest of the simulation, however, the AS run develops significant problems.

Fig. 5.41d shows the 3 h rain for the period ending 4/0000. Convective rain areas moved very little during this period and did not move much for the rest of the simulation. Convection continued to develop unrealistically in eastern Kansas behind MCS1. Numerical Point Storms formed along the Kansas-Missouri border east of TOP and in northeast New Mexico. There NPS's moved slowly eastward during the rest of the simulation. The low-level temperature fields (not shown) were generally similar to CTL at 4/0000, but the 900 mb temperature gradient was much broader than in CTL due to less downdraft cooling in northern Kansas. Also, the cold pool beneath the convection in the eastern Texas panhandle was much weaker in the MAS run, producing weaker convergence there. The weaker cold pool is related to differences in the downdraft scheme between the AS and KF parameterizations. In this weakly-forced case, the triggering and propagation of convection is influenced by these small differences in the schemes.

5.2.3 Precipitation Efficiency

Both the KF and AS parameterizations use precipitation efficiency to determine the mass flux of the downdraft. Fritsch and Chappell (1980a) fit a curve to observations of precipitation efficiency as a function of cloud-layer wind shear. Precipitation efficiency was defined as the ratio of surface rain to the vapor flux through the cloud base. The downdraft mass flux is then computed as that fraction of a unit updraft which results in convective rainfall which matches that predicted by the computed precipitation efficiency. Zhang and Fritsch (1986a) attempted to improve the accuracy of this approach by making use of the results of Fujita (1959). Fujita determined the precipitation efficiency (which he defined as the ratio of surface rain to surface rain plus rain evaporated in the downdraft) for precipitating convection with various cloud base heights. In general, the higher the cloud base, the smaller the precipitation efficiency. Zhang and Fritsch (1986a) simply fit a curve to Fujita's Fig. 13 and used a mean of the wind-shear-based efficiency and the cloud base height efficiency in their model calculations. While this approach has been recognized as a crude estimation of very complicated cloud dynamic processes it has proved to be a reasonable approach. However, an observational study by Fankhauser (1988) concluded that the precipitation efficiency is more complicated than a simple inverse dependency on wind shear. Figure 5.43 shows a plot of precipitation efficiency as a function of wind shear using Fritsch and Chappell's (1980a) Figure 2 and the data from Fankhauser (1988). The data exhibit considerable scatter so that a simple curve cannot be fit to the data. In addition, Fankhauser's efficiencies are smaller than many of those found in previous studies. He states that "a significant amount of water vapor inflow may have been overlooked in past work... resulting in overestimates in precipitation efficiency". Some of the other environmental factors which Fankhauser found to be positively correlated with

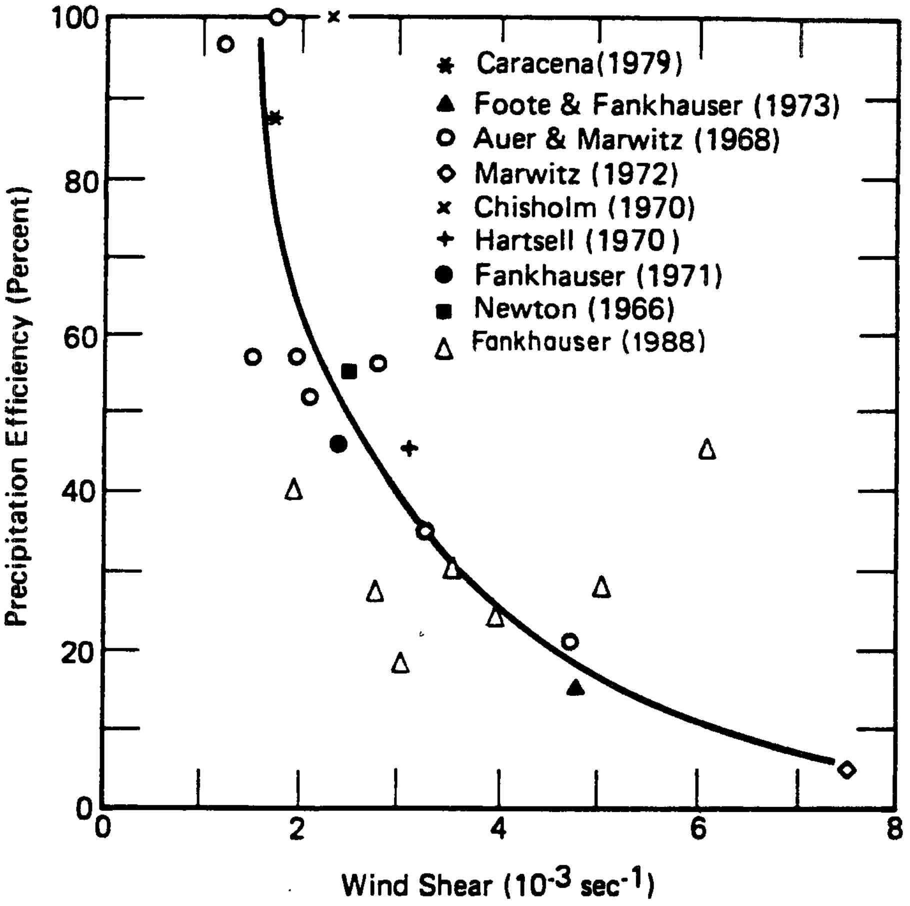

Figure 5.43: Precipitation efficiency as a function of wind shear. Adapted from Fritsch and Chappell (1980a), but with the additional results of Fankhauser (1988).

precipitation efficiency included subcloud mixing ratio, shear kinetic energy in the lower troposphere, and cloud base area. Higher water vapor content below cloud base and larger cloud base areas imply less evaporation would occur.

The convection within MCS1 over central Kansas was relatively high-based (700 mb) and thus would have a low precipitation efficiency (and therefore strong downdrafts) as computed by the application of Fujita's results by Zhang and Fritsch (1986a). However, the subcloud air over Kansas was generally saturated as indicated by surface reports of low clouds and fog and there was only relatively weak convective surface outflow (Green 1989). The computation of precipitation efficiency was therefore modified to account for subcloud layer relative humidity. Fujita (1959) provided a generalized expression for the cold air production (related to the precipitation efficiency) :

$$\Gamma^* - \Gamma_m = \lambda\,(\Gamma_d - \Gamma_m)$$

where Γ^* is the environmental lapse rate, Γ_d and Γ_m are the dry and moist lapse rates, respectively, and λ is a parameter which gives an arbitrary lapse rate. Thus, for a subcloud environmental lapse rate which was dry adiabatic, $\lambda = 1$ and for a subcloud lapse rate which was moist adiabatic (i.e. saturated) $\lambda = 0$. The efficiency used by Zhang and Fritsch (1986a) based on Fujita's (1959) Figure 13 assumes a dry adiabatic subcloud layer (i.e. $\lambda = 1$). This is valid for areas with surface-based convection in which the environmental lapse rate is nearly dry adiabatic. For convection above a warm front, the subcloud layer may be more nearly moist adiabatic and therefore some modification is necessary. For practicality, the environmental lapse rate was computed as the mean subcloud lapse rate. Since the moist adiabatic lapse rate is a function of temperature, Γ_m was computed at a point halfway between the cloud base and surface. The factor, λ, was then obtained and was constrained to be between 0.2 and 1.0. The expression for the cloud base precipitation efficiency, E_{CB} is then

$$E_{CB} = \frac{1}{1 + \lambda\, E_R}$$

where E_R is the curve fit to Fujita's Figure 13 as given by Zhang and Fritsch (1986a) Eq. 13. This efficiency was then averaged with that obtained by the wind shear expression for use by the KF parameterization.

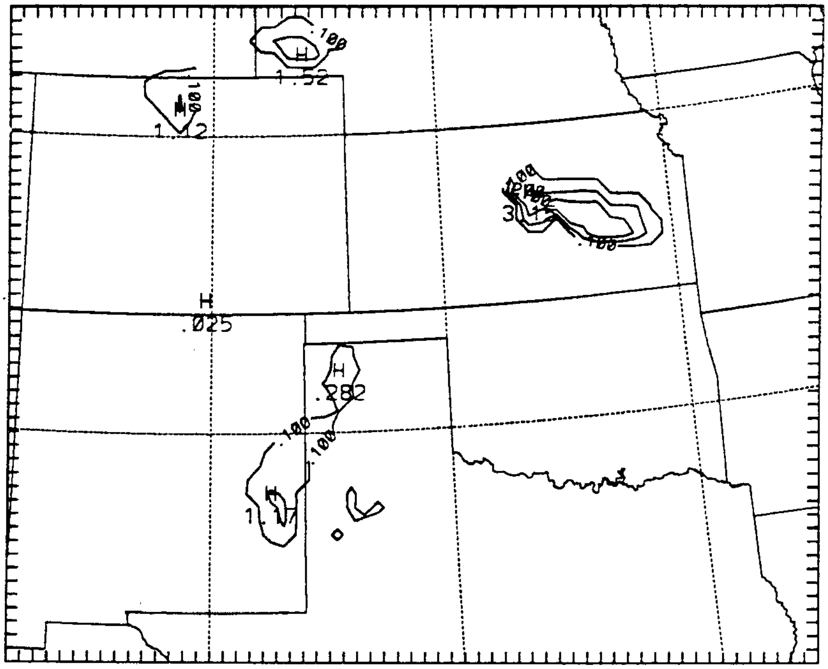

Figure 5.44: Three-hour convective rainfall tendency from PEF (as in Fig. 4.5a) for the period ending 3/1800.

Figure 5.44 shows the three-hour convective rainfall tendency for the period ending 3/1800 for a simulation using the original (Zhang and Fritsch 1986a) precipitation efficiency (PEF). The rainfall pattern is identical to CTL (Fig. 4.5a), but amounts are reduced because the calculated precipitation efficiences are lower than in CTL. As expected, the largest differences occur in the near-saturated airmass over Kansas where the CTL maximum is 50% greater than in PEF. Modest, but realistic improvements were found with the modified precipitation efficiency, so it was used in all the KF parameterization runs presented earlier.

5.2.4 Increased vertical resolution

Following the ideas of Lindzen and Fox-Rabinovitz (1989), Persson and Warner (1991) showed that the ratio of vertical to horizontal grid spacing is critical for accurate simulation of the circulations associated with sloped frontal systems. A nine hour simulation identical to CTL, but with 32 vertical levels was conducted to examine the impact of higher resolution on the 3-4 June simulation. Figure 5.45 shows the three-hour rainfall tendency from the 32-level run at 3/2100. In general, implicit rain amounts were higher in LV32. Convection occurred in northeast Oklahoma (Fig. 5.45a), but the maximum amounts were slightly farther north than in CTL (Fig. 4.10a). At this time, the simulated MCS1 was not split as in the CTL run. The explicit rainfall (Fig. 5.45b) was more extensive than in CTL (not shown) and led to a more realistic wake low / mesohigh couplet as in Z0. The MCS2 convection in the higher resolution run (Fig. 5.45a) was greater and farther north than in CTL, but still lagged observations. Implicit rain amounts in northwest Kansas and in Colorado were lower than in CTL. The isolated convective rain area in south-central Kansas is a significant feature of the 32-level run. The only other run to produce convection at that location was the 23-level CIN simulation.

While the addition of vertical levels produced a noticeable improvement in the simulation, the similarities of the high resolution run with the previous simulations suggests that other factors, such as the initial conditions or the trigger function, are of greater importance in determining the evolution of the convective systems.

5.3 Summary

Several sensitivity tests revealed important features about the 3-4 June case as well as the modeling of weakly-forced convective systems.

- The upper-level jet streak, shown in Chapter 4 to have been coupled with a LLJ which destabilized the airmass over Kansas, was not caused by outflow from the nascent MCS2 convection.
- The simulated upper-level jet streak was not a consequence of the initial wind field, but of other dry dynamic processes associated with confluent geostrophic flow in the region of a sloped tropopause.
- MCS1 had no significant impact upon the simulated LLJ across KS.
- The low-level (but above the surface) frontal gradient across Kansas in which the shear-parallel arm of MCS2 formed in CTL was in a region of frontogenesis.

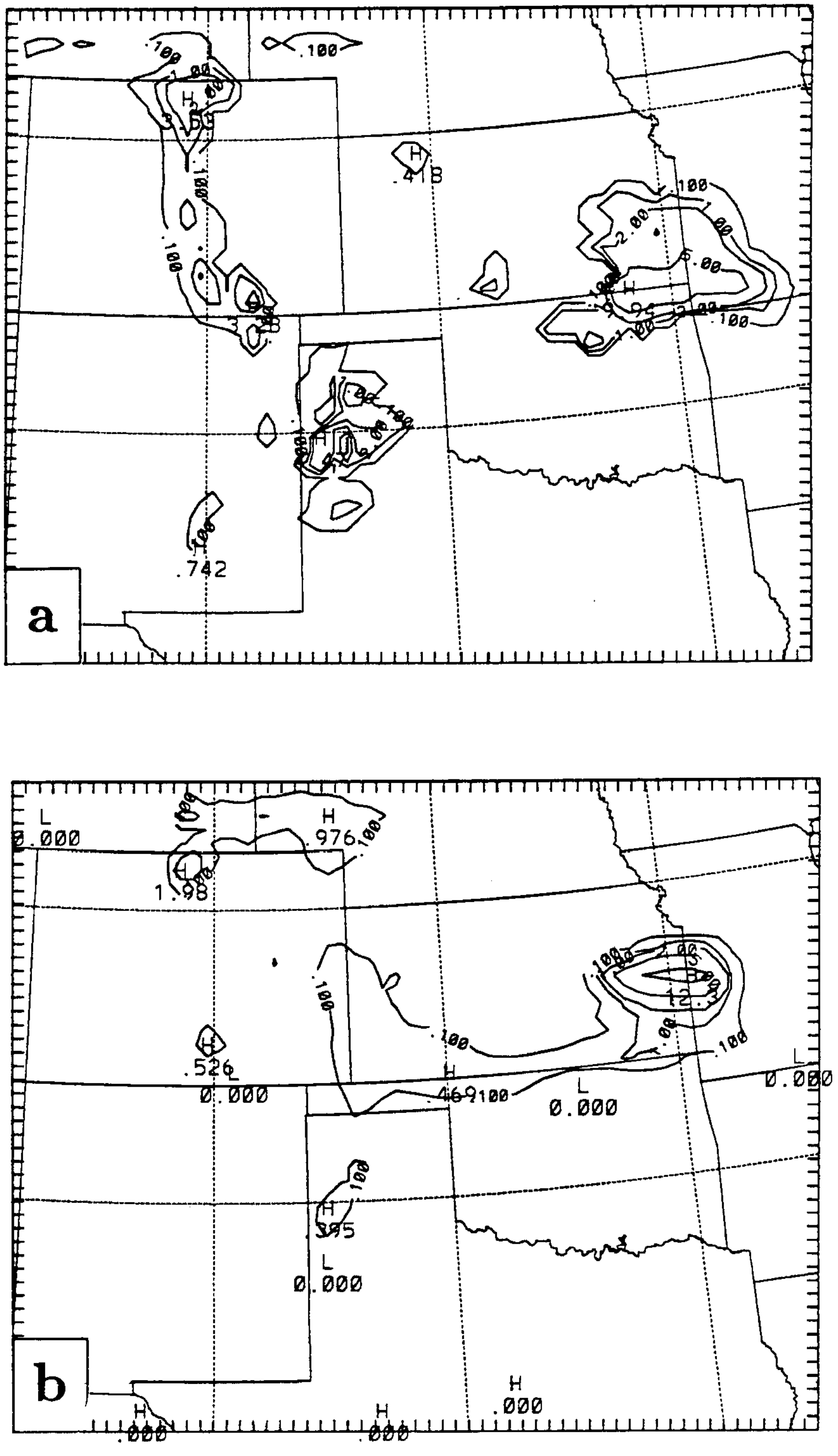

Figure 5.45: Three-hour rainfall tendency (contoured as in Fig. 4.5a) for the period ending 3/2100 from the 32-level run for a) implicit rainfall and b) explicit rainfall.

- Divergence and sinking motion in the lower troposphere over the panhandles and southwest Kansas, which prevented the trigger function from activating MCS2 convection, was a result of sinking beneath an area of explicit rain as well as speed divergence behind a LLJ.

- The first guess field has a significant impact upon the simulation of the 3-4 June MCSs. Of particular importance is the initial moisture distribution. These findings suggest that mesoscale details (not supplied by the current observational network) are important in developing initial conditions which lead to accurate simulations of weakly-forced convective systems. While Stensrud (1992) shows that mesoscale surface details are important for some simulations, when convection is based well above the surface (as in the present case) mesoscale details are needed aloft. Future observing systems need to measure temperature and moisture in addition to winds in order to provide mesoscale models with useful initial conditions.

- Trajectory analysis of source air parcels for MCS1 convection show that they originated the previous afternoon in the heated surface layer over Oklahoma and Texas. These air parcels rode up over the frontal surface, reaching their LFC over Kansas the following morning. This processes agrees with the findings of Trier and Parsons (1993).

- Within MM4, the surface pressure features commonly found with MCSs (i.e. the wake low) form only when there is an extensive explicit rain area. This result agrees with the squall-line findings of Zhang and Gao (1989).

- The formation of NPSs, occurring due to excessive grid-scale latent heating feedback, is not always eliminated by the simultaneous use of implicit and explicit moisture parameterizations. Zhang (*et al.* 1989) argued that implicit and explicit parameterizations when used together could prevent NPSs.

- In agreement with Kain and Fritsch (1992), the simulation of convective systems was found to be sensitive to the trigger function.

- Both the LDT and FCT were found to have significant deficiencies. A trigger based on convective inhibition shows some promise, but, like the LDT, has difficulty in dry regions.
- The downdraft formulation with the Arakawa-Schubert scheme as developed by Grell (1993) is inadequate for mid-latitude convection. The effects of rain evaporation below cloud base need to be considered.

Despite many changes to the initial data and convective parameterizations, an ideal simulation of all the aspects of the 3-4 June case was not obtained. This points to the difficulty in simulating a complex, weakly-forced case such as 3-4 June. Many components of the simulation (such as the upper-level flow field, its coupling with the low-level flow, the development of the heated boundary layer south of the front and the cloud formation and shading north of the front) must all be handled well by the model, as MCS2 is the end result of a complex sequence of events. However, signals do exist which may aid forecasting of these MCSs. A LLJ (though poorly sampled) riding over the frontal surface in the manner of Trier and Parsons (1993) was suspected of causing MCS1. MCS2 was associated with an identifiable upper-level jet streak throughout its lifetime. The findings of this study suggest that accurate simulation of weakly-forced convective cases are dependent upon mesoscale features in the initial data (as was found by Stensrud 1992) and components of the convective parameterization such as the trigger function (as found by Kain and Fritsch 1992).

Chapter 6

SUMMARY AND CONCLUSIONS

A case in which a series of MCSs occurred, 3-4 June 1985, was examined using both observations and a numerical model. The first two MCSs of the series were studied in detail in order to determine how they initiated and interacted. The main conclusion of the study is that despite the use of a detailed numerical model and the best available initial data, explicit simulation of MCSs is still, at best, difficult. This difficulty is due to our lack of understanding of the complicated behavior of convection. When synoptic forcing is dominant (as on 10-11 June 1985 (Zhang *et al.* 1989)) and the convection behaves in a manner for which the current parameterizations can account, simulations can be quite accurate. However, when there is weak forcing or the convective forcing is dominant, current models fail.

The analyses did reveal aspects of the case which may lead to better prediction of MCSs. It was found that MCS1 convection began above the surface in a region of strong low-level warm advection and moisture convergence at the nose of a LLJ, similar to the concept described by Trier and Parsons (1993). Upper-level forcing (such as lifting by a short wave or jet streak circulations) did not play a significant role in triggering the convection. Gravity waves were detected at initial time, but they did not appear to be linked to the triggering of MCS1. MPV analysis indicates that slantwise convective motions were possible in the MCS1 environment and may have helped trigger the upright convection.

The CTL simulation (using the MM4 model configured similarly to Zhang *et al.* 1989) was able to capture some of the observed features of the 3-4 June MCSs, although many of the meso-β-scale details were not well-simulated. The simulated MCS1 began as observations suggested at the nose of a low-level jet riding over the frontal surface into a region with enhanced moisture levels. The simulated MCS1 propagated to the east similar to the observed system, but produced less rainfall than actually occurred. Relative flow through the system indicates that MCS1 fed on unstable air riding over the frontal surface. The low-level stable air did not directly participate in the system's circulation. No front-to-rear flow developed within the system and only weak rear-to-front-flow was generated. The model never developed the observed large stratiform region and consequently the surface pressure features were also weaker than observed. The simulated MCS1 decayed prematurely when its inflow of high θ_E air was cut off by convection which developed erroneously along the surface front to the south.

A model run initiated 13 hours before the outbreak of MCS1 convection was able to develop a convective system in the right location over Kansas at about the right time. The source air for the MCS1 convection originated in the heated boundary layer over Texas and Oklahoma the previous afternoon, rose along the frontal surface during the night and arrived in southern Kansas in the morning. Triggering mechanisms for the elevated convection of this system were similar to CTL in which strong low-level warm advection and lifting allowed unstable parcels to reach their LFC. The simulated MCS1 in this run was able to generate an extensive stratiform area and realistic surface pressure features.

MCS2 was linked throughout its lifetime to an upper-level jet streak. The ULJ existed in the initial conditions, prior to any significant convection. Simulated, weak, high-based convection strengthened as it moved into an area with deeper low-level moisture. A LLJ developed beneath the exit region of the ULJ over western Kansas, destabilizing the air mass over the frontal surface. Convection broke out in western and central Kansas ahead of and apart from the original convective region. Sensitivity studies showed that this LLJ was not the result of outflow from MCS1. The ULJ was associated with confluent geostrophic flow in the region of a sloped tropopause and was not generated by MCS2 convection. The strong response of the low-level flow to the approach of the upper-level jet streak was aided by the decoupling of the low-level winds from surface friction by the frontal inversion. Figure 6.1 shows a conceptual diagram of the jet-frontal circulations for the early afternoon of 3 June. A strong LLJ is induced by the ageostrophic circulations about

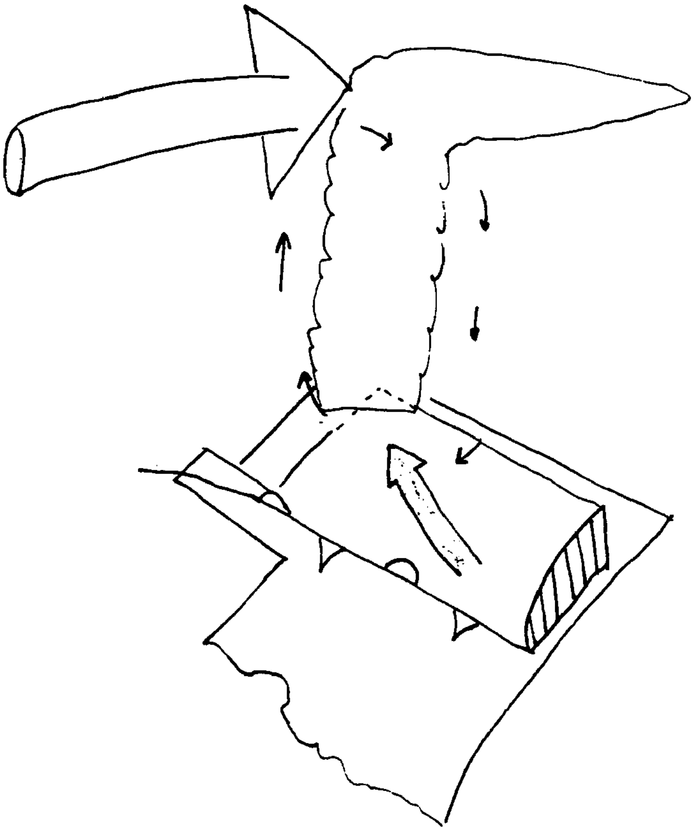

Figure 6.1: Conceptual diagram of the jet-frontal circulations in the vicinity of an east-west surface front. The broad open arrow represents the upper-level jet streak. The thin arrows represent the indirect transverse circulation. The low-level jet (shaded arrow) lies atop the cold wedge of air, destabilizes the airmass and leads to the development of deep convection.

the upper-level jet streak. The LLJ is able to advect high-θ_E air from the southeast, destabilizing the airmass over the front. This concept is different than the schematics shown by Shapiro (1982) and suggests that the area north of a shallow warm or stationary front might be particularly susceptible to the rapid development of low-level jets.

Strong downward motion beneath an explicit rain area and in the wake of the LLJ, prevented model convection from developing across southern Kansas as was observed with MCS2. The simulation did produce two precipitation bands as were observed within MCS2. The northeast-southwest shear-parallel band across central Kansas formed along a frontogenetic low-level thermal gradient while the north-south shear-perpendicular band across western Oklahoma and the Texas panhandle was forced by low-level convergence of convective outflow.

The simulation was found to be sensitive to the initial moisture distribution over Kansas. Mesoscale details (not supplied by the current observational network) are important in developing initial conditions which lead to accurate simulations of weakly-forced convective systems. While Stensrud (1992) shows that mesoscale surface details are important for some simulations, when convection is based well above the surface (as in the present case) mesoscale details are needed aloft. Future observing systems need to measure temperature and moisture in addition to winds in order to provide mesoscale models with useful initial conditions.

These results may have some applicability to numerical weather prediction in tropical regions. Like the tropics, the 3-4 June case had large areas of potential instability with only weak forcing. The sensitivity of the simulation to the initial data suggest that in the tropics, where there is often a paucity of data, numerical prediction of convective systems may be extremely difficult.

As also found by Kain and Fritsch (1992) for the 10-11 June 1985 case, simulation of the 3-4 June MCSs was found to be sensitive to the convective trigger function. Both the Fritsch-Chappell trigger and the lifting depth trigger exhibit noticeable deficiencies. A trigger function based on convective inhibition shows some promise, but further research, especially observational studies, are needed before a general trigger function can be designed.

The complexities of the 3-4 June 1985 case demonstrate that improved numerical prediction and understanding of MCSs will require improved parameterizations which, in turn, will require additional field observation programs with high spatial and temporal resolution. Because the evolution of a simulated convective system depends on when the convection is triggered, a better understanding of the initiation and early growth stages of MCSs is needed. Operational synoptic observations (as well as previous field programs) have permitted the determination of the general conditions favorable for MCS formation. Based on the numerical results of the current study, I would recommend the following strategy for identifying triggers. Upstream of the region of interest, such as along the spine of the Rocky Mountains extending into Mexico, a "picket fence" of wind profilers or rawindsondes need to be deployed to identify shortwaves or jets streaks that might act as triggers. Currently, forecasts can identify the general areas favorable for initiation. Mobile sounding units could be deployed in this region, launching soundings in the vicinity of suspected triggering features (e.g. on both sides of a dry-line or near a LLJ – frontal intersection). Since the triggering occurs on such small time and space scales, closely-spaced soundings would be needed – approximately 20 km and 1 h apart. The mobile teams could then travel along with the convective area to sample the MCS's early growth. At least four sounders would be needed. Additional units could sample the far-field environment. Current surface stations along with WSR-88D data (Crum and Alberty 1993) could serve to identify boundaries that may trigger the convection.

Improvement of convective parameterizations will also require a better understanding of the convection's source air. The KF scheme assumes that a 60 mb mixed layer of air is the source air for the cloud. Operational methods for computing lifted index lift the surface parcel or a 100 mb or 150 mb mixed parcel. The negative area on a sounding can vary greatly depending on the source layer chosen. Determining the source air of a convective cloud would require detection of winds in clear air - perhaps possible by using radar along with chaff releases.

The impact of convection on its environment depends on the spatial scale under consideration. The large-scale (i.e. much larger than the individual convective elements) impact is generally understood as indicated by the success of parameterizations such as the AS scheme in general circulation models. At smaller scales, such as on the order of 25 km (the "critical range" (Bougeault and Geleyn 1989)) details are not understood and parameterizations are prone to failure. For example, Stensrud (1992) attempted to delay the onset of the downdraft within the Fritsch-Chappell parameterization (as is observed in nature) and obtained significantly different results than with the standard FC scheme. For convection moving across a grid box, a fully developed cell doesn't move into a new box and start the life cycle all over again. A mature cell (perhaps a supercell) already has an established updraft and downdraft. The effects of directional shear are not accounted for by the convective time scale computation. Also, what about the case where cells are moving faster than the wind at any level as in MCS1? More field programs and numerical experiments (possibly with cloud models) are required before parameterizations on this scale can be improved.

A significant unsolved problem is the feedback between the implicit and explicit parameterization schemes (Molinari and Dudek 1992). Zack *et al.* (1985) pointed out some of the feedback problems with the Fritsch-Chappell scheme and conclude that the interaction between the grid and sub-grid scale moisture budgets needs to be carefully considered. Molinari and Dudek (1992) point out that transport of condensate from the convective scale to the grid scale (a significant source for the trailing stratiform region (Smull and Houze 1987a; Gallus 1993)) is not accounted for by the current MM4 approach.

Zhang *et al.* (1989) suggested that some cases can be accurately forecast using a mesoscale model with conventional synoptic input data. Based on the results from 3-4 June, some cases require more detailed initial data. It is quite possible that the majority of cases require detailed data. One approach, which was beyond the scope of this study, would be to use four dimensional data assimilation (FDDA). The failure of the simulation initialized at 3/0000 to accurately reproduce the MCSs (particularly MCS2) suggest that updated observations may be important. The results from the simulations initialized at 3/1200 suggest that the 0-6 hour forecasts require accurate initialization and mesoscale observations of temperature, moisture, and winds. In addition to FDDA simulations, high resolution model runs may reveal details about the triggering and upscale growth of the convection not captured by the 25 km runs.

While observational studies and numerical experiments have broadened our knowledge of MCSs, considerable work remains before these weather systems are completely understood and accurately predicted.

REFERENCES

Achtemeier, G. L., 1989: Modification of a successive corrections objective analysis for improved derivative calculations. *Mon. Wea. Rev.*, **117**, 78-86.

Anthes, R. A. and T. T. Warner, 1978: Development of Hydrodynamic models suitable for air pollution and other mesometeorological studies. *Mon. Wea. Rev.*, **106**, 1045-1078.

Anthes, R. A., Y.-H. Kuo, S. G. Benjamin and Y.-F. Li, 1982: The evolution of the mesoscale environment of severe local storms: Preliminary modeling results. *Mon. Wea. Rev.*, **110**, 1187-1213.

Anthes, R. A., E.-Y. Hsie and Y.-H. Kuo, 1987: Description of the Penn State/NCAR Mesoscale Model Version 4 (MM4). NCAR Tech. Note NCAR/TN-282+STR, 66 pp.

Anthes, R. A., Y. -H. Kuo, E. -Y. Hsie, S. Low-Nam and T. W. Bettge, 1989: Estimation of skill and uncertainty in regional numerical models. *Quart. J. Roy. Meteorol. Soc.*, **115**, 763-806.

Arakawa, A. and W. H. Schubert, 1974: Interaction of a cumulus cloud ensemble with the large-scale environment, Part I. *J. Atmos. Sci.*, **31**, 674-701.

Augustine and Zipser, 1987: The use of wind profilers in a mesoscale experiment. *Bull. Amer. Meteor. Soc.*, , 68, 4-17.

Augustine, J. A., and K. W. Howard, 1988: Mesoscale convective complexes over the United States during 1985. *Mon. Wea. Rev.*, **116**, 685-701.

Augustine, J. A. and F. Caracena, 1993: Lower tropospheric signals in the late afternoon that relate to nocturnal MCS development. NOAA Tech. Memo. NWS ER-87. Postprint volume, Third National Heavy Precipitation Workshop. Pittsburgh, PA, Nov. 16-20 1992, National Weather Service, Bohemia, NY, 299-319.

Barnes, S. L., 1973: Mesoscale objective map analysis using weighted time-series observations. NOAA Tech. Memo. ERL NSSL-62, Norman, Oklahoma, 60pp.

Beebe, R. G. and F. C. Bates, 1955: A mechanism for assisting in the release of convective instability. *Mon. Wea. Rev.*, **83**, 1-10.

Benjamin, S. G. and T. N. Carlson, 1986: Some effects of surface heating and topography on the regional severe storm environment. Part I: Three dimensional simulation. *Mon. Wea. Rev.*, **114**, 307-329.

Betts, A. K., 1986: A new convective adjustment scheme. Part I: Observational and theoretical basis. *Quart. J. Roy. Meteorol. Soc.*, **112**, 677-691.

Blackadar, A.K., 1957: Boundary layer wind maxima and their significance for the growth of nocturnal inversions. *Bull. Amer. Meteor. Soc.*, **38**, 283-290.

Blanchard, D. O., 1990: Mesoscale convective patterns of the southern high plains. *Bull. Amer. Meteor. Soc.*, **71**, 994-1005.

Bluestein H. B. and K. W. Thomas, 1984: Diagnosis of a jet streak in the vicinity of a severe weather outbreak in the Texas panhandle. *Mon. Wea. Rev.*, **112**, 2499-2520.

Bluestein, H. B., 1985: An observational study of a mesoscale area of convection under weak synoptic forcing. *Mon. Wea. Rev.*, **113**, 520-538.

Bluestein, H. B., 1993: *Synoptic-Dynamic meteorology in midlatitudes. Volume II: Observations and theory of weather systems.* Oxford University Press. 594 pp.

Bonner, W. D., 1966: Case study of thunderstorm activity in relation to the low-level jet. *Mon. Wea. Rev.*, **94**, 167-178.

Bosart, L. F. and F. Sanders, 1981: The Johnstown flood of July 1977: A long-lived convective system. *J. Atmos. Sci.*, 38 1616-1642.

Bougeault, P. and J. F. Geleyn, 1989: Some problems of closure assumption and scale dependency in the parameterization of moist deep convection for numerical weather prediction. *Meteor. Atmos. Phys.*, **40**, 123-135.

Brandes, E. A., 1990: Evolution and structure of the 6-7 May 1985 mesoscale convective system and associated vortex. *Mon. Wea. Rev.*, **118**, 109-127.

Brill, K. F., L. W. Uccellini, R. P. Burkhart, T. T. Warner and R. A. Anthes, 1985: Numerical simulations of a transverse indirect circulation and low-level jet in the exit region of an upper-level jet. *J. Atmos. Sci.*, **42**, 1306-1320.

Buzzi, A., M. Fantini and G. Lippolis, 1991: Quasi-stationary organized convection in the presence of an inversion near the surface: Experiments with a 2-D numerical model. *Meteor. Atmos. Phys.*, **45**, 75-86.

Byrd, G. P., 1989: A composite analysis of winter season overrunning precipitation bands over the southern plains of the United States. *J. Atmos. Sci.*, **46**, 1119-1132.

Cammas, J.-P. and D. Ramond, 1989: Analysis and diagnosis of the composition of ageostrophic circulations in jet-front systems. *Mon. Wea. Rev.*, **117**, 2447-2462.

Carbone, R. E., J. W. Conway, N. A. Crook, and M. W. Moncrieff, 1990: The generation and propagation of a nocturnal squall line. Part I: Observations and implications for mesoscale predictability. *Mon. Wea. Rev.*, **118**, 26-49.

Chadwick, R. B. and N. Hassel, 1987: Profiler: The next generation surface-based atmospheric sounding system. Preprints, *Third International Conference on Interactive*

Information and Processing Systems for Meteorology, Oceanography and Hydrology, New Orleans, Amer. Meteor. Soc., 15-21.

Chang, C. B., D. J. Perkey and C. W. Kreitzberg, 1981: A numerical case study of the squall line of 6 May 1975. *J. Atmos. Sci.*, **38**, 1601-1615.

Chang, C. B., D. J. Perkey and C. W. Kreitzberg, 1984: The impact of missing wind data on the accuracy of a numerical forecast of severe weather. Preprints, *Tenth Conf. on Weather Forecasting and Analysis*, Clearwater Beach, FL, Amer. Meteor. Soc., 513-520.

Chang, J.-T. and P. J. Wetzel, 1991: Effects of spatial variations of soil moisture and vegetation on the evolution of a pre-storm environment: A numerical case study. *Mon. Wea. Rev.*, **119**, 1368-1390.

Colby, F. P., Jr., 1984: Convective inhibition as a predictor of convection during AVE-SESAME II. *Mon. Wea. Rev.*, **112**, 2239-2252.

Colman, B. A., 1990a: Thunderstorms above frontal surfaces in environments without positive CAPE. Part I: A Climatology. *Mon. Wea. Rev.*, **118**, 1103-1121.

Colman, B. A., 1990b: Thunderstorms above frontal surfaces in environments without positive CAPE. Part II: Organization and instability mechanisms. *Mon. Wea. Rev.*, **118**, 1123-1144.

Cooper, I. M., A. J. Thorpe and C. H. Bishop, 1992: The role of diffusive effects on potential vorticity in fronts. *Quart. J. Roy. Meteorol. Soc.*, **118**, 629-647.

Cotton, W. R. and R. Anthes, 1989: *Storm and Cloud Dynamics.* Academic Press, 883 pp.

Cotton, W. R., M. S. Lin, R. L. McAnelly, and C. J. Tremback, 1989: A composite model of mesoscale convective complexes. *Mon. Wea. Rev.*, **117**, 765-783.

Cram, J. M., 1990: Numerical simulation and analysis of the propagation of a prefrontal squall line. Atmos. Sci. Paper No. 471, Colorado State University, 332 pp.

Cram, J. M., R. A. Pielke and W. R. Cotton, 1992a: Numerical Simulation and analysis of a prefrontal squall line. Part I: Observations and basic simulation results. *J. Atmos. Sci.*, **49**, 189-208.

Cram, J. M., R. A. Pielke and W. R. Cotton, 1992b: Numerical Simulation and analysis of a prefrontal squall line. Part II: Propagation of the squall line as an internal gravity wave. *J. Atmos. Sci.*, **49**, 209-225.

Crook, N. A., 1987: Moist convection at a surface cold front. *J. Atmos. Sci.*, **44**, 3469-3494.

Crook, N. A. and M. W. Moncrieff, 1988: The effect of large-scale convergence on the generation and maintenance of deep moist convection. *J. Atmos. Sci.*, **45**, 3606-3624.

Crook, N. A., R. E. Carbone, M. W. Moncrieff, and J. W. Conway, 1990: The generation and propagation of a nocturnal squall line. Part II: Numerical simulations. *Mon. Wea. Rev.*, **118**, 50-65.

Crum, T. D. and R. L. Alberty, 1993: The WSR-88D and the WSR-88D operational support facility. *Bull. Amer. Meteor. Soc.*, **74**, 1669-1687.

Cunning, J. B., 1986: The Oklahoma-Kansas Preliminary Regional Experiment for STORM-Central. *Bull. Amer. Meteor. Soc.*, **67**, 1478-1486.

Dexter, R. V., 1944: The diurnal variation of warm-frontal precipitation and thunderstorms. *Quart. J. Roy. Meteorol. Soc.*, **70**, 129-137.

Doswell, C. A. III, 1985: The operational meteorology of convective weather. Vol. II: Storm-scale analysis. NOAA Tech. Memo. ERL-ESG 15.

Doswell, C. A. III, 1987: The distinction between large scale and mesoscale contribution to severe convection: A case study example. *Wea. Forecasting*, **2**, 3-16.

Dudek, M. P., 1988: A numerical study of the formation of mesoscale convective systems. Ph.D. Dissertation, State University of New York at Albany, 266 pp.

Dudhia, J., M. W. Moncrieff and D. W. K. So, 1987: The two dimensional dynamics and simulation of West African squall lines. *Quart. J. Roy. Meteorol. Soc.*, **113**, 121-145.

Dudhia, J., 1989: Numerical study of convection observed during the Winter Monsoon Experiment using a two-dimensional model. *J. Atmos. Sci.*, **46**, 3077-3107.

Durran, D. R. and D. B. Weber, 1988: An investigation of the poleward edges of cirrus clouds associated with midlatitude jet streams. *Mon. Wea. Rev.*, **116**, 702-714.

Emanuel, K. A., 1983: The Lagrangian parcel dynamics of moist symmetric instability. *J. Atmos. Sci.*, **40**, 2368-2376.

Fankhauser, J. C., 1988: Estimates of thunderstorm precipitation efficiency from field measurements in CCOPE. *Mon. Wea. Rev.*, **116**, 663-684.

Flatau, P. J., G. J. Tripoli, J. Verlinde and W. R. Cotton, 1989: The CSU-RAMS cloud microphysics module: General theory and code documentation. Atmospheric Science Paper No. 451, Colorado State University, Dept. of Atmos. Sci., Fort Collins, Colorado, 88 pp.

Fletcher, N. H., 1962: *Physics of Rain Clouds.* Cambridge University Press, 386 pp.

Forbes, G. L., P. O. G. Heppner, J. J. Cahir and W. D. Lottes, 1984: Prediction of delayed-onset nocturnal convection based on air trajectories. Preprints, *Tenth Conf. on Weather Forecasting and Analysis*, Clearwater Beach, FL, Amer. Meteor. Soc., 474-479.

Fortune, M. A., 1989: The evolution of vortical patterns and vortices in mesoscale convective complexes. Atmospheric Science Paper No. 449, Colorado State University, Dept. of Atmos. Sci., Fort Collins, Colorado, 183 pp.

Fortune, M. A., W. R. Cotton and R. L. McAnelly, 1992: Frontal wave-like evolution in some mesoscale convective complexes. *Mon. Wea. Rev.*, **120**, 1279-1300.

Fovell, R. G., and Y. Ogura, 1988: Numerical simulations of a mid-latitude squall line in two dimensions. *J. Atmos. Sci.*, **45**, 3846-3879.

Frank, W. M., and J. L. McBride, 1989: The vertical distribution of heating in AMEX and GATE cloud clusters. *J. Atmos. Sci.*, **46**, 3464-3478.

Fritsch, J. M., and C. F. Chappell, 1980a: Numerical prediction of convectively driven mesoscale pressure systems. Part I: Convective parameterization. *J. Atmos. Sci.*, **37**, 1722-1733.

Fritsch, J. M., and C. F. Chappell, 1980b: Numerical prediction of convectively driven mesoscale pressure systems. Part II: Mesoscale model. *J. Atmos. Sci.*, **37**, 1734-1762.

Fritsch, J. M., and R. A. Maddox, 1981b: Convectively driven mesoscale weather systems aloft. Pat II: Numerical simulations. *J. Appl. Meteor.*, **20**, 20-26.

Fritsch, J. M., R. J. Kane and C. R. Chelius, 1986: The contribution of mesoscale convective weather systems to the warm-season precipitation in the United States. *J. Clim. Appl. Meteor.*, **25**, 1333-1345.

Fujita, T., 1959: Precipitation and cold air production in mesoscale thunderstorm systems. *J. Meteor*, **16**, 454-466.

Gallus, W. A., Jr., 1993: The dynamics of circulations within the stratiform regions of squall lines. Atmos. Sci. Paper No. 537, Colorado State University, 290 pp.

Gamache, J. F. and R. A. Houze, 1983: Water budget of a mesoscale convective system in the tropics. *J. Atmos. Sci.*, **40**, 1835-1850.

Gao, K., D.-L. Zhang, M. W. Moncrieff and H.-R. Cho, 1990: Mesoscale momentum budget in a midlatitude squall line: A numerical case study. *Mon. Wea. Rev.*, **118**, 1011-1028.

Gill, D. O., 1992: A user's guide to the Penn State/NCAR mesoscale modeling system. NCAR Tech. Note NCAR/TN-381+IA.

Giorgi, F., 1991: Sensitivity of simulated summertime precipitation over the western United States to different physics parameterizations. *Mon. Wea. Rev.*, **119**, 2870-2888.

Green, J. L., 1989: Analysis of surface pressure features during an episode of mesoscale convective systems. M.S. Thesis. Texas Tech. University, 75 pp.

Grell, G. A., Y.-H. Kuo and R. Pasch, 1991: Semiprognostic tests of cumulus parameterization schemes in the middle latitudes. *Mon. Wea. Rev.*, **119**, 5-31.

Grell, G. A., 1993: Prognostic evaluation of assumptions used by cumulus parameterizations. *Mon. Wea. Rev.*, **121**, 764-787.

Haltiner, G. J. and R. T. Williams, 1980: *Numerical prediction and dynamic meteorology.* John Wiley & Sons, Inc., 477 pp.

Hane, C. E., C. J. Kessinger and P. S. Ray, 1987: The Oklahoma squall line of 19 May 1977. Part II: Mechanisms for maintenance of the region of strong convection. *J. Atmos. Sci.*, **44**, 2866-2883.

Haynes, P. H. and M. E. McIntyre, 1987: On the evolution of vorticity and potential vorticity in the presence of diabatic heating and other forces. *J. Atmos. Sci.*, **44**, 828-841.

Hertenstein, R. F. A. and W. H. Schubert, 1991: Potential vorticity anomalies associated with squall lines. *Mon. Wea. Rev.*, **119**, 1663-1672.

Hoke, J. E. and R. A. Anthes, 1976: The initialization of numerical models by a dynamic-initialization technique. *Mon. Wea. Rev.*, **104**, 1551-1556.

Holle, R. L., A. I. Watson, R. Ortiz and R. E. Lopez, 1990: Spatial patterns of lightning, radar echoes, and severe weather in mesoscale convective systems. Preprints, *Sixteenth Conf. on Severe Local Storms*, Kananaskis, Alberta, Amer. Meteor. Soc., 721-726.

Houze, R. A., Jr., C.-P. Cheng, C. A. Leary and J. F. Gamache, 1980: Diagnosis of cloud mass and heat fluxes from radar and synoptic data. *J. Atmos. Sci.*, **37**, 754-773.

Houze, R. A., B. F. Smull, and P. Dodge, 1990: Mesoscale organization of springtime rainstorms in Oklahoma. *Mon. Wea. Rev.*, **118**, 613-654.

Hoxit, L. R., 1975: Diurnal variations in planetary boundary-layer winds over land. *Boundary-Layer Meteor.*, **8**, 21-38.

Hoxit, L. R., C. F. Chappell, and J. M. Fritsch, 1976: Formation of mesolows or pressure troughs in advance of cumulonimbus clouds. *Mon. Wea. Rev.*, **104**, 1419-1428.

Hsie, E.-Y., R. A. Anthes and D. Keyser, 1984: Numerical simulation of frontogenesis in a moist atmosphere. *J. Atmos. Sci.*, **41**, 2581-2594.

Hung, R. J. and Y. D. Tsao, 1991: Study of Ardmore, Oklahoma, storm clouds. I. Convective storm initiation and development based on the remote sensing gravity-wave-induced convection. *Int. J. Remote Sensing*, **12**, 831-862.

Johnson, R. H., 1976: The role of convective-scale precipitation downdrafts in cumulus and synoptic-scale interactions. *J. Atmos. Sci.*, **33**, 1890-1910.

Johnson, R. H., 1980: Diagnosis of convective-scale and mesoscale motions during Phase III of GATE. *J. Atmos. Sci.*, **37**, 733-753.

Kalb, M. W., 1985: Results from a limited area mesoscale numerical simulation for 10 April 1979. *Mon. Wea. Rev.*, **113**, 1644-1662.

Kalb, M. W., 1987: The role of convective parameterization in the simulation of a Gulf coast precipitation system. *Mon. Wea. Rev.*, **115**, 214-234.

Kain, J. S. and J. M. Fritsch, 1990: A one-dimensional entraining/detraining plume model and its application in convective parameterization. *J. Atmos. Sci.*, **47**, 2784-2802.

Kain, J. S. and J. M. Fritsch, 1992: The role of the convective "trigger function" in numerical forecasts of mesoscale convective systems *Meteor. Atmos. Phys.*, **49**, 93-106.

Kain, J. S. and J. M. Fritsch, 1994: Cumulus Parameterization. Meteor. Monographs, Amer. Meteor. Soc., in press.

Kane, R. J., C. R. Chelius, and J. M. Fritsch, 1987: Precipitation characteristics of mesoscale convective weather systems. *J. Clim. Appl. Meteor.*, **1345-1357.**,

Kaplan, M. L., J. W. Zack, V. C. Wong and J. J. Tuccillo, 1982: Initial results from a mesoscale atmospheric simulation system and comparisons with the AVE-SESAME I data set. *Mon. Wea. Rev.*, **110**, 1564-1590.

Kaplan, M. L., J. W. Zack, V. C. Wong and G. D. Coats, 1984: The interactive role of subsynoptic scale jet streak and planetary boundary layer processes in organizing an isolated convective complex. *Mon. Wea. Rev.*, **112**, 2212-2234.

Kessler, E., 1986: Thunderstorm Morphology and Dynamics. Thunderstorms: A Social, Scientific, and Technological Documentery, Vol. 2. University of Oklahoma Press., E. Kessler, ed., 412 pp.

Keyser, D. A. and D. R. Johnson, 1984: Effects of diabatic heating on the ageostrophic circulation of an upper tropospheric jet streak. *Mon. Wea. Rev.*, **112**, 1709-1724.

Keyser, D. and M. A. Shapiro, 1986: A review of the structure and dynamics of upper-level frontal zones. *Mon. Wea. Rev.*, **114**, 452-499.

Keyser, D. and L. W. Uccellini, 1987: Regional models: Emerging research tools for the synoptic meteorologist. *Bull. Amer. Meteor. Soc.*, **68**, 306-320.

Keyser, D., B. D. Schmidt and D. G. Duffy, 1989: A technique for representing three-dimensional vertical circulations in baroclinic disturbances. *Mon. Wea. Rev.*, **117**, 2463-2494.

Koch, S. E., 1985: Ability of a regional-scale model to predict the genesis of intense mesoscale convective systems. *Mon. Wea. Rev.*, **113**, 1693-1713.

Koch, S. E., and R. E. Golus, 1988: A mesoscale gravity wave event observed during CCOPE. Part I: Multiscale statistical analysis of wave characteristics. *Mon. Wea. Rev.*, **116**, 2527-2544.

Koch, S. E., R. E. Golus and P. B. Dorian, 1988: A mesoscale gravity wave event observed during CCOPE. Part II: Interactions between mesoscale convective systems and antecedent waves. *Mon. Wea. Rev.*, **116**, 2545-2569.

Koch, S. E. and P. B. Dorian, 1988: A mesoscale gravity wave event observed during CCOPE. Part III: Wave environment and possible source mechanisms. *Mon. Wea. Rev.*, **116**, 2570-2592.

Koch, S. E., 1993: Report of the proceedings of the colloquium and workshop on multiscale coupled modeling. NASA Conf. Publication 3217, S. E. Koch, ed.

Koch, S. E., M. DesJardins and P. J. Kocin, 1983: An interactive Barnes objective map analysis scheme for use with satellite and conventional data. *J. Clim. Appl. Meteor.*, **22**, 1487-1503.

Kocin, P. J., L. W. Uccellini, J. W. Zack and M. L. Kaplan, 1984: Recent examples of mesoscale numerical forecasts of severe weather events along the east coast. NASA Tech. Memo. 86172, Nov. 1984, 57 pp.

Kocin, P. J., L. W. Uccellini and R. A. Petersen, 1986: Rapid evolution of a jet streak circulation in a pre-convective environment. *Meteor. Atmos. Phys.*, **35**, 103-138.

Kuo, Y.-H., L. Cheng and J. -W. Bao, 1988: Numerical Simulation of the 1981 Sichuan Flood. Part I: Evolution of a Mesoscale Southwest Vortex. *Mon. Wea. Rev.*, **116**, 2481-2504.

Kuo, Y.-H. and R. J. Reed, 1988: Numerical simulation of an explosively deepening cyclone in the eastern Pacific. *Mon. Wea. Rev.*, **116**, 2081-2105.

Lanczos, D., 1956: *Applied Analysis.* Prentice-Hall, 539 pp.

Leary, C. A. and T. M. Bals, 1989: Evolution of the 3-4 June PRE-STORM mesoscale convective system. Preprints, *24th Conf. on Radar Meteorology*, Tallahassee, Amer. Meteor. Soc., 471-474.

Leary, C. A. and T. M. Bals, 1990: Physical processes associated with precipitation structuure in the 3-4 June 1985 OK PRE-STORM mesoscale convective system. Preprints, *Fourt Conf. on Mesoscale Processes*, Boulder, CO, Amer. Meteor. Soc., 210-211.

Lemaitre, Y. and G. Scialom, 1991: Three-dimensional mesoscale circulation within a convective post-frontal system. Possible role of Conditional Symmetric Instability for triggering convective motion. *Quart. J. Roy. Meteorol. Soc.*, **118**, 71-99.

Lin, Y.-L., R.D. Farley and H. D. Orville, 1983: Bulk parameterization of the snow field in a cloud model. *J. Climate Appl. Meteor.*, **22**, 1065-1092.

Lindzen, R. S., 1974: Wave-CISK in the tropics. *J. Atmos. Sci.*, **31**, 156-179.

Linzden, R. S. and M. Fox-Rabinovitz, 1989: Consistent vertical and horizontal resolution. *Mon. Wea. Rev.*, **117**, 2575-2583.

Lindstrom, S. S. and T. E. Nordeng, 1992: Parameterized slantwise convection in a numerical model. *Mon. Wea. Rev.*, **120**, 742-756.

Loehrer, S. M., 1992: The surface pressure features and precipitation structure of PRE-STORM mesoscale convective systems. Atmos. Sci. Paper No. 518, Colorado State University, 297 pp.

Lord, S., 1978: Development and observational verification of a cumulus cloud parameterization. Ph.D. dissertation, University of California, Los Angeles, 359 pp.

Maddox, R. A., C. F. Chappell and L. R. Hoxit, 1979: Synoptic and meso-α scale aspects of flash flood events. *Bull. Amer. Meteor. Soc.*, **60**, 115-123.

Maddox, R. A., 1980: Mesoscale convective complexes. *Bull. Amer. Meteor. Soc.*, **61**, 1374-1400.

Maddox,R. A., D. J. Perkey, and J. M. Fritsch, 1981: Evolution of upper tropospheric features during the development of a mesoscale convective complex. *J. Atmos. Sci.*, **38**, 1664-1674.

Maddox, R. A. and C. A. Doswell, 1982: An examination of jet stream configurations, 500 mb vorticity advection and low-level thermal advection patterns during extended periods of intense convection. *Mon. Wea. Rev.*, **110**, 184-197.

Maddox, R. A., 1983: Large-scale meteorological conditions associated with midlatitude, mesoscale convective complexes. *Mon. Wea. Rev.*, **111**, 1475-1493.

Manning, K. W. and P. L. Haagenson, 1992: Data ingest and objective analysis for the PSU/NCAR modeling system: Programs DATAGRID and RAWINS. NCAR Tech. Note, NCAR/TN-376+IA, 209 pp.

Mapes, B. E., 1993: Gregarious tropical convection. *J. Atmos. Sci.*, **50**, 2026-2037.

McAnelly, R. L., and W. R. Cotton, 1986: Meso-β-scale characteristics of an episode of meso-α-scale convective complexes. *Mon. Wea. Rev.*, **114**, 1740-1770.

McAnelly, R. L., and W. R. Cotton, 1990: Dual-Doppler analysis of the maturing stage of the "random convection" MCC of 4 June 1985 in PRE-STORM. Preprints, *Fourt Conf. on Mesoscale Processes*, Boulder, CO, Amer. Meteor. Soc., 212-213.

McAnelly, R. L., and W. R. Cotton, 1992: Early growth of mesoscale convective complexes: A meso-β-scale cycle of convective precipitation? *Mon. Wea. Rev.*, **120**, 1851-1877.

McAnelly, R. L., Nachamkin, J. E. and W. R. Cotton, 1993: Upscale growth processes in a mesoscale convective system. Preprints, *26th International Conf. on Radar Meteorology*, Norman, OK, Amer. Meteor. Soc., 94-95.

Means, L. L., 1952: On thunderstorm forecasting in the central United States. *Mon. Wea. Rev.*, **80**, 165-189.

Meitin, J. G. and J. B. Cunning, 1985: The Oklahoma-Kansas preliminary regional experiment for STORM-Central (OK PRE-STORM), Volume I. Daily operations summary. NOAA Tech. Memo. ERL ESG-20, Dept. of Commerce, Weather Research Program, Boulder, Colorado, 313pp.

Merritt, J. H. and J. M. Fritsch, 1984: On the movement of the heavy precipitation areas of mid-latitude mesoscale convective complexes. 10th Conf. on Wx Fcsting and Analysis, 529-536.

Meyers, M. P., P. J. DeMott and W. R. Cotton, 1992: New primary ice-nucleation parameterizations in an explicit cloud model. *J. Appl. Meteor.*, **31**, 708-721.

Miner, B. D., 1992: Opposing mesoscale flows in a broken midlatitude squall line. Atmos. Sci. Paper No. 519, Colorado State University, 115 pp.

Molinari, J. and T. Corsetti, 1985: Incorporation of cloud-scale and mesoscale downdrafts into a cumulus parameterization: Results of one- and three-dimensional integrations. *Mon. Wea. Rev.*, **113**, 485-501.

Molinari, J. and M. Dudek, 1986: Implicit versus explicit convective heating in numerical weather prediction models. *Mon. Wea. Rev.*, **114**, 1822-1831.

Molinari, J. and M. Dudek, 1992: Parameterization of convective precipitation in mesoscale numerical models: A critical review. *Mon. Wea. Rev.*, **120**, 326-344.

Moore, J. T. and G. E. Vanknowe, 1992: The effect of jet-streak curvature on kinematic fields. *Mon. Wea. Rev.*, **120**, 2429-2441.

Nachamkin, J. E., 1992: The upscale evolution of a midlatitude mesoscale convective complex. M.S. Thesis, Colorado State University, Dept. of Atmos. Sci., 122pp.

Nagata, M. and Y. Ogura, 1991: A modeling case study of interaction between heavy precipitation and a low-level jet over Japan in the Baiu season. *Mon. Wea. Rev.*, **119**, 1309-1336.

Namias, J. and P. F. Clapp, 1949: Confluence theory of the high tropospheric jet stream. *J. Meteor.*, **6**, 330-336.

Nicolini, M., K. M. Waldron and J. Paegle, 1993: Diurnal oscillation of low-level jets, vertical motion, and precipitation: A model case study. *Mon. Wea. Rev.*, **121**, 2588-2610.

Ninomiya, K., T. Akiyama and M. Ikawa, 1988: Evolution and fine structure of a long-lived meso-alpha-scale convective system in a Baiu frontal zone. Part II: Meso-gamma-scale characteristics of precipitation. *J. Meteor. Soc. Japan*, **66**, 351-371.

NOAA, 1985: *Storm Data*, U. S. Dept. of Commerce, Environmental Data and Information Service, National Climatic Data Center, Asheville, NC, 28801, Vol. 27, No. 6.

Nordeng, T. E., 1987: The effect of vertical and slantwise convection on the simulation of polar lows. *Tellus*, **39A**, 354-375.

Ogura, Y., H.-M. Juang, K.-S. Zhang and S.-T. Soong, 1982: Possible triggering mechanisms for severe storms in SESAME-AVE IV (9-10 May 1979). *Bull. Amer. Meteor. Soc.*, **63**, 503-515.

Ogura, Y. and J.-Y. Jiang, 1985: A modeling study of heating and drying effects of convective clouds in an extratropical mesoscale convective system. *J. Atmos. Sci.*, **42**, 2478-2493.

Orlanski, I. and B. B. Ross, 1984: The evolution of an observed cold front. Part II: Mesoscale dynamics. *J. Atmos. Sci.*, **41**, 1669-1703.

Perkey, D. J. and R. A. Maddox, 1985: A numerical investigation of a mesoscale convective system. *Mon. Wea. Rev.*, **113**, 553-566.

Persson, P. O. G. and T. T. Warner, 1991: Model generation of spurious gravity waves due to inconsistency of the vertical and horizontal resolution. *Mon. Wea. Rev.*, **119**, 917-935.

Pielke, R. A., W. R. Cotton, R. L. Walko, C. J. Tremback, W. A. Lyons, L. D. Grasso, M. E. Nicholls, M. D. Moran, D. A. Wesley, T. J. Lee and J. H. Copeland, 1992: A comprehensive meteorological modeling system – RAMS. *Meteor. Atmos. Phys.*, **49**, 69-91.

Pointin, Y., 1985: Numerical simulation of organized convection. Part I: Model description and preliminary comparisons with squall line observations. *J. Atmos. Sci.*, **42**, 155-172.

Potter, B. E., 1991: Improvements to a commonly used cloud microphysical bulk parameterization. *J. Appl. Meteor.*, **30**, 1040-1042.

Ralph, F. M. and P. J. Neiman, 1993: Wind profiler observations of a mesoscale convective system. Preprints, *26th th International Conf. on Radar Meteorology*, Norman, OK, Amer. Meteor. Soc., 567-569.

Raymond, D. J., 1987: A forced gravity wave model of self-organizing convection. *J. Atmos. Sci.*, **44**, 3528-3543.

Reiter, E. R., 1963: *Jet Stream Meteorology.* University of Chicago Press, 515 pp.

Rockwood, A. A., D. L. Bartels and R. A. Maddox, 1984: Precipitation characteristics of a dual mesoscale convective complex. NOAA Tech. Memo. ERL ESG-6. 50 pp.

Rosenthal, S. L., 1979: The sensitivity of simulated hurricane development to cumulus parameterization details. *Mon. Wea. Rev.*, **107**, 193-197.

Ross, B. B. and I. Orlanski, 1982: The evolution of an observed cold front. Part I: Numerical simulation. *J. Atmos. Sci.*, **39**, 296-327.

Rutledge, S. A. and P. V. Hobbs, 1983: The mesoscale and microscale structure and organization of clouds and precipitation in midlatitude cyclones. VIII: A model for the "Seeder-Feeder" process in warm-frontal rainbands. *J. Atmos. Sci.*, **40**, 1185-1206.

Rutledge, S. A. and R. A. Houze, Jr., 1987: A diagnostic modeling study of the trailing stratiform region of a midlatitude squall line. *J. Atmos. Sci.*, **2640-2656.**,

Ryan, B. F., G. J. Tripoli and W. R. Cotton, 1990: Convection in high stratiform cloud bands. Some numerical experiments. *Quart. J. Roy. Meteorol. Soc.*, **116**, 943-964.

Sanders, F., 1993: A case of frontogenesis and local flooding. Preprints, *Seventeenth Conf. on Severe Local Storms*, St. Loius, MO, Amer. Meteor. Soc., 602-604.

Sanders, F. and D. O. Blanchard, 1993: The origin of a severe thunderstorm in Kansas on 10 May 1985. *Mon. Wea. Rev.*, **121**, 133-149.

Schmidt, J. M. and W. R. Cotton, 1990: Interactions between upper and lower atmospheric gravity waves on squall line structure and maintenance. *J. Atmos. Sci.*, **47**, 1205-1222.

Schubert, W. H., 1974: Cumulus parameterization theory in terms of feedback and control. Atmospheric Science Paper No. 226, Colorado State University, Dept. of Atmos. Sci., Fort Collins, Colorado, 19 pp.

Shapiro, M. A., 1978: Further evidence of the mesoscale and turbulent structure of upper-level jet stream-frontal zone systems. *Mon. Wea. Rev.*, **104**, 892-906.

Shapiro, M. A., 1982: *Mesoscale Weather Systems of the Central United States.* CIRES, Univ. of Colorado/NOAA, Boulder, CO, 78 pp.

Shen, R., E. R. Reiter and J. F. Bresch, 1986: Vertical interpolation of meteorological variables. *Mon. Wea. Rev.*, **114**, 123-134.

Simpson, J., N. E. Westcott, R. J. Clerman and R. A. Pielke, 1980: On cumulus mergers. *Arch. Met. Geoph. Biocl. Ser. A*, **29**, 1-40.

Simpson, J., Th. D. Keenan, B. Ferrier, R. H. Simpson and G. J. Holland, 1993: Cumulus mergers in the maritime continent region. *Meteorol. Atmos. Phys.*, **51**, 73-99.

Slingo, J. M., 1987: The development and verification of a cloud prediction scheme for the ECMWF model. *Quart. J. Roy. Meteorol. Soc.*, **113**, 899-927.

Smull, B. F., and R. A. Houze, 1987a: Dual-Doppler radar analysis of a midlatitude squall line with a trailing region of stratiform rain. *J. Atmos. Sci.*, **44**, 2128-2148.

Smull, B. F., and R. A. Houze, 1987b: Rear inflow in squall lines with trailing stratiform precipitation. *Mon. Wea. Rev.*, **115**, 2869-2889.

Smull, B. F. and J. A. Augustine, 1989: Structure and environment of a non-squall mesoscale convective complex observed during PRE-STORM. Preprints, *24th Conf. on Radar Meteorology*, Tallahassee, Amer. Meteor. Soc., 502-504.

Smull, B. F. and D. P. Jorgensen, 1990: Pressure and buoyancy perturbations near an intense wake low in a midlatitude mesoscale convective system. Preprints, *Fourt Conf. on Mesoscale Processes*, Boulder, CO, Amer. Meteor. Soc., 214-215.

Smull, B. F., D. P. Jorgensen and C. E. Hane, 1991: Comparison of retrieved pressure and buoyancy perturbations with in situ observations of an intense wake low in a midlatitude mesoscale convective system. Preprints, *25th Conf. on Radar Meteorology*, Paris, Amer. Meteor. Soc., 135-138.

Smull, B. F. and J. A. Augustine, 1993: Multiscale analysis of a mature mesoscale convective complex. *Mon. Wea. Rev.*, **121**, 103-132.

Sortais, J.-L., J.-P. Cammas, X. D. Yu, E. Richard and R. Rosset, 1993: A case study of coupling between low- and upper-level jet-front systems: Investigation of dynamical and diabatic processes. *Mon. Wea. Rev.*, **121**, 2239-2253.

Stensrud, D. J., and R. A. Maddox, 1988: Opposing mesoscale circulations: A case study. *Wea. Forecasting*, **3**, 189-204.

Stensrud, D. J., 1992: Southward burst mesoscale convective systems: An observational and modeling study. Ph.D. Dissertation, Dept. of Meteorology, Pennsylvania State University, 184 pp.

Stumpf, G. J., 1988: Surface pressure features associated with a mesoscale convective system in OK PRE-STORM. M.S. Thesis, Colorado State University, Dept. of Atmos. Sci., 148 pp.

Stumpf, G. J. and R. H. Johnson, 1989: Lower tropospheric profiling needs in relation to the initiation of mesoscale convective systems. Preprints, *Conf. on Profiling Needs*, Boulder, CO, Amer. Meteor. Soc.

Stumpf, G. J., R. H. Johnson, and B. F. Smull, 1991: The wake low in a midlatitude mesoscale convective system having complex convective organization. *Mon. Wea. Rev.*, **119**, 134-158.

Thorpe, A. J. and S. A. Clough, 1991: Mesoscale dynamics of cold fronts: Structures described by dropsoundings in FRONTS 87. *Quart. J. Roy. Meteorol. Soc.*, **117**, 903-941.

Tollerud, E. I., J. A. Augustine and B. D. Jamison, 1992: Cloud top characteristics of mesoscale convective systems in 1986. Preprints, *Symp. on Weather Forecasting*, Atlanta, GA, Amer. Meteor. Soc., J3-J7.

Tollerud, E. I. and R. S. Collander, 1993: Mesoscale convective systems and extreme rainfall in the central United States. *IAHS Publ. no. 213*, 11-19.

Tremback, C. J., 1990: Numerical simulation of a mesoscale convective complex: Model development and numerical results. Atmospheric Science Paper No. 465, Colorado State University, Dept. of Atmos. Sci., Fort Collins, Colorado, 247 pp.

Tremback, C. J., R. Hertenstein, and W. R. Cotton, 1992: Analysis and simulation of the 3-4 June 1985 series of MCCs. Preprints, *Fifth Conf. on Mesoscale Processes*, Atlanta, GA, Amer. Meteor. Soc., 369-370.

Trier, S. B., and D. B. Parsons, 1993: Evolution of environmental conditions preceding the development of a nocturnal mesoscale convective complex. *Mon. Wea. Rev.*, 121 1078-1098.

Tripoli, G. J., 1986: A numerical investigation of an orogenic mesoscale convective system. Ph.D. Thesis, Dept. of Atmos. Sci., Colorado State Univ., 290 pp.

Uccellini, L. W. and D. R. Johnson, 1979: The coupling of upper and lower tropospheric jet streaks and implications for the development of severe convective storms. *Mon. Wea. Rev.*, **107**, 682-703.

Uccellini, L. W., R. A. Petersen, K. F. Brill, P. J. Kocin and J. J. Tuccillo, 1987: Synergistic interactions between an upper-level jet streak and diabatic processes that influence the development of a low-level jet and a secondary coastal cyclone. *Mon. Wea. Rev.*, **115**, 2227-2261.

Uccellini, L. W. and S. E. Koch, 1987: The synoptic setting and possible energy sources for mesoscale wave disturbances. *Mon. Wea. Rev.*, **115**, 721-729.

Uccellini, L. W., 1990: The relationship between jet streaks and severe convective systems. Preprints, *Sixteenth Conf. on Severe Local Storms*, Kananaskis, Alberta, Amer. Meteor. Soc., 121-130.

Wakimoto, R. M., 1985: Forecasting dry microburst activity over the High Plains. *Mon. Wea. Rev.*, **113**, 1131-1143.

Wang, W. and T. T. Warner, 1988: Use of four-dimensional data assimilation by newtonian relaxation and latent-heat forcing to improve a mesoscale-model precipitation forecast: A case study. *Mon. Wea. Rev.*, **116**, 2593-2613.

Zack, J. W., M. L. Kaplan and V. C. Wong, 1985: A comparison of the prognostic performance of several cumulus parameterizations in mesoscale simulations of the 10 April 1979 Sesame I case. Preprints, *Seventh Conf. on Numerical Weather Prediction*, Montreal, Amer. Meteor. Soc., 415-422.

Zack J. W. and M. L. Kaplan, 1987: Numerical simulations of the subsynoptic features associated with the AVE-SESAME I case. Part I: The preconvective environment. *Mon. Wea. Rev.*, **115**, 2367-2394.

Zehr, R. M., 1992: Tropical cyclogenesis in the western North Pacific. Ph.D. Dissertation, Colorado State University, Dept. of Atmos. Sci., 213 pp.

Zhang, D.-L. and R.A. Anthes, 1982: A high-resolution model of the planetary boundary layer – Sensitivity tests and comparisons with SESAME-79 data. *J. Appl. Meteor.*, **21**, 1594-1609.

Zhang D.-L., H.-R. Chang, N. L. Seaman, T. T. Warner and J. M. Fritsch, 1986: A two-way interactive nesting procedure with variable terrain resolution. *Mon. Wea. Rev.*, **114**, 1330-1339.

Zhang D.-L. and J. M. Fritsch, 1986a: Numerical simulation of the meso-beta scale structure and evolution of the 1977 Johnstown flood. Part I: Model description and verification. *J. Atmos. Sci.*, **43**, 1913-1943.

Zhang D.-L. and J. M. Fritsch, 1986b: A case study of the sensitivity of numerical simulation of mesoscale convective systems to varying initial conditions. *Mon. Wea. Rev.*, **114**, 2418-2431.

Zhang, D.-L., and J. M. Fritsch, 1987: Numerical simulation of the mesoβ-scale structure and evolution of the 1977 Johnstown flood. Part II: Inertially stable warm-core vortex and the mesoscale convective complex. *J. Atmos. Sci.*, **44**, 2593-2612.

Zhang, D.-L., and J. M. Fritsch, 1988a: Numerical sensitivity experiments of varying model physics on the structure, evolution and dynamics of two mesoscale convective systems. *J. Atmos. Sci.*, **45**, 261-293.

Zhang, D.-L. and J. M. Fritsch, 1988b: Numerical simulation of the meso-beta scale structure and evolution of the 1977 Johnstown flood. Part III: Internal gravity waves and the squall line. *J. Atmos. Sci.*, **45**, 1252-1268.

Zhang, D.-L., and J. M. Fritsch, 1988c: A numerical investigation of a convectively generated inertially stable, extratropical warm-core mesovortex over land. Part I: Structure and evolution. *Mon. Wea. Rev.*, **116**, 2660-2687.

Zhang, D.-L., E.-Y. Hsie and M. W. Moncrieff, 1988: A comparison of explicit and implicit predictions of convective and stratiform precipitating weather systems with a meso-β-scale numerical model. *Quart. J. Roy. Meteorol. Soc.*, **114**, 31-60.

Zhang, 1989: The effect of parameterized ice microphysics on the simulation of vortex circulation with a mesoscale hydrostatic model. *Tellus*, **41A**, 132-147.

Zhang, D.-L., K. Gao and D. B. Parsons, 1989: Numerical simulation of an intense squall line during 10-11 June 1985 PRE-STORM. Part I. Model verification. *Mon. Wea. Rev.*, **117**, 960-994.

Zhang, D.-L., and K. Gao, 1989: Numerical simulation of an intense squall line during 10-11 June 1985 PRE-STORM. Part II: Rear inflow, surface pressure perturbations and stratiform precipitation. *Mon. Wea. Rev.*, **117**, 2067-2094.

Zhang, D.-L. and H.-R. Cho, 1992: The development of negative moist potential vorticity in the stratiform region of a simulated squall line. *Mon. Wea. Rev.*, **120**, 1322-1341.

Zhang, D. -L., 1992: The formation of a cooling-induced mesovortex in the trailing stratiform region of a midlatitude squall line. *Mon. Wea. Rev.*, **120**, 2763-2785.

Ziegler, C. and C. Hane, 1993: Convective initiation in the dryline environment. Preprints, *26th International Conf. on Radar Meteorology*, Norman, OK, Amer. Meteor. Soc., 199-201.

Zipser, E. J., 1977: Mesoscale and convective-scale downdrafts as distinct components of squall-line structure. *Mon. Wea. Rev.*, **105**, 1568-1589.

APPENDIX A

List of Acronyms

ADP – Automated Data Processing

CIN – Convective INhibition

FAA-604 – Federal Aviation Administration surface airway observations

FCT – Fritsch-Chappell Trigger

GOES – Geostationary Operational Environmental Satellite

LDT – Lifting Depth Trigger

MM4 – PSU/NCAR Mesoscale Model version 4

MCC – Mesoscale Convective Complex

MCS – Mesoscale Convective System

MPV – Moist Potential Vorticity NASA – National Aeronautics and Space Administration

NCAR – National Center fo Atmospheric Research

NCDC – National Climatic Data Center

NMC – National Meteorological Center

NSSL – National Severe Storms Laboratory

PAM – Portable Automated Mesonet

PBL – Planetary Boundary Layer

PRE-STORM – Oklahoma-Kansas Preliminary Regional Experiment for STORM-Central

RAMS – Regional Atmospheric Modeling System

SAM – Surface Automated Mesonet

SCC – Series of Convective Complexes

APPENDIX B

Modifications to RAWINS

The program RAWINS combines surface and upper air data with a gridded first guess analysis to produce model initial conditions. A few modifications were made to the standard version of RAWINS (Manning and Haagenson 1992) to produce more realistic initial conditions for the present case study.

- In order to be consistent with the rest of the MM4 modeling system, virtual temperature was used in the computations of surface and sea level pressure.
- The standard version of RAWINS automatically eliminates super-adiabatic lapse rates. Super-adiabatic lapse rates near the surface were quite common across much of the nested grid region at 0000 UTC. Because RAWINS analyzes relative humidity (rather than specific humidity), the automatic replacement of super-adiabatic lapse rates with dry-adiabatic lapse rates caused an unrealistic reduction in low-level moisture. Super-adiabatic lapse rates were, therefore, permitted at the surface. The resulting low-level moisture fields were then more reasonable.
- The number of scan passes performed by the successive correction objective analysis was increased from four to five.
- Subroutine SORT (Manning and Haagenson 1992) is a black-box routine which rearranges data levels within a sounding report, based on some objective criteria. The code was modified so that SORT was not called to check bogus (user-supplied) soundings.
- The code was modified to use surface pressure and station elevation when incorporating bogus sounding data, rather than the default use of sea level pressure and model elevation.

APPENDIX C

Modifications to INTERP

INTERP is the MM4 modeling system program which vertically interpolates gridded data between coordinate systems. As part of the pre-processor, INTERP converts data from the pressure-surface analyses produced by RAWINS to the analyses on σ-surfaces used as model input. The interpolation used by INTERP is a linear function of the logarithm of pressure. Shen *et al.* (1986) have shown that using a higher order function of pressure produces more accurate results particularly for low-resolution models, but also where there are strong vertical gradients such as near jet cores. Because of the significance of jets in the present case, INTERP's default interpolation was replaced with a second order Lagrange polynomial interpolation (Shen *et al.* 1986, Equation 19). For the 23 vertical levels used in this study, little difference between the two methods was found except in regions with sharp maxima in wind speed and moisture (not shown). The modified scheme produced more realistic wind analyses, particularly in the vicinity of the upper level jets.

While developing initial data fields for this case, it was noticed that unobserved, sharp discontinuities appeared in some of the low-level σ-surface fields. (This was particularly noticeable over Kansas and New Mexico). These discontinuities occurred near where RAWINS pressure-surface analyses levels intersected the sloping terrain. Because RAWINS doesn't make use of surface data when performing its pressure-level analyses, the fields can differ from the observed where the data must be extrapolated from a distant sounding site. INTERP, meanwhile, vertically interpolates data to a σ-surface from the two pressure surfaces which the σ-level lies between. The lower pressure surface may be the surface analysis. Problems can arise when the surface pressure is just higher than a RAWINS analysis level and there are significant vertical or horizontal meteorological gradients. For example, if the surface pressure at La Junta, Colorado is 851 mb, the next-to-lowest σ-surface data are interpolated from the 850 mb and 825 mb analyses. The 850 mb analysis there is influenced only by distant sounding data or the first guess field. Therefore, the interpolation scheme was modified so that only pressure surfaces more than

20 mb above the surface were used in the interpolation. Instead, the scheme would use the surface analysis as the lower data level. In effect, it is assumed that surface data are more representative of the lowest 20 mb, than interpolated and perhaps distant sounding data. A better fix would be to incorporate the surface analysis into the RAWINS pressure-level analyses, however, this is not a trivial task. The new modification significantly reduced the analyses discontinuities.